Group III-nitride based UVC LEDs and lasers with transparent AlGaN:Mg layers and tunnel junctions grown by MOVPE

vorgelegt von

Master of Science in Physics

Christian Kuhn

an der Fakultät II - Mathematik und Naturwissenschaften
der Technischen Universität Berlin
zur Erlangung des akademischen Grades

Doktor der Naturwissenschaften
-Dr. rer. nat.-

genehmigte Dissertation

Promotionsausschuss:

Vorsitzende:	Prof. Dr. Ulrike Woggon
Gutachter:	Prof. Dr. Michael Kneissl
	Dr. habil. Jean-Yves Duboz
	Prof. Dr. Markus Weyers

Tag der wissenschaftlichen Aussprache:

29.07.2020

Berlin 2020

Gruppe III-Nitrid basierte UVC LEDs und Laser mit transparenten AlGaN:Mg Schichten und Tunneldioden, hergestellt mittels MOVPE

In dieser Arbeit werden AlGaN-basierte Leuchtdioden (LEDs) und Laser mit Emissionswellenlängen im tiefen ultravioletten (UVC) Spektralbereich hergestellt, charakterisiert und optimiert. Dabei liegt die UV-Transparenz der Strukturen im Fokus, die hohe Lichtextraktionseffizienz für UVC LEDs ermöglicht und eine notwendige Bedingung für UVC Laserdioden darstellt, gleichzeitig aber aufgrund geringer elektrischer Leitfähigkeit herausfordernd ist. AlN und AlGaN Schichten sowie Heterostrukturen für Bauelemente werden mittels metallorganischer Gasphasenepitaxie hergestellt und der Einfluss einzelner Schichteigenschaften auf die Emissionseigenschaften von LEDs und Lasern systematisch analysiert.
Defektreduzierte (ELO) AlN Schichten auf Saphirsubstraten sowie AlN Substrate dienen als Basis für das epitaktische Wachstum von AlN und AlGaN Schichten. Durch die Analyse des Einflusses des Substratfehlschnittes auf die Oberflächenmorphologie konnten atomar glatte AlN Schichten auf beiden Substrattypen für Fehlschnittwinkel $< 0.17°$ reproduzierbar hergestellt werden. Die AlGaN:Si Wachstumsparameter Temperatur, Gasphasenzusammensetzung und Wachstumsrate wurden separat variiert. Leitfähige, homogene und glatte AlGaN:Si Schichten konnten durch die Umsetzung eines Übergitterkonzeptes mit je 10 s Wachstumsunterbrechung zur Erhöhung der Diffusionslänge von Metalladatomen realisiert werden. Pseudomorphe Laserstrukturen mit Dreifach-Quantenfilmen und Emissionswellenlängen von 270 nm wurden trotz stark kompressiver Verspannung mittels $Al_{0.7}Ga_{0.3}N$ Wellenleitern realisiert, wogegen geringere Aluminiumgehalte zu Teilrelaxation der Verspannung führen. Zudem konnte die Ausbildung von V-Pits als Streuzentren im Wellenleiter durch Erhöhung der Wachstumstemperatur von 900 °C auf 1080 °C erfolgreich reduziert werden. Schließlich wurde der Einfluss dieser einzelnen Optimierungsschritte auf die Lasereigenschaften analysiert. Optisch gepumpte UVC Laser mit spektraler Einschnürung, Laserschwelle sowie TE polarisierter Emission nahe 270 nm wurden gezeigt. Durch Reduktion der Oberflächenrauheit konnte die Laserschwelle schrittweise um den Faktor sieben reduziert werden.
Elektrische Injektion wurde mittels Elektrolumineszenz an transparenten UVC LEDs mit Wellenleitersystem experimentell analysiert und mit Simulationen optischer Moden und deren Verluste kombiniert. Durch die Variation von Zusammensetzung und Schichtdicke von Wellenleiter- bzw. Mantelschichten konnte ein optimiertes Heterostrukturdesign für UVC Laserdioden mit 200 nm dicken $Al_{0.76}Ga_{0.24}N$:Mg Mantelschichten gefunden werden, welches gleichzeitig effiziente Ladungsträgerinjektion und ausreichenden Modeneinschluss mit geringen optischen Verlusten von $40\,cm^{-1}$ ermöglicht.
Als unkonventionelle Alternative zu resistiven AlGaN:Mg Schichten wurden Tunneldioden (TJ) zur Löcherinjektion implementiert. Durch die anfängliche Optimierung individueller Komponenten wie der Zusammensetzung einer Zwischenschicht oder der Dotierlevel an der Grenzfläche, wurde die erste Demonstration AlGaN-basierter TJ-LEDs ermöglicht, die mit metallorganischer Gasphasenepitaxie gewachsen wurden. Auf dieser Basis wurde die Zwischenschichtdicke gezielt variiert, um Polarisationsladungen an der Grenzfläche zur Reduktion der Raumladungszonenbreite auszunutzen und die Tunnelwahrscheinlichkeit zu erhöhen. Mit 8 nm GaN Zwischenschichten wurde eine Spannungsreduktion um 20 V erreicht, sowie TJ-LEDs mit externer Quanteneffizienz von 2,3% und Emissionsleistung von 6,6 mW bei 268 nm und 0,26 mW bei 232 nm.

Group III-nitride based UVC LEDs and lasers with transparent AlGaN:Mg layers and tunnel junctions grown by MOVPE

In this work, AlGaN-based light-emitting diodes (LEDs) and lasers with emission wavelengths in the deep ultraviolet (UVC) spectral range are produced, analyzed, and optimized. Here, the focus is on the UV transparency of the structures, enabling high light extraction efficiency for UVC LEDs and being a necessary condition for UVC laser diodes, however at the same time challenging due to low electrical conductivity. AlN and AlGaN layers as well as heterostructures for devices are grown by metalorganic vapor phase epitaxy. A systematic analysis of the influence of individual layer properties on the emission properties of LEDs and lasers is provided.

Defect reduced (ELO) AlN layers on sapphire and AlN substrates serve as basis for the epitaxial growth of AlN and AlGaN layers. By analyzing the influence of substrate offcut on surface morphology, atomically smooth AlN layers are reproducibly obtained on both types of substrates for offcut angles $< 0.17°$. For the realization of n-type AlGaN:Si cladding layers, the influence of growth parameters such as temperature, gas phase composition and growth rate was separately analyzed. Highly conductive, uniform and smooth AlGaN:Si layers were obtained by the implementation of a superlattice concept with 10 s growth interruptions to increase the diffusion length of metal adatoms. Despite high compressive strain, pseudomorphic laser structures with three-fold quantum wells were obtained with emission wavelength at 270 nm by the choice of $Al_{0.7}Ga_{0.3}N$ waveguide composition, whereas lower aluminum contents lead to partial strain relaxation. In addition, the formation of V-pits acting as scattering centers in the waveguide was successfully reduced by increasing the growth temperature from 900 °C to 1080 °C. Finally, the influence of these individual optimization steps on laser properties was analyzed. Optically pumped UVC lasers with laser threshold, spectral linewidth reduction, and TE polarized emission above threshold were shown near 270 nm. By reducing the surface roughness, the laser thresholds were reduced by a factor of seven.

Electrical injection mechanisms were experimentally analyzed by electroluminescence measurements on transparent UVC LEDs with waveguide system, and combined with simulations of optical modes and the corresponding losses. By the variation of composition and layer thickness of waveguide and cladding layers an optimized heterostructure design for UVC laser diodes with 200 nm thick $Al_{0.76}Ga_{0.24}N$:Mg cladding layers was found. This design simultaneously enables efficient carrier injection and sufficient mode confinement with low optical losses of $40\,cm^{-1}$.

As an unconventional alternative to resistive AlGaN:Mg layers, tunnel junctions (TJ) in reverse bias configuration were implemented into the UVC LED heterostructure for efficient injection of holes. By the initial optimization of individual TJ components, such as doping concentrations at the TJ interface or the composition of an interlayer, the first demonstration of functional TJ-LEDs with AlGaN tunnel homojunction was achieved, as well as the first demonstration of AlGaN-based TJ-LEDs grown by metalorganic vapor phase epitaxy. Based on these devices, the interlayer thickness was varied to exploit polarization charges at the interface in order to reduce the space charge region width and enhance tunneling probabilities. Using 8 nm thick GaN interlayers, a reduction of the operation voltage by 20 V was achieved, as well as TJ-LEDs with external quantum efficiencies of 2.3% and emission powers of 6.6 mW at 268 nm and 0.26 mW at 232 nm.

Contents

1 Introduction and state-of-the-art of edge-emitting UV lasers

Electronic transitions like the creation and dissociation of chemical bonds or the excitation and recombination of carriers in wide band gap semiconductors are fundamental physical processes in the energy range of 3 eV to 6 eV that is covered by ultraviolet radiation. These basic mechanisms are directly translating into applications like sensing of gases or purification of water using UV light. The key advantage of AlGaN-based optoelectronic devices, such as UV LEDs and UV lasers, is the tunable emission wavelength that can be specifically adjusted to individual applications in the spectral range from 200 nm to 360 nm by the choice of the AlGaN material band gap. Further advantages of such semiconductor devices include small-size, low-cost, energy-efficient, non-toxic and therefore more environmentally-friendly device properties compared to conventional UV light sources, such as mercury lamps or excimer lasers [1]. In a large scale production, these properties strongly align with the United Nations' Sustainable Development Goals (SDG) [2]. As an example, GaN-based solid state lighting is nowadays already contributing to responsible consumption and production patterns described in SDG 12. Further materials and device developments are actively discussed at scientific conferences [3] that include contributions to balanced nutrition (SDG 2) by UVB plant growth lighting, to good health (SDG 3) by UVC sterilization of medical equipment or treatment of skin diseases, or to clean water (SDG 6) by UVC purification of drinking water [1]. Similar to the successful implementation of solid state lighting by visible LEDs in the past decade, such application fields are driving the development of UV LED device technology. Their market penetration can be expected within the next decade [4]. One further step is the development of UV laser diodes (LDs) [5], which is a current research topic and a focus of this work.

First of all, the current state-of-the-art of UV laser diode development is outlined, including the required components of UV laser diodes and the fundamental properties of laser emission. The basic concept of any laser includes a gain medium and a resonator. For most edge-emitting UV laser diode concepts, the gain medium is provided by AlGaN multiple quantum wells (MQW) and the resonator cavity is formed by cleaved or etched crystal facets that can be improved by high reflection coatings.

AlGaN-based lasers with optical excitation have been demonstrated in the UV spectral region (Figure 1.1) with emission wavelength down to 237 nm in the UVC range [6–8]. Using such optically pumped structures, laser emission properties can be studied in terms of threshold behavior of the emitted intensity combined with a reduction of the spectral linewidth, polarized emission (TE or TM), directional far field pattern, or the observation of longitudinal modes or photon coherence [9].

With electrical excitation, the shortest emission wavelength of AlGaN-based edge-emitting laser diodes at 336 nm was published by Hamamatsu Photonics in 2008 [10]

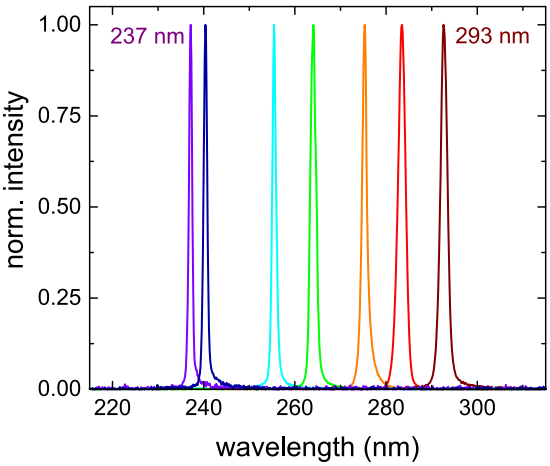

Figure 1.1: Emission spectra of UVC and UVB lasers above threshold with optical excitation by a 193 nm emitting ArF excimer source. (© 2018 Martin Martens. Reprinted from M. Martens, "Optical gain and modal loss in AlGaN based deep UV lasers", dissertation, TU Berlin.)

and amended in a conference presentation on a 326 nm emitting laser diode [11]. These LDs with UVA emission were measured at room temperature in pulsed operation. Especially within the UVB or UVC spectral range, no edge-emitting laser diode with current injection has been reported before 2019. Very recently, Zhang et. al. reported a 271.8 nm emitting UVC laser diode grown on bulk AlN with threshold current densities of 25 kA/cm^2 [12], Sato et. al. reported a 298 nm emitting UVB laser diode grown on lattice-relaxed $Al_{0.6}Ga_{0.4}N$/AlN/sapphire templates with threshold current densities of 41 kA/cm^2 [13]. Both reports include a demonstration of spectral linewidth reduction and TE polarized emission above threshold.

Lasing is characterized by a threshold behavior of the emitted intensity, as shown in Figure 1.2a. When the losses of the system are compensated at a certain threshold of the excitation, the emitted intensity is rapidly increasing. The threshold property is a necessary condition to prove lasing, with the exception of threshold-less high-β nanolasers. However, threshold observation is not sufficient as a threshold-like behavior can also result from other mechanisms, e. g. amplified spontaneous emission (ASE). Even in UVC LEDs a threshold-like behavior of the emitted light with increasing current can be observed, if the carrier injection efficiency is low. In presence of low-resistive parasitic current paths, a large amount of injected current can flow parallel to the radiative recombination channel of the MQW active region. If these parasitic current paths are saturated at a certain current level, the radiative recombination is suddenly rising with increasing current, resulting in a super-linear behavior of the light emission. Such behavior must not be confused with a lasing threshold.

Near laser threshold the spectral linewidth of the emission is strongly reduced [14]. As shown for the UVA LD in Figure 1.2b, a spectral narrowing can be observed starting from a linewidth near 10 nm below threshold (comparable to spontaneous emission of UV LEDs) to a linewidth smaller than 1 nm of the stimulated laser emission above threshold.

Above laser threshold, the light emitted by stimulated emission exhibits clear linear polarization, whereas mixed polarization can be expected from the spontaneous emission below threshold. Figure 1.2c shows the polarization-resolved UVA laser spectra above threshold, exhibiting exclusively TE polarized emission at the lasing wavelength without any intensity with TM polarization.

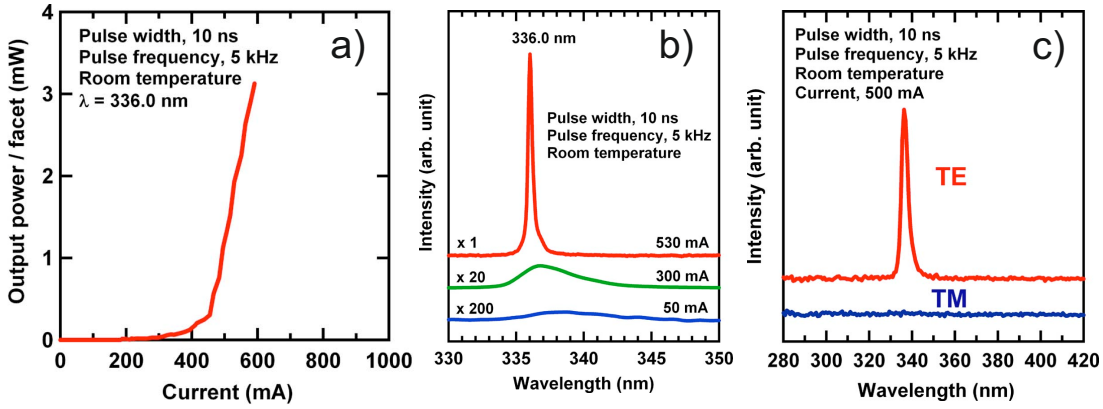

Figure 1.2: Edge-emitting UV laser diode with emission wavelength at 336 nm reported by Hamamatsu Photonics in 2008, showing (a) threshold behavior, (b) spectral linewidth reduction, and (c) entirely TE polarized emission above threshold. (Reprinted from [10], with the permission of AIP Publishing.)

Lasing is further characterized by a well-defined beam with directed far field pattern, e. g. an elliptical shape for edge-emitting semiconductor lasers [15], which has been observed for UVC laser emission with optical excitation [16]. As the exit facet of edge emitting-lasers typically exhibits asymmetric geometrical dimensions of the aperture sizes, the emitted laser beam shows different divergence angles. In vertical direction (growth direction) the mode can be confined within hundreds of nanometers by the refractive index contrast of the separate confinement heterostructure (SCH) design that includes waveguide and cladding layers. In case of gain guiding, however, the mode is less confined in lateral direction and can extend over several micrometers. Due to diffraction of the emitted optical wave at the facet, the small vertical aperture results in a large divergence angle in vertical direction, whereas the larger lateral aperture results in a smaller divergence angle in lateral direction. This combination leads to an elliptically shaped far field pattern of the emitted light. Furthermore, longitudinal modes have been observed from UVC lasers using ultra short resonators with cavity length less than 200 µm [16].

Even with these investigations on edge-emitting UVC lasers with optical excitation published, the step towards UVC laser diodes with current injection is very challenging. To a certain extent, this is due to specific AlGaN material properties. The AlGaN system, a ternary III-V compound semiconductor alloyed from the binary semiconductors AlN and GaN, is characterized by full miscibility and a direct band gap within the entire AlGaN composition range [17, 18]. From this perspective, AlGaN is ideally suited for the design of UVC laser diodes with SCH profile. However, next to specific requirements regarding morphology, defect density and conductivity of AlGaN:Si bottom cladding layers, the major challenges include the conductivity of UV transparent AlGaN:Mg top cladding layers with wide band gap as well as p-contact resistivities and maximum achievable current densities. An alternative hole injection concept is the implementation of tunnel junctions in reverse bias configuration. All of these points are addressed within this work. The thesis is connecting fundamental materials research with applied device physics in the semiconductor framework of AlGaN-based UVC light emitters.

2 Heterostructure design for UVC LEDs and UVC LDs

In this chapter, the basic heterostructure design of UVC light emitting diodes (LEDs) with emission through the substrate as well as of edge-emitting UVC laser diodes (LDs) near 265 nm or 4.7 eV is presented, which will be frequently referred to within subsequent chapters of this thesis on experimental investigations of individual layers. The fundamental concept of both types of devices is given by a multiple quantum well (MQW) placed within a pn junction. Therefore, the heterostructure design of both UVC LEDs and UVC LDs consists of four basic parts: substrate, AlGaN:Si n-layers, MQW active region as well as AlGaN:Mg p-layers. In the sections on UVC LEDs and on UVC LDs, their basic individual requirements for heterostructure layers are discussed, including similarities and differences.

2.1 UVC LED heterostructure

A schematic AlGaN heterostructure sequence of UVC LEDs is shown in Figure 2.1. **The substrate** has to provide UV transparency for bottom light extraction as well as hexagonal, c-oriented crystallinity for subsequent epitaxial growth of AlN buffer layers. Therefore, bulk AlN substrates are the native choice, ideally providing zero mismatch of lattice constant and thermal expansion coefficient to AlN buffer layers, very low threading dislocation densities (TDDs) lower than $10^4\,\mathrm{cm}^{-2}$ that should be preserved during AlN buffer growth, as well as UV transparency due to a band gap of 6 eV, larger than emitted UVC photon energies [19]. Despite ongoing research and commercialization, the availability of AlN substrates, however, is still limited by small diameters, low quantities, high costs, challenging AlN buffer growth, and –most severe– still insufficient control of UV transparency due to sub band gap absorption by point defects [20]. However, using substrate thinning or substrate removal techniques, detrimental UV absorption in the AlN substrate can be circumvented at the cost of development and execution of such procedures. Also wurtzite silicon carbide or silicon (111) substrates are options with insufficient UV transparency, as high light extraction efficiency (LEE) through the bottom of UV LEDs requires transparent substrates [21, 22]. Sapphire substrates that are entirely UV transparent provide hexagonal c-oriented symmetry with a considerable lattice mismatch of 13% to the lateral AlN lattice constant. Nevertheless, AlN buffer layers containing high temperature or low temperature AlN nucleation steps can be grown on sapphire, obtaining TDDs in the range of $10^{10}\,\mathrm{cm}^{-2}$ [23]. Using more advanced defect reduction techniques, such as growth of thick and crack-free layers, epitaxial lateral overgrowth (ELO), or high temperature annealing (HTA), TDDs in the range of $10^9\,\mathrm{cm}^{-2}$ or even $10^8\,\mathrm{cm}^{-2}$ can be achieved for AlN/sapphire templates [24, 25]. A subsequent epitaxial growth of AlN buffer layers typically preserves high UV

transparency due to comparably low point defect incorporation. By limiting the AlN buffer thickness, any strain accumulation due to lattice mismatch or thermal mismatch can be prevented in order to obtain low dislocation densities at the AlN buffer layer surface. Large AlN surface steps, however, might affect the homogeneity of subsequently grown AlGaN layers. Therefore, the influence of the substrate offcut angle on AlN morphology is investigated in section 3.2 in order to obtain smooth AlN surfaces.

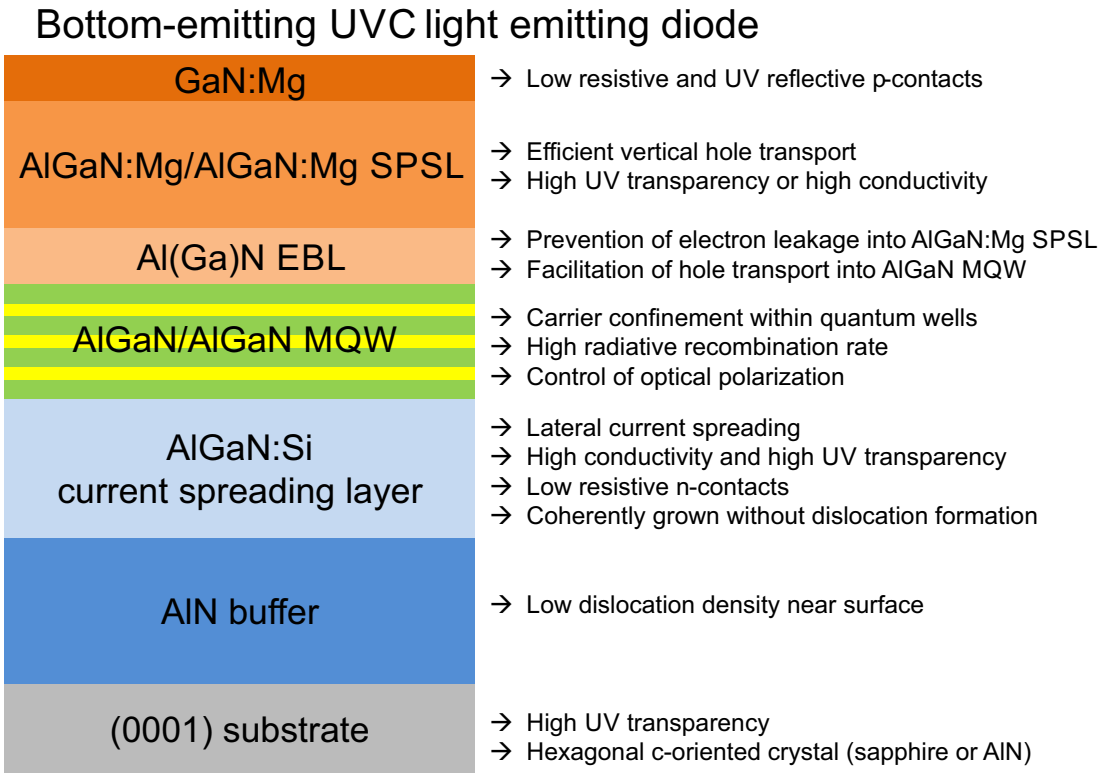

Figure 2.1: Schematic heterostructure of an AlGaN-based bottom-emitting UVC LED, with fundamental requirements for the individual layers.

The AlGaN:Si n-layer needs to facilitate lateral current spreading by a high conductivity, as n-contacts are fabricated on the AlGaN:Si besides an etched mesa with dimensions of several hundreds of micrometers. Vanadium- or titanium-based metal stacks are typically deposited and thermally annealed in order to obtain low resistive n-contacts to AlGaN:Si. However, the fabrication of ohmic n-contacts to AlGaN:Si with high aluminum content is very challenging [26]. In addition to the described electrical properties, UV transparency is required for the AlGaN:Si n-layer, restricting the band gap to values larger than the UVC photon energy of 4.7 eV for the targeted emission at 265 nm. Therefore, the $Al_xGa_{1-x}N$:Si composition needs to exceed $x = 0.5$. In order to maintain a low dislocation density and smooth morphology –provided by the AlN buffer layer– during AlGaN:Si growth, plastic relaxation and three-dimensional growth should be prevented. This can be realized with coherently grown AlGaN:Si current spreading layers with thicknesses below the critical layer thickness for dislocation formation by adjusting the growth conditions or applying AlGaN:Si-based superlattices (section 3.3).

The MQW active region within the pn junction is consisting of AlGaN quantum wells for carrier confinement separated by AlGaN barriers (section 3.4, section 4.2, and in section 4.3). Charge carriers injected from the AlGaN:Si n-side and the AlGaN:Mg SPSL p-side are distributed within the MQW, generating UV photons by radiative recombination of electrons and holes. The internal quantum efficiency (IQE) describes the efficiency of radiative recombination with coefficient B in contrast to non-radiative recombination processes [27]. Defect-related Shockley-Read-Hall recombination with coefficient A, which is correlated to the TDD and point defect density, can impact the IQE at low carrier densities n; many particle processes such as Auger-recombination with coefficient C can impact the IQE at high carrier densities, see Equation 2.1.

$$IQE = \frac{Bn^2}{An + Bn^2 + Cn^3} \tag{2.1}$$

Due to strong spontaneous and piezoelectric polarization fields in AlGaN-based heterostructures, a MQW band structure is formed that exhibits tilted valence bands and conduction bands within the quantum wells and barrier layers [28]. As described by the quantum-confined Stark effect (QCSE) [29], such strong polarization fields lead to reduced B coefficients due to a reduced overlap of electron and hole wavefunctions as well as a red shift of the emission wavelength, all of which can be reduced by employing very thin quantum wells [27]. Further, electrical confinement and QCSE can be influenced by the barrier height – the band gap offset between AlGaN barriers and AlGaN quantum wells. As AlGaN-based MQWs can be categorized as type I semiconductor heterostructures with straddling gap, the band gap offset is divided into fractions for conduction band and valence band, e. g. with 70/30 ratio [30]. The optical polarization of the MQW emission is determined by conduction and valence bands involved in the radiative recombination and can be controlled by adjusting the Al mole fraction in quantum wells and barriers, quantum well thickness, or strain state in order to obtain higher transverse-electric (TE) or transverse-magnetic (TM) emission polarization [31].

An electron blocking layer (EBL) is required in order to provide high carrier injection efficiency (CIE). The main purpose is the prevention of electron leakage into the p-side layers such as the AlGaN:Mg SPSL, as parasitic recombination channels with holes in the p-layers would reduce the efficiency of LEDs. At the same time an EBL needs to facilitate efficient hole injection into the MQW. The performance of an EBL is affected by the respective band alignment to the last barrier of the MQW as well as to the AlGaN:Mg SPSL, mainly influenced by band gap, doping or thickness of the EBL.

The AlGaN:Mg short-period superlattice (SPSL) is the p-type layer of the LED heterostructure, responsible for efficient vertical transport of holes from the p-contact to the EBL and MQW layers. Therefore, the AlGaN:Mg SPSL needs to provide high p-type conductivity. In order to obtain high LEE, strong UV absorption has to be avoided, e. g. by using UV transparent AlGaN:Mg SPSLs with wide band gap in combination with UV reflective contacts. However, achieving both high conductivity and high UV transparency at the same time appears outstandingly challenging for Mg-doped AlGaN alloys (section 4.3 and section 4.4).

A GaN:Mg layer is typically grown in UV LEDs in order to fabricate low resistive metal contacts to the p-type layers of nitride semiconductor heterostructures. Although

obtaining ohmic p-contacts is challenging even with GaN:Mg, the contact resistances can be substantially reduced compared to AlGaN:Mg. However, any potential LEE improvement by using UV transparent AlGaN:Mg and UV reflective contacts can be spoiled due to fundamental absorption of thick GaN:Mg layers. In contrast, high LEE can be achieved by using very thin, quasi-transparent GaN:Mg layers.

In combination, the external quantum efficiency (EQE) of UV LEDs, which describes the ratio of emitted photons per injected carriers, is given by the product of CIE, IQE, and LEE. The EQE can be determined by LI measurements using the emission wavelength λ and the drive current I (Equation 2.2). By taking the operation voltage V into account, the wall-plug efficiency (WPE) is given by the ratio of emission power P divided by injected electrical power (Equation 2.3).

$$EQE = CIE \cdot IQE \cdot LEE = \frac{P/(h\nu)}{I/e} = \frac{P}{I}\frac{\lambda e}{hc} \tag{2.2}$$

$$WPE = \frac{P}{I \cdot V} \tag{2.3}$$

2.2 UVC LD heterostructure

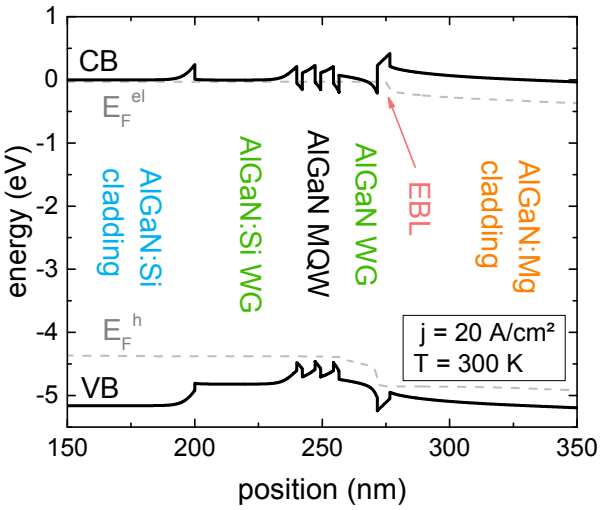

Figure 2.2: Band structure simulation of a UVC LD heterostructure near the MQW active region, including AlGaN waveguide and cladding layers. (Simulation by Martin Guttmann - TU Berlin)

The UVC LD heterostructure consists of the parts substrate, AlGaN:Si n-layers, MQW active region, and AlGaN:Mg p-layers. As many requirements, including pseudomorphic growth or efficient carrier injection, are very similar to UVC LEDs, some properties of substrates or AlGaN:Si layers are highly comparable, allowing for utilization of synergy effects during UV LD development. A UVC LD band structure simulation is shown in Figure 2.2, demonstrating the alignment of valence band (VB) and conduction band (CB) as well as the quasi-Fermi levels of electrons (E_F^{el}) and holes (E_F^{h}) at moderate current densities. Some properties of edge-emitting UVC LDs strongly differ from UVC LEDs, such as stimulated light emission at high current densities, wave guiding with transparent AlGaN:Mg cladding layers and light extraction from resonator facets. Some of these requirements for individual layers are shown in Figure 2.3.

In this section, the main requirements for UVC LDs and the main differences to UVC LEDs are highlighted. Similar to UVC LEDs, high TDDs near the MQW can lead to high non-radiative recombination rates, acting as electrical losses that are detrimental for UVC LDs. Therefore, AlN buffer and AlGaN:Si layers need to provide low TDDs, based on the c-oriented hexagonal crystal substrate (section 4.1). In contrast to bottom-emitting UVC LEDs, no UV transparency is required for the substrate, as the lasing mode will be confined within a waveguide system near the MQW without overlap to the substrate.

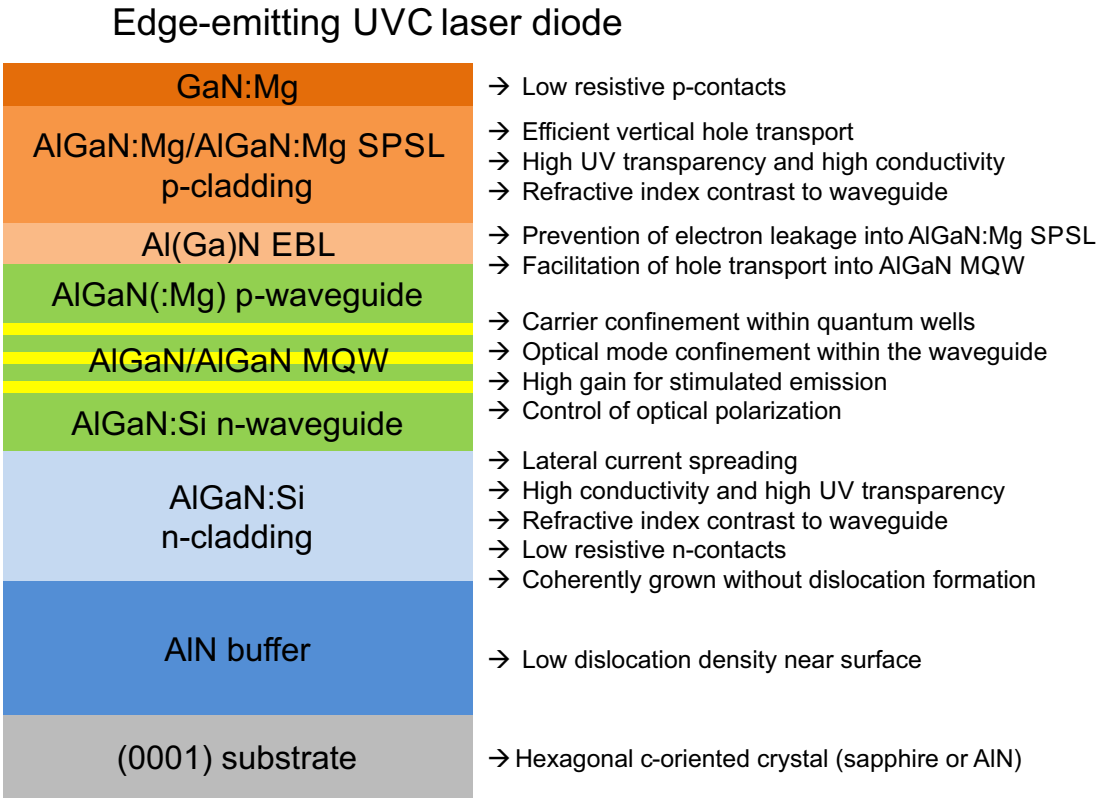

Figure 2.3: Schematic heterostructure of an AlGaN-based edge-emitting UVC LD with waveguide system, with fundamental requirements for the individual layers.

In the **gain medium**, realized with quantum wells in this case, stimulated radiative recombination of charge carriers can be amplified by sufficient material gain. The material gain is dependent on the carrier density, both can be increased using carrier confinement within quantum wells by a separate confinement heterostructure (SCH). Population inversion of conduction band and valence band needs to be achieved by electrical (or optical) pumping of a 4-level-system, providing transparency and high stimulated recombination rates compared to absorption rates as interaction with an incoming photon [15]. In contrast to LEDs, most spontaneous radiative recombination is contributing to losses in laser diodes.

Such **waveguide (WG) system** provides transverse mode confinement by a vertical refractive index profile that is realized within the heterostructure by growing AlGaN waveguide layers with high refractive index (low aluminum content) embedded in AlGaN

cladding layers with lower refractive index (higher aluminum content) at the bottom and the top. Therefore, high band gap of the AlGaN:Mg SPSL is required in order to provide UV transparency and in addition sufficient refractive index contrast (section 4.3). In lasers with SCH, only a fraction of the optical mode overlaps with the gain medium. This mode overlap is called confinement factor Γ. Lateral mode confinement can simply be realized by gain guiding that is given by contact geometries and resulting current paths or by index guiding that requires a lateral index step formed by more advanced laser diode micro fabrication techniques [15]. In the direction of light propagation, etched or cleaved facets, potentially with facet coating, are forming the resonator mirrors of the laser cavity.

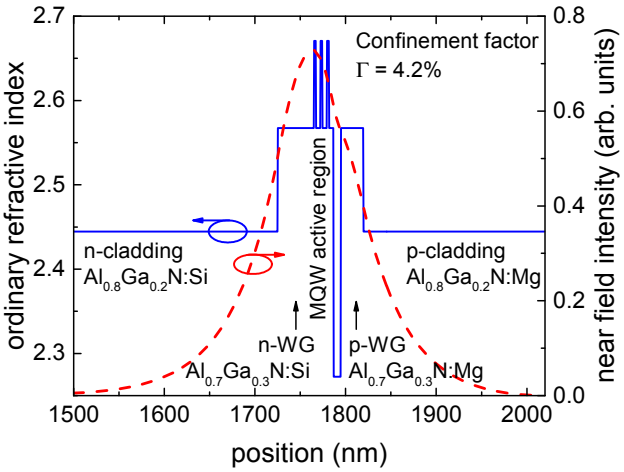

Figure 2.4: Refractive index profile and transverse optical mode simulation of a UVC laser diode heterostructure. (Simulation by Martin Martens - TU Berlin)

In Figure 2.4, the refractive index profile of such AlGaN-based SCH UV laser diode with $Al_{0.8}Ga_{0.2}N$ cladding layers and $Al_{0.7}Ga_{0.3}N$ waveguide is shown in blue. The transverse optical mode is confined within the waveguide, exhibiting the intensity maximum close to the position of the quantum wells, as shown by the simulated near field intensity distribution in red. Therefore, a large overlap Γ of optical mode and gain medium (quantum wells) can be achieved, in this case $\Gamma = 4.2\%$. In InAlGaN-based laser diodes with violet, blue, or green emission, also lower confinement factors in the range of 1% to 2% are sufficient for laser diode operation [32]. It should be noted that an EBL with low refractive index near the MQW could negatively impact the mode confinement. However, a small EBL thickness such as 5 nm can effectively minimize this impact.

The basic mechanism of carrier injection from contacts into the MQW is principally comparable for UVC LEDs and UVC LDs. Nevertheless, CIE can be different for carrier injection into UVC LEDs with lower current densities (e. g. 10 - 100 A/cm^2) compared to carrier injection into UVC LDs with higher current densities (e. g. $>1000\,A/cm^2$). Furthermore, in LDs contacts and heterostructures need to sustain such high current densities in combination with the required voltages.

Carrier injection via tunnel junctions, that might overcome challenges in hole injection related to AlGaN:Mg layers, is a separate topic described in chapter 5.

3 MOVPE growth of AlGaN-based heterostructures on sapphire and bulk AlN

In order to obtain smooth surfaces of AlN buffer layers for subsequent MOVPE growth of AlGaN-based heterostructures and devices, the influence of substrate offcut angles on AlN morphologies is experimentally investigated after an introduction to MOVPE growth of AlN and AlGaN layers. Furthermore, the effect of different AlGaN growth parameters, such as temperature, growth rate, and V/III partial pressure ratio on the morphology of $Al_{0.8}Ga_{0.2}N$:Si is examined and AlGaN-based superlattices are employed to enable both pseudomorphic growth as well as smooth surfaces by enhanced adatom migration and reduced spiral heights. Moreover, the MOVPE growth of MQWs is examined on both sapphire and AlN substrates in order to prevent plastic relaxation and formation of V-pits or other surface defects. Additionally, the effect of MQW growth temperature and growth interruptions on AlGaN MQW interface properties is analyzed. Finally, the findings are used to fabricate UVC lasers for optical pumping. Laser emission is demonstrated with threshold behavior, spectral line width reduction, and TE polarization above threshold. With optical pumping experiments, the influence of different types of surface defects on the lasing threshold and optical losses is analyzed.

3.1 Introduction of the MOVPE method for AlN and AlGaN growth

Metalorganic vapor phase epitaxy (MOVPE), or metalorganic chemical vapor deposition (MOCVD), describes the formation process of crystalline solids from the gas phase by chemical reactions on the surface of heated substrates using metalorganic (MO) and gaseous precursors. This epitaxial growth method is capable of preparing thin films with defined material composition and layer thickness in the nanometer range with atomically sharp interfaces enabling research, development, as well as industrial fabrication of semiconductor devices such as transistors, photo detectors, or light emitters.

An MOVPE system typically includes a gas mixing system and a reactor chamber (Figure 3.1a). In the gas mixing system, a carrier gas flow with controlled supply of precursors is prepared. Hydrogen (H_2), nitrogen (N_2), or less frequently argon (Ar), are used as inert carrier gases. Material type and quantities of the reactive precursors are defined by the target crystal properties. For the epitaxial growth of ternary AlGaN alloys, trimethylaluminum (TMAl), trimethylgallium (TMGa) or triethylgallium (TEGa) are used as precursors for the group-III component, as well as ammonia (NH_3) for the group-V component. Silane (SiH_4) and biscyclopentadienyl-magnesium (Cp_2Mg) are

used as n-type and p-type dopant sources for this work, respectively. The supply of gaseous sources (NH_3, SiH_4) from compressed gas cylinders at room temperature is adjusted by mass-flow-controllers (MFC). MO precursors are stored in bubbler containers at individually controlled temperature and pressure. Under equilibrium conditions, MO precursor molecules of the liquid (TMAl, TMGa, TEGa) or solid powder (Cp_2Mg) are vaporized until saturation of the gas phase, defining an individual MO partial pressure for each source material. Using a carrier gas flow through the bubblers to the reactor chamber, the MO supply is adjusted by MFCs, pressure controllers (PC) as well as temperature controllers.

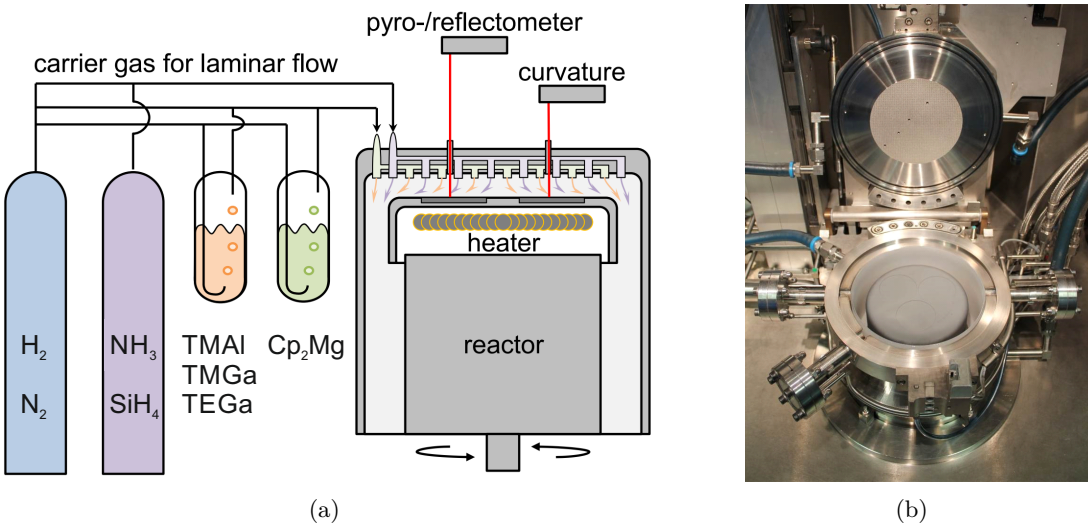

(a) (b)

Figure 3.1: (a) MOVPE schematic including gas mixing cabinet and reactor chamber, and (b) image of the used 3x2-inch close-coupled showerhead reactor [33].

From the gas mixing system, the carrier gas flow is transported and injected into the reactor chamber, separately for NH_3 and the other components. In the close-coupled showerhead system with vertical reactor geometry used for this work (Figure 3.1b), the gas inlet is in close proximity to the substrate with a gap size adjustable between 5 mm and 26 mm. Up to three substrates with 2-inch diameter are placed in pockets on the resistively heated susceptor made from graphite with silicon carbide coating. At controlled process temperatures, the III-V-semiconductor crystal is synthesized on the substrate surface by chemical reactions of the precursor materials. The chemical reaction for AlN growth from TMAl and NH_3 can be summarized by the net reaction equation $Al(CH_3)_3 + NH_3 \rightarrow AlN + 3\,CH_4$. The reaction path includes pyrolysis of precursor molecules, adsorption to the substrate surface, as well as adatom diffusion, incorporation, or desorption. At typical temperatures for AlGaN growth ranging between 900 °C to 1100 °C the growth rate is not kinetically limited by MO pyrolysis. However, due to a comparably high ammonia pyrolysis temperature and high volatility of nitrogen atoms, MOVPE growth of III-nitrides typically requires excess ammonia supply with V/III ratios of 100 to 1000 or even above in order to obtain stoichiometric III-nitride growth [34]. Due to sufficient thermal energy at the process temperature, chemisorbed adatoms can diffuse on the surface by exceeding the potential barrier between two minimum positions of the periodic potential. Due to lower Ga-N binding energies ($\approx 9\,eV$),

gallium adatoms are more mobile compared to aluminum adatoms (Al-N binding energy $\approx 12\,eV$) [35], which can be described by a lower Ga sticking coefficient and results in a larger Ga diffusion length at a given temperature. Both of them can be controlled by the supplied V/III ratio. The adatom binding energies to the surface are resulting in a desorption probability that is larger for gallium adatoms and increases with increasing temperature. The incorporation of adatoms into the crystal lattice is energetically favorable at positions with a high number of bonds which is discussed in the context of AlGaN morphology in subsection 3.3.2. The composition of ternary compounds such as AlGaN is controlled by the respective supply of Al- and Ga-containing precursors. Heterostructures with abrupt atomic interfaces can be obtained by carrier gas switching with short transition times within the reactor. Finally, p-type and n-type doping of AlGaN layers enables the fabrication of functional electronic and optoelectronic devices.

3.2 Influence of substrate offcut on macro steps in AlN

Aluminum nitride buffer layers, which can be grown on c-oriented bulk AlN substrates or sapphire substrates, are frequently used for the epitaxial growth of UVC emitters as the AlN lattice constant allows for the growth of crack-free AlGaN layers within certain limits [36]. However, device applications require suitable surface properties of AlN buffer layers, such as smooth surfaces ideally with monoatomic steps that can be obtained by step flow growth. For AlN, the monoatomic step height equals 0.249 nm, half of the vertical AlN lattice constant c [37]. In contrast, surface morphology can be governed by step bunching. In that case, macro steps with a height of up to hundreds of monolayers are providing a rougher surface, which can be characterized by an increased root mean square (RMS) roughness value in atomic force microscopy (AFM) measurements. Besides atomic steps and step bunching, other AlN surfaces can be characterized by transition states exhibiting certain features of both morphologies. All of these types of surfaces are shown in Figure 3.2 including their respective height profiles. Using such AFM images of surface topologies, a systematic investigation of the correlation between substrate offcut and AlN morphology is carried out.

5 µm AlN was homoepitaxially grown on bulk AlN as native substrate. AlN crystal growth by physical vapor transport (PVT) was performed at growth temperatures between 2030 °C and 2100 °C at Leibniz-Institut für Kristallzüchtung (IKZ) [20]. After wafering and polishing, homoepitaxial AlN was grown by MOVPE at a temperature of T = 1200 °C and a partial pressure ratio of V/III = 250 at Ferdinand-Braun-Institut, Leibniz-Institut für Höchstfrequenztechnik (FBH). From AFM measurements, the morphology type was determined and the local offcut angle was calculated by triangulation using the height of the respective mono steps or macro steps and the step distance as shown in Figure 3.3. Investigated offcut values are ranging between $\alpha = 0.1°$ and 0.9°. Depending on the offcut values three different regimes with typical surface morphology were identified: For low offcut angles $\alpha < 0.17°$ the surfaces are determined by AlN mono steps with a height of 0.25 nm. Due to the constant mono step height h_S, the mono step distance d_S decreases with increasing offcut angle from 110 nm to 90 nm in this regime according to $h_S = d_S \cdot \tan\alpha$. For larger offcut angles ($0.19° < \alpha < 0.34°$) macro steps with unstable step orientation and increasing step height and distance are present at the surface. In this transition state, the macro step height is ranging

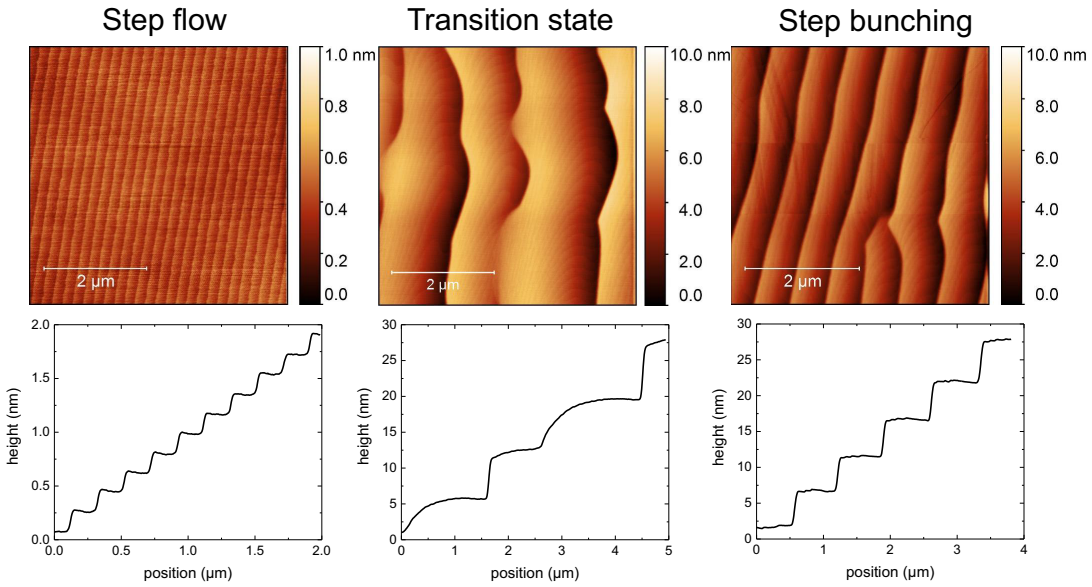

Figure 3.2: Different observed types of AlN surface morphology grown homoepitaxially on bulk AlN.

from 1.3 nm to 4.0 nm with macro step distances between 0.9 µm and 1.8 µm. For even larger offcut angles $\alpha > 0.35°$, the step bunching regime is characterized by macro steps with stable step orientation and locally constant step height and distance. The macro step height H_S is ranging from 4.8 nm to 6.4 nm, approaching a constant value near 6 nm for offcut values up to 0.9°, as shown in Figure 3.3a. Due to the constant H_S, the correlated macro step distance D_S is decreasing from 1200 nm at $\alpha = 0.4°$ to 400 nm at $\alpha = 0.9°$ according to the relation $H_S = D_S \cdot \tan\alpha$, analog to the mono step distance (Figure 3.3b). Such behavior of AlN surfaces homoepitaxially grown on bulk AlN substrates has also been reported by Bryan et. al. [38]. However, in that case an offcut range limited to values below 0.65° prevented the observation of constant macro step heights at larger offcut values up to 0.9°. Including the full range of offcut values, a macro step height saturation combined with terrace width reduction can be observed in Figure 3.3, correlated to the adatom diffusion length that is constant at a specific set of growth parameters. Here, the individual offcut values separating two surface regimes, e. g. mono steps from macro steps, are different to reported values in [38] due to different sets of growth parameters in the respective MOVPE reactors.

The morphology transition between mono steps and macro steps is governed by surface kinetics of adatom diffusion on vicinal terraces and incorporation at step edges or desorption from the surface. As the vicinal terrace width is determined by the substrate offcut, diffusion and incorporation at step edges are highly correlated to the offcut value. The motion of adatoms on vicinal surfaces has been described with the BCF surface diffusion theory (Burton, Cabrera, and Frank [39]) and the Schwoebel model [40] using the Ehrlich-Schwoebel energy barrier for adatom diffusion across step edges dependent on the diffusion direction to the upper terrace or to the lower terrace. In connection with a varying terrace width during growth by adatom incorporation at the step edges, implemented using a Monte-Carlo simulation approach, predictions of the growth morphology have been made and experimentally verified [41]. For AlN, the

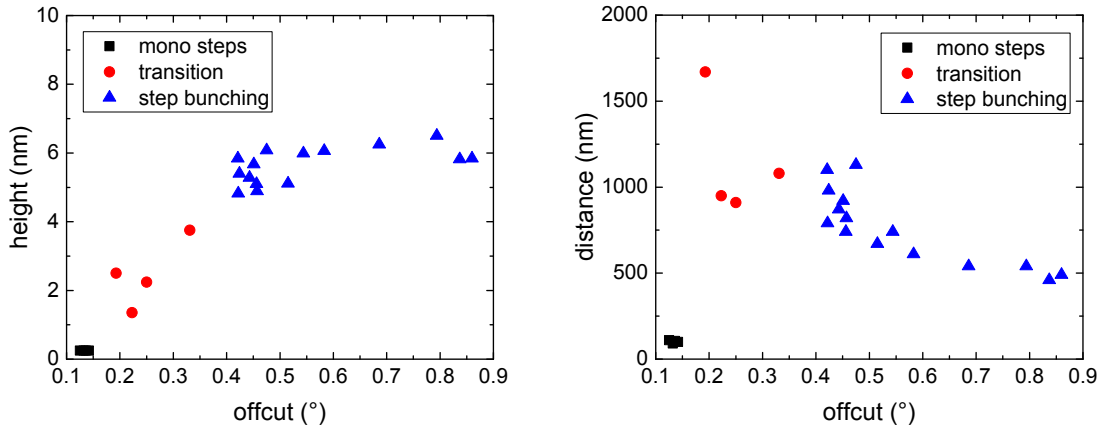

(a) (b)

Figure 3.3: Evaluated step height (a) and step distance (b) for AlN epitaxially grown at T = 1200 °C and V/III = 250 on bulk AlN with different local substrate offcut, distinguishing surfaces with mono steps, transition, and step bunching.

surface transition between mono steps and macro steps was experimentally investigated for growth on sapphire substrates [33, 41, 42] as well as on native AlN substrates in this work and by Bryan et. al. [38]. Nevertheless, surface diffusion and incorporation probabilities are not only influenced by terrace dimensions but also by growth parameters. Therefore, by varying temperature and V/III partial pressure ratio, the resulting surface morphology can additionally be influenced. Compared to a surface dominated by mono steps, the formation of surface step bunches is becoming more likely with increasing offcut angle, increasing temperature, decreasing V/III ratio, and decreasing growth rate that may be summarized with decreasing supersaturation [38]. With the supersaturation concept, crystal growth conditions are compared to thermal equilibrium conditions, e. g. for MOVPE growth of AlN the vapor supersaturation σ_V is given by the ratio $\sigma_V = \frac{P_{Al} - P^0_{Al}}{P^0_{Al}}$ with the aluminum partial pressure P_{Al} and the aluminum equilibrium vapor pressure P^0_{Al}. Positive supersaturation represents the driving force for crystal growth, negative supersaturation for etching.

The morphology control of AlN surfaces is highly relevant for device fabrication as the AlN buffer layer properties strongly influence the heterostructure growth of AlGaN-based UV LEDs or LDs. In order to provide smooth AlN buffer layers, a substrate offcut in the range of 0.1° to 0.17° can guarantee ideal surfaces with monoatomic steps for the respective set of AlN growth parameters, that will be used in following chapters.

3.3 Strain and morphology of AlGaN:Si cladding layers

The MOVPE growth of silicon-doped $Al_xGa_{1-x}N$ layers with composition near x = 0.8 and low resistivities $\rho = 0.026\,\Omega$cm was reported by Mehnke et. al. in 2013 [43]. These layers were grown on c-oriented, epitaxially laterally overgrown (ELO) AlN/sapphire templates with threading dislocation densities (TDDs) in the range of $0.5\text{-}2 \cdot 10^9\,\mathrm{cm}^{-2}$. The fabrication of such templates includes stripe patterning and etching of planar AlN

buffer layers and subsequent AlN overgrowth with enhanced lateral growth rates. After coalescence, the average TDD near the AlN surface is strongly reduced compared to the TDD of AlN buffer layers [24, 44]. Highly conductive $Al_{0.8}Ga_{0.2}N$:Si layers with thickness of 1200 nm can be used as n-type current spreading layers in UVC LEDs with emission near 265 nm [25] or as cladding layers in optically pumped UVC lasers [45]. However, such $Al_{0.8}Ga_{0.2}N$:Si layers have not been systematically investigated and optimized regarding pseudomorphic strain state and smooth surface morphology, both are highly important for UVC laser diodes. Therefore, the effect of growth parameters and AlGaN-based superlattices is examined in order to obtain pseudomorphic, smooth, homogeneous, and conductive AlGaN:Si layers.

The following parameters are defined as required $Al_xGa_{1-x}N$:Si cladding layer properties for the incorporation into a UVC LD heterostructure design:

(I) Thickness d = 1000 - 1500 nm

(II) Uniform composition x = 0.8

(III) Resistivity $\rho < 0.03\,\Omega$cm

(IV) Roughness 0.25 nm < RMS < 7.0 nm

(V) Strain state $\varepsilon = 0.5$ (pseudomorphic AlGaN on AlN buffer, relaxation R = 0)

3.3.1 Relaxation and critical layer thickness of AlGaN

In this study, the heteroepitaxial growth of AlGaN layers on ELO AlN/sapphire templates with a lattice constant close to the relaxed AlN lattice constant is investigated. Therefore, a possible relaxation of the compressively strained AlGaN layers has to be considered after exceeding a critical layer thickness. The elastic energy E_{el} per unit area A stored in the layer due to misfit strain can be calculated from the layer thickness d as well as the lateral lattice constants of the strained AlGaN layer (a_{layer}) and a relaxed AlGaN layer ($a_{relaxed}$) with the same composition [46].

$$E_{el}/A = 2\mu \cdot \frac{1+\nu}{1-\nu} \cdot d \cdot \varepsilon^2, \qquad \text{with } \varepsilon = \frac{a_{relaxed} - a_{layer}}{a_{relaxed}} \tag{3.1}$$

Here, μ is the elastic shear modulus, ε is the in-plane strain and ν is the Poisson´s ratio of the layer that can differ from the bulk value. For AlGaN growth on AlN substrates or AlN buffer layers, the comparably large AlGaN lattice constant causes compressive stress to the AlGaN layer. For thin AlGaN layers with high aluminum content, pseudomorphic growth with compressive strain is expected. Exceeding the critical layer thickness for the respective composition leads to plastic relaxation. In reciprocal space maps (RSMs) measured near the asymmetric (10.5) X-ray diffraction (XRD) peak of AlN shown in Figure 3.4, this mechanism is investigated for the growth of $Al_xGa_{1-x}N$:Si layers with varied composition x between 0.50 and 0.76 and thickness near 1200 nm as required for UV laser cladding layers. The AlGaN reciprocal lattice constants Q_x and Q_z are shown in Figure 3.5a, and the evaluated XRD FWHM and AFM RMS roughness of these AlGaN samples is shown in Figure 3.5b. For $x \geq 0.64$, the lower AlGaN:Si XRD peak is located at the same Q_x position as the ELO AlN template layer without strong lateral shift or FWHM broadening, indicating coherent or almost coherent growth of these

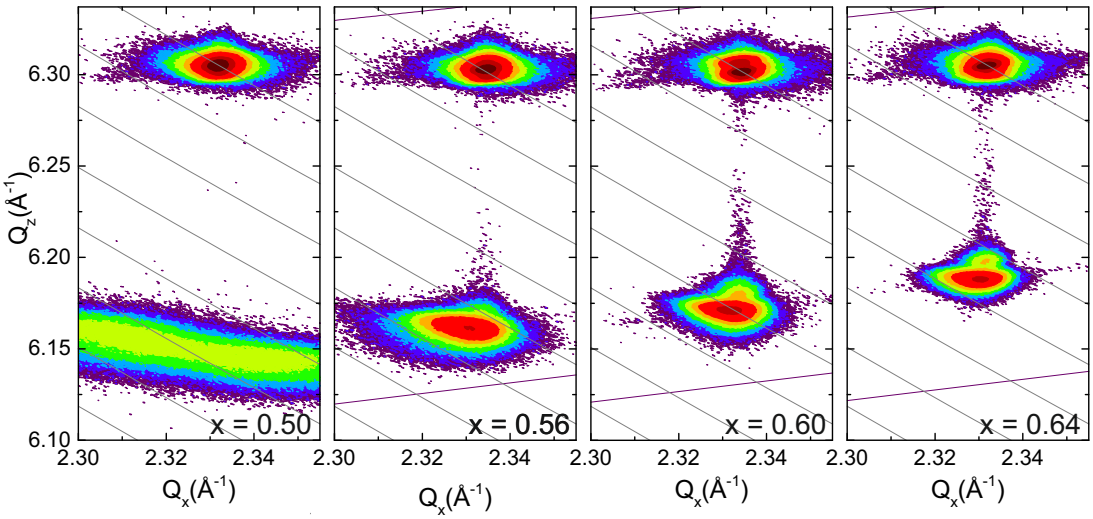

Figure 3.4: XRD RSM of 1200 nm thick $Al_xGa_{1-x}N$:Si layers reveal increasing partial relaxation with decreasing aluminum content below x = 0.6.

AlGaN layers. Furthermore, the RMS roughness is constant near 4 nm. A weaker peak at slightly higher Q_z values corresponds to a 100 nm thick AlGaN buffer layer in the heterostructure with 2% to 3% higher aluminum content. For $x < 0.60$, the AlGaN peak positions are shifting to smaller Q_x values in combination with FWHM broadening of the AlGaN peak and RMS roughness increase, indicating plastic relaxation. In the case of x near 0.50, the AlGaN reflection is extremely broadened and the RMS roughness is strongly increased, far from a perfect crystalline layer. For strained $Al_{0.60}Ga_{0.40}N$:Si layers grown on AlN, these results indicate a critical layer thickness for plastic relaxation with dislocation generation near 1200 nm, and strained AlGaN cladding layers with $x \geq 0.70$ are available for UV lasers.

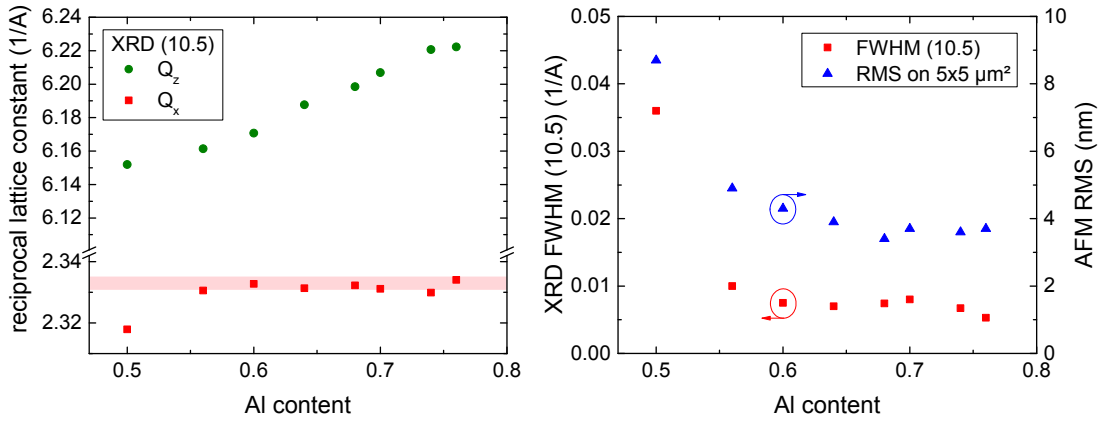

Figure 3.5: Structural analysis of 1200 nm thick AlGaN:Si layers with varying composition: (a) AlGaN reciprocal lattice constants Q_x and Q_z from XRD (10.5) RSMs with the ELO AlN Q_x range indicated in light red and (b) evaluated XRD FWHM and AFM RMS roughness.

However, the determination accuracy of relaxation by XRD RSM evaluation might be insufficient to resolve a slight partial relaxation without dislocation generation, such as climb of existing dislocations that would be less detrimental for MQW luminescence. Next to the insufficient layer quality of AlGaN:Si with x $\leq$ 0.60, the UV transparency has to be considered. Relative UV transmission spectra of $Al_xGa_{1-x}N$:Si layers with $0.50 \leq x \leq 0.76$ are shown in Figure 3.6. For $Al_{0.50}Ga_{0.50}N$:Si, the long-wavelength tail of the fundamental absorption near 260 nm extends beyond 275 nm, potentially causing absorption of 270 nm UVC laser modes. With increasing aluminum mole fraction, the AlGaN:Si absorption edge is shifted to shorter wavelengths and UV transparency near 270 nm is obtained. In addition, contactless resistance measurements exhibit no significant change of resistivity with values of $\rho = (0.026 \pm 0.005)\,\Omega$cm in the investigated composition range $0.50 \leq x \leq 0.80$ of AlGaN:Si layers whereas for AlGaN:Si with $x > 0.8$ strongly increasing resistivity is expected [43].

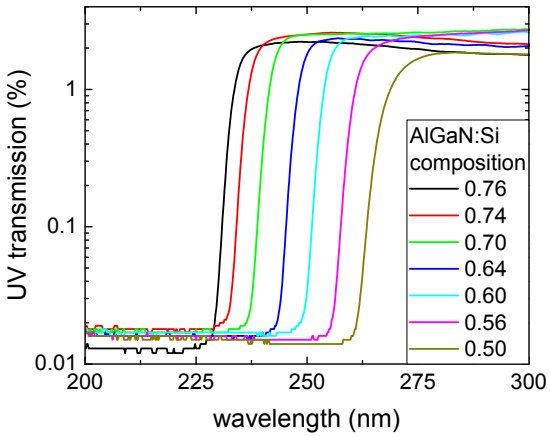

Figure 3.6: Relative UV transmission spectra of AlGaN:Si layers with varying composition between x = 0.50 and 0.76.

3.3.2 Effect of growth parameters on AlGaN morphology

In section 3.2, the surface morphology transition between monoatomic steps and macro steps was examined for the case of AlN. For AlGaN growth, however, surfaces are dominated by spiral hillocks (Figure 3.7a with V/III = 650). Therefore, the surface morphology transition between monoatomic steps and growth spirals is investigated in this section. In the terrace-ledge-kink (TLK) model or Kossel crystal model, the bonding energies and incorporation probabilities of adatoms on the growth surface can be described by the number N_B of bonds to neighboring atoms that increases from terrace ($N_B = 1$), to ledge ($N_B = 2$) to the kink position ($N_B = 3$). Based on the BCF theory of adatom surface diffusion [39], the incorporation at step edges (ledge or kink) depends on the adatom diffusion length and terrace width (step distance). For adatom diffusion lengths much shorter than the step distance, most adatoms will nucleate on the terraces [47]. Taking dislocations into account, such nucleation is resulting in island growth in the presence of low screw dislocation (SD) densities [38] or spiral growth in the presence of high screw dislocation densities [48]. However, the adatom diffusion length and the terrace width can be influenced by experimental parameters. Compared to the formation of islands or spirals on AlGaN surfaces, step flow growth is becoming more likely with increasing offcut angle, increasing growth temperature, decreasing

V/III ratio, and decreasing growth rate which may be summarized with decreasing supersaturation [38]. For AlGaN growth, the physical mechanisms are identical for different species of adatoms, however, certain quantitative parameters might change for the individual species, e. g. gallium desorption can start at temperatures below 1000 °C, whereas no significant desorption of aluminum from AlGaN surfaces is expected for such temperatures. Therefore, the desired step flow growth requires to carefully tune the set of process and substrate parameters, avoiding step bunching at low supersaturation and island or spiral growth at high supersaturation.

Variation of V/III partial pressure ratio with constant group-III supply

$Al_{0.8}Ga_{0.2}N$:Si layers without strong relaxation (Figure 3.7a) frequently exhibit spiral hillocks with RMS roughness near 7 nm, compositional non-uniformities, and partial relaxation [49]. These samples with 1200 nm thickness are grown at temperatures of 1080 °C and at a reactor pressure of 200 mbar with V/III = 650 partial pressure ratio. In order to compensate for the high vapor pressure of nitrogen, the MOVPE growth of AlGaN and other nitride alloys is typically conducted under highly nitrogen-rich conditions in contrast to MOVPE growth of GaAs or InP. By changing the V/III ratio during AlGaN growth, more nitrogen-rich or less nitrogen-rich conditions can be adjusted, determining the surface mobility of metal adatoms [50]. In order to analyze the influence of the V/III ratio on the surface morphology, a variation of ammonia supply was conducted at a constant supply of metal precursors TMAl and TMGa.

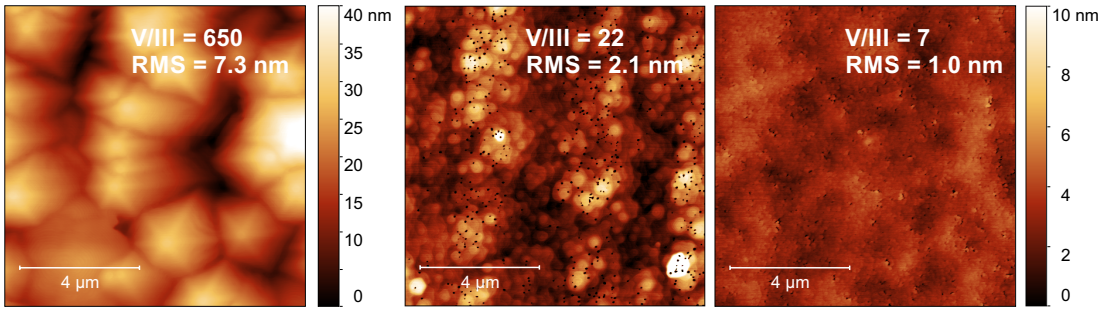

Figure 3.7: AFM topograms of AlGaN layers grown with different V/III partial pressure ratio. (Measurements by Tino Simoneit - TU Berlin)

Table 3.1: Influence of V/III partial pressure ratio on RMS surface roughness, composition, and growth rate of AlGaN:Si layers grown at 1080 °C and 200 mbar.

V/III ratio	**7**	**22**	**87**	**650**	**1310**
RMS roughness	1.0 nm	2.1 nm	5.7 nm	7.3 nm	6.4 nm
Composition	≥ 0.96	0.93	0.89	0.82	0.76
Growth rate	2.91 µm/h	2.78 µm/h	2.36 µm/h	1.42 µm/h	1.04 µm/h

In this experiment, a range between V/III = 7 and 1300 was covered. Figure 3.7 shows AFM images of AlGaN layers grown at V/III = 650, 22 and 7. With decreasing V/III ratio, the RMS roughness values are strongly decreasing from 7.3 nm down to 1.0 nm

and much smoother surfaces are obtained as summarized in Table 3.1. In the case of Figure 3.7b and c, the formation of small pits was observed, most probably caused by a high oxygen concentration in the glovebox contaminating the AlGaN growth. Spiral formation is becoming less dominant and step flow growth is promoted at reduced V/III ratios, as expected. However, no pure step flow growth is obtained due to step pinning at such pit defects.

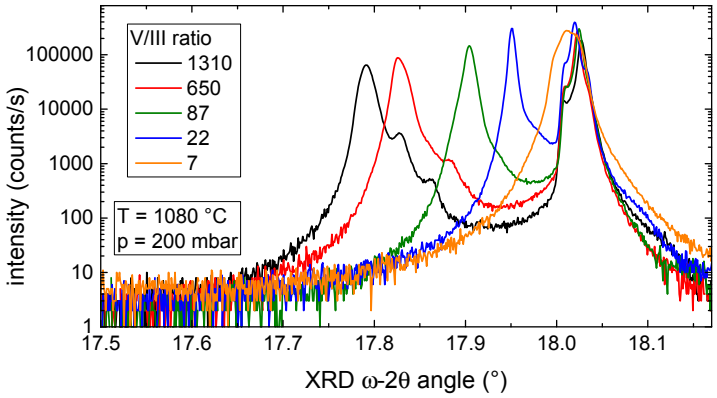

Figure 3.8: Symmetric (00.2) XRD rocking curves of AlGaN layers grown with varying V/III ratio between 7 and 1310, realized by NH_3 variation. (Measurements by Tino Simoneit - TU Berlin)

In order to determine the composition and uniformity of these AlGaN layers grown with varying V/III ratio, symmetric (00.2) XRD rocking curves were conducted and are shown in Figure 3.8. The AlGaN composition is strongly affected by the V/III ratio, increasing from $x = 0.76$ at 1300 to $x = 0.96$ at V/III = 7. Furthermore, strong non-uniformities are present for the samples with low aluminum contents which are reducing for AlGaN with higher aluminum contents. AlGaN growth rates were measured by in-situ reflectometry and are increasing with decreasing V/III ratio (Figure 3.9a). The combination of AlGaN composition and the total AlGaN growth rate allows for a separation of individual contributions from AlN and GaN to the growth rate and to the growth efficiency, defined as growth rate per supplied precursor partial pressure in Pascal. The total AlGaN growth rate is dominated by the AlN component for stoichiometry reasons (Figure 3.9a). The growth rate of the GaN component is much smaller. With decreasing V/III ratio, the total growth rate increases from 1 µm/h to almost 3 µm/h in combination with the described increase in aluminum content. The MO partial pressure ratio (TMAl/[TMAl+TMGa] = 0.87) is constant for all samples. Therefore, all changes to the growth rate and AlGaN composition are due to pre-reactions in the gas phase or surface reactions such as adsorption, desorption, and incorporation. Individual contributions from AlN and GaN to the growth efficiency are shown in Figure 3.9b. Whereas the AlN fraction is continuously increasing with decreasing V/III ratio, indicating strong pre-reactions of ammonia with aluminum-containing species, the growth efficiency of the GaN fraction is constant in a V/III range between 87 and 1300. At lower V/III ratios, the growth efficiency of the GaN fraction is reduced. This could be related to desorption of gallium due to lower nitrogen levels. However, due to uncertainties in the AlGaN composition determination by XRD ($x = 0.96 \pm 0.04$), the calculated growth efficiency of the GaN fraction exhibits considerable uncertainties. Even almost constant GaN incorporation is not fully excluded. In summary, with a constant Al/III ratio, variations of the the V/III ratio allow for a modification of the surface morphology but also strongly influence the AlGaN growth rate and composition.

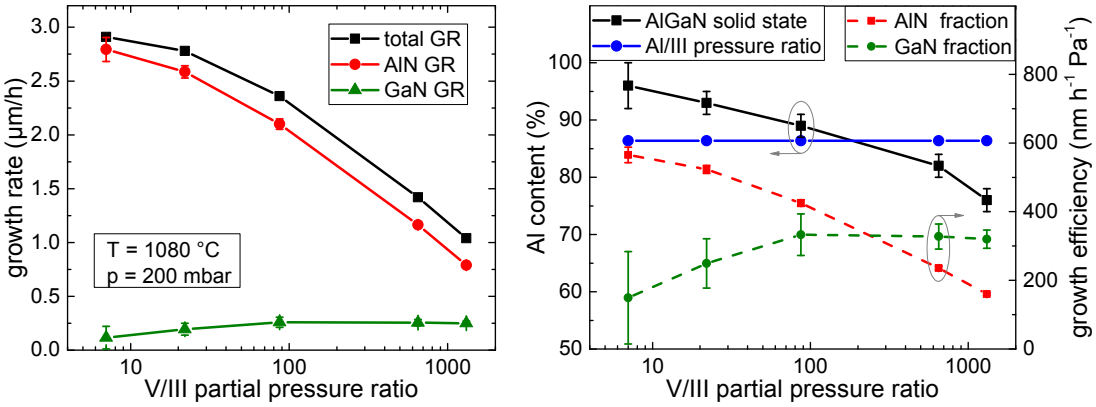

Figure 3.9: Influence of the V/III partial pressure ratio on the growth rate (a) and composition (b) of AlGaN, separated for AlN and GaN contributions.

Influence of AlGaN layer thickness and composition on morphology and uniformity

In order to identify the impact of a selected growth parameter on the morphology or uniformity of AlGaN layers, cross correlations with a second affected parameter should be excluded by the design of the experiment. As shown in the previous section, the V/III ratio is affecting AlGaN morphology and uniformity as well as composition and growth rate; cross correlations cannot be fully excluded for this sample series. By a statistic approach, the general impact of AlGaN composition and layer thickness on roughness and uniformity can be analyzed using various combinations of growth parameters. An AlGaN growth study with more than 100 individual samples including variations of the growth rate, the V/III partial pressure ratio, and the growth temperature was conducted for this purpose.

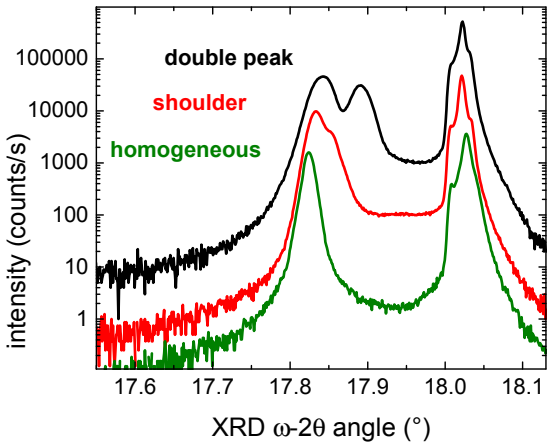

Figure 3.10: Different examples for XRD rocking curves of AlGaN layers exhibiting homogeneous, shoulder, or double peak features, relative intensities adjusted.

Target parameters of this investigation are the AlGaN surface morphology and uniformity. The surface morphology is characterized by the RMS roughness value determined from AFM scans. Uniformity will be classified according to distinctive features in XRD ω-2θ-curves, as illustrated in Figure 3.10: A single AlGaN reflection indicating homogeneous composition and strain state is the desired case (homogeneous). If AlGaN layers exhibit

partial relaxation or partially inhomogeneous composition, which is the undesired case, the XRD peak shape can show different features such as a significant peak broadening or shoulder formation (shoulder), or even formation of multiple peaks (double peak).

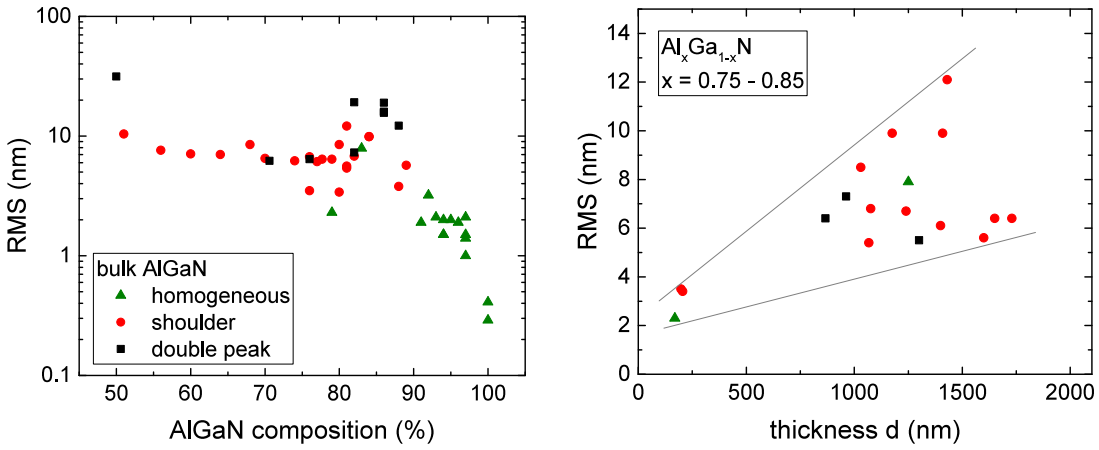

Figure 3.11: Influence of the AlGaN composition (a) and AlGaN layer thickness (b) on surface roughness and structural uniformity, indicated by XRD signature. Straight gray lines indicate the envelope of the scattering data points. (Measurements partly by Tino Simoneit - TU Berlin)

In Figure 3.11, the RMS roughness values of AlGaN samples grown at various reactor parameters are shown. In general, composition and thickness are both strongly influencing the roughness and uniformity of such AlGaN surfaces. As shown in Figure 3.11a, very smooth AlN layers can be realized with RMS roughness values near 0.3 nm close to the height of an AlN mono layer. For $Al_xGa_{1-x}N$ layers with $x > 0.9$, homogeneous composition is achieved with slightly increased RMS roughness values of 1 - 2 nm. Near the target composition of $x = 0.8$, AlGaN layers with a large variation of properties can be obtained, ranging from inhomogeneous and very rough (RMS > 10 nm) to uniform and comparably smooth AlGaN. For $x < 0.7$, all AlGaN layers exhibit non-uniformities and large RMS roughness near 10 nm. Consequently, obtaining pseudomorphic growth is becoming increasingly difficult. Therefore, the influence of AlGaN composition on morphology and uniformity in question needs to be considered and following experiments will, thus, focus on the composition range of $0.75 < x < 0.85$ as the device target value. AlGaN layers in that specific composition range with varying thickness are shown in Figure 3.11b. A first finding is the trend of increasing RMS roughness with increasing AlGaN layer thickness caused by increasing spiral dimensions (diameter and height). However, at a fixed thickness (and composition), roughness and uniformity can only vary due to the individual set of growth parameters. Therefore, a reliable analysis of the influence of AlGaN growth conditions on the layer morphology and roughness requires not only comparable composition but also comparable thickness. For following investigations, two distinct thickness values (d_1 and d_2) have been chosen: first, $d_1 = 200$ nm allowing for the extraction of results while keeping short growth times hence more growth samples and, second, $d_2 = 1000$ - 1500 nm which is the target thickness for AlGaN:Si current spreading layers in UVC emitting devices.

$Al_{0.8}Ga_{0.2}N$: Influence of V/III ratio, temperature, and growth rate

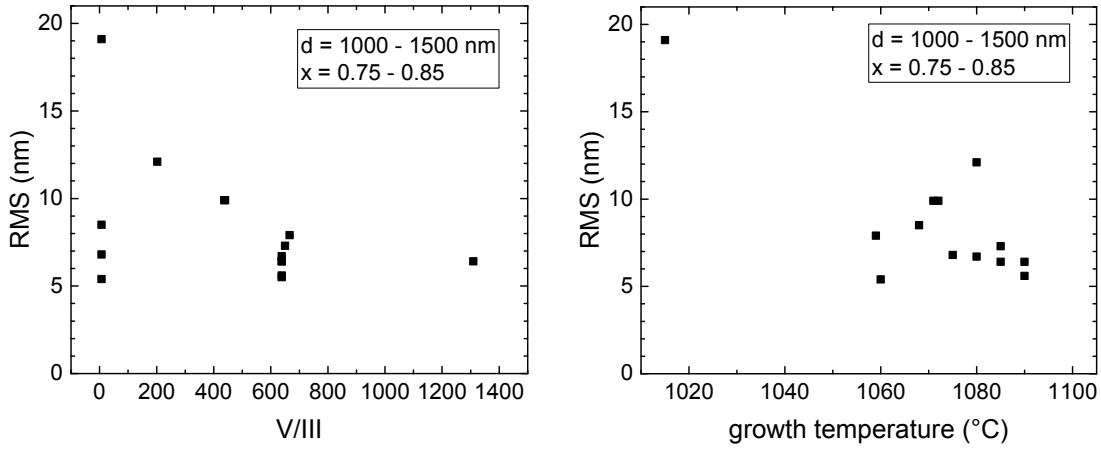

Figure 3.12: Influence of growth conditions on $Al_{0.8}Ga_{0.2}N$ surface roughness: a) V/III partial pressure ratio and b) growth temperature. (Measurements partly by Tino Simoneit - TU Berlin)

For $Al_xGa_{1-x}N$ layers with fixed composition in the range x = 0.75 - 0.85 and thickness of 1000 - 1500 nm, the influence of V/III ratio, growth temperature, and growth rate was investigated with respect to a potential impact on the structural properties, e. g. morphology. As shown in Figure 3.12, parameters such as the V/III partial pressure ratio as well as the pyrometrically measured susceptor temperature exhibit no strong correlation with the RMS roughness of $Al_{0.8}Ga_{0.2}N$ layers within the investigated parameter ranges ($7 < V/III < 1300$, $1050\,°C < T < 1100\,°C$). Growth parameters exceeding the investigated ranges could lead to more significant changes of the surface morphology, however, technological limitations or physical side effects are preventing these steps: With decreasing V/III ratio, increasing carbon concentrations have to be expected [51] causing point defects that are electrically compensating the silicon donors. In contrast, very high V/III ratios > 1300 are reducing the AlGaN growth rate due to an increasing impact of pre-reactions, as discussed before.

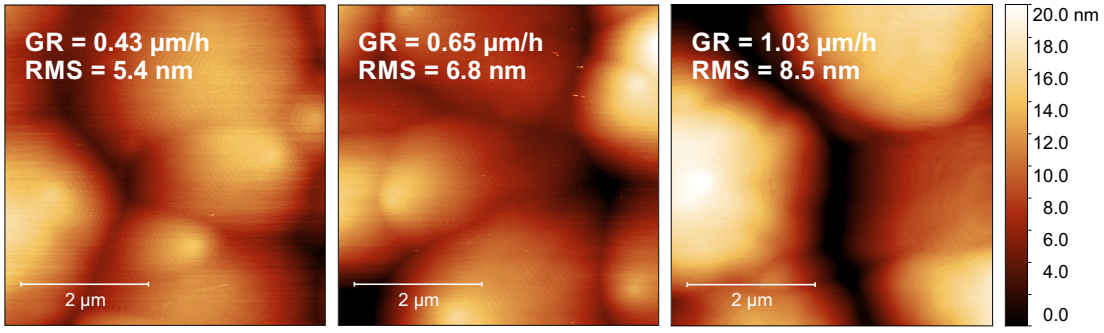

Figure 3.13: AFM topograms of 1 - 1.5 µm thick $Al_{0.8}Ga_{0.2}N$ layers grown at different growth rates with constant V/III = 7.

In principle, growth rates in the range of 0.5 µm/h or below would allow for the growth and analysis of single, thin AlGaN:Si samples, however, due to time reasons such growth rates would be insufficient for the frequent growth of thick AlGaN:Si layers or AlGaN-based LEDs and laser structures. Very low temperatures are not promising for the growth of AlGaN with smooth surfaces as 1015 °C leads to a very rough morphology with RMS roughness values near 20 nm (Figure 3.12b). AlGaN growth at very high temperatures T > 1100 °C was not experimentally covered because of machine limitations regarding the maximum process temperature.

Nevertheless, the surface roughness exhibits a certain correlation with the AlGaN growth rate, shown by AFM images in Figure 3.13 for AlGaN with comparable composition and thickness. With decreasing growth rate the roughness is decreasing due to decreasing spiral height. This correlation holds true even for very different growth regimes with very low V/III = 7 as well as higher V/III ratios of several hundred as shown in Figure 3.14.

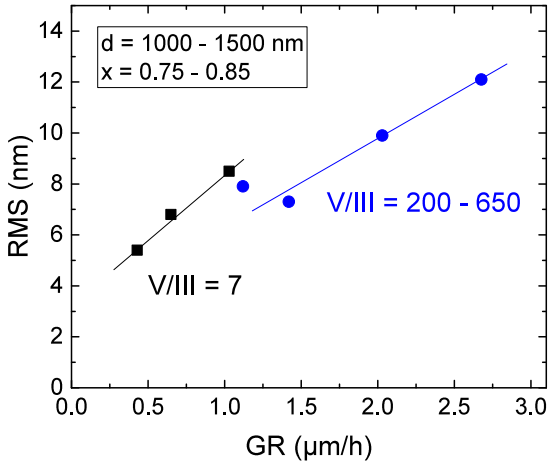

Figure 3.14: Influence of AlGaN growth rate on surface roughness for two different V/III regimes.

In summary, the impact of MOVPE growth parameters on AlGaN morphologies was analyzed. Concerning the target AlGaN parameters (composition x = 0.8 and thickness d = 1000 - 1500 nm), only the variation of the growth rate exhibits a correlation with surface roughness. RMS roughness values of 5.4 nm without compositional uniformity were obtained, demonstrating only a minor RMS reduction compared to the initial state with RMS = 7 nm. Additionally, this roughness reduction could be achieved only for growth rates GR < 0.5 µm/h which is insufficient for the growth of UVC devices with 1200 nm thick AlGaN:Si layers. Therefore, alternative approaches for AlGaN:Si cladding layer growth are required such as superlattices that will be discussed in the next section.

3.3.3 Si-doped AlGaN-based superlattices with smooth morphology

In this section, the growth of AlGaN-based superlattices with growth interruptions is examined in order to obtain smooth surfaces and pseudomorphic AlGaN:Si layers [49, 52].

Compared to thick AlGaN layers, AlGaN-based superlattices (SL) with same average composition enable tunable structural, optical and electrical properties and can be employed as functional layers in light emitting devices [53]. Regarding structural properties, (Al,Ga)N-based SLs with low average aluminum mole fractions enable

effective reduction of threading dislocation densities and prevention of crack formation on sapphire substrates [54–56]. With increased aluminum contents ($0.5 < x < 0.6$) SLs can significantly influence electrical conductivity and V-pit formation, however, strain relaxation remains a major issue for AlGaN SLs in this composition range [57, 58]. Pseudomorphic SLs with very high aluminum contents ($x > 0.9$) have been demonstrated on AlN which enables dislocation filters or partial strain relief functionality [59, 60]. However, obtaining low resistance AlGaN becomes increasingly challenging with increasing aluminum content due to increasing Si activation energies, DX center formation and tensile stress [61].

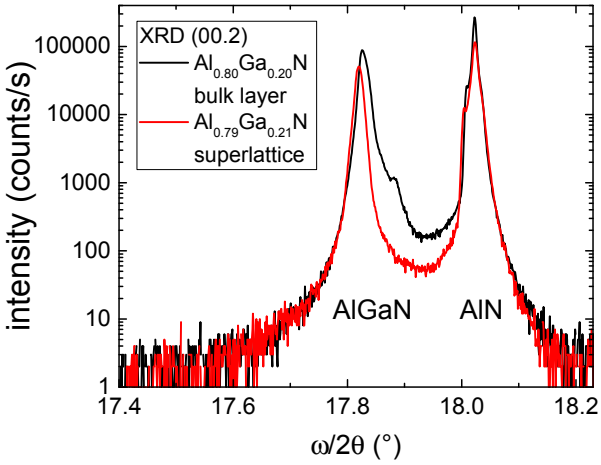

Figure 3.15: (00.2) XRD rocking curves of a bulk AlGaN layer and an AlGaN/AlGaN superlattice with 1 µm thickness and comparable average composition to evaluate the layer uniformity [49].

In this section the growth of silicon doped AlGaN/AlGaN superlattices and their influence on the surface morphology and compositional uniformity is analyzed. Additionally, growth interruptions (GRI) between these SL layers are introduced to further reduce inhomogeneities and interface roughness. To achieve both high conductivity and coherent growth, AlGaN superlattices with an average composition of $x = 0.8$ are utilized. The Si-doped AlGaN/AlGaN superlattices consist of 50 to 250 periods of alternating AlGaN layers with different composition, each with 2 nm nominal thickness. Further studies were carried out on SLs with growth interruptions between the SL layers. Here, the growth after each single SL layer was interrupted by stopping the supply of metalorganic precursors TMAl and TMGa as well as SiH_4, while NH_3 was supplied continuously. The length of the GRI was varied between 0 s (without GRI) and 10 s which approaches the time scale of the growth of a single SL layer.

In Figure 3.15, symmetrical XRD ω-2θ-scans of a 1 µm thick bulk $Al_{0.80}Ga_{0.20}N$ layer and an AlGaN/AlGaN SL with comparable thickness and average composition are shown. The bulk layer (black line) exhibits the AlGaN (00.2) reflection with a notable shoulder at larger diffraction angles indicating a small fraction of the AlGaN material with higher gallium content or partial strain relaxation. In contrast, the superlattice shows a sharp AlGaN reflection without additional broadening, indicating a more uniform layer. SL satellite peaks appear at high and low diffraction angles (which are discussed later), indicating that the periodicity is not disturbed.

In order to differentiate between strain relaxation and compositional inhomogeneities, RSM measurements near the AlN (10.5) reflection of both samples have been carried out (Figure 3.16) and analyzed according to Ref. [62]. The lower reflection at $Q_z = 6.22$

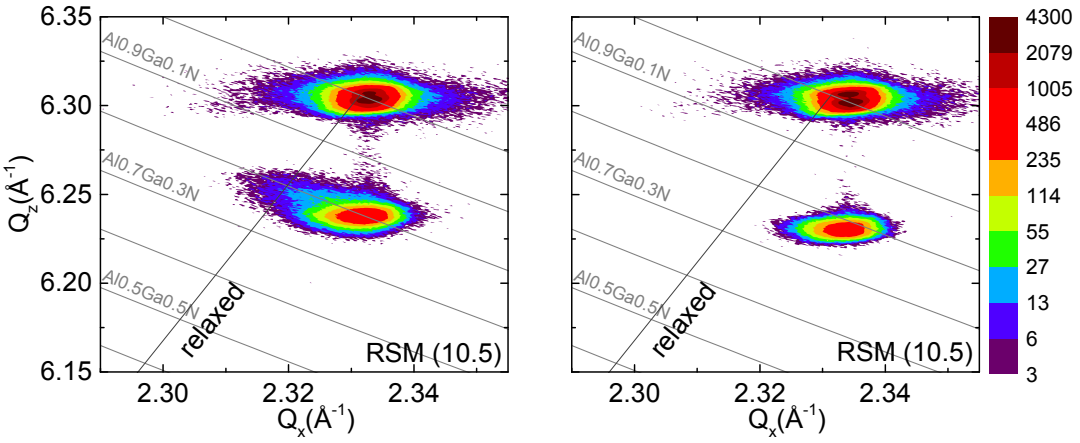

(a) (b)

Figure 3.16: XRD RSMs of a bulk AlGaN layer (a) and an AlGaN/AlGaN SL (b) with comparable average composition of x = 0.79 ± 0.01. The broadened reflection of the bulk AlGaN layer indicates partial strain relaxation, the sharp single AlGaN peak of the SL indicates uniform growth [49].

- 6.25 Å^{-1} originates from the 1 µm thick bulk AlGaN layer (Figure 3.16a) and the AlGaN/AlGaN SL (Figure 3.16b) with an average composition of x = 0.79 ± 0.01. The reflection of the bulk AlGaN layer is notably broadened towards smaller Q_x values (Figure 3.16a). This indicates that a part of this AlGaN layer exhibits inhomogeneous partial strain relaxation and slightly lower aluminum content, comparable to the shoulder formation shown in Figure 3.10. In contrast, the SL sample shows a sharp single AlGaN SL reflection at the same Q_x value as the AlN layer (Figure 3.16b) without indication for broadening originating from compositional fluctuations or inhomogeneous strain relaxation. Hence, the superlattice approach enables the growth of AlGaN with uniform average composition of x = 0.79 and pseudomorphic strain state.

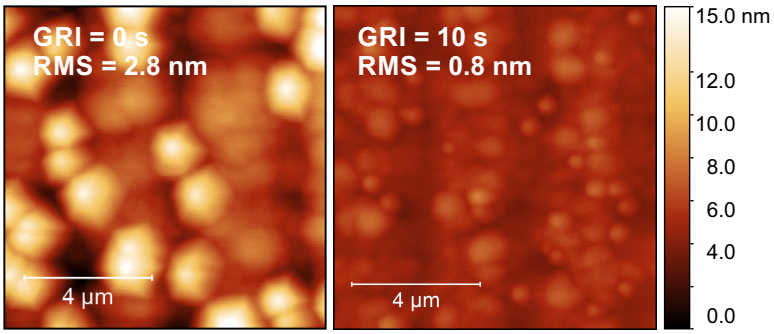

Figure 3.17: AFM topograms of 200 nm thick AlGaN-based superlattices with growth interruption of 0 s and 10 s. Spiral height and RMS roughness are strongly reduced with increasing growth interruption length [49].

In order to provide beneficial n-cladding properties for UVC LDs, smooth morphologies need to be achieved. Therefore, an approach using growth interruptions between the layers of a SL with intended composition of $Al_{0.80}Ga_{0.20}N/Al_{0.60}Ga_{0.40}N$ is investigated. In Figure 3.17, the impact of growth interruptions on spiral hillocks is shown for AlGaN SLs with 50 periods and nominally 200 nm thickness. With increasing GRI time from 0 s to 10 s, the spiral height is strongly decreasing from 6 nm to 2.5 nm and the RMS roughness is decreasing from 2.8 nm to 0.8 nm measured by AFM on (10 µm)^2 scan area.

In Figure 3.18a, XRD ω-2θ-scans of coherent AlGaN:Si SL layers with GRI of 0 s, 5 s, and 10 s are shown, exhibiting an increasing average aluminum content of the SL with increasing GRI, as the 0-order peak shifts from 17.75° (average composition x = 0.70) to 17.87° (x = 0.83). Furthermore, a reduction of the period thickness and total SL thickness with increasing GRI was determined by analyzing the SL satellite and fringe positions as summarized in Table 3.2. This is due to desorption of gallium atoms during the growth interruptions in hydrogen-ammonia ambient [63] at the wafer temperature of 1080 °C. Such gallium-selective etching results in higher average aluminum content and lower layer thickness for increased GRI times.

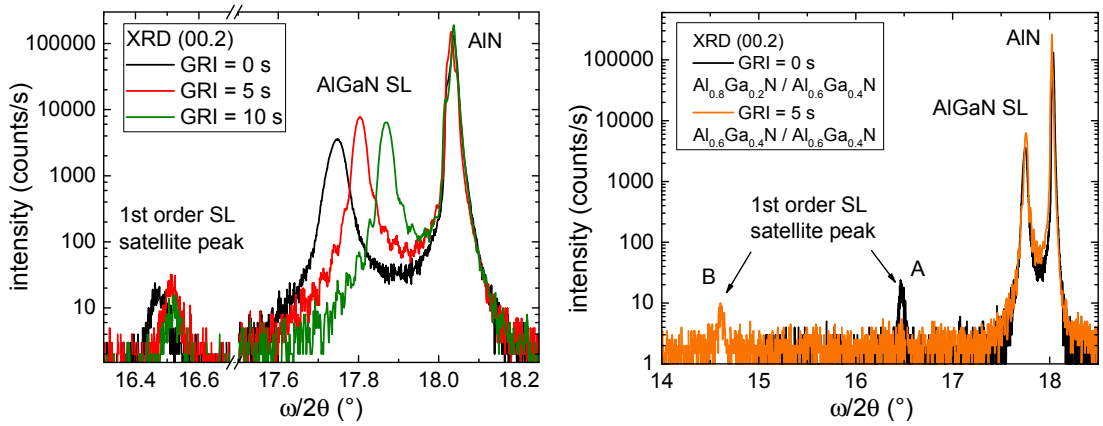

Figure 3.18: Symmetric XRD rocking curves of (a) AlGaN-based superlattices with growth interruption varying from 0 s to 10 s and (b) a pseudo-superlattice containing 100 periods of nominally 2 nm $Al_{0.60}Ga_{0.40}N$ separated by 5 s GRI (orange) indicating the desorption of gallium: The average composition is increased to x = 0.7 and SL satellites (B) are appearing due to the GRI. An $Al_{0.80}Ga_{0.20}N/Al_{0.60}Ga_{0.40}N$ SL without GRI (black) is shown for comparison [49].

Table 3.2: Influence of growth interruption time on composition and thickness of superlattices with 50 periods, evaluated from symmetrical XRD rocking curves.

Growth interruption	**0 s**	**5 s**	**10 s**
Average composition	0.70	0.77	0.83
Period thickness	3.63 nm	3.57 nm	3.45 nm
Total SL thickness	182 nm	178 nm	172 nm

In order to investigate the impact of gallium desorption on SL growth, two different AlGaN-based layer stacks have been compared: Structure A is composed of an $Al_{0.80}Ga_{0.20}N/Al_{0.60}Ga_{0.40}N$ SL without GRI as shown in Figure 3.18a. Structure B is containing the repeated growth of $Al_{0.60}Ga_{0.40}N$ layers of nominally 2 nm thickness with 5 s GRI after each layer. XRD rocking curves in Figure 3.18b are illustrating the influence of GRIs on the properties of these structures. The XRD rocking curve of structure A exhibits an AlGaN SL reflection with average composition of x = 0.7 and a SL satellite peak near 16.5° indicating a periodicity of 3.6 nm. Structure B, however, exhibits the same average composition of x = 0.7, which is the result of gallium

desorption out of each $Al_{0.60}Ga_{0.40}N$ layer during the GRI. Additionally, the XRD data of structure B show a satellite peak at very low diffraction angles near 14.6° indicating the formation of a SL structure although only $Al_{0.60}Ga_{0.40}N$ was grown. Consequently, the combination of repeated growth of AlGaN and desorption can form a periodic structure with 1.7 nm period length in this case, which is generating the observed SL satellite peak near 14.6° in XRD measurements.

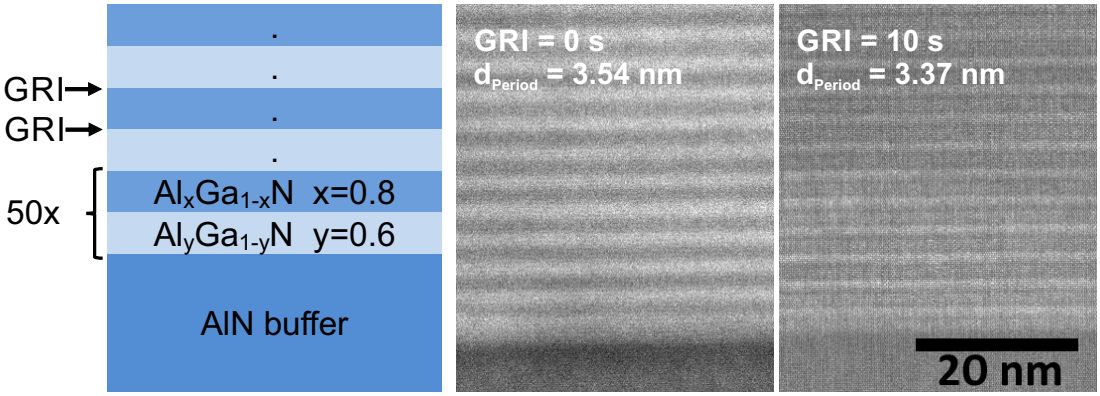

Figure 3.19: Growth schematic and cross section STEM-HAADF images of AlGaN/AlGaN superlattices with growth interruption of 0 s and 10 s. (Measurements by Toni Markurt - IKZ).

To investigate the microscopic structure within the SL-periods, scanning transmission electron microscopy (STEM) measurements were performed on the SL samples without GRI as well as with 10 s GRI. High angle annular dark field imaging (HAADF) and local Z-contrast analysis enable the determination of SL periodicity, layer composition, and interface roughness on a microscopic length scale [64]. The STEM measurements were carried out with a FEI Titan 80–300 microscope using an acceleration voltage of 300 kV. In Figure 3.19, cross section STEM images of both SL samples are shown next to a growth schematic illustrating the SL layer sequence and growth interruptions after each layer. From these STEM images with large field of view, significant differences of the interface quality can be observed in combination with a slight reduction of the period length up to almost 5% for the sample with GRI = 10 s.

In order to examine the interface properties on an atomic scale, STEM-HAADF images with atomic resolution are shown in Figure 3.20 for both SL samples. Microscopic aluminum content profiles, shown in Figure 3.20c and d, were extracted by averaging over a lateral range of 20 nm within the central part of Figure 3.20a and b which is marked by the white dashed frames. According to the STEM-HAADF analysis, the SL without GRI has an average composition of x = 0.70 with 3.6 nm period thickness which fits very well to the data obtained by XRD and exhibits a sinusoidal modulation of the aluminum content in growth direction varying between x = 0.64 and 0.76 (Figure 3.20c) instead of abrupt and independent SL layers with x = 0.6 and 0.8. In this case, gas phase intermixing of the two components with different Al/III ratio for $Al_{0.60}Ga_{0.40}N$ and $Al_{0.80}Ga_{0.20}N$ growth leads to such non-abrupt interfaces. Before entering the reactor chamber, the transition time of gases within the showerhead distribution chamber is close to 1 s. For the AlGaN growth rate of 1.8 µm/h, growth times are as short as 8 s per period. This results in a finite temporal overlap and intermixing of the subsequent gas mixtures within the chambers, explaining the observed non-abrupt

interfaces. Additionally, the incorporation of gallium atoms into layers with different composition can be influenced by gallium segregation during growth of AlGaN SL layers with different compressive strain [65].

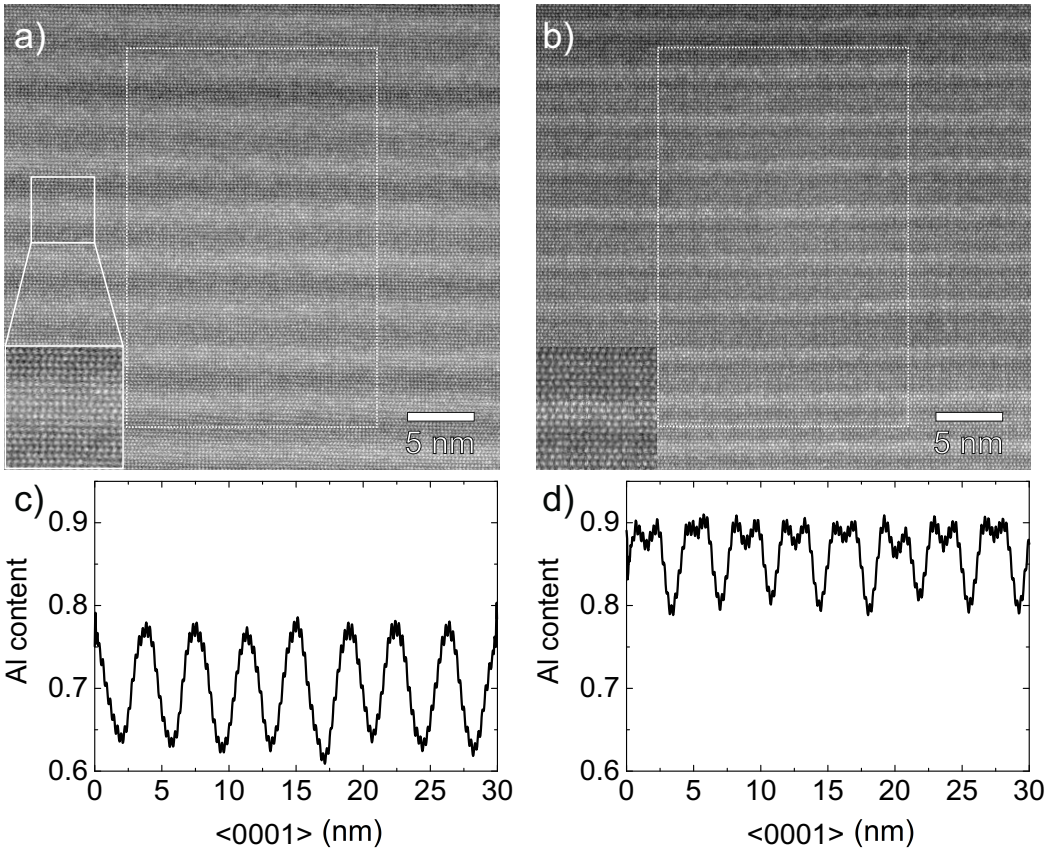

Figure 3.20: Atomic resolution STEM-HAADF images of AlGaN/AlGaN superlattices with growth interruption of (a) 0 s and (b) 10 s. Corresponding composition profiles shown in (c) and (d) are indicating differences of average composition and interface properties [49]. (Measurements by Toni Markurt - IKZ)

The AlGaN-based SL with 10 s GRI exhibits very abrupt interfaces between the two AlGaN layers with different composition (Figure 3.20b). Furthermore, the formation of one to two monolayers of aluminum-rich AlGaN with $x = 0.91$ can be observed after each single SL layer (Figure 3.20d). The average aluminum content of the SL is increased to $x = 0.85$, period thickness and total SL thickness are reduced to 3.4 nm and 170 nm, respectively, which is in agreement with the trend determined from XRD analyses. With 10 s GRI, the gas phase intermixing can be successfully suppressed. Gallium is shown to partially desorb from each single layer during the GRI, affecting most strongly the topmost one to two monolayers.

In order to generalize the findings from such 200 nm thin AlGaN layers, 1 µm thick bulk AlGaN:Si layers and silicon-doped AlGaN/AlGaN SLs with similar average composition of $x = 0.8$ are compared. These might be employed for n-AlGaN cladding layers in deep UV laser diodes requiring sufficient thickness for current spreading. The compositions of both bulk AlGaN and SL with 10 s GRI were individually adjusted to 0.8 by a modified supply of MO precursors to compensate for gallium desorption within the

GRI. In Figure 3.21, AFM images of both samples measured on $(10\,\mu m)^2$ are compared, exhibiting decreasing RMS roughness from 5.8 nm for the bulk AlGaN:Si layer to 2.5 nm for the smooth SL with 10 s GRI between the SL layers due to a significant reduction of the spiral height from 20 nm to 8 nm.

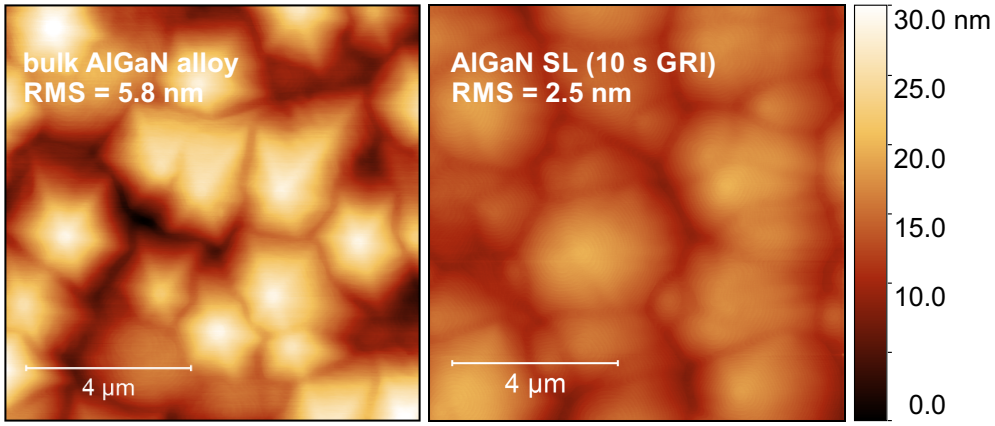

Figure 3.21: AFM topograms of a bulk AlGaN layer (left) versus an AlGaN-based superlattice with growth interruption of 10 s (right), both with 1 µm thickness and similar average composition of x = 0.8. Compared to bulk AlGaN, the superlattice surface exhibits reduced spiral height and RMS roughness [49].

In order to summarize the discussed results, the structural properties of bulk AlGaN layers and AlGaN-based superlattices from this growth study are shown in Figure 3.22. Whereas no smooth and uniform bulk $Al_{0.8}Ga_{0.2}N$ layers (filled symbols) could be obtained, the superlattice approach (hollow symbols) enabled successful growth of smooth and uniform $Al_xGa_{1-x}N$ layers within the composition range x = 0.75 - 0.85 matching the requirements defined at the beginning of this section 3.3. For AlGaN-based SLs with 200 nm thickness, very smooth surfaces with RMS = 0.44 nm were obtained even near x = 0.8, which is comparable to the smoothest AlN surfaces obtained from step flow growth.

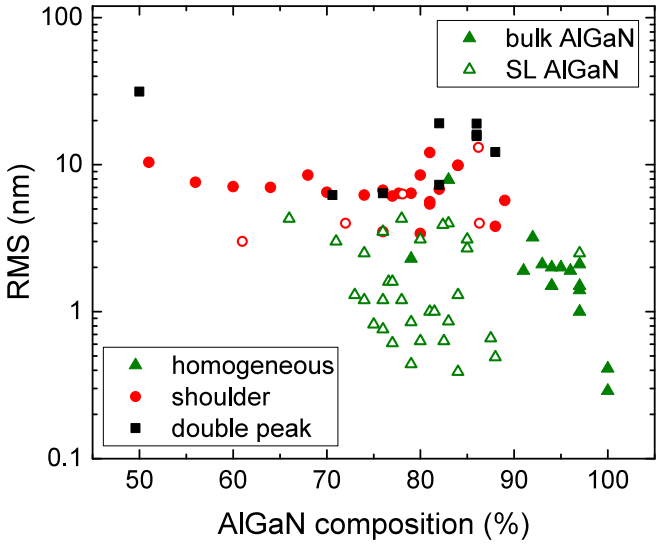

Figure 3.22: Summary of RMS roughness values versus composition of the investigated bulk AlGaN layers and superlattice samples. While atomically smooth surfaces can be realized for AlN layers, only the superlattice approach allows for smooth morphology and uniform composition of AlGaN with a composition near x = 0.8.

Next to the achieved structural uniformity and smooth surfaces of $Al_{0.8}Ga_{0.2}N$:Si superlattices, high electrical conductivity and UV transparency need to be demonstrated in order to fully match the target values for AlGaN:Si cladding layer properties for UV laser diodes introduced at the beginning of this section. From I-V-measurements in Van-der-Pauw-geometry, the resistivity of both 1 µm thick samples shown in Figure 3.21 was determined to be 0.025 Ωcm, which was confirmed by contactless resistance measurements. Therefore, compared to bulk $Al_{0.80}Ga_{0.20}N$:Si layers, similarly high conductivity is obtained for the SL sample with comparable average composition. From UV transmission spectroscopy measurements of the bulk AlGaN:Si sample and the SL sample, a clear absorption edge at a wavelength 235 nm was confirmed without any sub band gap absorption near the target emission wavelength of UVC laser diodes of 270 nm.

The achieved $Al_xGa_{1-x}N$:Si superlattice cladding layer properties can be summarized as follows:

(I) Thickness d = 1000 - 1500 nm (and d = 200 nm)

(II) Uniform composition x = 0.8

(III) Resistivity $\rho = 0.025\,\Omega$cm

(IV) Roughness RMS = 2.5 nm (and 0.44 nm for d = 200 nm)

(V) Strain state $\varepsilon = 0.5$ (fully strained to AlN buffer, relaxation R = 0)

In conclusion, such transparent, conductive, smooth, and homogeneous AlGaN-based superlattices can be considered as superior alternative for bulk AlGaN layers to be used as n-type cladding layers for UVC laser diodes.

3.4 Pseudomorphic and smooth AlGaN MQWs with abrupt interfaces

In this section, the growth of AlGaN-based MQWs and waveguide layers is investigated in order to obtain laser structures with pseudomorphic and smooth MQWs as well as abrupt interfaces. In subsection 3.4.1, the influence of AlGaN composition on waveguide (WG) relaxation is examined for MOVPE growth on ELO AlN/sapphire templates. For coherent structures, the effect of growth temperature on V-pit formation and the correlation to screw dislocations is discussed in subsection 3.4.2. Obtaining smooth MQW surfaces in absence of a high screw dislocation density is demonstrated in subsection 3.4.3 for the growth on bulk AlN substrates whereas the effect of growth temperature and growth interruptions on MQW growth is explored in subsection 3.4.4 in order to obtain abrupt MQW interfaces in UVC lasers.

3.4.1 Pseudomorphic growth of AlGaN MQWs

In order to analyze the strain state of AlGaN waveguides, AlGaN-based MQW laser heterostructures with varying waveguide composition were grown on c-oriented ELO AlN/sapphire templates with 0.25° offcut towards the $[1\bar{1}00]$ sapphire direction and threading dislocation densities of $0.5 - 2 \cdot 10^9\,\mathrm{cm}^{-2}$ [66–68]. In Figure 3.23a, the laser

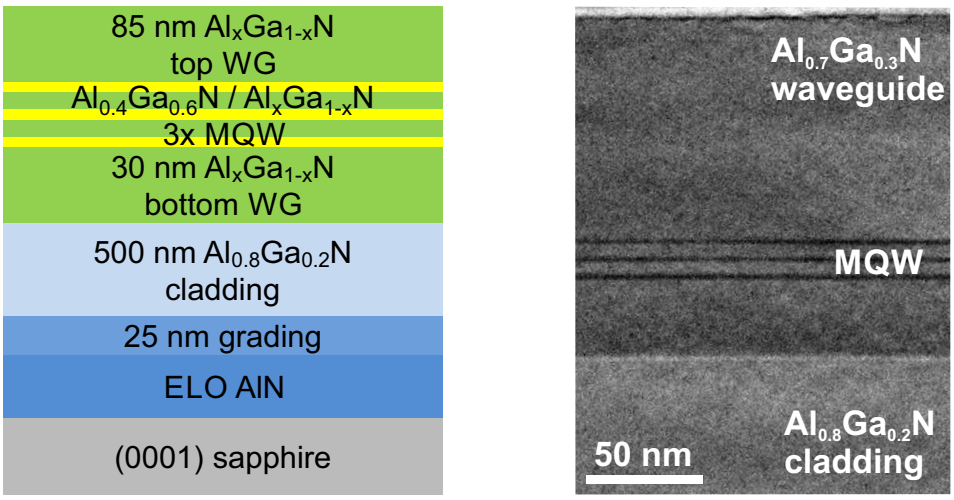

(a) (b)

Figure 3.23: (a) Schematic UVC laser heterostructure for optical excitation with MQW active region, AlGaN waveguide system, $Al_{0.80}Ga_{0.20}N$ bottom cladding layer and a grading to AlN, grown on ELO AlN/sapphire templates. (b) Cross section TEM image of a laser structure showing the MQW within $Al_{0.70}Ga_{0.30}N$ waveguide layers confined by a bottom $Al_{0.80}Ga_{0.20}N$ cladding layer and the top surface [66]. (Measurement by Jae Bum Park - TU Berlin)

heterostructure is schematically shown, consisting of a threefold MQW with 2.2 nm thick $Al_{0.4}Ga_{0.6}N$ quantum wells for emission near 280 nm and 5 nm thick $Al_xGa_{1-x}N$ barriers with varying composition x. The MQW is embedded in an asymmetric $Al_xGa_{1-x}N$ waveguide system with WG thicknesses of 85 nm above and 30 nm below the MQW. At a later stage, such thicknesses would be suitable for mode confinement in electrically injected laser structures with doped WG layers. Similar to the barriers, the WG composition is varied in the experiment between $x = 0.45$ and 0.70. A 500 nm thick $Al_{0.80}Ga_{0.20}N$ layer is used as cladding layer below the WG and the upper WG interface is realized by air.

Laser heterostructures with $Al_xGa_{1-x}N$ WG composition of $x = 0.45$, $x = 0.55$, and $x = 0.70$ with total waveguide thickness of 130 nm were grown. Figure 3.23b shows a TEM cross section of a laser structure with $Al_{0.70}Ga_{0.30}N$ waveguide including the MQW as well as parts of the $Al_{0.80}Ga_{0.20}N$ cladding layer. The two-dimensional growth mode enables the realization of smooth and homogeneous MQW, waveguide, and cladding layers. The TEM analysis of the three-fold AlGaN MQW region reveals (2.4 ± 0.4) nm thick quantum wells and (5.0 ± 0.4) nm thick barriers. In order to analyze the strain state, XRD RSMs near the AlN (10.5) reflection are shown in Figure 3.24. Similar to RSMs shown in the previous section, the topmost peak at the largest reciprocal lattice units $Q_z = 6.31\,\text{Å}^{-1}$ corresponds to the AlN layer followed by the $Al_xGa_{1-x}N$ cladding layer ($x = 0.80 \pm 0.02$). The lower peaks at $Q_z \leq 6.20\,\text{Å}^{-1}$ are originating from the $Al_xGa_{1-x}N$ WG layer stack with different composition $x = 0.45$, $x = 0.55$, and $x = 0.70$. The strain state of these WGs strongly depends on the composition: The $Al_{0.45}Ga_{0.55}N$ WG peak center is shifted to lower Q_x values clearly indicating partial plastic relaxation by the formation of additional threading dislocations or inclination of existing threading dislocations [68, 69] due to the large lattice mismatch (Figure 3.24a). However, a

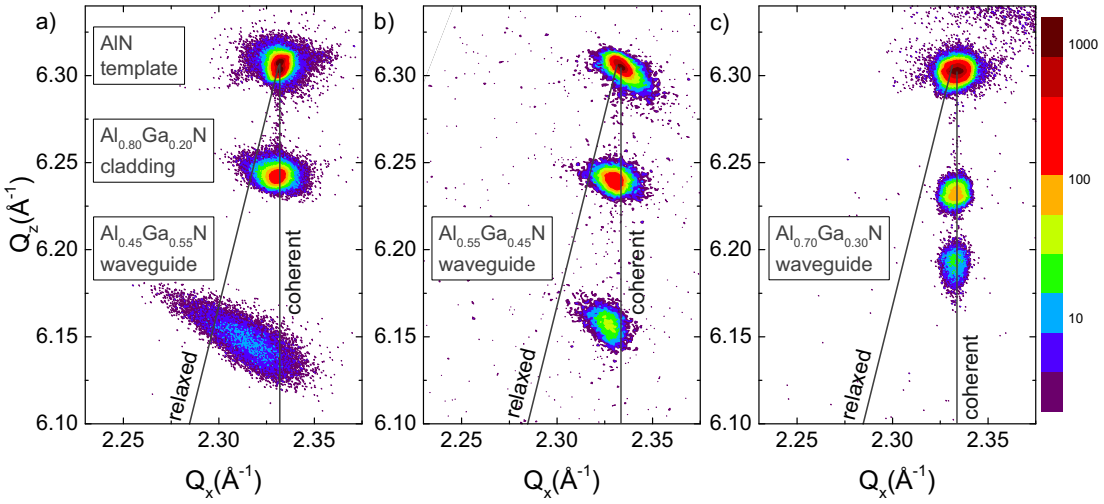

Figure 3.24: (10.5) XRD RSM of UV laser structures with $Al_xGa_{1-x}N$ waveguide composition varied between (a) x = 0.45, (b) x = 0.55, and (c) x = 0.70. Plastic relaxation is observed for WGs with x = 0.45 and x = 0.55 whereas pseudomorphic growth is obtained for the WG with x = 0.70 [66].

certain amount of strain remains for the partially relaxed $Al_{0.45}Ga_{0.55}N$ layer, as the peak is located off the indicated line for relaxed AlGaN. Additionally, a strong peak broadening in ω-direction (FWHM = 0.041°) is indicating an increased defect density or other mechanisms of inhomogeneous relaxation or compositional broadening. Also, the $Al_{0.55}Ga_{0.45}N$ layer exhibits an onset of partial relaxation as shown in Figure 3.24b. Only with an $Al_{0.70}Ga_{0.30}N$ waveguide a coherent AlGaN laser heterostructure is obtained (Figure 3.24c). Both of these WG peaks exhibit a FWHM of 0.033°, mainly determined by broadening due to the small WG thickness of 130 nm (Scherrer equation [70]) in combination with broadening due to the random AlGaN alloy.

The strain state ε of these waveguide layers is evaluated according to equation 3.1. Minimum and maximum strain values for the AlGaN material system are given by the AlN/AlN interface with $\varepsilon = 0$ and the AlN/GaN interface with $\varepsilon = 2.4\%$. Within this range, the strain of coherent AlGaN WGs would become increasingly compressive with decreasing WG aluminum content due to an increasing lattice misfit to the AlN buffer layer. However, as observed, the strain can be reduced by relaxation. The coherent $Al_{0.70}Ga_{0.30}N$ layer exhibits $\varepsilon = 0.7\%$. For the $Al_{0.55}Ga_{0.45}N$ layer ε is slightly increased to 0.9%, whereas a pseudomorphic $Al_{0.55}Ga_{0.45}N$ layer would exhibit $\varepsilon = 1.2\%$, demonstrating slight partial relaxation. In contrast, for the partially relaxed $Al_{0.45}Ga_{0.55}N$ layer the strain is reduced to $\varepsilon = 0.7\%$, whereas a pseudomorphic $Al_{0.45}Ga_{0.55}N$ layer would exhibit $\varepsilon = 1.3\%$. In order to avoid such plastic relaxation of AlGaN MQWs, aluminum contents near x = 0.70 or above are necessary for these 130 nm thick waveguide structures. However, the strain relaxation of compressively grown AlGaN layers is also dependent on the lattice constant and dislocation density of the respective substrates. In previous studies, pseudomorphic AlGaN layers with slightly lower aluminum content (x < 0.7) were obtained for the growth on nearly dislocation-free bulk AlN substrates [19, 71].

3.4.2 Suppression of V-pit formation in AlGaN MQWs

Topographic AFM images of laser surfaces with pseudomorphic $Al_{0.70}Ga_{0.30}N$ waveguides can show diverse morphological features, such as hexagonally shaped V-pits, step bunching, and spiral hillocks (Figure 3.25a) [66]. Similar to AlN growth on bulk AlN substrates discussed in section 3.2, formation of step bunches is also observed for AlN growth on c-oriented sapphire substrates with 0.25° offcut. Due to the trench pattern of the ELO process, the average step spacing is fixed to 3.5 µm resulting in macro steps with 15 nm height [24, 68]. Spiral hillocks, however, are formed during the growth of $Al_{0.8}Ga_{0.2}N$ cladding layers at 1080 °C, compare to subsection 3.3.2. These cladding layers are grown under nitrogen-rich conditions with a V/III ratio of 650 and a high growth rate (1.8 µm/h), similar to Figure 3.7a, resulting in spiral growth due to high supersaturation [72] in combination with present screw dislocations. The surfaces of such $Al_{0.80}Ga_{0.20}N$ cladding layers are almost pit-free (density $< 10^6\,cm^{-2}$). The surfaces of complete MQW laser heterostructures exhibit V-pit densities of $2.2 \cdot 10^7\,cm^{-2}$ determined by AFM measurements (Figure 3.25a). Therefore, these V-pits are developing mainly during the growth of AlGaN WGs and MQWs, and can be influenced by the growth conditions of these layers.

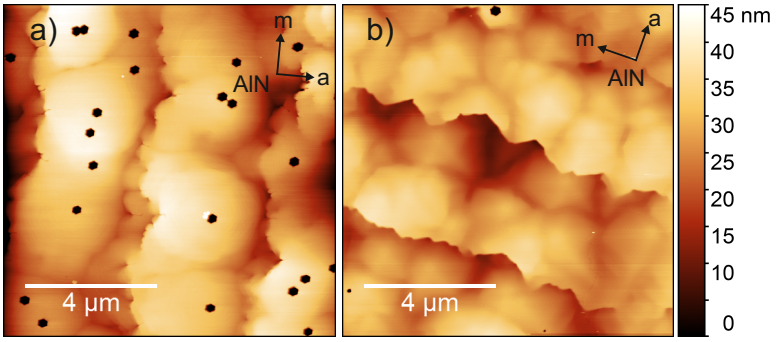

Figure 3.25: AFM topographs of UV lasers with varied growth temperature of active region and waveguides from (a) 900 °C to (b) 1070 °C, leading to reduced V-pit densities at elevated temperatures [66].

The observed V-pits are shaped like inverted, hexagonal pyramids with $\{10\bar{1}1\}$ sidewalls. A growth rate of $\{10\bar{1}1\}$ facets less than the growth rate of the (0001) surface would lead to stable facets of the V-pits, which can be described by a kinetic Wulff plot [73]. These growth rates can be influenced by growth parameters, e. g. temperature, enabling a modification of the surface morphology. V-pit formation can be controlled in analogy to reports for the InGaN/GaN material system [74, 75]. However, in AlGaN-based MQWs, parameters like growth temperature, strain state and defect densities are different from InGaN requiring individual investigations for the case of AlGaN. In this study, the growth temperature of MQW and WG layers was intentionally varied from 900 °C to 1070 °C in order to investigate the impact of growth temperature on the resulting layer properties, e. g. V-pit formation. As shown in Figure 3.25b, surface morphologies are affected by the temperature and V-pit densities are decreasing from $2.2 \cdot 10^7\,cm^{-2}$ at 900 °C to $3 \cdot 10^6\,cm^{-2}$ at 1070 °C [66]. These nearly pit-free WG surfaces can provide a reduced scattering potential and less optical losses in a laser cavity. The effect on optically pumped UVC laser thresholds will be discussed in section 3.5.

3.4.3 Morphology of AlGaN MQWs grown on AlN substrates

AlGaN MQWs with low TDDs are needed for efficient UV LEDs, requiring AlN buffer layers with low TDDs. Without applied advanced defect reduction techniques, planar AlN buffer layers grown on c-oriented (0001) sapphire substrates typically exhibit dislocation densities beyond TDD = 10^{10} cm^{-2} and broad asymmetric XRD peaks (30.2) with FWHM $\geq$ 2000" [23]. While the density of screw- and mixed-type dislocations can be strongly reduced [23], a high edge-type dislocation density is typically dominating the high TDD of planar AlN layers, which still allows for UV emission with reduced IQE [76]. By AlN epitaxial lateral overgrowth (ELO) of stripe patterned and etched AlN layers, reduced dislocation densities of 0.5 to $2 \cdot 10^9$ cm^{-2} can be achieved, as indicated by a strong FWHM reduction of asymmetric XRD peaks (10.2) to FWHM = 240" for 8 µm thick ELO AlN layers on sapphire [24, 44, 77]. As a third option, AlN epitaxy on nearly defect-free native bulk AlN substrates with TDD < 1000 cm^{-2} promises the best crystal quality and highest IQE of UV emitters [19]. UVC emitting MQWs with IQE of 20% to 30% and laser heterostructures with optically pumped UVC lasing have already been demonstrated by TU Berlin together with FBH and IKZ, for the growth on ELO AlN/sapphire templates as well as on bulk AlN substrates [45].

In this section, the MOVPE growth of AlGaN MQWs on bulk AlN substrates is investigated with emphasis on the morphology. For the heterostructure growth at the same growth conditions like in the previous section, similar challenges could be expected including spiral growth or V-pit formation. In this experiment, 550 µm thick bulk AlN substrates provided by IKZ were homoepitaxially overgrown with 5 µm AlN by MOVPE at FBH. The laser heterostructure design includes a 400 nm AlN layer, a 1.2 µm thick $Al_{0.75}Ga_{0.25}N$:Si cladding layer, and the AlGaN MQW for UVC emission near 270 nm, all grown in the same MOVPE reactor at TU Berlin. Figure 3.26 shows the morphology development at different stages of the growth of these heterostructures. In Figure 3.26a, an AFM image of the 400 nm thick AlN layer is shown, exhibiting surfaces with atomic steps provided by almost ideal step flow growth. The average height of these steps was measured to be 0.5 nm, which demonstrates that bilayer steps with the height of two AlN monolayers are present in this case. Taking this step height into account, the measured step density of 5 µm^{-1} reveals a local substrate offcut of $\alpha = 0.14°$. For such smooth surfaces, very low RMS roughness values of 0.21 nm on (5 µm)^2 are obtained. In Figure 3.26b, the MOVPE growth was stopped after the $Al_{0.75}Ga_{0.25}N$:Si layer and the surface still exhibits smooth morphology with an RMS roughness of 0.27 nm. However, the atomic step edges are not perfectly straight but exhibit a certain curvature. Also the nucleation of small AlN islands with monolayer height can be observed on some step terraces. These features are typically observed in III-nitride growth at high supersaturation [38]. In absence of screw dislocations with high density, AlGaN growth at even higher supersaturation would lead to the formation of larger islands that are more separated from each other. Nevertheless, in Figure 3.26b the preferred direction of the step flow growth towards the top right of the image is clearly visible, given by the offcut direction of the substrate. The surface of the AlGaN MQW is shown in Figure 3.26c. In contrast to the AlN and AlGaN growth, the MQW exhibits grain-like features on the surface with 300 - 1000 nm lateral size, 5 - 15 nm height, and a density of $1 \cdot 10^8$ cm^{-2}. The roughness is increased by an order of magnitude to an RMS value of 2.8 nm.

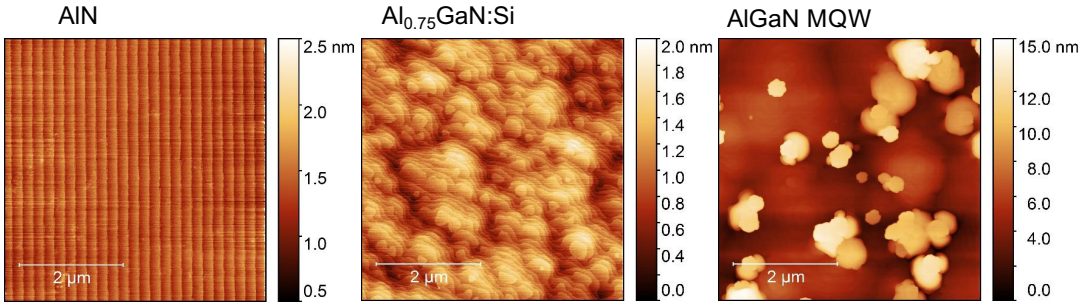

Figure 3.26: AFM topograms of AlN, AlGaN:Si, and an AlGaN MQW grown by MOVPE on bulk AlN substrate, exhibiting smooth AlN and AlGaN:Si surfaces and increased roughness for the MQW.

One possible origin for the formation of three-dimensional structures such as grains could be AlGaN growth near screw-type threading dislocations, as investigated in section 3.3. However, low total TDDs $< 10^3$ cm^{-2} are expected from the growth on bulk AlN substrates. Also the generation of additional threading dislocations during pseudomorphic AlGaN and MQW overgrowth was avoided by using waveguide and barrier layers with high aluminum contents ($Al_{0.7}Ga_{0.3}N$) comparable to Figure 3.24c. Furthermore, AFM topograms show no evidence for a high SD density, because SDs typically lead to the formation of spirals that would be reliably detected by AFM. Therefore, screw-type threading dislocations can be excluded as the origin for the observed grain formation with a density of $1 \cdot 10^8$ cm^{-2}.

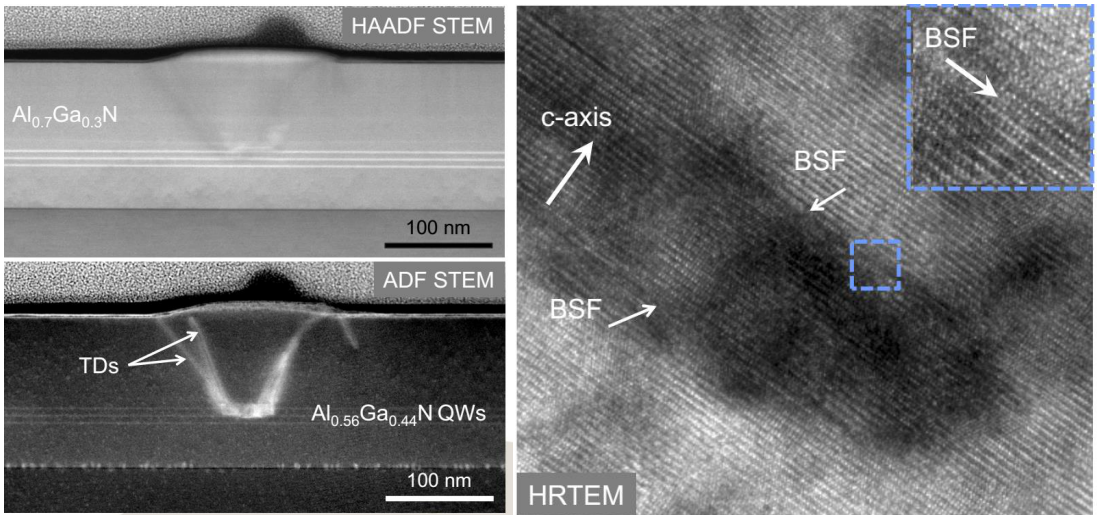

Figure 3.27: Cross-section TEM images of an AlGaN MQW grown on bulk AlN substrate showing the region around a grain structure in HAADF, ADF and HRTEM measurement mode. The TEM analysis exhibits no large compositional fluctuations near the grain region but TD generation starting from BSFs at the QWs. (Measurement by Anna Mogilatenko - FBH and HU Berlin)

The observed grains on the AlGaN MQW surface in Figure 3.26c exhibit no dominant crystal facets with hexagonal symmetry which would be expected for wurtzite AlGaN growth. In order to examine the origin for such grain formation, cross-section TEM measurements in the vicinity of a grain structure have been carried out, images are shown in Figure 3.27. The HAADF-STEM image exhibits AlGaN material contrast

with bright Ga-rich regions, e. g. three quantum wells, and dark Al-rich regions such as the bottom $Al_{0.8}Ga_{0.2}N$ layer. The $Al_{0.7}Ga_{0.3}N$ WG exhibits intermediate gray contrast. The grain structure located in the center shows no strong contrast fluctuations in the HAADF-STEM image, hence, the composition here is similar to the surrounding $Al_{0.7}Ga_{0.3}N$ WG layer. However, the annular dark field (ADF) STEM image is sensitive to dislocations, revealing a deterioration of crystal quality by defect formation in the highly strained Ga-rich QW region and TD generation and propagation towards the surface. The high resolution (HRTEM) image of the highly defective QW region reveals a combination of two basal plane stacking faults (BSF) involving the formation of a-type threading dislocations. Such BSF formation associated to TD generation has also been observed in strained InGaN layers grown on c-oriented GaN substrates [78]. Basically, BSFs describe the interruption of the typical ABAB atom stacking sequence in wurtzite crystal structures like AlGaN by a cubic insertion with ABC stacking sequence [79]. The formation energies of BSFs in GaN are much lower compared to BSFs in AlN [80], which is in agreement with the observed BSF formation in QWs with comparably low aluminum content. Furthermore, the formation of BSFs is correlated with surface kinetics during growth and can be influenced by growth parameters [78, 81].

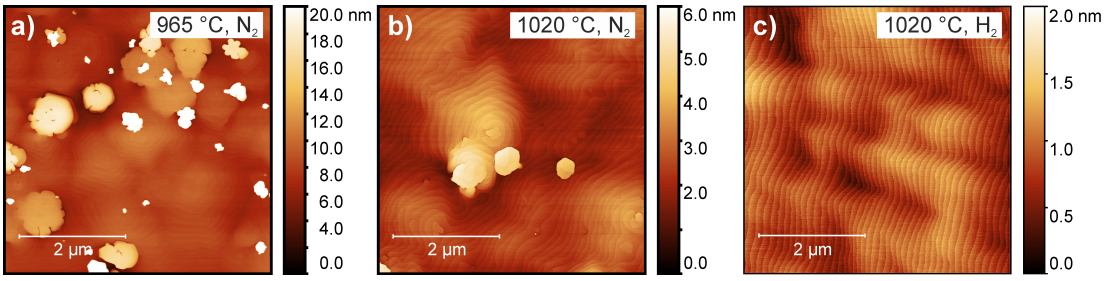

Figure 3.28: Influence of different growth parameters on the morphology of AlGaN MQWs grown on AlN substrates.

In order to investigate the influence of MQW growth conditions on the surface morphology, different growth parameters such as temperature and carrier gas were investigated with the focus on grain formation. The MQW sample grown at 965 °C under nitrogen exhibits a grain density of $1 \cdot 10^8$ cm^{-2} (Figure 3.28a). By increasing the temperature to 1020 °C the surface becomes much smoother, which is due to a significant reduction of the grain density to $1 \cdot 10^7$ cm^{-2} (Figure 3.28b). This can be explained by an increased mobility of adatoms for diffusion on the sample surface at higher temperatures. Adatoms can be prevented from a kinetically limited sticking to the cubic crystal position that would be generating a BSF with ABC stacking sequence. In contrast, the wurtzite position continuing the ABAB stacking sequence is more likely occupied leading to a strong suppression of BSFs. As calculated for GaN MOVPE growth, this wurtzite position is energetically favorable [50]. Hence, the probability of BSFs with subsequent grain formation is strongly reduced by increasing the thermal energy.

A further increase of the growth temperature could be beneficial for further grain reduction. However, such high temperature AlGaN MQW growth at low growth rates becomes less reproducible due to gallium desorption and stronger temperature sensitivity of AlGaN composition and MQW emission wavelength. Therefore, the temperature was kept constant at 1020 °C while the influence of the carrier gas type during growth was

investigated. For GaN layers, a strong influence of the carrier gas type on the surface metal adatom distribution was reported: for hydrogen-rich carrier gas gallium-rich surfaces are enhancing the gallium adatom mobility and can influence the macroscopic morphology such as island formation or coalescence [82, 83]. Figure 3.28c shows an AFM image of an AlGaN MQW that was grown under hydrogen as the carrier gas. The surface is grain-free on that $(5\,\mu m)^2$ AFM scan as well as on an $(25\,\mu m)^2$ area, which corresponds to a grain density $\leq 1 \cdot 10^5$ cm^{-2}. This demonstrates that even at intermediate temperatures of 1020 °C nearly grain-free AlGaN MQW growth with very smooth mono-atomic surfaces is possible on bulk AlN substrates. In that case, using hydrogen as a carrier gas allows for complete suppression of BSF generation and subsequent grain formation.

3.4.4 Obtaining abrupt interfaces in AlGaN MQWs

In the previous sections, the growth of smooth and pseudomorphic AlGaN MQWs on sapphire as well as on AlN substrates was achieved. In the following step, the influence of growth parameters on the MQW interfaces is examined on microscopic length scales in order to obtain abrupt interfaces between AlGaN QWs and AlGaN barriers. The analyzed samples include MQWs grown at low temperatures of 965 °C (LT), at high temperatures of 1020 °C (HT) as well as two MQWs grown at these temperatures with growth interruptions after each single MQW layer (LT-GRI and HT-GRI). During such GRI, the supply of MO precursors was interrupted while ammonia was continually supplied. The intention of the GRI was to promote adatom diffusion to achieve sharper interfaces and a more homogeneous QW composition. The MQW variation was performed within the growth of full UVC LED structures.

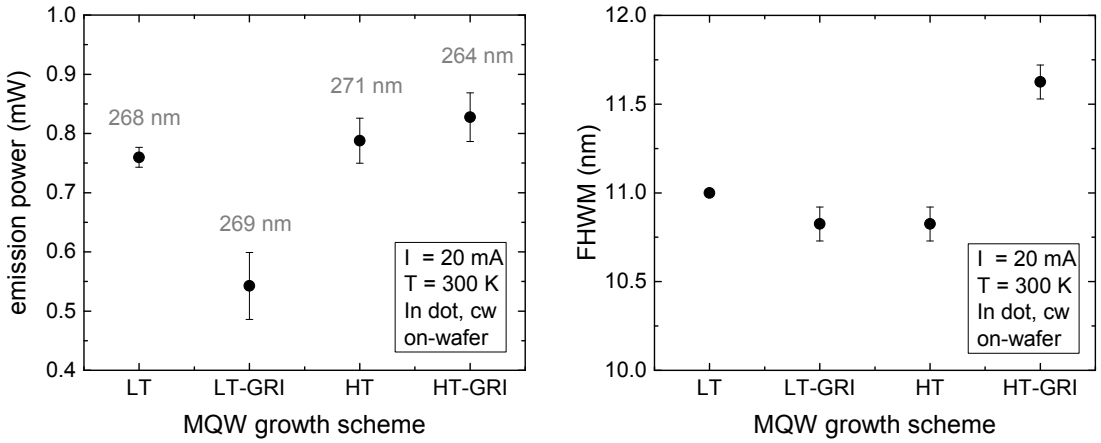

Figure 3.29: EL emission power (a) and spectral FWHM (b) of UVC LEDs with MQWs grown at 965 °C (LT) and 1020 °C (HT), combined with growth interruptions (GRI) after the QW and barrier layers. Mean value and standard deviation of four LEDs across the wafer diameter are shown.

STEM-HAADF measurements of the LED samples were performed in cross section focusing on the MQW region to evaluate the interface properties. Furthermore, the LEDs were characterized by electroluminescence spectroscopy measurements for evaluation

of the emission power, emission wavelength, and spectral FWHM of the spontaneous emission. In order to analyze the spatial variation of the emission properties, mean value and standard deviation of four LEDs at different wafer positions were evaluated, shown in Figure 3.29a and Figure 3.29b. The LED sample with MQW grown at LT exhibits an emission wavelength of 268 nm with FWHM of 11 nm and an emission power near 0.8 mW at 20 mA with a very homogeneous distribution of emission power and FWHM. Similar spectral properties were obtained from LEDs grown at 965 °C with growth interruption (LT-GRI) exhibiting no or only minor influence of growth interruptions on the composition and thickness of AlGaN quantum wells grown at low temperatures. The LED emission power, however, shows a larger variation and is significantly reduced on average for the LT-GRI sample. A possible explanation is incorporation of point defects during growth interruptions [84, 85] reducing the IQE by increased non-radiative recombination rates.

For the HT sample, the supply of TMAl and TMGa as well as the growth times were separately calibrated and adjusted in order to obtain MQWs with the same composition and thickness compared to the LT sample. In this HT case, a peak emission wavelength of 271 nm with FWHM of 10.8 nm and 0.8 mW emission power at 20 mA was obtained, which is similar to the LT sample. The HT-GRI sample, however, exhibits significantly reduced emission wavelength and a slight FWHM increase. The emission power is comparable, near 0.8 mW at 20 mA. With the exception of the LT-GRI sample showing reduced emission power near 0.5 mW, the measured emission power and FWHM is almost constant within this parameter variation exhibiting very stable spontaneous emission from UVC LEDs that are not sensitive to variations in MQW growth.

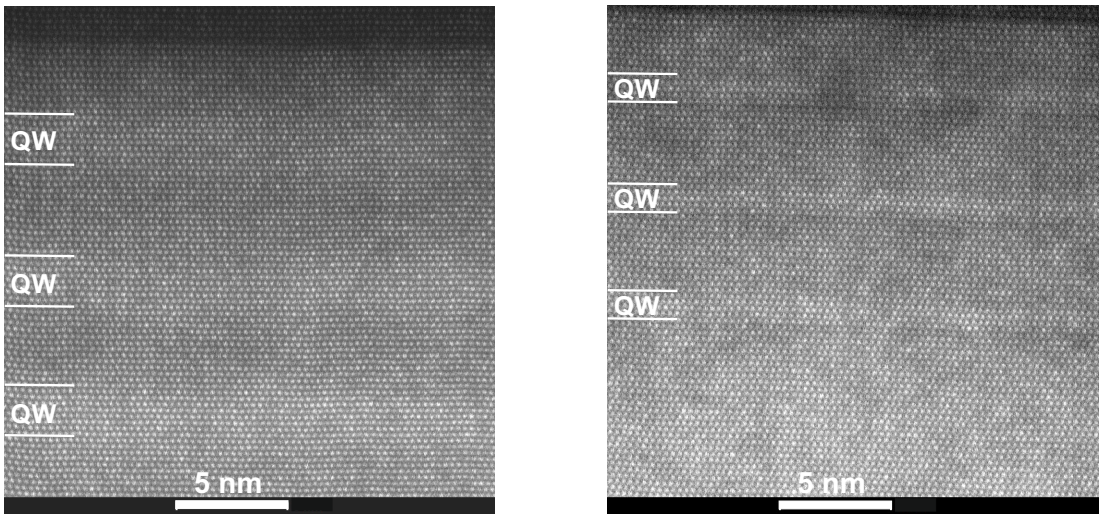

(a) (b)

Figure 3.30: STEM-HAADF transmission electron microscopy images of UVC LEDs with MQWs grown (a) at 965 °C and (b) at 1020 °C with growth interruptions after the QW and barrier layers exhibiting less abrupt interfaces for QWs grown at lower temperature as well as very sharp interfaces and slightly reduced thickness for QWs grown at higher temperature with growth interruption. (Measurement by Leonardo Cancellara - IKZ)

STEM-HAADF measurements of UVC LED samples with MQWs grown under LT condition and HT-GRI condition were performed in cross section focusing on the MQW region. The TEM image of the LT-MQW, shown in Figure 3.30a, shows interfaces between the AlGaN QWs and AlGaN barriers that are not perfectly abrupt but have a more sinusoidal composition profile. In contrast, the imaged MQW with HT-GRI exhibits more abrupt interfaces, shown in Figure 3.30b. Due to Ga desorption during growth interruptions the QW width is reduced from 2.25 nm to 1.25 nm, each with ±0.25 nm evaluation error (one monolayer). Increased quantization energy partially explains the shorter emission wavelength of this particular LED. However, also a change in QW composition influences the emission wavelength. Given the fact of similar FWHM of the EL emission from both samples (LT and HT-GRI), the observed compositional differences of the interface properties are not the exclusive mechanism of spectral broadening. Additionally, alloy broadening caused by statistical fluctuations of the ternary AlGaN QWs on an atomic scale is affecting the FWHM of the spontaneous LED emission. However, in contrast to QWs with large compositional modulations like in the LT case, more homogeneous QWs with abrupt interfaces to barriers with different AlGaN or AlN composition could provide higher gain at high excitation in UVC lasers. This might be one option to achieve lower threshold power densities.

3.5 Impact of surface morphology on UVC laser performance

In this section, AlGaN-based MQW lasers emitting near 270 nm are investigated by optical pumping experiments in order to verify the impact of AlGaN material optimization on device performance. After MOVPE growth of UVC lasers the wafers were scribed and cleaved into individual laser bars along m-facets or a-facets in order to form laser cavities with lengths ranging from 600 µm to 1400 µm. As no additional reflective coating was applied to the cleaved facets, cavity mirrors are provided by the refractive index contrast between nitride layers and surrounding air. For optical excitation, an argon fluoride (ArF) excimer laser with 193 nm emission wavelength, 5 ns pulse length, and 50 Hz repetition rate is used providing non-resonant excitation of the MQWs as the photon energy of 6.4 eV is exceeding the band gap of all nitride layers. The excitation beam is shaped to form an excitation stripe on the sample surface with 20 µm width and variable length exceeding the length of the resonator. Emitted light from the AlGaN MQW laser is collected from the facet using an optical fiber and detected by a spectrometer. For polarization dependent spectroscopy the sample emission is collimated and passing a polarizer before detection [86].

As previously described, the threshold behavior is a required characteristic for the demonstration of lasing operation. Different optical losses will cause variations of the threshold excitation power densities that can be analyzed in order to compare the properties of different laser samples. For samples with non-pseudomorphic $Al_xGa_{1-x}N$ waveguides ($x < 0.7$, see subsection 3.4.1) no lasing operation was obtained. In Figure 3.31, the AFM images of four UVC MQW lasers with similar heterostructure design (according to Figure 3.23 with $Al_{0.7}Ga_{0.3}N$ WG) are shown. The surface topologies are ranging from comparably rough surfaces exhibiting large hillocks, macro steps, and V-pits with an RMS roughness of 11.2 nm (Figure 3.25a) to comparably smooth surfaces

exhibiting only small hillocks and atomic steps with an RMS roughness of 3.6 nm, as described in subsection 3.3.3 and subsection 3.4.2.

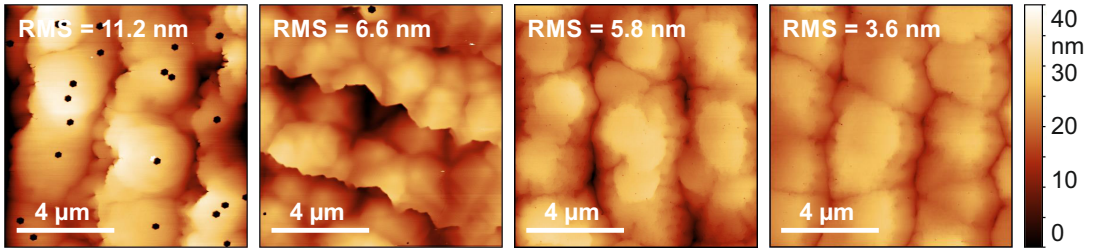

Figure 3.31: AFM topographs of UVC lasers with different surface morphology and RMS roughness grown under varied growth conditions of AlGaN:Si cladding and waveguides, as described in subsection 3.3.3 and subsection 3.4.2 [42, 49, 66].

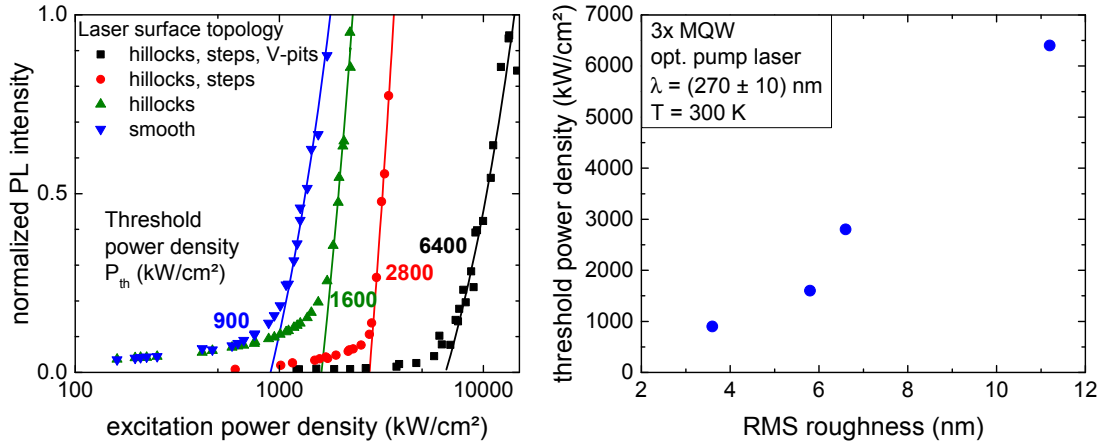

(a) (b)

Figure 3.32: (a) Threshold power density for optical pumping with 193 nm excitation wavelength of UVC lasers with different surface morphology and (b) correlation of RMS roughness with threshold power density [42, 49, 66]. (Optical measurements by Martin Martens - TU Berlin)

All of these MQW lasers with emission wavelength near 270 nm show a threshold behavior of the emitted photoluminescence (PL) intensity, however, the respective threshold power density is strongly varying. For the sample with highest roughness exhibiting large hillocks, macro steps, and V-pits, the threshold power density is as high as 6400 kW/cm^2, shown in Figure 3.32a (black). For samples with smoother surface without V-pits, threshold power densities are reduced by more than a factor of two to 2800 kW/cm^2 (red) [66] and can be further reduced to 1600 kW/cm^2 when no macro steps but only hillocks are present on the surface (green), detailed description in [42]. For UVC MQW lasers with smoothest surfaces with an RMS roughness of 3.6 nm, the lowest threshold power densities of 900 kW/cm^2 have been obtained (blue) [49], which means a total improvement of the lasing threshold by a factor of seven due to WG morphology control. The correlation of RMS roughness and threshold power density is shown in Figure 3.32b.

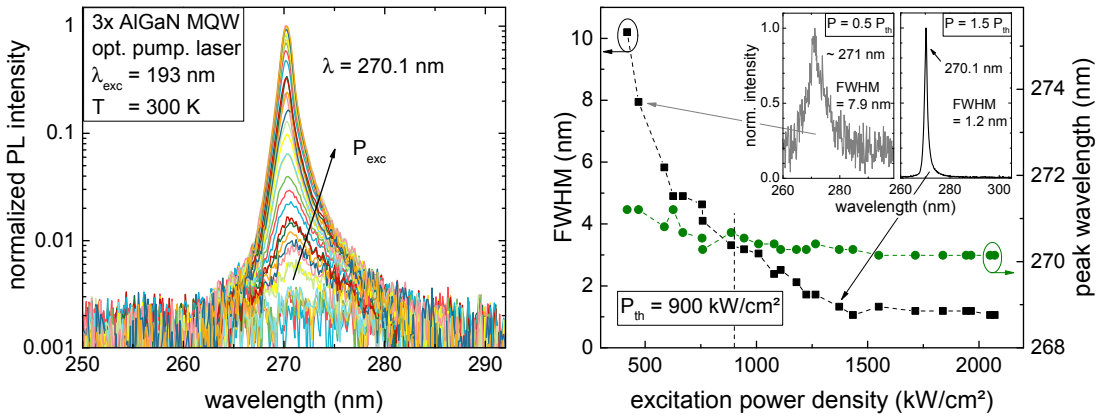

(a) (b)

Figure 3.33: (a) Normalized emission spectra and (b) evaluation of FWHM and peak wavelength of an optically pumped AlGaN MQW laser with smooth morphology (RMS = 3.6 nm) exhibiting a reduction of line width and stable emission wavelength for lasing operation above threshold excitation power density at 900 kW/cm^2 [86]. (Measurement by Martin Martens - TU Berlin)

In relation to values reported by other groups, such threshold power densities appear comparably high, which can be due to different reasons including fluctuations of the ArF laser excitation power, stripe beam shaping, or heterostructure design and growth. However, as sample preparation and threshold measurement routine are carried out reproducibly, a reliable comparison of the performance characteristics of these samples is possible. According to Figure 3.32b, laser surface RMS roughness and lasing threshold are highly correlated. A decreasing surface roughness is reducing optical scattering centers and therefore optical losses within the resonator as well as increasing homogeneity of the QW composition and gain profile. Next to optical mirror losses, internal losses such as scattering or absorption have to be compensated by sufficient gain before lasing can start. The reduced threshold power density of 900 kW/cm^2 for the smoothest sample without large hillocks, macro steps, or V-pits is complemented by further optical measurements demonstrating lasing operation.

In Figure 3.33a, the emission spectra of this sample are shown, recorded at different excitation power densities (P_{exc}). At low excitation, the AlGaN MQW laser exhibits a broad spontaneous emission spectrum near 271 nm. At high excitation, the spectra show a sharp single laser emission peak at 270.1 nm. Evaluations of FWHM line width and peak wavelength of the emission spectra are shown in Figure 3.33b. The analysis reveals a spectral narrowing of the line width reducing from approximately 10 nm (170 meV) below threshold to 1.2 nm (20 meV) above threshold as well as a slight reduction of the peak wavelength from 271 nm below threshold to a constant value of 270.1 nm above threshold. Such reduced line width above threshold is comparable to the FWHM of UV laser emission in the range of 0.4 nm to 1.6 nm (7 meV to 27 meV) reported in literature for pulsed electrical excitation [10, 12, 87] and optical excitation [19, 88] with averaging over multiple pump pulses that excite modes with slightly different energies, especially for broad area excitation of multiple lateral modes and considerable pulse fluctuations of an ArF excimer laser source. In case of detection of the laser emission from a single pump pulse, the measured spectral FWHM can be strongly reduced; values as low as

0.02 nm (0.3 meV) have been shown by Xie et. al. [16]. The insets of Figure 3.33b show the emission spectra recorded at excitation power densities half of threshold power density ($P = 0.5\,P_{th}$) and above threshold power density ($P = 1.5\,P_{th}$) with evaluated FWHM values, respectively.

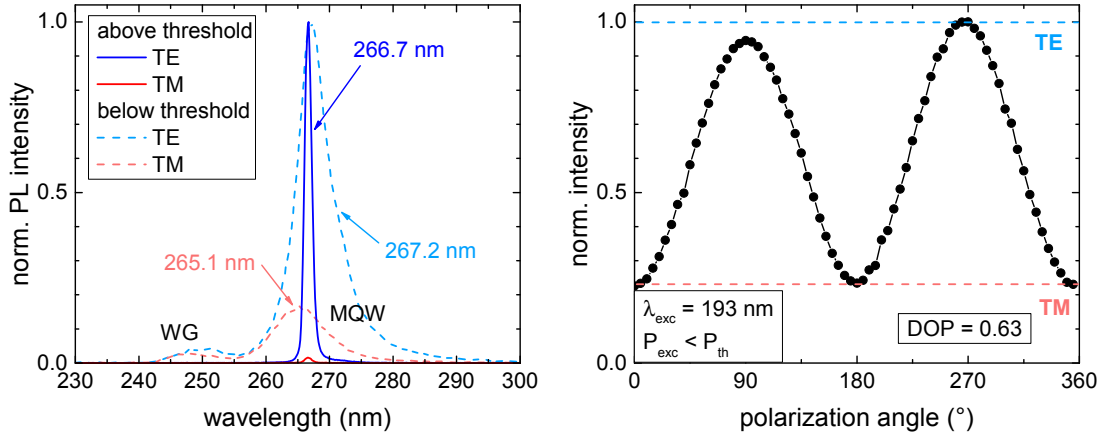

(a) (b)

Figure 3.34: (a) Polarization resolved spectra of optically pumped UVC laser emission below and above threshold. (b) Polarization of the integrated MQW emission (without WG emission) at low excitation power density exhibiting a degree of polarization DOP = 0.63 for the spontaneous MQW emission at 267 nm [86]. (Measurement by Martin Martens - TU Berlin)

As laser emission is characterized by one distinct optical polarization, the emission spectrum of a comparable MQW laser with smooth morphology emitting near 267 nm was characterized, shown in Figure 3.34a. Below threshold, polarization resolved spectra exhibit emission peaks related to the MQW as well as to the WG layers. The MQW emission is consisting of strong TE polarized emission centered at 267.2 nm and weak TM polarized emission centered at 265.1 nm. The polarization state of the emission is correlated to the valence band ordering. As the direct band gap is determined by the topmost valence band with highest population, the corresponding TE emission is stronger compared to the TM emission from the valence band with larger energetic separation emitting at shorter wavelength. The degree of polarization (DOP) can be determined from the intensity oscillations during polarizer rotation associated to TE emission (here at 90° and 270°) or TM emission (here at $0° \equiv 360°$ and 180°) using $DOP = \frac{I_{TE}-I_{TM}}{I_{TE}+I_{TM}}$ (Figure 3.34b). Below threshold power density, the degree of polarization of the MQW emission near 267 nm is DOP = 0.63 with an evaluation error of ΔDOP = 0.1. Above threshold, however, the system alignment for accurate measurements is very challenging as the DOP is close to one. At a TM position (e. g., 180°), slightly imperfectly collimated TE emission will partially pass the polarizer and be calculated as TM fraction decreasing the DOP. Nevertheless, in case of Figure 3.34a the laser emission is TE polarized above threshold with measured DOP > 0.96.

AlGaN-based MQW lasers with deep UV emission between 255 nm and 295 nm were realized with the same basic heterostructure design according to Figure 3.23b by variation of the quantum well composition with fixed $Al_{0.70}Ga_{0.30}N$ barrier and waveguide composition as well as $Al_{0.80}Ga_{0.20}N$ cladding layers, which was shown in Figure 1.1.

Spectral narrowing of the emission line width, threshold behavior of the emitted intensity as well as entirely TE polarized laser emission above threshold was observed for all structures. For these lasers with emission wavelength between 255 nm and 295 nm and surfaces with step bunching morphologies, similar threshold power densities near 3 MW/cm^2 were obtained. As the material gain depends on the QW composition [89], these similar thresholds must be governed by other effects such as comparable internal losses due to mode scattering. In order to obtain optically pumped lasing with even shorter emission wavelength (< 250 nm), the heterostructure design has to be adjusted to provide sufficient mode confinement, e. g. by employing AlN cladding layers. Lasing spectra of such structures are also included in Figure 1.1. In this case, the heterostructure is less compatible for further development towards UVC emitters with current injection due to challenging doping and conductivity of AlN in contrast to AlGaN alloys. In contrast to TE polarized emission from optically pumped UV lasers with emission wavelength between 255 nm and 295 nm, UV laser emission at 241 nm and shorter wavelengths switches to TM polarization for pseudomorphic growth on AlN [7, 45, 90].

3.6 Summary

In this chapter, the MOVPE growth of AlGaN-based heterostructures on sapphire and bulk AlN has been discussed, including the influence of substrate offcut on epitaxial AlN surfaces, strain and morphology of AlGaN:Si cladding layers as well as the growth of pseudomorphic and smooth AlGaN MQWs. UVC lasing near 270 nm has been obtained by optical excitation that enabled investigating the impact of different surface morphologies on the UV laser performance. Following statements are concluded from the experiments:

(I) Due to surface kinetics, AlN morphologies can be controlled by the substrate offcut. Whereas large offcut values $\alpha > 0.19°$ are causing AlN macro steps, smooth surface morphologies with AlN mono steps can be obtained for the same MOVPE growth conditions with lower offcut angles $\alpha < 0.17°$ providing ideal starting surfaces for the growth of AlGaN-based UV lasers.

(II) For 1200 nm thick $Al_xGa_{1-x}N$:Si cladding layers, strong plastic strain relaxation and UV absorption can be excluded for compositions of $x \geq 0.6$. However, partial relaxation, compositional non-uniformities and rough morphologies caused by the growth of spirals are detrimental for the laser performance. Spiral formation during $Al_{0.8}Ga_{0.2}N$ growth is barely affected by variations of MOVPE growth conditions such as V/III-ratio, temperature, or growth rate.

(III) Using the superlattice approach with growth interruptions, silicon-doped AlGaN-based superlattice cladding layers with coherent strain state, uniform composition, smooth morphology, high conductivity, and full UV transparency below band gap have been obtained.

(IV) 130 nm thick, pseudomorphic MQWs with $Al_{0.4}Ga_{0.6}N$ quantum wells can be obtained with a waveguide composition of $x = 0.7$. Such pseudomorphic growth of waveguide and MQW layers is a requirement for UVC lasing, as no laser operation was obtained from samples with partial relaxation.

(V) MOVPE growth conditions are affecting the morphology of AlGaN MQW and waveguide layers. V-pit formation during MQW growth can be controlled by the growth temperature. MQWs grown at 1070 ℃ exhibit smooth surfaces with strongly reduced V-pit density compared to samples grown at 900 ℃.

(VI) UVC lasing has been obtained from coherently grown AlGaN-based MQW lasers with optical excitation including measurements of the lasing threshold, spectral narrowing, and TE polarized emission above threshold. By controlling the surface morphology, threshold power densities could be reduced by almost one order of magnitude to 900 kW/cm^2 due to reduced scattering losses with smooth laser surfaces.

4 UVC LED and LD structures with transparent AlGaN:Mg SPSL layers

AlGaN-based UVC LEDs are experiencing tremendous scientific and economic interest: New record efficiencies are reported frequently (EQE > 20% [91, 92]), device performances are approaching physical limits of the materials (emission wavelength $\lambda < 220\,\mathrm{nm}$ [93, 94]), and market penetration is expected within the next decade [4]. The success story was emphasized by the Nobel Prize 2014, honoring the early work of Isamu Akasaki, Hiroshi Amano, and Shuji Nakamura on III-nitride semiconductors "for the invention of efficient blue light-emitting diodes which has enabled bright and energy-saving white light sources." [95].

Nevertheless, from new scientific findings more questions are arising, and the development of new materials and advanced characterization techniques allows for an investigation of such questions. One AlGaN-related topic questions the feasibility of edge-emitting UVC laser diodes (LD). Whereas III-nitride-based LDs emitting in the blue-violet [96], and UVA spectral range have been demonstrated [10, 97, 98], no edge-emitting quantum well LD in the UVB or UVC spectral range has been reported before 2019. Very recently, Zhang et. al. reported a 271.8 nm emitting UVC laser diode grown on bulk AlN with threshold current densities of $25\,\mathrm{kA/cm^2}$ [12], Sato et. al. reported a 298 nm emitting UVB laser diode grown on lattice-relaxed $Al_{0.6}Ga_{0.4}N$/AlN/sapphire templates with threshold current densities of $41\,\mathrm{kA/cm^2}$ [13]. Both reports include a demonstration of spectral linewidth reduction and TE polarized emission above threshold.

Similar to UVC LEDs, suitable substrates for UVC LD growth have been identified, such as bulk AlN substrates or ELO AlN/sapphire templates [19, 45]. Also, optically pumped lasing with low threshold power densities has been obtained from cleaved facets of edge-emitting UVC laser structures [88, 99]. In contrast to UVC LEDs, however, UVC LDs need to implement a waveguide system within the heterostructure for vertical mode confinement. The n-side waveguide system must contain AlGaN:Si cladding layers with high aluminum content, comparable to transparent current spreading layers of bottom-emitting UVC LEDs [43, 100]. The p-side waveguide system needs to be composed of transparent AlGaN:Mg cladding layers with high aluminum content and therefore with wide band gap. The conductivity of such required wide band gap AlGaN:Mg layers represents a major challenge to the electronic system in UVC LDs, in contrast to UVC LEDs which typically use more conductive GaN:Mg or AlGaN:Mg p-layers with lower band gap [4, 101].

The conductivity $\sigma = 1/\rho = \mu \cdot p \cdot e$, inverse to the resistivity ρ, basically depends on carrier mobility μ and carrier density p. Carrier mobilities exhibit a comparably weak dependency on temperature that can be described with a $\mu \propto T^{3/2}$ relation for carrier scattering at ionized impurities or with a $\mu \propto T^{-3/2}$ relation in case of carrier scattering at acoustic phonons [102]. However, other types of scattering sources, such

as scattering at neutral impurities, optical phonons, or extended defects may not be fully neglected. On the contrary, carrier densities in n-type or p-type semiconductors are exponentially dependent on temperature, basically following a Boltzmann behavior such as $p \propto exp(-E_A/k_BT)$ in case of holes. While the acceptor density N_A can be controlled to a certain extent within the MOVPE growth process by the supply of dopant precursors, the acceptor activation energies E_A strongly depend on the material composition. This also holds for donors in the III-nitride material system. For GaN:Si, the activation energy is in the range of 12 - 17 meV [103] and increases with increasing AlGaN aluminum mole fraction up to 85 - 180 meV in AlN:Si [104, 105]. Next to group-III vacancy formation, high donor activation energies are preventing efficient n-type doping with high free electron concentrations in AlN:Si and AlGaN:Si with Al mole fraction exceeding 0.8 [61]. For p-type doping, the situation is even more severe, as reported activation energies of GaN:Mg range between 0.125 - 0.17 eV [106, 107], increasing to 0.5 - 0.63 eV for AlN:Mg [93, 108, 109]. For example, with an acceptor density of $N_A = 5 \cdot 10^{18}\,\mathrm{cm}^{-3}$ and an activation energy of $E_A = 0.4\,\mathrm{eV}$ in $Al_{0.70}Ga_{0.30}N$:Mg [110], a free hole density as low as $p = 7 \cdot 10^{11}\ \mathrm{cm}^{-3}$ can be expected at room temperature, corresponding to the compensation regime [111]. With such low hole densities, no high conductivity can be achieved, preventing efficient charge carrier injection in AlGaN-based devices [112]. Even though short-period superlattices (SPSL) are promising to reduce acceptor activation energies [53, 113], obtaining p-type conductivity remains a major challenge.

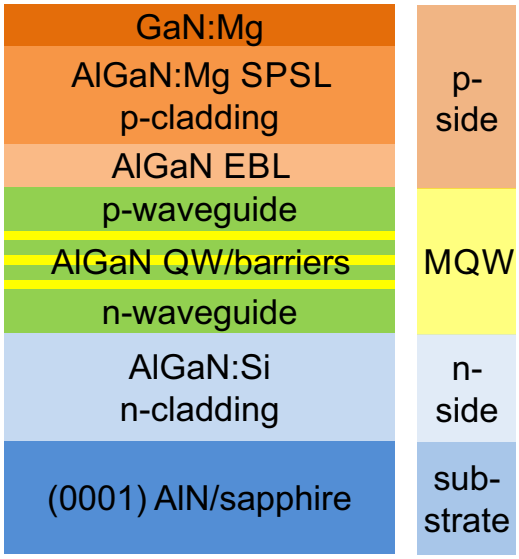

Figure 4.1: UVC laser diode heterostructure scheme including waveguide and cladding layers for optical confinement as well as an MQW structure for electrical confinement.

Therefore, the investigations presented in this chapter mainly focus on the growth and characterization of AlGaN:Mg SPSL layers with wide band gap for their application in UVC laser diodes. Due to the absence of functional UVC laser diodes, the properties of such AlGaN:Mg SPSL layers are investigated in UVC LEDs with comparable heterostructure that allow for electroluminescence spectroscopy measurements of spontaneous UV light emission as well as current-voltage characteristic. In a systematic study of the influence of heterostructure design on device performance, the key effects and limiting mechanisms can be identified. Direct experimental verification enables to determine a compromise between opposing requirements such as obtaining a large confinement

factor and efficient carrier injection. In addition, the presented investigations will allow for an identification of remaining challenges as well as suggestions to address those.

Figure 4.1 shows a heterostructure scheme for AlGaN-based UVC laser diodes. Edge-emitting laser diodes with vertical separate confinement heterostructure (SCH) design consist of n-cladding layers, an active region embedded in a waveguide system and p-cladding layers, all grown on suitable substrates. According to the SCH design, a multiple quantum well (MQW) active region provides carrier accumulation within AlGaN quantum wells that are confined by AlGaN barrier layers. Electron overflow to the p-side is prevented by an AlN or AlGaN electron blocking layer (EBL). The waveguide system with total thickness of about 100 nm consists of an AlGaN:Mg p-side waveguide layer and an AlGaN:Si n-side waveguide, without the necessity of exactly symmetric geometry. Cladding layers are required to provide optical confinement by a lower refractive index than the waveguide layers as well as carrier injection of electrons by the AlGaN:Si n-cladding and injection of holes by the AlGaN:Mg SPSL p-cladding layer.

In order to realize functional UVC laser diodes, three important key aspects of the heterostructure design have been identified and will be discussed in the following sections.

1. Morphology and relaxation
2. Mode confinement
3. Carrier injection

Morphology and relaxation are structural properties of crystalline AlGaN layers and surfaces that can be accessed by AFM and XRD measurements. In case of AlGaN-based UVC LD heterostructures grown on AlN, misfit relaxation of compressive strain may reduce the crystal quality in thick, highly strained AlGaN layers with low Al content. In detail, defect generation and a transition from two-dimensional to three-dimensional growth needs to be avoided. Smooth surface morphology and low defect density without lattice relaxation are intended.

Mode confinement can be quantified with mode simulations of the vertical optical system using parameters such as thickness and refractive index of the heterostructure, especially of waveguide and cladding layers. High spatial overlap of the optical mode with the quantum wells, called confinement factor Γ, is desired, with low overlap of the optical mode with absorbing layers at the same time. Consequently, mode confinement is mainly influenced by the thickness and composition of waveguide and cladding layers.

Carrier injection describes the fraction of electrons and holes from the metal contacts that are successfully transported and injected into the AlGaN quantum wells. It is mainly influenced by the heterostructure design of AlGaN MQW active region, AlGaN:Si n-side, and AlGaN:Mg p-side layers. Using UVC LEDs, electroluminescence measurements of emission spectra, emission power, and EQE enable experimental access to the injection efficiency, especially to the crucial injection of holes. However, low resistive AlGaN:Si and AlGaN:Mg layers are one requirement for efficient electrical injection, as resulting LED operation voltages strongly affect the wall-plug efficiency (WPE) of such devices. With experimental variations of the heterostructure design, carrier injection has to be optimized with parallel consideration of the mode confinement as well as morphology and relaxation that should not be detrimentally affected.

More than one of these key aspects might be affected by the experimental investigation of a single layer of the heterostructure, e. g. AlGaN:Mg SPSL composition. In the following sections a systematic experimental variation of crucial parts of the heterostructure is presented, aiming for the optimization of these three key aspects.

4.1 EL characterization of UVC LEDs grown on AlN and sapphire substrates

Based on the results in AlGaN MQW growth on AlN discussed in subsection 3.4.3, the growth and characterization of UVC LEDs and laser diode heterostructures with wide band gap AlGaN:Mg SPSL layers on two types of substrates –ELO AlN/sapphire templates as well as bulk AlN substrates– will be discussed in this section.

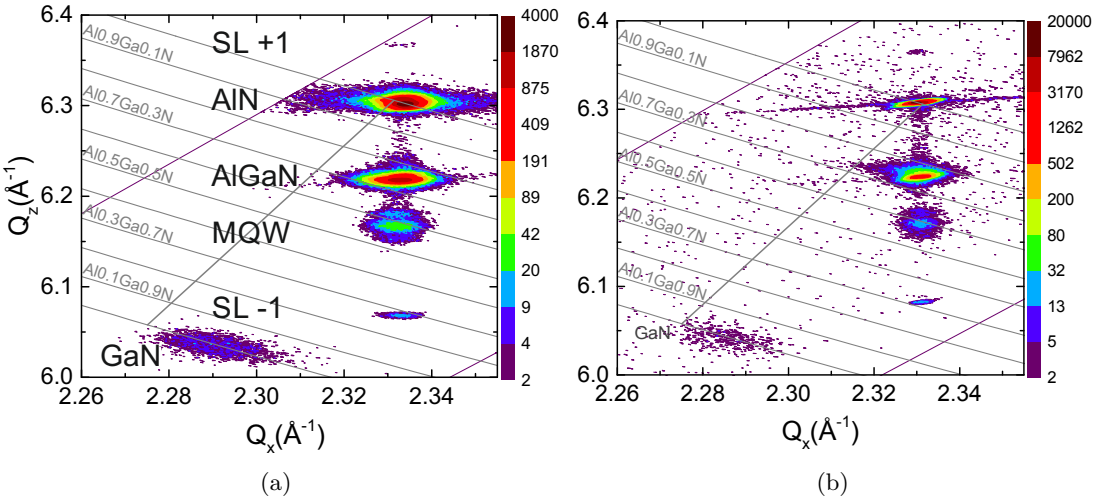

Figure 4.2: Asymmetric (10.5) XRD RSMs of UVC LEDs with wide band gap AlGaN:Si SL and AlGaN:Mg SPSL grown on c-oriented ELO AlN/sapphire template (a) and bulk AlN substrate (b).

AlGaN-based heterostructures containing AlGaN:Si superlattice cladding layers with average aluminum content of 75%, $Al_{0.48}Ga_{0.52}N/Al_{0.6}Ga_{0.4}N$ MQW active region, $Al_{0.95}Ga_{0.05}N$ EBL, $Al_{0.72}Ga_{0.28}N$:Mg SPSL, and 40 nm GaN:Mg were grown by MOVPE on both ELO AlN/sapphire templates as well as on bulk AlN substrates in the same growth process. XRD reciprocal space maps near the (10.5) reflection are shown in Figure 4.2. With the exception of the strongly relaxed GaN:Mg layer (reflection near $Q_x = 2.29$), all peaks are at the same lateral coordinates $Q_x = 2.332$ as the respective AlN buffer layer peak. Hence, the AlGaN layers are grown almost or entirely pseudomorphically on both types of substrates. The determination of strain state of such AlGaN layers has been extensively discussed in subsection 3.3.3 and section 3.4. Here, special features of the heterostructure as well as differences between AlGaN heterostructures on both substrates shall be discussed in more detail. Figure 4.2a shows the UVC LED grown on ELO AlN/sapphire template. Reflections from the AlGaN:Si and the AlGaN:Mg superlattices are overlapping at the peak near 75% aluminum content. At $Q_z = 6.07$, a first order satellite peak (SL -1) can be found as signature from the

AlGaN:Si SL (similar to SLs discussed in subsection 3.3.3). A very weak feature at $Q_z = 6.37$ (SL +1) can be assigned to the AlGaN:Si SL as well. These features are also observed in the RSM of the LED grown on bulk AlN substrate (Figure 4.2b). However, in XRD RSM of the AlGaN heterostructure grown on this native AlN substrate, the FWHM of all peaks is considerably lower than on the ELO template, which is indicating higher crystal quality with lower defect density, especially for AlN. Additional FWHM broadening on the ELO template could be expected due to wing tilt in the overgrown areas of the stripe pattern. This effect was minimized by XRD measurements that were conducted with incidence direction parallel to the ELO stripes.

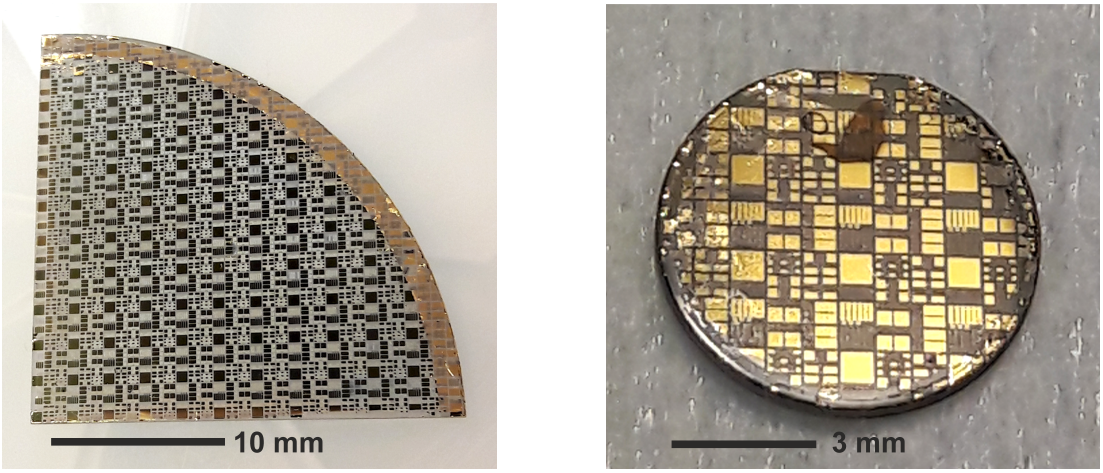

(a) (b)

Figure 4.3: Photographic images of processed UVC LEDs grown on ELO AlN/sapphire template (a) and bulk AlN substrate (b).

For electroluminescence spectroscopy characterizations, UVC LEDs have been processed using standard micro-fabrication techniques including deposition of V-based n-contacts and Pd-based p-contacts. Photographic images of the processed LEDs grown on quarter 2-inch ELO AlN/sapphire templates (Figure 4.3a) as well as round bulk AlN substrates with 8 mm diameter (Figure 4.3b) illustrate the LED and TLM (transfer length method) contacts for on-wafer investigation of both samples. EL measurements were performed at room temperature under cw current operation without active cooling. Spectra and emission power were detected from the bottom through the respective substrate, which is not entirely UV transparent in case of the AlN substrate, as discussed below.

Figure 4.4a shows the emission spectra of LEDs grown on both substrates at 20 mA, exhibiting dominant MQW emission at 270 nm for both samples. No parasitic luminescence can be observed from the UVC LED grown on ELO AlN/sapphire template. For the UVC LED grown on bulk AlN substrate, a broad parasitic luminescence peak between 400 nm and 500 nm can be observed with spectral power density almost three orders of magnitude below the MQW emission. In order to determine the origin of this parasitic luminescence of LEDs grown on bulk AlN, the influence of different defects on sub-band gap emission needs to be considered. As these UVC LEDs were grown in the same MOVPE growth process, the expected differences can be confined to point defects in the substrates as well as the threading dislocation density in the LED heterostructure. The

bulk AlN substrates were grown by physical vapor transport (PVT). Without advanced methods for point defect reduction, PVT-grown AlN crystals typically exhibit Si, O, or C impurity levels above 10^{18} cm^{-2} [114]. Furthermore, photoluminescence investigations of the sub-band gap luminescence of AlN crystals report on several emission bands related to point defects, e. g. oxygen-related emission at 2.05 eV (605 nm), silicon-related emission at 2.4 eV (516 nm), or carbon-related emission at 2.7 eV (460 nm) [115, 116]. Threading dislocations, however, act as non-radiative recombination centers in nitride semiconductors. Without any interaction with point defects or other extended defects, TDs are not considered as a contribution to sub-band gap emission, such as reported for yellow luminescence in GaN [117]. These considerations provide a strong evidence for carbon-related recombination at 2.7 eV from the AlN substrate as origin of the detected parasitic luminescence from the UVC LED between 400 nm and 500 nm.

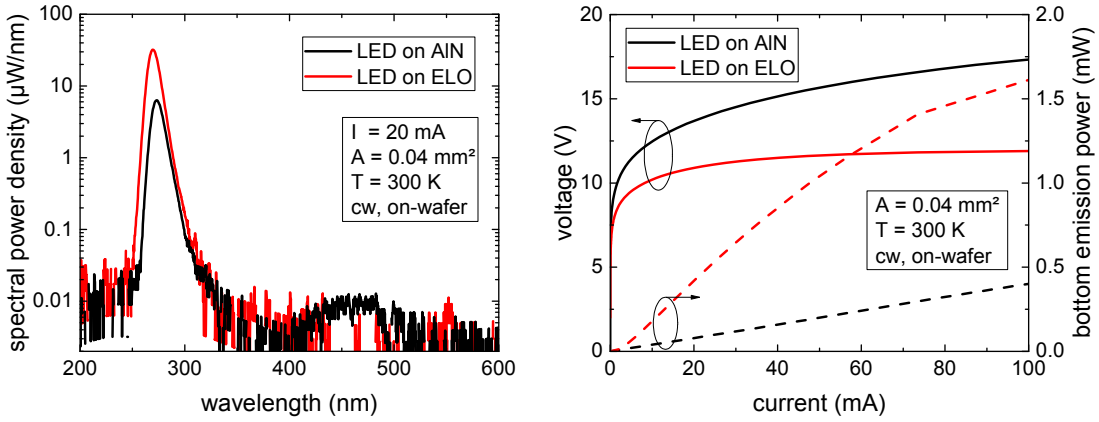

(a) (b)

Figure 4.4: Emission spectra (a) and LIV characteristics (b) of processed UVC LEDs grown on ELO AlN/sapphire templates and bulk AlN substrates, measured in bottom emission configuration.

The emission power of UVC LEDs on both types of substrates is shown in Figure 4.4b. Here, the emission power is measured by a large-area Si photodiode in bottom emission configuration through the respective substrate. For UVC emission at a wavelength of 270 nm, the 440 µm thick sapphire substrate is entirely transparent, whereas the 550 µm thick AlN substrate exhibits partial absorption with absorption coefficient near $\alpha = 30\,\mathrm{cm}^{-1}$ [20]. In a single normal pass through a layer with such thickness and α, the transmission would be as low as 19%, calculated with the exponential Lambert-Beer absorption model. The measured emission power is 0.08 mW for the UVC LED grown on AlN and 0.43 mW for the UVC LED grown on sapphire, both at 20 mA. This difference by a factor of approximately five matches the attenuation expected from the absorption in AlN. A precise estimation of the light extraction efficiency, however, would require ray tracing simulations of both devices including the UVC LED heterostructure, the substrate absorption, and the rough substrate backside which can be different. At this point, UVC LEDs grown on potentially advantageous AlN substrates with low dislocation densities cannot outperform or break even with UVC LEDs grown on ELO AlN/sapphire templates, mainly due to the strong impact of AlN absorption on the light extraction efficiency. However, thinning or removal of the AlN substrates could be

one practical option to reduce the absorption. In the future, further developments of point defect control during PVT AlN crystal growth can be promising to control and reduce absorption at specified wavelengths in the UVC spectral range [118].

Next to the emission power, also the measured operation voltages are different on both types of substrate, as shown in Figure 4.4b. At 20 mA, the operation voltages are 10.9 V on ELO AlN/sapphire and 13.7 V on AlN, whereas the difference increases at 100 mA to 11.9 V on ELO AlN/sapphire and 17.5 V on AlN. Due to the same UVC emission wavelength at 270 nm corresponding to 4.6 eV, a similar voltage drop within the MQW pn-junction is expected for LEDs on both types of substrates. A fraction of the excess voltage depends on non-ohmic n- and p-contacts with Schottky-behavior. However, next to a slightly increased turn-on voltage, mainly the series resistance is increased for the LED on AlN substrate compared to the ELO AlN/sapphire template. Despite side-by-side LED growth within the same MOVPE growth process, differences in contact resistances or layer resistivities of the AlGaN:Si SL n-side or the AlGaN:Mg SPSL p-side apparently need to be considered.

In principle, from the evaluation of TLM (transfer length method) measurements, information on the lateral conduction of carriers within a layer between metal contacts can be obtained, such as layer resistivity, contact resistance, or carrier transfer length. In case of anisotropic resistivity, the vertical conduction might be different, however, vertical resistivity and lateral resistivity in AlGaN layers are not expected to be entirely uncorrelated. A strong evidence for differences in the resistivity of AlGaN:Si and (Al)GaN:Mg p-type layers is given from TLM measurements on both structures, shown in Figure 4.5. TLM data of AlGaN:Si layers grown on both types of substrate exhibit similar resistivities near 0.03 Ωcm, independent of current density. Compared to AlGaN:Si, the resistivity of the p-type layers is several orders of magnitude larger, which is mainly due to very high Mg acceptor activation energies for the combination of GaN:Mg and wide band gap AlGaN:Mg SPSL layers with aluminum contents of more than 70%, as discussed at the beginning of this chapter. The measured resistivity of (Al)GaN:Mg p-type layers in UVC LEDs grown on ELO AlN/sapphire templates is in the range of $4 - 8 \cdot 10^2$ Ωcm, independent of current density. For the same UVC LEDs grown on bulk AlN substrates, the (Al)GaN:Mg p-type layer resistivity is increased by more than one order of magnitude to $10^4 - 10^5$ Ωcm, as measured in a broad range of current densities around 10 A/cm^2. Due to the very high resistivity and low measurement currents, the data scattering and error bars are comparably large. Nevertheless, this significant difference in (Al)GaN:Mg resistivity explains the increased operation voltage observed for UVC LEDs grown on bulk AlN substrates compared to LEDs grown on ELO AlN/sapphire templates shown in Figure 4.4. Considering this measured voltage difference, the calculated resistivity of a 100 nm thick layer is $(3 \pm 1) \cdot 10^4$ Ωcm, which agrees with the TLM result for the AlGaN:Mg SPSL on bulk AlN. In contrast, a negligible voltage drop below 0.2 V is expected for the SPSL on ELO AlN/sapphire templates, even with $\rho = 800$ Ωcm. The TLM measurements further demonstrate an n-contact resistivity which is constantly near $6 \cdot 10^{-3}$ Ωcm^2 at 100 A/cm^2 for both samples. Nevertheless, the operation voltage can also be affected by the p-contact resistivities, which could not be reliably evaluated.

A systematic investigation of AlGaN:Mg SPSL growth on bulk AlN substrates with comparable qualities and sufficient quantities would be required in order to identify the

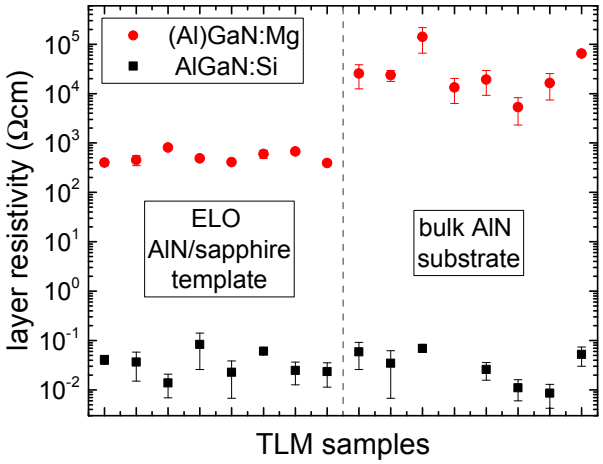

Figure 4.5: Resistivity of AlGaN:Si and (Al)GaN:Mg p-type layers in UVC LEDs grown on ELO AlN/sapphire templates and bulk AlN substrates, determined by TLM measurements.

detailed mechanism preventing a lower (Al)GaN:Mg p-type layer resistivity. Compared to the (Al)GaN:Mg p-type layer growth on ELO AlN/sapphire templates in the same MOVPE growth process, a different thermal coupling of the AlN substrates to the susceptor and heat distribution at the growth surface can be expected. Such temperature variations can lead to different incorporation probabilities of gallium atoms as well as magnesium dopants. At higher temperatures the AlGaN:Mg resistivity might be affected by both a decreased Mg concentration as well as by an increased Mg acceptor activation energy due to higher Al content. For the AlGaN:Mg SPSL layer, a maximum difference of the average Al content of 75% ± 2% on both substrates was derived from XRD RSM measurements, which can only partially explain the observed difference in resistivity. A further difference could be the actual thickness and lateral distribution of the thin GaN:Mg layer. In combination with the AlGaN:Mg SPSL, insufficient GaN:Mg coalescence would lead to increased uncertainties in the lateral resistivity measured by TLM. In addition, relaxation mechanisms at the interface between AlGaN:Mg SPSL and GaN:Mg might be affected by the respective strain state and dislocation density of both types of substrates.

These investigations demonstrate that in principle, UVC LED growth with wide band gap AlGaN:Mg SPSL p-side can be realized with the same set of MOVPE growth parameters and device fabrication steps on both ELO AlN/sapphire templates and bulk AlN substrates, despite the comparably complex heterostructure design of such UVC LEDs and the difficult challenges associated to (Al)GaN:Mg resistivity. However, compared to the findings in subsection 3.4.3, a second challenge limits a direct transfer of a UVC LED growth process from ELO AlN/sapphire templates to bulk AlN substrates: In addition to the discussed changes in UVC MQW morphology, the (Al)GaN:Mg p-type layer resistivity of UVC LEDs is affected by the choice of substrate. Hence, adequate adjustments need to be made in order to perform a successful transfer of an established UVC LED growth process from ELO AlN/sapphire templates to bulk AlN substrates with similar device performance.

In terms of the three required key aspects for UVC laser diodes introduced in the beginning of this chapter, it was demonstrated that ELO AlN/sapphire templates as well as bulk AlN substrates are suitable for pseudomorphic growth of the entire AlGaN heterostructure without any indication for relaxation, except for the GaN:Mg cap layer.

No statement on mode confinement can be made from this investigation. In fact, the discussed substrate absorption in bottom-emitting UVC LEDs is not relevant for edge-emitting UVC LDs with SCH approach, as the optical mode will be vertically confined by a refractive index contrast between AlGaN waveguide and AlGaN cladding layers and not extend into the substrate. It was found that the operation voltage is affected by the choice of substrate, as the (Al)GaN:Mg p-type layer resistivity is increased for UVC LEDs grown on bulk AlN, preventing efficient carrier injection with low voltage drop that could enable high WPE for the case of hole injection.

4.2 Effect of UV LED emission wavelength 250 - 300 nm

The external quantum efficiency of UV LEDs is strongly correlated with the emission wavelength [92]. Compared to LEDs with near UV or visible light emission with EQE > 80%, state-of-the-art deep UV LEDs exhibit much lower efficiencies. In the UVC spectral range, maximum EQE values of 20% were reported near 270 nm with strong reduction for longer wavelength in the UVB and for shorter wavelength in the UVC [4]. In order to identify the main mechanisms for efficiency reduction within the investigated wavelength range 250 - 300 nm and to find a wavelength range that allows for highest EQE, the AlGaN MQW composition of deep UV LEDs was systematically varied. Optimized UV LED heterostructures with high EQE will then be used as starting point for the investigations and development of UVC laser diodes.

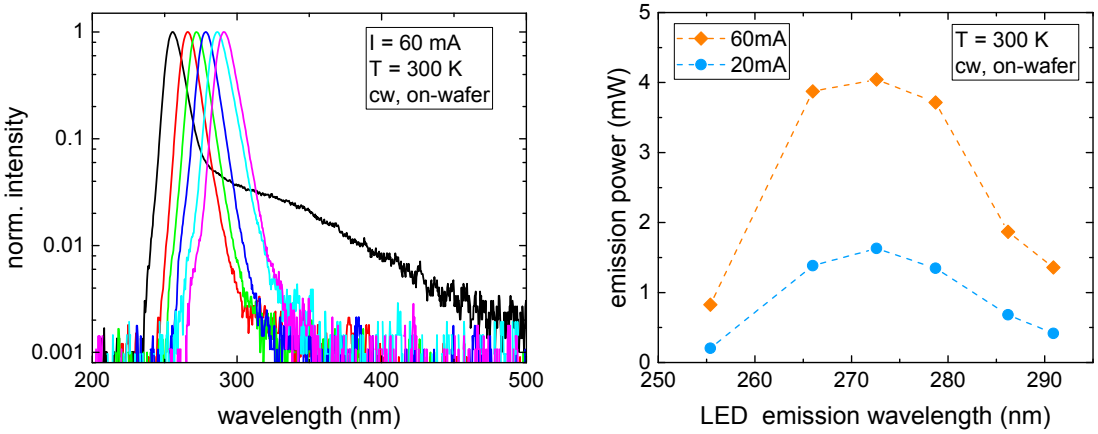

Figure 4.6: Variation of LED emission with peak wavelength between 255 nm and 291 nm: (a) normalized emission spectra and (b) emission power at 20 mA and 60 mA.

Deep UV LEDs with varying emission wavelengths were realized with a fixed heterostructure design according to Figure 2.1 using an $Al_{0.78}Ga_{0.22}N$:Si current spreading layer, an AlGaN MQW active region, a 1.5 nm thick $Al_{0.92}Ga_{0.08}N$ EBL and 100 nm $Al_{0.66}Ga_{0.34}N$:Mg SPSL plus a 20 nm thick GaN:Mg cap. Here, the composition of the $Al_xGa_{1-x}N$/ $Al_yGa_{1-y}N$ MQW layers was varied between $0.36 < x < 0.60$ in the QWs and $0.48 < y < 0.72$ in the barriers, while the difference in band gap between quantum wells and barriers was fixed to 330 meV in order to provide sufficient carrier confinement

within the QWs [119]. The LEDs are emitting at wavelengths between 255 nm and 291 nm. The normalized spectra, recorded at 60 mA and shown in Figure 4.6a, exhibit a single emission peak of all UV LEDs without any indication of parasitic luminescence, with the exception of the LED emitting at the shortest wavelength near 255 nm. In this case, a broad parasitic luminescence peak with low spectral intensity was measured between 300 nm and 400 nm; the parasitic intensity is about a factor of 30 less compared to the dominant QW emission peak at 255 nm. The emission power of those LEDs strongly depends on the QW emission wavelength, shown in Figure 4.6b. Around the reference LED emission wavelength at 272 nm, a 15 nm wide spectral range between 265 nm and 280 nm can be identified which shows a constantly high LED emission power of 4 mW at 60 mA. For LEDs emitting at longer wavelengths (286 nm and 291 nm) the emission power is reduced to values below 2 mW at 60 mA. For emission at shorter wavelength (255 nm) the emission power is even further reduced to values below 1 mW at 60 mA. Hence, the emission power of LEDs with optimized heterostructure appears very stable against wavelength fluctuations within the described spectral range. In Figure 4.7a, the current dependent emission power of LEDs with varying emission wavelengths is shown. LI curves of UV LEDs emitting between 266 nm and 278 nm are very similar at high emission power levels. UV LEDs emitting at longer or shorter wavelengths exhibit less emission power in the current range up to 100 mA. In order to investigate these different regimes, the current-dependent EQE of three representative LEDs is shown in Figure 4.7b. As described below, for LED emission exceeding this spectral range, the reduction of emission power can be assigned to two different physical mechanisms.

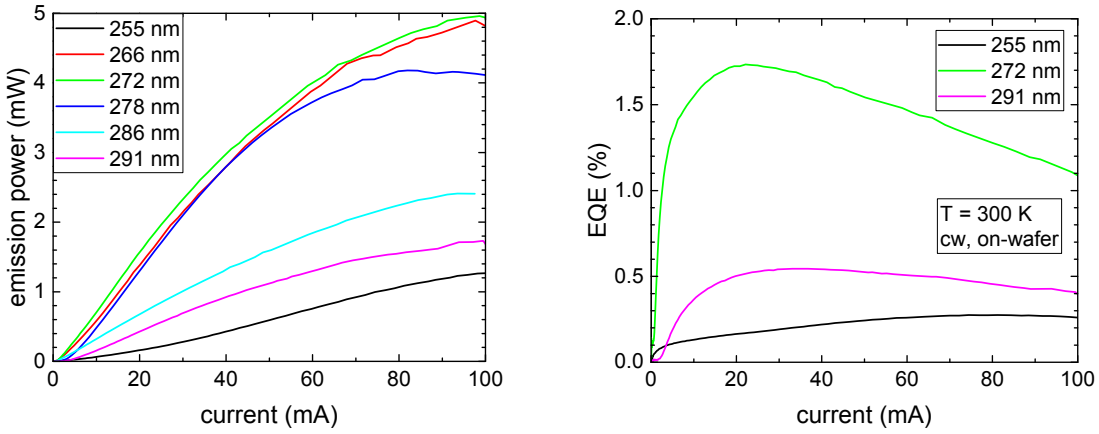

Figure 4.7: Current-dependent emission power (a) and EQE (b) of UV LEDs with different peak emission wavelengths between 255 nm and 291 nm.

For UV LEDs emitting at shorter wavelength (255 nm), the emission power is strongly reduced and broad parasitic luminescence near 320 nm is observed. The LED heterostructure was fixed in this experiment except for the variation of the AlGaN MQW composition. However, carrier injection can be influenced by the band gap offset between the MQW (quantum wells and barriers) and the EBL and subsequent layers. A higher aluminum content of the $Al_{0.66}Ga_{0.34}N$:Mg SPSL compared to the barrier layers is

contributing to electron blocking in LED operation, leading to high emission power of a 266 nm emitting LED with $Al_{0.64}Ga_{0.36}N$ barriers. However, for an LED emitting at 255 nm the $Al_{0.72}Ga_{0.28}N$ barriers have larger band gap than the $Al_{0.66}Ga_{0.34}N$:Mg SPSL. In that case, the conduction band offset between barriers and AlGaN:Mg is negative and the 1.5 nm thick $Al_{0.92}Ga_{0.08}N$ EBL is providing insufficient electron blocking performance. This leads to reduced carrier injection efficiency and allows for electron leakage and recombination in the AlGaN:Mg SPSL layer. Electrons can pass the EBL, e. g. by thermally activated drift or tunneling, causing the observed reduction of emission power as well as increase of parasitic luminescence. Compared to the reference LED exhibiting maximum EQE = 1.75% near 20 mA, the EQE of such LED emitting at 255 nm is reduced over the entire current range. Especially at low currents < 40 mA a strong reduction of the EQE is caused by carrier leakage.

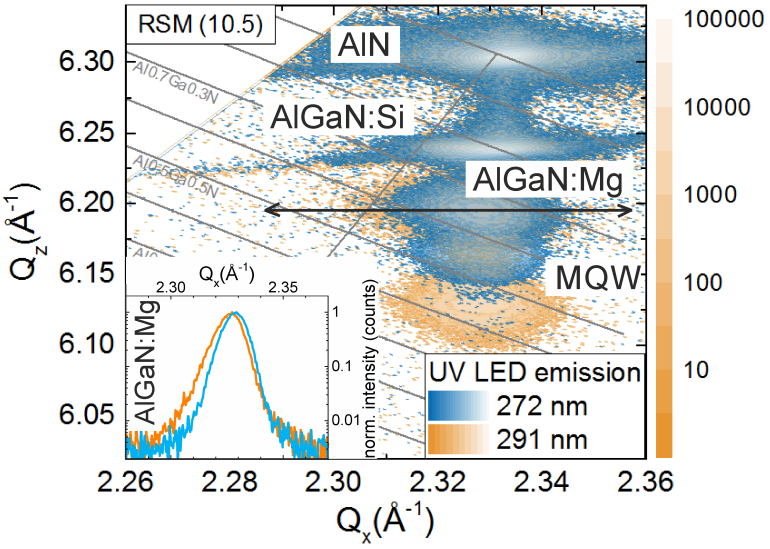

Figure 4.8: XRD reciprocal space map of UV LEDs with different AlGaN MQW composition and emission wavelength for evaluation of the MQW strain state. The inset shows a lateral line profile at Q_z = 6.195Å, exhibiting different Q_x position and broadening of the AlGaN:Mg SPSL peaks.

For UV LEDs emitting at longer wavelength > 280 nm, the compressive strain is increased within the AlGaN QW and barrier layers with comparably low aluminum content due to the large lattice mismatch to the AlN buffer layer of the ELO AlN/sapphire template. In case of pseudomorphic growth of the AlGaN QW and barrier layers, which is the desired case, the lateral lattice constant a_{layer} of the QWs would be the same as the lateral lattice constant of the AlN in the substrate but different from the lateral lattice constant $a_{relaxed}$ of relaxed AlGaN with same composition as the QWs. The compressive strain increases with increasing difference of the lateral lattice constants, see Equation 3.1. In case of non-pseudomorphic growth, the strain energy would exceed the defect formation energy and additional strain is relieved by re-adjustment of the lattice constant by formation of defects, e. g. misfit dislocations. Such relaxation mechanisms can be accessed by XRD measurements. In reciprocal space map images, one single AlGaN MQW peak is visible formed from contributions of both the AlGaN QW and barrier layers. As the Q_x value of such AlGaN MQW peaks contains information about the strain state, RSMs of two UV LEDs emitting at 272 nm and 291 nm are shown in Figure 4.8. The superposition of both RSMs allows for analysis of the differences of both structures. First, the MQW peak of the LED with long wavelength emission (orange) is located at lower $Q_z = 6.13\,Å^{-1}$ values and corresponding to lower average composition

of $Al_{0.45}Ga_{0.55}N$, compared to the $Al_{0.56}Ga_{0.44}N$ MQW peak at $Q_z = 6.16\,Å^{-1}$ of the LED with 272 nm emission (blue). Relaxation within the QWs or barriers would impact the AlGaN MQW peak as well as the AlGaN:Mg peak position. As the AlGaN:Mg SPSL was grown with the same conditions, any differences observable in the superposed RSM can be attributed to the strain state of the AlGaN MQW. Indeed, the AlGaN:Mg peak of the 291 nm emitting LED is located at lower Q_x values than the LED emitting at 272 nm and exhibits additional peak broadening that can also be seen in the inset of Figure 4.8, demonstrating partial relaxation and less strain. However, both are far from the position of relaxed AlGaN, demonstrating only slight partial relaxation even for the sample with 291 nm emission. Such slight partial relaxation that is barely detectable by a single XRD RSM measurement is causing a reduction of emission power by more than 50%, as shown in Figure 4.7. The EQE is reduced in comparison to the reference LED: Almost no emission (EQE ≈ 0) was recorded for low currents up to 3 mA, and up to 20 mA the EQE is only slowly increasing, reaching a maximum of 0.53%, three times less than the reference LED. Hence, any partial relaxation, especially of the emitting QWs, must be avoided in order to achieve UVC LEDs with high emission power.

Based on the presented investigations, the conclusion can be drawn that obtaining efficient carrier injection in a broad wavelength range requires a consideration of the interaction of multiple layers within UV LED heterostructures that includes MQW (quantum wells and barriers), EBL, as well as the AlGaN:Mg SPSL. An optimized UVC LED heterostructure enables stable emission power, in this case within a wavelength range between 265 nm and 280 nm. Two physical mechanisms were identified reducing the emission power of UV LEDs outside of this wavelength range: electron leakage and relaxation. Therefore, an intentional shift of the emission wavelength to values below 260 nm or beyond 290 nm requires adjustments of the heterostructure design, preventing electron leakage and recombination within the AlGaN:Mg SPSL in case of UVC LEDs with shorter emission wavelength, or moderating relaxation and defect generation in case of UVB LEDs with longer emission wavelength. For very short UVC LED emission wavelengths < 240 nm, however, reduced light extraction efficiency due to the dominant light polarization switching from TE to TM as well as reduced internal quantum efficiency are additionally affecting the emission power [94, 120, 121], which in combination governs the trend of reported EQE values of UV LEDs [92]. In general, it was shown that for the investigated spectral range the MQW composition affects relaxation as well as carrier injection. The influence of barrier and waveguide composition on mode confinement is separately discussed in the next section.

4.3 Optical confinement, modal absorption, and carrier injection in UVC laser diodes

4.3.1 Influence of AlGaN waveguide composition

In laser diodes with separate confinement heterostructure, waveguides are crucial for optical mode confinement. For AlGaN-based UVC laser diodes, waveguide layers are additionally crucial for carrier injection as band offsets and layer resistivities strongly depend on the composition of such wide band gap materials. In detail, electron leakage

or hole injection as well as carrier confinement within quantum wells strongly depend on the band offset potential of AlGaN waveguide and barrier layers in the MQW. In this experiment, waveguide and barriers exhibit equal composition that is systematically varied between $Al_{0.55}Ga_{0.45}N$ and $Al_{0.76}Ga_{0.24}N$. The waveguide system consists of a 40 nm thick n-side AlGaN:Si waveguide located between the AlGaN:Si cladding layer and the MQW. A 15 nm thick AlGaN:uid waveguide is located between MQW and EBL close to the p-side. The nominal thickness of the entire waveguide system including p-side and n-side waveguides, MQW, and barriers is 72 nm.

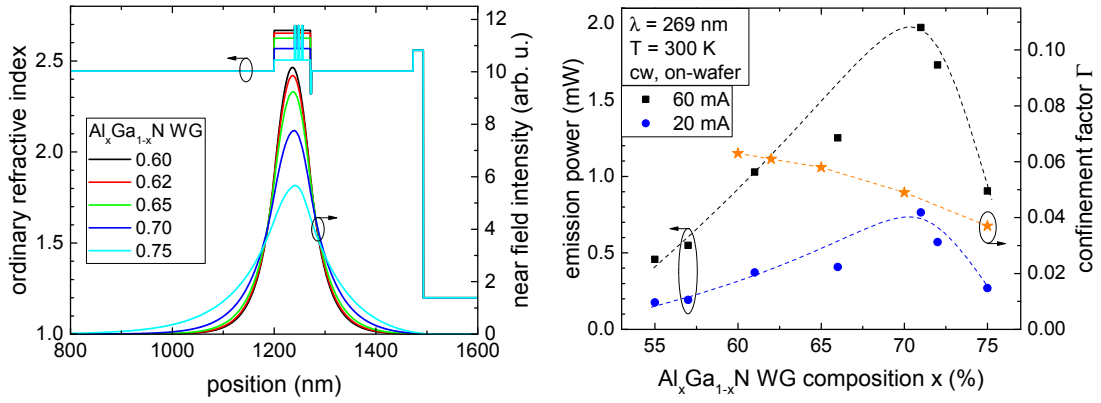

(a) (b)

Figure 4.9: Influence of the AlGaN waveguide composition on optical mode confinement (a) as well as on spontaneous EL emission power and confinement factor (b). Waveguide and barrier layers are grown at the same growth conditions and with the same AlGaN composition. (Simulation by Martin Martens - TU Berlin)

Figure 4.9a shows simulations of the vertical near field intensity distribution of an optical mode with 270 nm wavelength, in connection with the ordinary refractive index of the respective LD heterostructures. The refractive index of the $Al_{0.8}Ga_{0.2}N$:Si cladding layer is constant at 2.45 until a step increase to the WG layer. The largest refractive index corresponds to the three quantum wells near the position of 1250 nm. After the p-side WG, and a thin $Al_{0.92}Ga_{0.08}N$ EBL with low refractive index near 2.3, the p-side AlGaN:Mg SPSL cladding layer is providing mode confinement within the WG as well as preventing strong mode overlap with the absorbing GaN:Mg cap layer or the absorbing p-contact metal. As the aluminum content of the $Al_xGa_{1-x}N$ WG increases from 0.60 to 0.75, the ordinary WG refractive index decreases from 2.7 to 2.5, almost approaching the refractive index of the $Al_{0.8}Ga_{0.2}N$ cladding layers. Therefore, the refractive index step between WG and cladding layers is strongly reduced, which also reduces the mode confinement. The maximum of the simulated near field intensity decreases by almost 50% and its FWHM is increased from 83 nm to 137 nm at the same time. Due to insufficient vertical confinement, the optical mode spreads out into the cladding layers, which negatively affects the overlap of optical mode and quantum wells. The confinement factor Γ is shown in Figure 4.9b in orange. Γ decreases with increasing WG aluminum content from 6.2% at x = 0.60 to 3.7% at x = 0.75.

In an experimental study, the $Al_xGa_{1-x}N$ composition of waveguide and MQW barrier layers was simultaneously varied between $x = 0.55$ and $x = 0.75$ in LD heterostructures

comparable to the discussed simulations. The spontaneous EL emission spectra from these structures are slightly shifting to shorter wavelength for higher WG aluminum content within (269 ± 3) nm due to increasing quantum confinement that is overcompensating a small red-shift due to QCSE [119]. The electroluminescence characteristics of the emission power of these devices are shown in Figure 4.9b. For low aluminum mole fraction in waveguides and barriers, the emission power is comparably low (0.5 mW at 60 mA) due to insufficient carrier confinement within the quantum wells. With increasing aluminum content the MQW confinement potential increases and more charge carriers are recombining radiatively within the QWs which increases the LED emission power up to 2 mW at 60 mA for $Al_{0.71}Ga_{0.29}N$ WGs. By further increase to $Al_{0.75}Ga_{0.25}N$ the emission power strongly decreases to 0.9 mW at 60 mA. Hence, in this experiment optimum carrier injection is achieved for WG composition near $Al_{0.7}Ga_{0.3}N$ [119].

When the waveguide composition is increasing to $Al_{0.72}Ga_{0.28}N$, the band gap is exceeding the band gap of the $Al_{0.67}Ga_{0.33}N$:Mg SPSL p-cladding. However, the emission power is not abruptly reduced by electron leakage which could be expected from the results of the previous experiment discussed in section 4.2. In contrast to section 4.2, the thickness of the $Al_{0.92}Ga_{0.08}N$ EBL is increased from 1.5 nm to 5 nm in this experiment. Here, the 5 nm thick EBL can provide sufficient electron blocking without the immediate necessity of a wide band gap AlGaN:Mg SPSL contributing to the electron blocking. Therefore, the observed reduction of emission power by further increase of the waveguide aluminum content to $Al_{0.75}Ga_{0.25}N$ is attributed to the reduced potential barrier between WG and EBL.

In this investigation, it was demonstrated that in such UVC emitting devices the spontaneous emission power increases with WG aluminum content until an optimum carrier injection into the quantum wells is achieved for waveguide compositions near $Al_{0.7}Ga_{0.3}N$. Optimizing the mode confinement, however, follows the opposite trend, as the confinement factor is decreasing with increasing aluminum content. Therefore, the design of UVC LD heterostructures requires to carefully balance both effects, as the variation of WG composition affects carrier injection as well as mode confinement. Depending on the composition and thickness of cladding layers, the optimized $Al_xGa_{1-x}N$ WG composition can be fixed within the range $0.6 < x < 0.7$. Furthermore, plastic relaxation is an increasing issue for waveguides with very low aluminum content $x < 0.55$, discussed in section 3.4 and section 4.2.

4.3.2 Impact of the AlGaN:Mg SPSL cladding composition

One of the most crucial layers in UVC LD heterostructures is the AlGaN:Mg p-cladding layer, as it needs to provide both hole injection and vertical optical confinement. As the Mg acceptor ionization energy increases with increasing AlGaN:Mg aluminum content [18], efficient hole injection becomes more challenging, which was discussed in the introduction of this chapter. The opposing trend is given by the vertical mode confinement, becoming more effective with increasing AlGaN:Mg p-cladding aluminum content. Basic requirement for the optical properties of cladding layers is transparency at the LD emission wavelength. For LDs emitting at 270 nm a composition of $Al_{0.6}Ga_{0.4}N$ is required to avoid fundamental absorption [122]. Furthermore, sufficient refractive index contrast to the WG layers needs to be provided, considering that the composition

of such WGs can vary, e. g. between $Al_{0.55}Ga_{0.45}N$ and $Al_{0.75}Ga_{0.25}N$ (subsection 4.3.1). In order to verify the influence of the refractive index on properties of the optical system, mode simulations with varying p-cladding composition but fixed $Al_{0.80}Ga_{0.20}N$:Si n-cladding and $Al_{0.63}Ga_{0.37}N$ WG are shown in Figure 4.10a. For transparent p-cladding layers with average composition of $Al_{0.7}Ga_{0.3}N$:Mg, the refractive index is comparably high, enabling only low refractive index contrast to the $Al_{0.63}Ga_{0.37}N$ WG. In such a case of asymmetric confinement, the optical mode is extended towards the p-side which increases the overlap with absorbing layers, such as GaN:Mg and the palladium p-contact metal. The modal absorption $g_{mod} = \Gamma_{mat} \cdot g_{mat}$ is determined by the absorption coefficient of certain layer materials g_{mat} and the mode overlap Γ_{mat} with the respective layer. In such UVC LD heterostructures, the absorption coefficients of the p-side layers are as high as $g_{mat}^{AlGaN:Mg} = 50\,\mathrm{cm}^{-1}$ for Mg-induced absorption losses in wide band gap AlGaN:Mg p-cladding layers, $g_{mat}^{GaN:Mg} = 170000\,\mathrm{cm}^{-1}$ for the fundamental absorption of GaN near 270 nm, and $g_{mat}^{Pd} = 10^6\,\mathrm{cm}^{-1}$ for palladium metal contacts [123–125]. All of these layers contribute to the total modal absorption in the p-side, their calculated individual contribution is shown in Figure 4.10b. The modal losses in the GaN:Mg and p-contact metal layers each are exceeding $300\,\mathrm{cm}^{-1}$, adding up with the $Al_{0.7}Ga_{0.3}N$:Mg p-cladding losses of $25\,\mathrm{cm}^{-1}$ to total modal absorption in the p-side of $740\,\mathrm{cm}^{-1}$. The confinement factor is 4.5%.

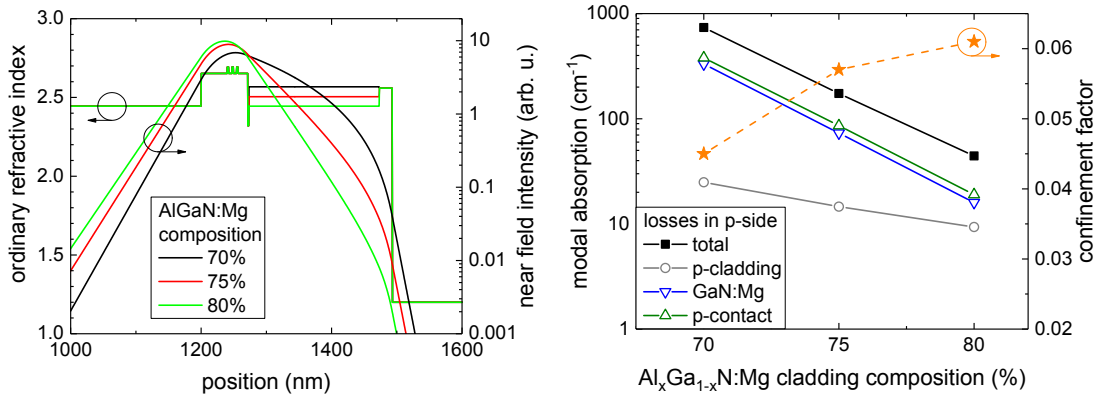

(a) (b)

Figure 4.10: Influence of AlGaN:Mg SPSL p-cladding composition on optical mode distribution and modal absorption in UVC LD heterostructures with $Al_{0.63}Ga_{0.37}N$ WG and 270 nm emission wavelength. (a) Refractive index profile with optical mode simulation, (b) modal absorption losses in the p-side and confinement factor. (Simulation by Martin Martens - TU Berlin)

With increasing Al content in AlGaN:Mg p-cladding layers, the optical mode is more symmetric and less extended to the p-side. Therefore, the mode overlap with GaN:Mg and p-contact metal layers decreases and modal losses in these layers are strongly reduced to values below $20\,\mathrm{cm}^{-1}$ each. With reduced p-cladding losses near $10\,\mathrm{cm}^{-1}$, the total p-side losses are as low as $44\,\mathrm{cm}^{-1}$ for $Al_{0.8}Ga_{0.2}N$:Mg p-cladding layers, with an increased confinement factor of 6.1%. Compared to the losses with symmetric cladding, the p-side losses could be further reduced by increasing the aluminum content in the p-cladding beyond $x = 0.8$. However, achieving efficient hole injection becomes even more challenging in this case. In summary, the optical mode simulations show that with

increasing Al content in AlGaN:Mg p-cladding layers the confinement factor is increased and modal losses in the p-side are reduced, including losses in p-cladding, GaN:Mg and p-contact layers. For the optical system, high aluminum mole fraction cladding layers are beneficial.

The growth and fabrication of LD structures is enabling an experimental verification of the hole injection into UVC LDs heterostructures with the discussed aluminum content variation in AlGaN:Mg SPSL p-cladding layers. From EL measurements of the spontaneous emission power, variations of injection efficiency can be detected, as internal quantum efficiency and light extraction efficiency are not directly affected by the composition variation of the transparent AlGaN:Mg SPSL p-cladding. Broad area waveguide structures with stripe p-contacts of 5 - 40 µm width and 1000 µm length have been fabricated and the wafers were cleaved into laser bars with 15 diodes each. Due to very unstable results of cw measurements, pulsed EL measurements with 25 kHz repetition rate and 1 µs pulse length (2.5% duty cycle) have been carried out using a current-less dc bias voltage between 6 V and 12 V, depending on the varying turn-on voltage of each diode. Here, a bias-tee with inductive dc coupling and capacitive ac coupling was used in order to improve impedance matching.

Figure 4.11a shows the spontaneous emission power from pulsed EL measurements of UVC LD structures with varying composition of the AlGaN:Mg SPSL p-cladding layer. The emission power of devices at a given current was found to be independent of stripe contact width, enabling a comparison of emission power within a series of varying p-cladding composition independent of contact geometry. For average aluminum content up to 76% in the p-cladding layers, the measured emission power is almost constant at a given current. More than 6 mW at 150 mA (0.4 kA/cm^2) were recorded for the sample with $Al_{0.61}Ga_{0.39}N$:Mg p-cladding. However, due to the highly resistive AlGaN:Mg SPSL and non-optimized contacts, the instability of certain samples leads to device failures already at current values below 100 mA, no current densities exceeding 0.9 kA/cm^2 could be obtained in this experiment. Outstandingly, the sample with highest aluminum content in the p-cladding exhibits strongly reduced emission power, shown in Figure 4.11b for currents of 20 mA and 60 mA. For these current levels, the emission power is constant or only slightly decreasing with increasing p-cladding Al mole fraction between 61% and 76%, whereas for 82% the emission power is reduced by a factor of more than ten. This indicates nearly constant carrier injection efficiency for the variation of p-cladding composition between $Al_{0.61}Ga_{0.39}N$ and $Al_{0.76}Ga_{0.24}N$, whereas UVC LDs with $Al_{0.82}Ga_{0.18}N$:Mg p-cladding layer exhibit strongly reduced injection efficiency and external quantum efficiency. However, even for such an extreme case, transparent AlGaN:Mg SPSLs provide p-type conductivity and certain carrier injection could be obtained.

From the presented investigations, the best compromise for an AlGaN:Mg SPSL p-cladding composition in UVC LD heterostructures is fixed to $Al_{0.76}Ga_{0.24}N$, which is considering improved optical confinement and reduced modal losses with increasing aluminum content as well as avoiding the injection efficiency reduction for aluminum content exceeding 82%.

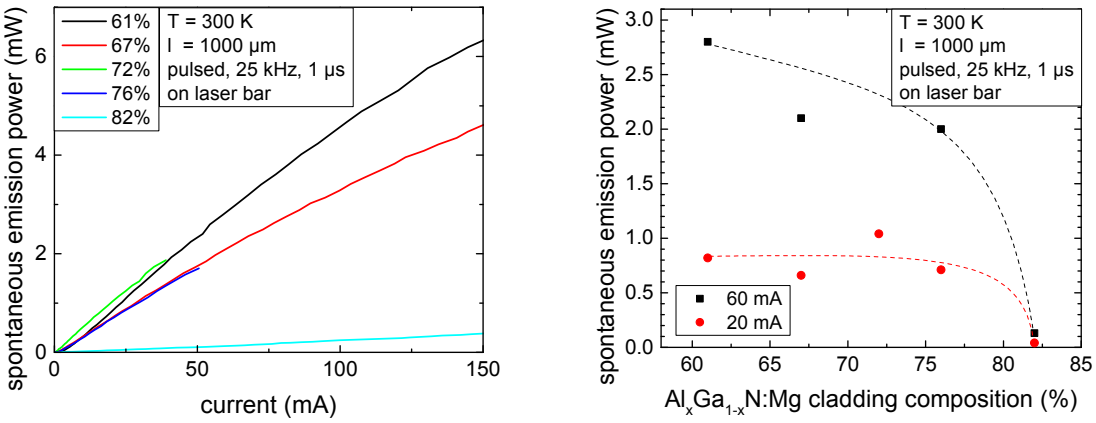

(a) (b)

Figure 4.11: Spontaneous EL emission power of UVC laser diode heterostructures with $Al_{0.63}Ga_{0.37}N$ WG and varied composition of 200 nm thick AlGaN:Mg SPSL p-cladding. (Measurements by Verena Montag - TU Berlin)

4.3.3 Impact of the AlGaN:Mg SPSL cladding thickness

In the previous section, the composition of AlGaN:Mg SPSL p-cladding layers within UVC light emitters has been investigated and was fixed to $Al_{0.76}Ga_{0.24}N$ in order to achieve improved optical confinement and reduced modal losses. In this section, the influence of the $Al_{0.76}Ga_{0.24}N$:Mg SPSL thickness on optical and electrical properties of UVC laser diode heterostructures will be investigated.

In UVC LD heterostructures the p-side cladding layer provides vertical confinement of the optical mode by a refractive index contrast to the WG layer. Therefore, a higher aluminum content compared to an $Al_{0.63}Ga_{0.37}N$ WG is required for the p-cladding. The p-cladding also impacts the mode extension towards the p-side and must prevent a large overlap with highly absorbing layers such as GaN:Mg or the metal contact. With fixed cladding composition, that overlap can be modified with varying thickness of the AlGaN:Mg SPSL p-cladding. In Figure 4.12a, the refractive index profile of such LD structures and simulations of the optical mode are shown. For these simulations, Mg-doped SPSLs with average composition of $Al_{0.8}Ga_{0.2}N$ were used, however, resulting trends are transferable within a certain compositional range. With increasing AlGaN:Mg SPSL p-cladding thickness the distance between MQW and strongly absorbing layers increases. The optical mode distribution is very similar in the WG and the n-cladding regions. However, in the p-side the mode distribution is strongly affected by the p-cladding thickness. With increasing thickness the mode extends further to the p-side, at the same time the mode overlap with GaN:Mg and metal contacts is strongly reduced which potentially reduces absorption losses. In Figure 4.12b, the calculated modal absorption losses in p-side layers is shown, assuming low Mg-induced absorption coefficients in the AlGaN:Mg p-cladding ($50\,cm^{-1}$), and higher absorption coefficients from fundamental absorption in the GaN:Mg ($170000\,cm^{-1}$) and in the p-contact metal ($10^6\,cm^{-1}$) [123–125]. Almost independent of its thickness, the absorption losses in a $Al_{0.8}Ga_{0.2}N$:Mg SPSL cladding are near $10\,cm^{-1}$, which is due to an almost constant mode overlap of $\Gamma_{mat}^{AlGaN:Mg} = 0.18 \pm 0.01$. The mode overlap with GaN:Mg and metal

p-contact is much smaller, and for geometrical reasons $\Gamma_{mat}^{GaN:Mg}$ and Γ_{mat}^{Pd} are highly correlated ($\Gamma_{mat}^{GaN:Mg} \approx 5 \cdot \Gamma_{mat}^{Pd}$). For 100 nm thick $Al_{0.8}Ga_{0.2}N$:Mg SPSL cladding layers, a considerable overlap causes very high modal absorption losses of more than 300 cm^{-1} both in GaN:Mg as well as in the Pd layer. Such high modal absorption would prevent any lasing operation. However, for increasing $Al_{0.8}Ga_{0.2}N$:Mg SPSL cladding thickness, these absorption losses are approximately exponentially decreasing to values below 10 cm^{-1} near a thickness of d = 200 nm. Whereas the total absorption losses in the p-side are decreasing, mainly determined by GaN:Mg and Pd absorption for $d \leq 200$ nm, a saturation towards 10 cm^{-1} is calculated for $d > 200$ nm due to almost constant absorption in the AlGaN:Mg SPSL. From these optical mode simulations, a minimum $Al_{0.8}Ga_{0.2}N$:Mg SPSL cladding thickness of 200 - 300 nm is required to reduce the mode overlap with highly absorbing GaN:Mg and Pd layers and to obtain low total modal losses in the p-side. The modal overlap with the quantum wells, however, is almost not affected by the variation of the cladding thickness: For these structures the calculated confinement factor is 0.061-0.062 (Figure 4.12b).

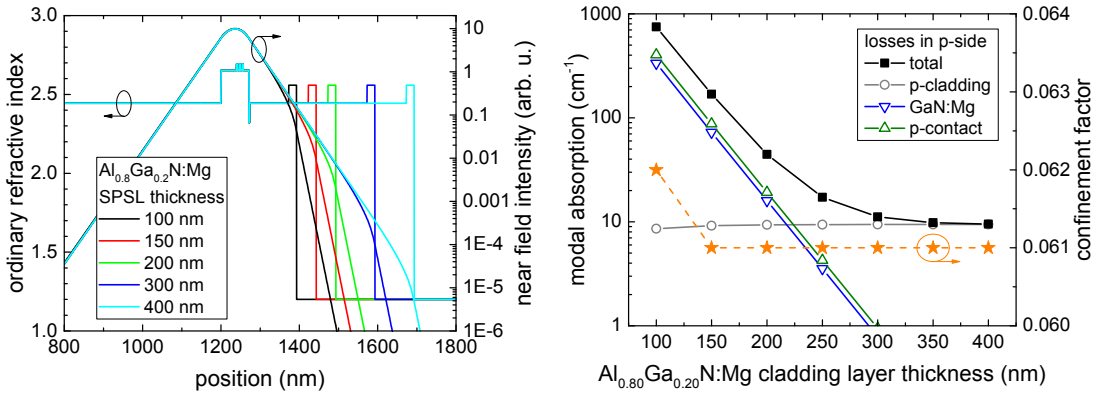

(a) (b)

Figure 4.12: Influence of AlGaN:Mg SPSL p-cladding thickness on optical mode distribution in UVC LD heterostructures with $Al_{0.63}Ga_{0.37}N$ WG and 270 nm emission wavelength. (a) Refractive index profile with optical mode simulation, (b) modal absorption losses in the p-side and confinement factor. (Simulation by Martin Martens - TU Berlin)

However, the influence of the AlGaN:Mg cladding layer thickness on the emission of UVC LD heterostructures must be subject to experimental investigation, as it influences not only mode confinement and absorption, but carrier injection as well. Therefore, UVC LD heterostructures with $Al_{0.76}Ga_{0.24}N$:Mg SPSL cladding layer thickness varying from 0 nm to 400 nm were grown by MOVPE and processed using standard micro fabrication techniques. The measured spontaneous EL emission power from LEDs with 0.04 mm^2 mesa size is shown in Figure 4.13. Without any AlGaN:Mg (0 nm), no UVC emission from the structures could be detected. In this case, the formation of a pn-junction is disturbed and electrons injected from the n-contact are basically flowing directly through the heterostructure into the p-contact, without radiative recombination in the MQW. In contrast, with a 50 nm thick AlGaN:Mg SPSL p-cladding layer, a diode IV-characteristic as well as UVC emission can be observed. With increasing AlGaN:Mg SPSL thickness, the recorded emission power increases to a maximum of 1.3 mW at

60 mA near d = 200 nm. For a thickness of 400 nm, the emission power is strongly reduced and current levels of 60 mA could not be achieved due to device failures. In this case, the very thick and highly resistive $Al_{0.76}Ga_{0.24}N$:Mg SPSL requires extremely high voltages > 40 V that cause breakthroughs and short-circuit behavior in the second measurements, which will be discussed in section 4.4. This excludes a 400 nm thick $Al_{0.76}Ga_{0.24}N$:Mg SPSL for UVC LD operation. Instead, $Al_{0.76}Ga_{0.24}N$:Mg SPSLs with 100 to 200 nm thickness provide highest emission power and therefore highest carrier injection efficiency in this comparison.

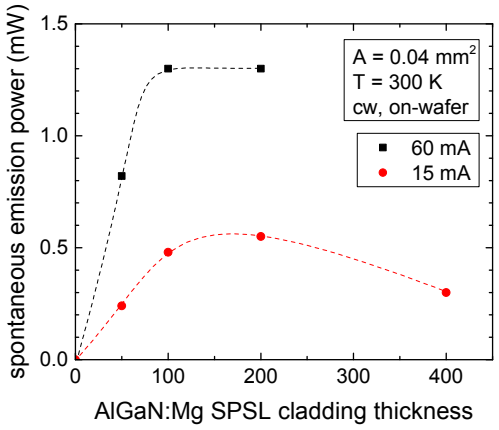

Figure 4.13: Spontaneous EL emission power of UVC laser diode heterostructures with $Al_{0.63}Ga_{0.37}N$ WG and varied $Al_{0.76}Ga_{0.24}N$:Mg SPSL p-cladding thickness at drive currents of 15 mA and 60 mA.

Although the AlGaN:Mg cladding thickness also affects operation voltages, which will be investigated in the next section, following conclusions on the heterostructure design can be drawn at this point: The impact of increasing AlGaN:Mg cladding thickness requires to consider the respective trends of a reduction of optical losses on the one hand and the emission power maximum at d = 100 - 200 nm on the other hand. An $Al_{0.76}Ga_{0.24}N$:Mg SPSL with 200 nm thickness provides the best compromise with comparably low modal losses in the p-side ($g_{mod} \approx 40$ cm^{-1}) and high injection efficiency. Furthermore, the operation voltage is strongly affected by increasing AlGaN:Mg SPSL thickness that can cause problems such as Joule heating, reduced lifetime, or device failure. Therefore, the correlations between operation voltage, electrical resistivity, and thickness of AlGaN:Mg SPSLs will be investigated in the next section.

4.4 Vertical resistivity of $Al_{0.76}Ga_{0.24}N$:Mg SPSL p-cladding layers

Both achieving low electrical resistivity of AlGaN:Mg-based SPSL p-cladding layers with high aluminum content x ≥ 0.6 and its accurate measurement is very challenging. In resistivity estimations based on IV-measurements, such as Hall experiments using the van-der-Pauw method [126] or TLM experiments, the current path covers lateral distances of several micrometers or even millimeters. In this case, a high layer resistivity requires very high voltages and causes only low measured currents, preventing a high measurement accuracy. Additionally, in Hall and TLM measurements as well as in contact-less resistance measurements, which record the damping of induced eddy currents, the electrical resistivity of samples is determined for the lateral direction. For the

operation of UVC laser diodes, however, the current density points mainly in vertical direction, ideally demanding direct measurements of the vertical resistivity. Although vertical resistivity and lateral resistivity in AlGaN:Mg layers are not expected to be entirely uncorrelated, in general they can be different due to anisotropic wurtzite crystal directions as well as a preferred direction given by the growth of the SPSL in c-direction and the associated polarization fields. Therefore, accurate measurements of the vertical resistivity of AlGaN:Mg SPSL layers are desired.

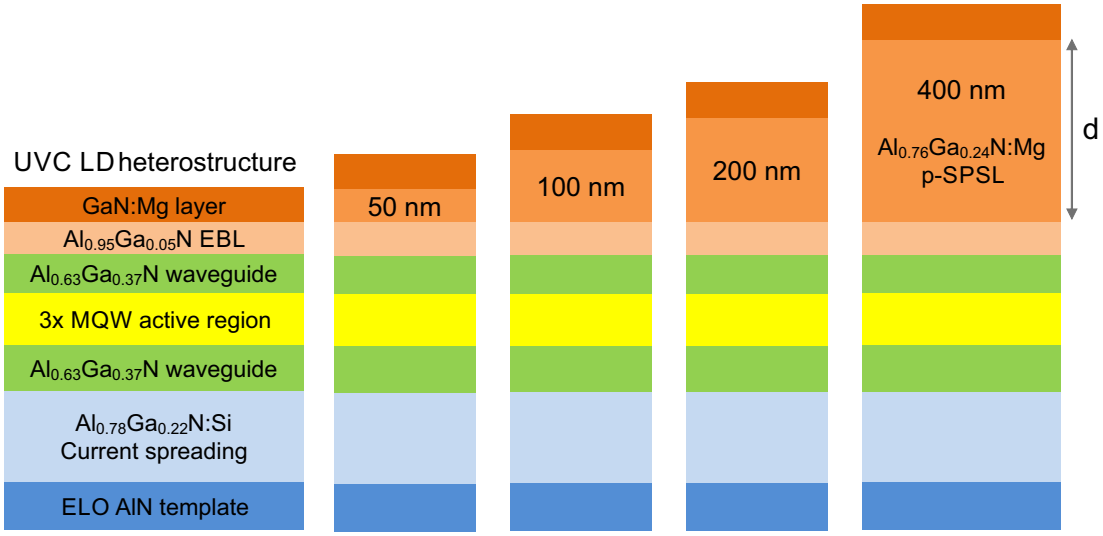

Figure 4.14: Schematic of UVC laser diode heterostructures with increasing $Al_{0.76}Ga_{0.24}N$:Mg p-SPSL thickness.

In order to determine the vertical resistivity from IV-measurements, the operation voltages of UVC laser diode heterostructures with AlGaN:Mg SPSL p-cladding layers are evaluated. As AlGaN:Mg SPSLs with high aluminum content exhibit comparably high resistivity, the operation voltages are strongly affected by these cladding layers. In a growth series of UVC LD heterostructures, the thickness of Mg-doped $Al_{0.86}Ga_{0.14}N/Al_{0.66}Ga_{0.34}N$ SPSL layers with average aluminum content of 76% was varied between 0 nm and 400 nm, schematically shown in Figure 4.14. Emission power measurements of these samples are discussed in subsection 4.3.3. In general, IV-characteristics of semiconductor pn diodes obey the exponential Shockley diode equation (Equation 4.1), with the reverse bias saturation current I_S and the ideality factor n. In a basic equivalent circuit, UVC LDs with increasing p-cladding thickness can be represented by an ideal pn diode plus series resistor with increasing resistance R, as indicated in Figure 4.15a. In this case, the total device voltage equals the sum of both voltage drops V_D at the diode and V_R at the resistor. In Figure 4.15a, the expected IV-curves calculated according to this equivalent circuit using $I_S = 10^{-20}A$ and $n = 10$ are shown. In III-nitride-based LEDs, ideality factors exceeding $n = 2$ have been reported, in certain cases as high as $n = 18$ [127, 128]. With increasing p-cladding thickness the calculated IV-curves are reducing in slope due to the increasing series resistance in combination with a constant turn-on voltage. IV-measurements on real diode structures, however, exhibit an unexpected behavior: Increasing turn-on voltages and almost comparable slopes for an increasing AlGaN:Mg SPSL p-cladding thickness

(Figure 4.15b). Therefore, the basic equivalent circuit has to be modified. Instead of a series resistor with constant resistance R, the series resistance R(V) must be dependent on the operating point of the circuit, which implies a correlation of the AlGaN:Mg SPSL resistivity with the operating voltage [5].

$$I = I_S \left(\exp \frac{q \cdot V}{n \cdot k_B T} - 1 \right) \tag{4.1}$$

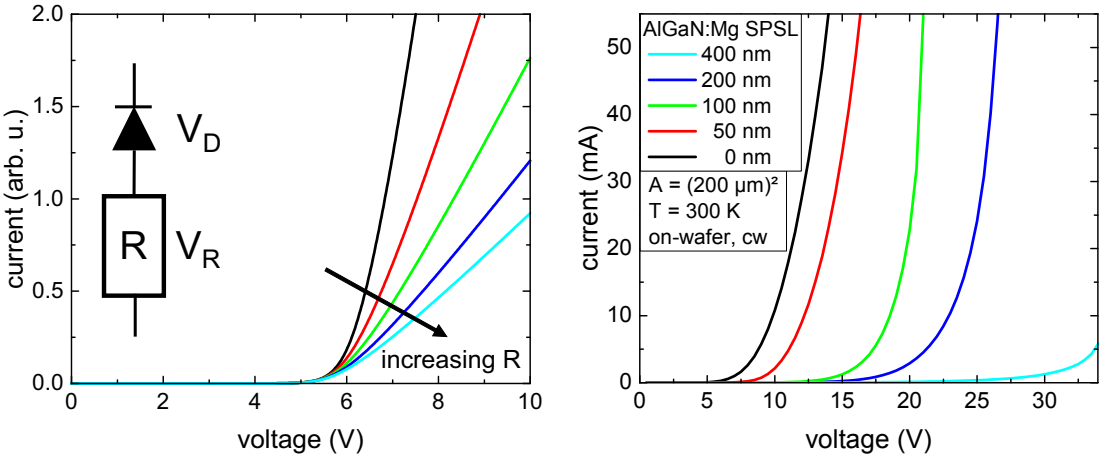

(a) (b)

Figure 4.15: (a) Calculated IV-curves of an equivalent circuit composed of an ideal pn diode plus series resistor and (b) measured IV-characteristics of UVC laser diode heterostructures with increasing $Al_{0.76}Ga_{0.24}N$:Mg SPSL p-cladding thickness [5].

In order to extract the AlGaN:Mg SPSL resistivity, the operating voltages are evaluated at a fixed current, e. g. 10 mA. As shown in Figure 4.16, the operation voltages V are increasing with rising AlGaN:Mg SPSL thickness d. From a linear fit, the voltage slope $\Delta V/\Delta d$ can be calculated, which only depends on the influence of the AlGaN:Mg SPSL layer properties. A voltage slope of $0.055\,\mathrm{V\,nm^{-1}}$ is equal to an additional voltage of 5.5 V required per 100 nm additional SPSL thickness. In particular, any influence of other layers in the UVC LD heterostructure on the operation voltage is automatically excluded by calculating the voltage slope. If comparable, those potential sources of error, such as AlGaN:Si resistivity, or the resistance of metal-semiconductor contacts, are just affecting the offset of the linear fit. The calculated voltage slope represents the external electric field $F = \Delta V/\Delta d$ in the AlGaN:Mg SPSL, e. g. $F = 0.55\,\mathrm{MV\,cm^{-1}}$ for the voltage slope of $0.055\,\mathrm{V\,nm^{-1}}$. For varying drive currents, different electric fields were evaluated. Furthermore, the AlGaN:Mg SPSL resistivity ρ can be calculated from the voltage slope using the current density j: $\rho = \Delta V/\Delta d \cdot 1/j$. In Figure 4.17a, the electric field in the AlGaN:Mg SPSL as well as the calculated resistivity are shown with respect to the drive current. Both parameters F and ρ strongly depend on the operation point; the electric field is increasing to values near $0.6\,\mathrm{MV\,cm^{-1}}$ and the AlGaN:Mg SPSL resistivity is decreasing to values near 20000 Ωcm with increasing drive current.

In combination, the influence of the electric field on the resistivity is shown in Figure 4.17b. By increasing the electric field from $0.1\,\mathrm{MV\,cm^{-1}}$ to $0.6\,\mathrm{MV\,cm^{-1}}$, the vertical

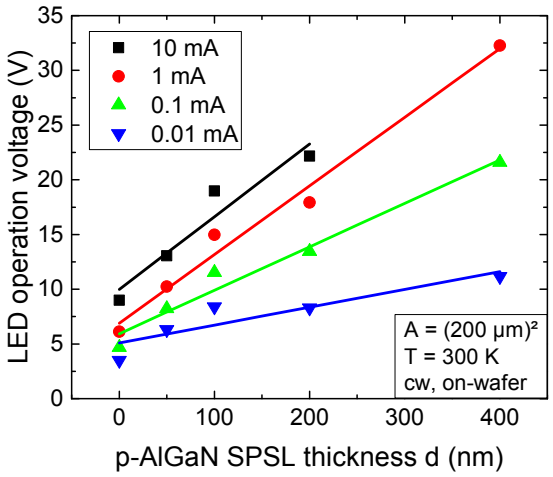

Figure 4.16: Evaluation of the operation voltage of LEDs with different $Al_{0.76}Ga_{0.24}N$:Mg SPSL thickness for different current levels as well as the linear regression of these data.

AlGaN:Mg SPSL resistivity strongly decreases by more than two orders of magnitude from 8 MΩcm to 20000 Ωcm. Such resistivity reduction with increasing electric field is unexpected, as an ohmic semiconductor layer would exhibit a constant, field-independent resistivity at a fixed temperature. Other fixed values in this experiment are the Mg concentration ($[\mathrm{Mg}] = 5 \cdot 10^{19}\,\mathrm{cm}^{-3}$) of the investigated samples as well as the concentration of the impurities oxygen, carbon, and hydrogen. The concentration of ionized acceptors [Mg^-], neutral acceptors [Mg^0], and free holes p, however, varies with the Fermi level. According to the equation $\sigma = 1/\rho = \mu \cdot p \cdot e$, the resistivity is determined by the free hole density p and the mobility μ, both can be affected by the electric field. A field-ionization of Mg acceptors leads to increased p, to increased [Mg^-], and to decreased [Mg^0] concentrations. The increasing p can partly explain the resistivity reduction with increasing electric field. On the contrary, scattering at ionized acceptors [Mg^-] with increased density would lead to a reduction of the mobility. Also, a drift velocity saturation due to mobility collapse can occur at very high electric fields. Both of these mechanisms are apparently not dominating the conduction of charge carriers, as they would lead to increased resistivity which is not observed in the experiment.

The measured field-dependence of the resistivity could be expected for field-induced ionization processes of magnesium acceptors in AlGaN, generally referred to as Poole-Frenkel (PF) effect [129–132]. The PF effect describes a reduction of the effective ionization energy of a localized state in materials by an external electric field. For dopants in semiconductors, a reduced ionization energy leads to increasing free carrier concentration that enhances the conductivity of the material. Therefore, the PF effect is a description of field-enhanced thermionic emission of charge carriers, without contribution of tunneling processes. In periodic structures, such as superlattices or MQWs, however, the description of conduction mechanisms is more complex [133]. Due to the valence band discontinuity in periodic Mg-doped AlGaN/AlGaN structures, acceptors are more likely ionized in AlGaN:Mg barriers and free holes then are confined within the AlGaN:Mg wells. Compared to the bulk AlGaN:Mg alloy, the preferred Mg ionization in periodic structures results in an increased carrier density, and the spatial separation of [Mg^-] scattering centers and holes p results in an enhanced in-plane mobility [134]. Therefore, the in-plane resistivity of periodic structures can be increased by more than two orders of magnitude compared to the alloy, especially for

periodic structures with modulation doping [135]. Furthermore, polarization-induced band bending increases the total valence band edge variation. In conjunction with a constant Fermi level, this effect further enhances the free hole concentration [113]. The vertical conductivity in periodic structures, however, is limited by the barrier layers. For short-period superlattices, wave functions of each well are coupled and minibands are formed. For long-period MQW structures with thick barriers, an insignificant overlap of the individual wave functions prevents miniband formation. Vertical transport is then dominated by tunneling or thermally surmounting the barriers, limiting the vertical conductivity. Similar to the TLM analysis of AlGaN:Mg on ELO AlN/sapphire templates presented in Figure 4.5, the lateral resistivity of the structures discussed in this section is in the range 100 - 1000 Ωcm (measured at low external electric fields $< 0.1\,\mathrm{MV\,nm^{-1}}$). These values are much lower than the vertical resistivity evaluated at low fields. However, results from TLM measurements are not exactly comparable since lateral conduction is facilitated by both the AlGaN:Mg superlattice and the more conductive GaN:Mg cap layer. In the experimental IV measurements of UVC LEDs, hole injection might be not perfectly vertical but has an in-plane component resulting from different areas of p-contact metallization and etched mesa. Due to the complexity of modeling and experiment, a simplified experimental approach or more elaborated characterization (e. g., temperature dependent IV measurements) would be required for a conclusive interpretation of the field-dependent vertical conduction mechanisms in AlGaN:Mg-based periodic structures.

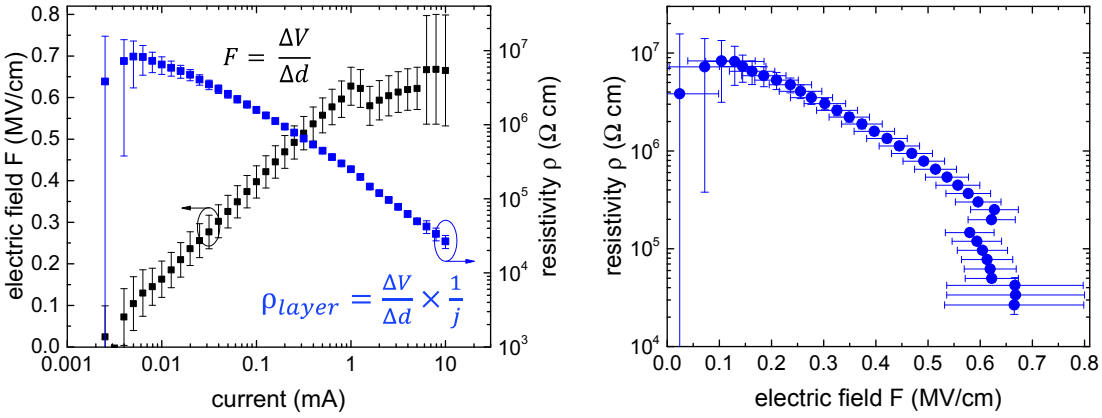

(a) (b)

Figure 4.17: (a) Evaluated electric field and vertical resistivity of Mg-doped $Al_{0.86}Ga_{0.14}N/Al_{0.66}Ga_{0.34}N$ SPSLs at different LED operation points (currents), (b) strong reduction of the vertical resistivity by two orders of magnitude with increasing external electric field from $0.1\,\mathrm{MV\,cm^{-1}}$ to $0.6\,\mathrm{MV\,cm^{-1}}$ [5].

This investigation illustrates the potential use of AlGaN:Mg SPSL p-cladding layers in UV laser diodes and indicates a field-induced ionization of Mg acceptors (Poole-Frenkel effect) supported by the measured AlGaN:Mg SPSL resistivity reduction in LED operation. The described method enables a determination of vertical resistivities even for highly resistive layers such as AlGaN:Mg SPSL with high aluminum content. Certain limitations of this method need to be considered. One of these is the assumed comparability of heterostructure and contact properties. Furthermore, current scattering at low currents,

heating at high currents, and scattering of properties between different samples can affect the accuracy of the evaluation, indicated by the error bars in Figure 4.17. However, even with these limitations considered, a significant trend of resistivity reduction in AlGaN:Mg SPSLs has been observed [5]. Parts of this investigation will be published by Muhin et. al. [136] in combination with temperature dependent IV measurements enabling a determination of the bulk ionization energy. In addition, advanced modeling considering proximity effects of overlapping Mg acceptor potentials as well as ionization probabilities for thermionic carrier emission in multiple directions with respect to the electric fields will be applied [137, 138]. The presented method for vertical resistivity determination enables systematic optimizations of the AlGaN:Mg superlattice resistivity that can be impacted by the SL periodicity, doping profile, or composition of the individual SL layers.

4.5 Summary

In this chapter, AlGaN-based UVC LED and LD structures have been investigated specifically focusing on heterostructures with transparent AlGaN:Mg SPSL layers in order to identify crucial components, to find best compromises for their parameters, and to go a further step towards current-injected edge-emitting UVC laser diodes. Therefore, parameters such as AlGaN composition or layer thickness of MQW, waveguide, or cladding layers have been investigated based on a combination of optical mode simulations and experimental analysis of MOVPE heterostructure growth and device performance. In a systematic variation of individual parameters, an optimal range was found as well as limitations for extreme ranges, based on the categorization introduced at the beginning of the chapter. One outstanding example is the thickness of AlGaN:Mg SPSL p-cladding layers that leads to decreasing modal losses in the p-side while maintaining an almost constant confinement factor and increasing UVC emission power with increasing thickness up to 200 nm. Here, an optimal cladding thickness near 200 nm was identified without detrimentally affecting modal absorption or carrier injection, which is the case for much lower or for much higher thickness, respectively. This is schematically summarized in Figure 4.18, showing the UVC LD heterostructure scheme (Figure 4.18a) as well as the results of the parameter variations of thickness and composition from this chapter 4 in combination with results discussed in chapter 2, chapter 3, and results from MOVPE-grown heterostructures published in Refs. [45, 66, 86, 119, 139] (Figure 4.18b).

For UVC LED operation with typical current densities near 100 A/cm^2, the developed transparent heterostructure scheme allows for sufficient current densities and high light extraction efficiency. As wave guiding is no requirement for UVC LEDs, the mode confinement limitation indicated by the green symbols in Figure 4.18b can be neglected. This opens up further optimization potentials regarding reduced operation voltages that can be realized by more conductive AlGaN:Si and AlGaN:Mg SPSL layers with reduced Al contents as long as the UV transparency is maintained.

For electrically injected UVC MQW laser diode operation, remaining challenges need to be addressed in addition to the demonstrated achievements. Optically pumped UVC lasing has been demonstrated from various AlGaN MQW heterostructures including threshold behavior of the emitted intensity and reduction of the spectral linewidth near

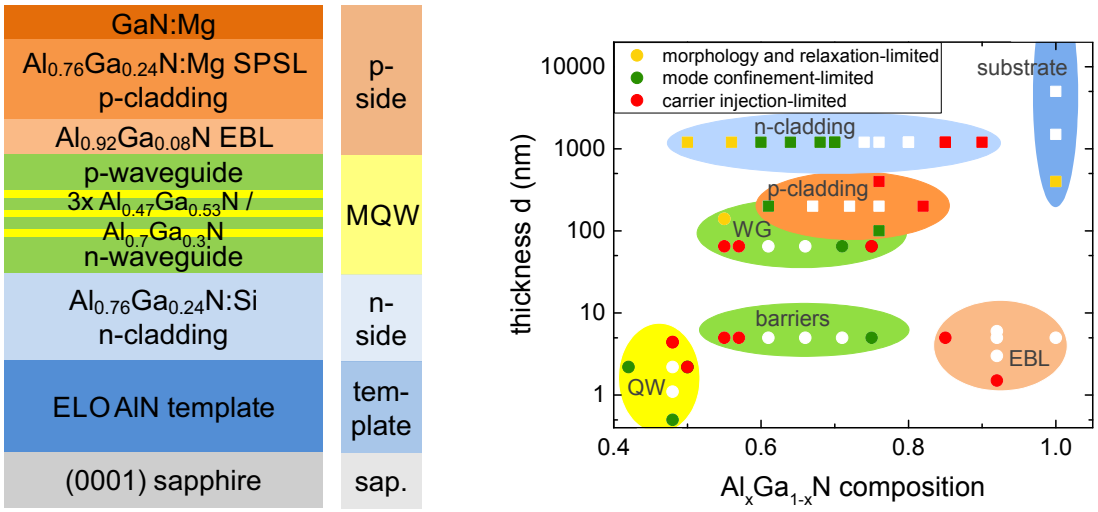

(a) (b)

Figure 4.18: UVC laser diode: (a) Heterostructure concept and (b) summarized experimental analyses and simulations of thickness and composition limitations for individual layers, discussed in chapter 2, chapter 3, chapter 4, and published in Refs. [45, 66, 86, 119, 139]. White points indicate parameters for efficient heterostructures which are not strongly affected by these limitations.

threshold in combination with dominant TE polarization above threshold power density, e. g., for lasers emitting at 270 nm. Pseudomorphic growth of laser heterostructures with smooth surface morphology has been obtained on ELO AlN/sapphire templates and bulk AlN substrates. For current-injected UVC devices, heterostructure variations of composition and thickness enabled the identification of optimized parameter ranges in order to maximize EQE and optical confinement. Also, AlGaN QW thickness, composition, and QW number, as well as waveguide doping have been investigated, as described in [86]. The concentration of point defects within the MQW or WG layers, such as carbon or vacancies, can be influenced by the choice of growth parameters [140]. This can be a promising option which may impact internal losses to further reduce the lasing threshold, as indicated in [99]. The maximum levels of current density need to be increased to values exceeding 10 kA/cm^2 [141]. Furthermore, optimizations of AlGaN:Mg layer resistivity and contact resistances can allow for decreasing operation voltages in combination with reduced Joule heating, performance degradation, and device failures in the high current density regime.

From the presented investigations it can be concluded that

(I) the MOVPE growth process of UVC LEDs and UVC LDs can be successfully transferred between different types of substrates, in this case from ELO AlN/sapphire templates to bulk AlN substrates. However, in order to obtain similar device performance, such as operation voltage or emission power, the MOVPE growth process needs to be adjusted and in case of bottom emitting LEDs the substrate absorption coefficient needs to be taken into account as well. The choice of substrate affects morphology and relaxation as well as carrier injection.

(II) obtaining efficient carrier injection in a broad wavelength range requires the consideration of multiple layers within UV LED heterostructures, such as MQW, EBL, and AlGaN:Mg SPSL p-side layers. Constantly high emission power levels of 4 mW at 60 mA with peak EQE = 1.75% were demonstrated for UVC LEDs emitting between 265 nm and 280 nm. For shorter emission wavelengths below 260 nm, carrier injection becomes more challenging. For longer emission wavelengths above 290 nm, plastic relaxation and defect generation start to increase.

(III) with UVC LD waveguide composition varying from $Al_{0.75}Ga_{0.25}N$ to $Al_{0.60}Ga_{0.40}N$ the confinement factor of the optical mode increases from 3.7% to 6.2% due to an increasing refractive index contrast to $Al_{0.80}Ga_{0.20}N$ cladding layers. However, the experimental emission power at a fixed current -and with it the external quantum efficiency- shows the opposite trend and rises with increasing WG aluminum content by a factor of 4 to a peak value near 70%. This requires a compromise of mode confinement and emission power for the heterostructure design of UVC laser diodes.

(IV) the composition of a 200 nm thick AlGaN:Mg SPSL p-cladding layer affects the confinement factor as well as the modal absorption losses in p-side layers such as p-cladding, GaN:Mg, and the p-contact metal. While high p-cladding aluminum contents are increasing confinement and reducing losses, a strong reduction of the emission power was observed for devices with very wide band gap $Al_{0.82}Ga_{0.18}N$:Mg p-cladding. From these investigations, the best compromise for the composition of AlGaN:Mg SPSL p-cladding layers in UVC LD heterostructures is fixed to $Al_{0.76}Ga_{0.24}N$.

(V) in combination with an $Al_{0.63}Ga_{0.37}N$ WG, the thickness of an $Al_{0.76}Ga_{0.24}N$:Mg SPSL p-cladding layer is barely affecting the confinement factor, but modal losses can be strongly reduced with increasing thickness. As peak emission powers were obtained for devices with 100 - 200 nm thick p-cladding layers, the best compromise is near 200 nm, providing high emission power as well as reasonably low modal losses of 40 cm^{-1} in the p-side layers.

(VI) the vertical resistivity of $Al_{0.76}Ga_{0.24}N$:Mg SPSL layers in UVC LD heterostructures is affected by external electric fields. With increasing electric field the vertical resistivity decreases by two orders of magnitude to values near 20000 Ωcm at 0.6 MV cm^{-1}. The applied method evaluating the operation voltage of UVC LEDs with different AlGaN:Mg SPSL thicknesses allows for the determination of vertical resistivities even for highly resistive layers. This enables systematic optimizations of the vertical AlGaN:Mg superlattice resistivity regarding the SL periodicity, doping profile, or composition of the individual layers.

5 AlGaN-based tunnel junctions enabling transparent UVC emitters

In this chapter, the development of MOVPE grown AlGaN-based tunnel junctions (TJs) for reverse bias tunneling is pursued, which enable fully transparent UVC LEDs with high EQE [142]. AlGaN-based tunnel junctions serve as an alternative concept for hole injection into the AlGaN MQW active region of deep UV LEDs in contrast to widely used conductive (but absorbing) GaN:Mg. For this concept, a tunnel heterojunction in reverse bias configuration is replacing the p-side of a UVC LED heterostructure, ideally providing a low resistive contact for hole injection via interband tunneling processes. After a description of the fundamentals of tunnel diodes and the current state-of-the-art of tunnel diodes in III-nitride optoelectronics, MOVPE growth experiments of test structures are conducted in order to determine optimal AlGaN composition as well as AlGaN:Si and AlGaN:Mg doping concentrations of individual components of tunnel junctions. These findings resulted in the successful realization of efficient UVC LEDs with AlGaN-based tunnel junctions.

5.1 Fundamentals and state-of-the-art of III-nitride tunnel junctions

5.1.1 Fundamentals of tunnel diodes

In 1957, Leo Esaki and his co-workers Yuriko Kurose and Takashi Suzuki investigated a germanium semiconductor pn homojunction with a band gap of 0.66 eV [143]. They reported acceptor concentrations of $1.6 \cdot 10^{19}$ cm^{-3} and donor concentrations in the range of 10^{19} cm^{-3} [144]. In 1958, Esaki published a "New Phenomenon in Narrow Germanium p-n Junctions" [145], which is considered the first experimental demonstration of semiconductor tunnel pn junctions. Esaki showed that for positive voltages above 0.3 V, any measured current-voltage curves can be approximated by the typical exponential diode characteristic (Equation 4.1) as expected for germanium pn junctions. For lower positive voltages, however, a maximum of the current was found at a voltage of 0.035 V, followed by a minimum, meaning a negative differential resistance $R_{diff} = \frac{dU}{dI} < 0$, and then the exponential increase, shown in Figure 5.1a from Ref. [145]. Additionally, in reverse bias direction the pn junction was found to be more conductive than in forward direction, independent of temperature. Hence, Esaki described the two general features of tunnel diodes that are different from regular pn diodes [146, 147].

In general, tunnel diodes are characterized by:

- Low resistance with zero voltage offset in backward direction
- Negative differential resistance (NDR) in forward direction

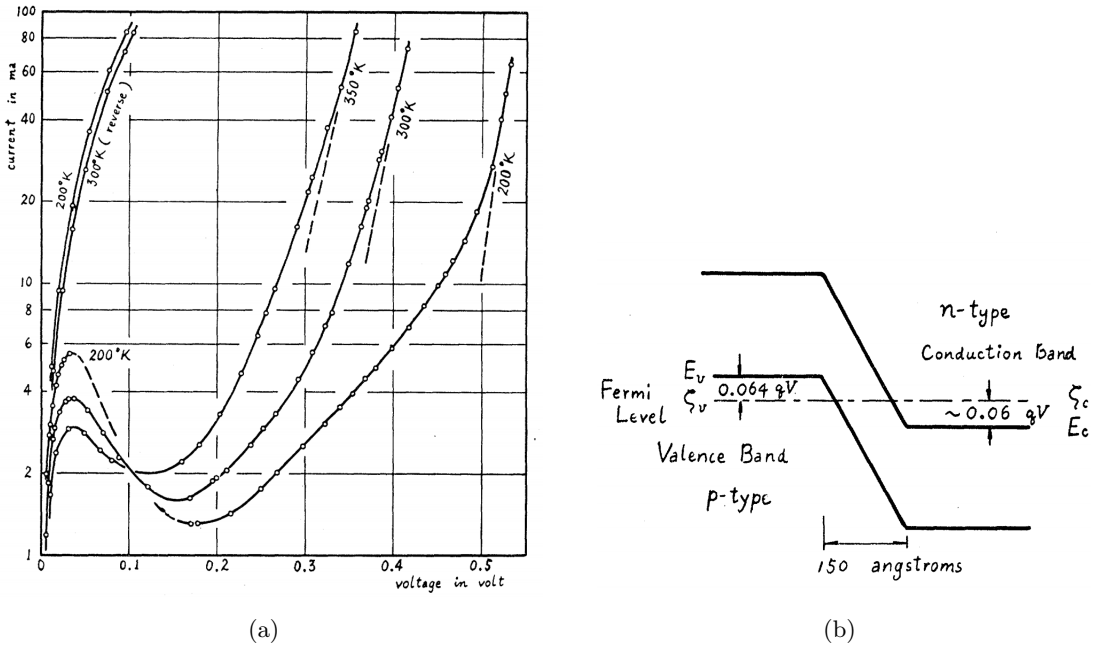

(a) (b)

Figure 5.1: (a) Current-voltage characteristics of a germanium pn junction considered as first experimental report on semiconductor tunnel junctions. Such reverse bias characteristics are exploited for carrier injection in TJ-LEDs. (b) Esaki's basic band structure model suggestion, figures reprinted with permission from [145]. Copyright (2019) by the American Physical Society.

Furthermore, Esaki proposed a basic band diagram model, shown for zero bias in Figure 5.1b, in order to explain the conduction mechanisms by tunneling processes in forward and reverse direction of the tunnel junction [145]. Honoring this pioneering work, Leo Esaki and Ivar Giaever were jointly awarded the Nobel prize in Physics 1973 "for their experimental discoveries regarding tunneling phenomena in semiconductors and superconductors, respectively", together with Brian David Josephson "for his theoretical predictions of the properties of a supercurrent through a tunnel barrier, in particular those phenomena which are generally known as the Josephson effects" [148], and textbooks are referring to Esaki's findings as the first experimental demonstration of semiconductor tunnel diodes (Esaki diodes).

In regular pn junction diodes, the current-voltage correlation can be described by the Shockley diode equation which includes forward conduction by thermal current, a very low saturation current at reverse bias, and breakdown at high reverse voltages (Equation 4.1). Such rectifying pn diode characteristic is schematically shown in Figure 5.2. In contrast, the IV curves of tunnel diodes are more complex and can be segmented in four operation regimes (see Figure 5.2).

1. Reverse current region with low resistance and zero voltage offset
2. Forward tunneling current at low voltages
3. Negative differential resistance region
4. Forward conduction approaching pn junction diode characteristic

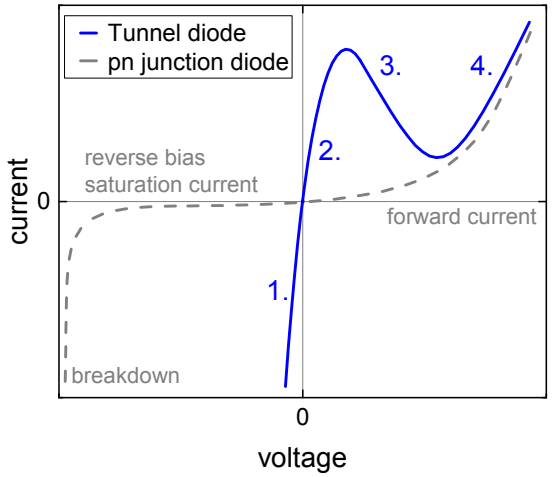

Figure 5.2: Schematic current-voltage correlation of tunnel diodes showing the characteristic regions of low resistance backward conduction with zero voltage offset (1.) and negative differential resistance (3.), compared to a pn junction diode.

In the non-equilibrium case of negative bias voltage, tunneling processes of valence band electrons from the p-type semiconductor into the conduction band of the n-type semiconductor are occurring, generating a reverse current with zero voltage offset and low resistance (Region 1. reverse bias tunneling). Ideally, elastic tunneling processes are obeying the rule of energy conservation. At zero bias voltage (Figure 5.3, equilibrium case), tunneling probabilities are equal in both directions resulting in zero net current. Low positive bias voltages, however, are allowing for similar tunneling processes in opposite direction (Region 2. forward bias tunneling). With further voltage increase, electron states are becoming increasingly misaligned with hole states and tunneling current decreases (Region 3. negative differential resistance). Due to an excess current by inelastic tunneling processes, the minimum current is larger than zero. For higher voltages, conduction is dominated by thermal diffusion of charge carriers and current is approaching the pn diode current (Region 4. forward conduction).

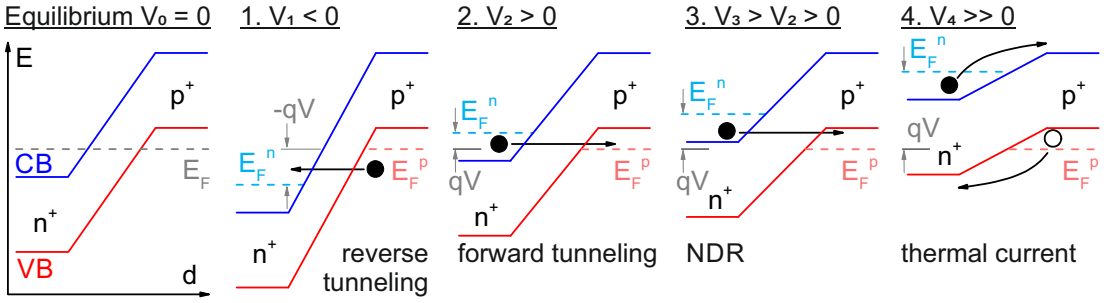

Figure 5.3: Schematic band structure of tunnel diodes in the case of thermal equilibrium, negative bias voltage, and different positive bias voltages.

Such IV characteristics may directly translate into device applications of tunnel diodes exploiting the NDR characteristic in forward direction or the low resistance in backward direction. For example, backward diodes are a special case of tunnel diodes operated in reverse bias configuration that can be used for rectification of small signals [149]. In regular tunnel diodes the low resistance in reverse direction enables highly conductive carrier injection into semiconductor devices such as (UV) LEDs [147], which is the application case investigated within the following sections of this chapter.

Key element of tunnel diodes is a very thin space charge region (SCR) with thickness near 10 nm or even below, depending on materials and device design [149]. As the space charge region of a pn junction acts as tunnel barrier, the quantum mechanical tunneling effect becomes increasingly dominant for very thin space charge regions. The width of such a space charge region, however, strongly depends on the acceptor and donor concentration in the p-type and n-type layers of the tunnel junction, respectively. The barrier height is influenced by the band gap of the semiconductor tunnel junction.

Quantum mechanical tunneling processes of carriers with potential energy E through a barrier can be described with the tunneling probability T that depends on the shape of the potential barrier V(x) including the barrier thickness as well as the effective mass (Equation 5.1) [149]. Here, the WKB-approximation -named after Wentzel, Kramers, and Brillouin- is applied that assumes a slowly varying potential barrier. For a triangular potential barrier, the tunneling probability can be approximated by Equation 5.2.

$$T = exp\left(-2\int_0^d |k(x)|\,dx\right), \qquad \text{with } k^2(x) = \frac{2m^*\left[E - V(x)\right]}{\hbar^2} \tag{5.1}$$

$$T(E_g, d_{SCR}) \approx exp\left(-\frac{4}{3}\sqrt{\frac{2m^*E_g}{\hbar^2}} \cdot d_{SCR}\right) \tag{5.2}$$

Pursuing the idea of utilizing tunnel diodes in backward configuration for hole injection into UV LEDs, the analytical description of carrier tunneling in an (In,Al,Ga)N tunnel junction LED would be much more complex as multiple semiconductor layers with different band gap, thickness, and doping levels as well as polarization fields are involved. Compared to a triangular barrier, this may result in a more complex shape of the real potential barrier which is not necessarily exactly known or accessible, but may strongly influence the width of the space charge region and decisively the tunneling probabilities. However, tunneling probabilities will mostly depend on two fundamental parameters of this type of tunnel junction: The band gap E_g that is determined by the composition of the nitride tunnel diode having a moderate square root influence, as well as strong impact of the space charge region thickness d_{SCR}.

5.1.2 Application of reverse biased III-nitride tunnel junctions in LEDs

One challenge in III-nitride based LEDs is the p-type doping of GaN or AlGaN layers by magnesium acceptors. Even for gallium nitride, the conductivity of GaN:Mg is much lower compared to GaN:Si. Due to increasing Mg acceptor ionization energies, achieving sufficient conductivity of AlGaN:Mg layers and its accurate determination becomes even more challenging with increasing aluminum mole fraction, as summarized in chapter 4. Furthermore, no ohmic contacts to AlGaN:Mg have been realized so far due to the large work function mismatch between available metals and the high electron affinity of p-type III-nitrides. Employing tunnel junctions in reverse bias configuration, the highly resistive p-doped layers can be replaced by more conductive n-doped layers, and rectifying p-contacts can be replaced by ohmic n-contacts. Hence, contact fabrication will be simplified as only n-contacts are required. This concept has been applied to III-nitride based LEDs emitting in the visible and UV spectral

range. In literature, visible LEDs and LDs with tunnel junctions grown or regrown by molecular beam epitaxy (MBE) have been investigated by several groups [150–154]. In contrast to MOVPE growth, the MBE approach can be advantageous to achieve very abrupt doping profiles, e. g., at a tunnel junction interface. Also less problems with Mg doping can be expected with MBE, e. g., regarding acceptor activation, Mg diffusion, or Mg concentrations exceeding $10^{20}\,\mathrm{cm}^{-3}$ [155, 156]. However, MOVPE growth of tunnel junction LEDs is an interesting option, as TJ-LEDs could be grown in a single MOVPE growth step without the necessity of a two step growth or reactor change like in a hybrid approach combining TJs grown by MBE with LEDs and templates grown by MOVPE. Once developed, TJ-LED growth by MOVPE is a scalable process that can be interesting for potential industrial LED fabrication [46].

In GaN-based tunnel diodes, the following approaches have been investigated to reduce the TJ space charge region width in order to obtain high tunnel currents.

- Heavily doped tunnel homojunction
- Polarization-induced tunnel heterojunction

MOVPE-grown tunnel junction LEDs using 20 - 30 nm wide GaN/GaN tunnel junctions with very high doping concentrations ($> 1\cdot 10^{20}$ cm^{-3}) at the GaN:Mg^{++}/GaN:Si^{++} or GaN:Mg^{++}/GaN:Ge^{++} interface have been successfully demonstrated (tunnel homojunction) [157–159]. Such high doping concentrations can result in degenerate semiconductor layers for n-type GaN [160], but may cause severe structural degradation of the respective layers as well as subsequently grown layers.

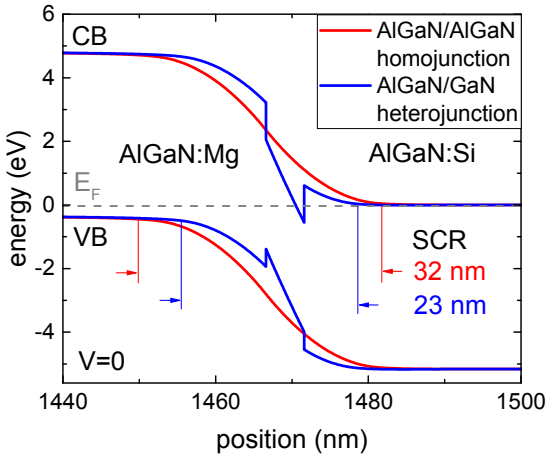

Figure 5.4: Reduction of the space charge region (SCR) width of an AlGaN/GaN tunnel heterojunction in comparison to a AlGaN/AlGaN homojunction with 75% Al, illustrated by a band structure simulation using doping concentrations of $[\mathrm{Si}] = [\mathrm{Mg}] = 1 \cdot 10^{19}\mathrm{cm}^{-3}$. (Simulations by Martin Guttmann - TU Berlin)

One alternative option to achieve functional TJ-LEDs with non-degenerate interface doping is the implementation of a nanometer-thin interlayer with lower band gap (tunnel heterojunction) [161]. As shown in Figure 5.4, due to the generation of polarization charges at the interfaces of a tunnel heterojunction, the SCR width of the junction can be reduced, leading to thinner tunnel barriers and ideally enhancing tunnel probabilities. In this case, doping concentrations $< 1\cdot 10^{20}$ cm^{-3} at the TJ interface can enable sufficient tunnel probabilities, which is beneficial to prevent structural damage of the interlayer and to preserve a high crystal quality of subsequently grown layers. Additionally, device performance can be influenced by polarization engineering due to a more flexible heterostructure design. However, as polarization fields are required, polarization-induced

tunnel heterojunctions are restricted to polar crystal planes (e. g., c-plane in nitride semiconductors) and cannot be applied to non-polar crystal planes or semi-polar planes with low polarization. Certain disadvantages could arise from parasitic absorption of low band gap interlayers or from plastic relaxation due to large misfit of lattice constants.

In the InGaN/GaN material system, LEDs with MOVPE-grown tunnel heterojunctions using an InGaN interlayer between GaN:Mg and GaN:Si were reported [162–165]. In the AlGaN material system, however, reduced tunneling probabilities are expected due to the wide band gap especially for $Al_xGa_{1-x}N$ with high aluminum mole fraction $x > 0.6$ [147]. However, AlGaN-based UV LEDs with MBE-grown tunnel heterojunctions combined with MOVPE-grown AlGaN:Si templates have already been reported [166–168]. This proves the general applicability to the concept of TJ-LEDs in the AlGaN material system. Furthermore, simulations of tunneling probabilities indicate that sufficient levels of tunnel currents can be achieved in such AlGaN-based TJ-LEDs, if the TJ layer properties such as layer thicknesses, graded or non-graded AlGaN compositions and doping profiles are carefully adjusted [169, 170]. In this work, the realization of UVC LEDs with the first MOVPE-grown AlGaN-based tunnel junction as well as the first AlGaN-based tunnel homojunction will be presented, which was reported in Ref. [142]. This may pave the way for the development of high power UVC LEDs with tunnel junctions completely grown by MOVPE, which is the method of choice for a potential low-cost and industry-applicable growth process implementation.

Regarding future perspectives, with a fully developed MOVPE process for the growth of AlGaN-based tunnel junctions, even more advanced applications beyond UVC LEDs are open to be explored: UV laser diodes with lateral current injection via buried TJs as reported for InGaN LDs [171], or cascaded UV LEDs or LDs with multiple active regions connected via TJs [87, 172] that may enable EQE > 1 due to multiple photons generated by multiple interband transitions of one single injected electron-hole pair. This can be interesting for very small and powerful devices with high photon densities exploiting a power enhancement by voltage scaling instead of current scaling [147]. Since 2019, publications from companies are indicating efforts to pursue a commercialization of the TJ technology, e. g., GaN-based TJ-LEDs for blue light emission aiming for cascaded LEDs in order to compensate the efficiency droop at high currents [173, 174].

5.2 UVC LED heterostructure with tunnel junction

One possible heterostructure design for the growth of TJ-LEDs is shown in Figure 5.5a. Key findings from the investigation of AlGaN:Mg SPSLs with high aluminum mole fraction described in the previous chapter have been implemented. The heterostructure consists of a c-oriented sapphire substrate with 0.1° offcut, 5 µm ELO AlN buffer layer with transition to the 1200 nm thick $Al_{0.75}Ga_{0.25}N$:Si bottom current spreading layer, AlGaN-based MQW active region designed for emission between 260 nm and 280 nm, 5 nm $Al_{0.85}Ga_{0.15}N$ electron blocking layer as well as 100 nm transparent AlGaN:Mg SPSL with average aluminum mole fraction of 75%. The tunnel heterojunction under investigation consists of a 10 - 20 nm transparent AlGaN:Mg^{++} SPSL, a low band gap interlayer, 15 nm transparent AlGaN:Si^{++} as well as 200 - 300 nm transparent AlGaN:Si top current spreading layer.

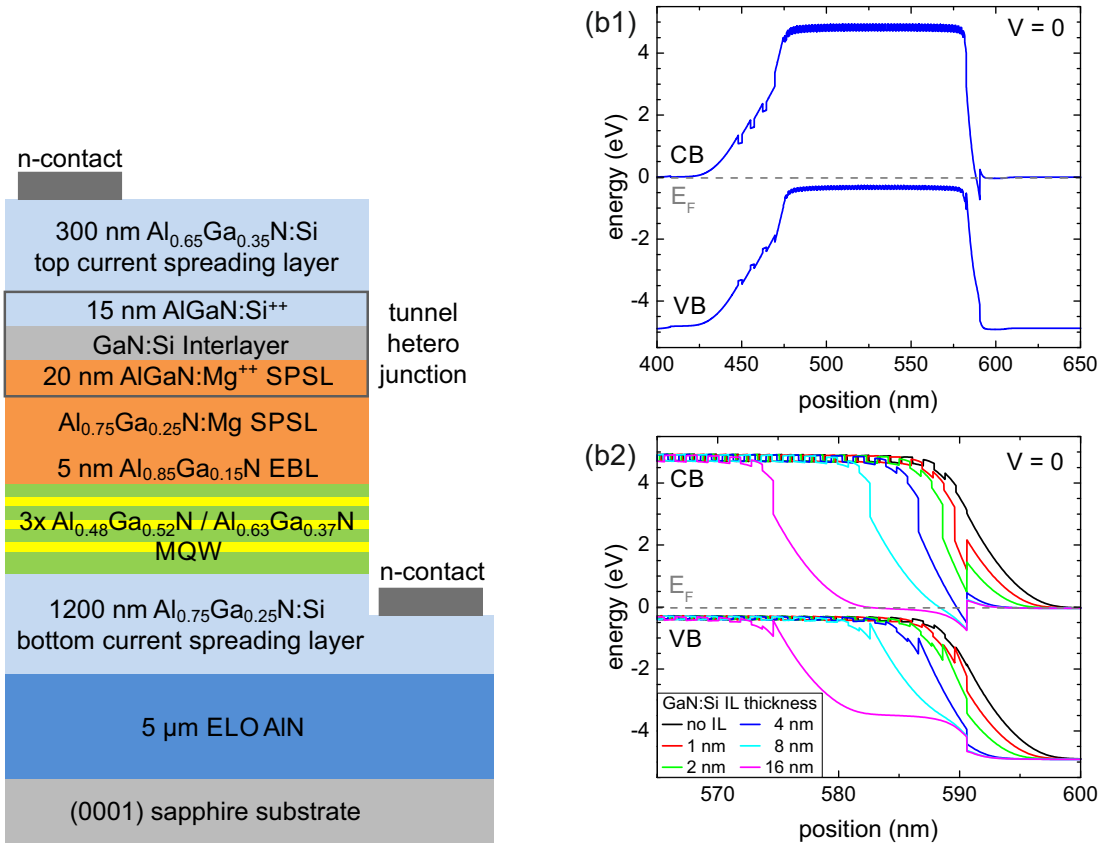

Figure 5.5: (a) Heterostructure concept of a UVC LED with tunnel junction and (b1) band structure simulation of the complete LED under thermodynamic equilibrium conditions (0 V bias voltage) as well as (b2) the tunnel heterojunction part with varied thickness of the low band gap interlayer. [142] (Simulations by Martin Guttmann - TU Berlin)

In Figure 5.5b, a band structure simulation of TJ-LEDs with the described heterostructure is shown for thermodynamic equilibrium. The two diodes (pn-junction of the LED as well as pn-junction of the tunnel heterojunction) are placed in back-to-back configuration, in this case at zero bias voltage (0 V). In the case of positive bias voltage (with respect to the pn-junction of the LED), electrons are injected from the bottom n-contact through the bottom AlGaN:Si current spreading layer into the MQW active region, whereas the tunnel heterojunction facilitates the injection of holes. In detail, the applied bias voltage causes electron drift in the conduction band of the top AlGaN:Si current spreading layer towards the top n-contact, which lowers the conduction band edge of the top AlGaN:Si in relation to the AlGaN:Mg SPSL. Polarization charges at the interfaces of the low band gap interlayer generate a very thin space charge region at the tunnel heterojunction (Figure 5.5b2). The resulting band alignment enables interband tunneling processes of electrons from the AlGaN:Mg SPSL valence band into the top AlGaN:Si conduction band that generate free holes inside the AlGaN:Mg SPSL. Such free holes can drift into the active region and eventually recombine in the MQW.

In order to increase tunnel probabilities by means of low band gap interlayers, a large band gap difference between the nanometer-thin TJ-interlayer and the AlGaN matrix is required in order to maximize polarization-induced charges. A further strategy to favor tunneling is a high doping concentration of the AlGaN:Mg^{++} and the AlGaN:Si^{++} layers, however, high structural quality of those layers should be preserved as relaxation and excess doping may lead to detrimental crystal damage. To match these requirements, dedicated growth experiments were executed and are summarized in the following section.

5.3 Optimization of individual components of AlGaN-based tunnel junctions

In the first experiments, four components of the tunnel heterojunction were systematically investigated in order to evaluate crucial components and their associated parameter windows. In the following subsections, the growth of the top AlGaN:Si current spreading layer at low temperatures, the AlGaN:Si^{++} doping concentration, the (Al)GaN interlayer composition as well as the doping concentration of the AlGaN:Mg^{++} layer are outlined and the results discussed.

5.3.1 Low resistivity AlGaN:Si grown at reduced temperature

In the UVC LEDs described in the previous chapter, the $Al_{0.75}Ga_{0.25}N$:Si bottom current spreading layer is typically grown at a pyrometrically measured susceptor temperature of 1080 °C. In TJ-LEDs, however, the top AlGaN:Si current spreading layer is grown after the low band gap interlayer, which is composed of GaN or gallium-rich AlGaN and requires lower growth temperatures (e. g. 960 °C) to avoid gallium desorption. One possibility is to afterward overgrow with AlGaN:Si at reduced temperatures. However, changes in growth temperature can influence the incorporation of compensating defects and thus affect the AlGaN:Si resistivity [175, 176]. Other approaches could include an AlGaN:Si cap layer grown at low temperatures combined with an AlGaN:Si layer grown at high temperature conditions. This strategy is typically implemented in the growth of heterostructures with two or more components requiring strongly different growth temperatures, e. g. GaN quantum dots (QD) in AlN matrix [177, 178], or InGaN/AlGaN interfaces in blue LDs [179, 180].

In order to exclude strong AlGaN:Si donor compensating effects at low temperatures, $Al_{0.75}Ga_{0.25}N$:Si layers with standard silicon concentration ($[Si] = 4 \cdot 10^{18}$ cm^{-3}) were grown at 960 °C and analyzed by contactless resistance measurements. Compared to the resistivity $\rho = 0.026$ Ωcm of standard $Al_{0.75}Ga_{0.25}N$:Si grown at 1080 °C, the resistivity of $Al_{0.75}Ga_{0.25}N$:Si grown at 960 °C is only slightly higher (i. e. $\rho = 0.037$ Ωcm), suggesting no detrimental compensation effects at lower growth temperatures.

5.3.2 AlGaN:Si with very high silicon concentrations

In order to obtain a narrow tunnel barrier at the heterojunction, the thickness of the space charge region within the AlGaN:Si^{++} layer needs to be very thin. This can

be achieved by very high donor concentrations provided by high silicon doping levels. However, excess doping can cause self compensation effects reducing the total donor concentration. This results in an upper limit for the silicon doping level, especially in wide band gap III-nitride semiconductors [181]. Furthermore, silicon doping induces tensile stress in AlGaN layers due to the interaction with threading dislocations [182–184]. In the case of excess doping (i. e. $[Si] > 1 \cdot 10^{20}$ cm^{-3}), this can lead to the formation of large defects such as pits or cracks at the surface of AlGaN:Si layers [185].

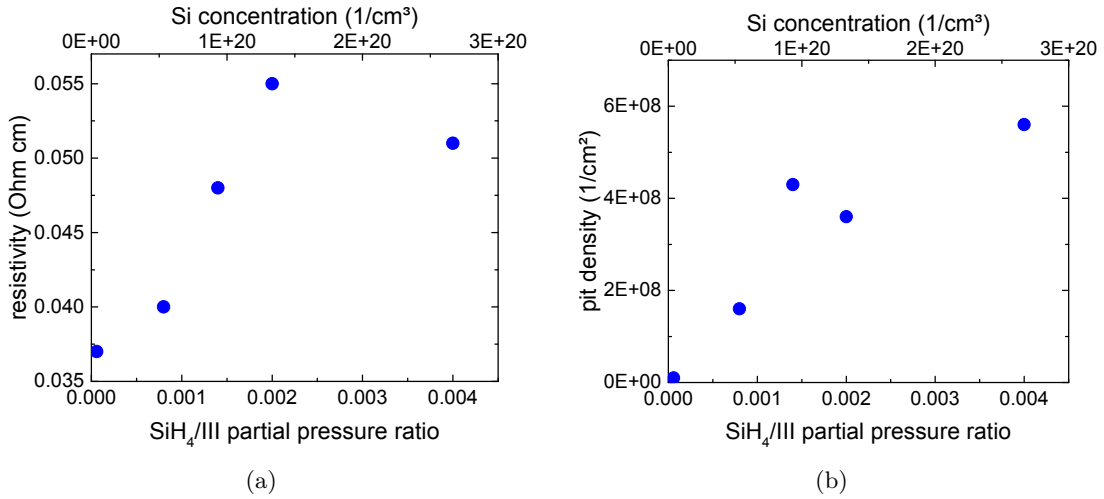

Figure 5.6: (a) Resistivity and (b) pit density of AlGaN:Si layers grown at 960 °C in dependence of AlGaN:Si^{++} doping level and SiH_4/III partial pressure ratio.

In order to find a balanced parameter range for the highest possible doping level without structural or electrical damage, AlGaN:Si test structures with different silicon doping concentration were grown. The test structures are designed close to a simplified TJ heterostructure, i. e. 15 nm thick $Al_{0.75}Ga_{0.25}N$:Si layers with silicon concentrations between $[Si] = 4 \cdot 10^{18}$ cm^{-3} and $[Si] = 4 \cdot 10^{20}$ cm^{-3}, as well as a 200 nm thick $Al_{0.75}Ga_{0.25}N$:Si layer with standard doping level of $[Si] = 4 \cdot 10^{18}$ cm^{-3}. The silicon concentration was adjusted by the partial pressure ratio SiH_4/III within the gas phase and calibrated by secondary ion mass spectrometry (SIMS) on thick AlGaN:Si layers. After growth, the test structures were analyzed by contactless resistance measurements in order to evaluate the influence of potential compensating effects on the resistivity. Additionally, the surface morphology was studied on different length scales using atomic force microscopy and optical microscopy. Finally, XRD reciprocal space maps of the samples were performed: no indication of different strain state was found. Figure 5.6 shows the integrated resistivity of the test structures as well as the evaluated surface pit density as a function of the SiH_4/III ratio and the calibrated silicon concentration. For low and medium silicon concentrations (i. e. $[Si] \leq 5 \cdot 10^{19}$ cm^{-3}), low integrated resistivities (0.037 - 0.040 Ωcm, Figure 5.6a) and low pit densities ($<1.8 \cdot 10^8$ cm^{-2}, Figure 5.6b) were measured. In contrast, for high silicon concentration $[Si] > 1 \cdot 10^{20}$ cm^{-3}, the resistivity (> 0.05 Ωcm) as well as the pit density ($>3.5 \cdot 10^8$ cm^{-2}) are strongly increasing. Clearly, the silicon concentration in the 15 nm thin AlGaN:Si^{++} layer strongly affects the electrical and structural properties of the subsequent AlGaN:Si layer. Hence, an optimized silicon concentration of $[Si] = 5 \cdot 10^{19}$ cm^{-3} (adjusted by SiH_4/III = 0.0008)

provides high AlGaN:Si^{++} donor concentration combined with a structurally intact and electrically conductive AlGaN:Si current spreading layer.

5.3.3 Pseudomorphic (Al)GaN interlayers for tunnel heterojunctions

In order to realize strong polarization charges at the TJ interface by a large difference in band gap between the nanometer-thin TJ interlayer and the surrounding AlGaN layers, an interlayer composed of GaN or AlGaN with low aluminum mole fraction is required. In this case, strong compressive strain is induced by a large mismatch of the lateral a-lattice constants with strain up to $\varepsilon = 2.4\%$ for GaN, which can cause potentially detrimental relaxation processes similar to the discussion in section 3.3. In order to avoid such relaxation and to realize pseudomorphic interlayers, a critical layer thickness has to be considered which mainly depends on the composition of the interlayer. Therefore, in this experiment, the $Al_xGa_{1-x}N$ composition x of the interlayer was varied between $x = 0$ and $x = 0.3$ for a constant thickness of 3 nm. The strain state is determined by XRD reciprocal space maps of the asymmetric (10.5) reflection.

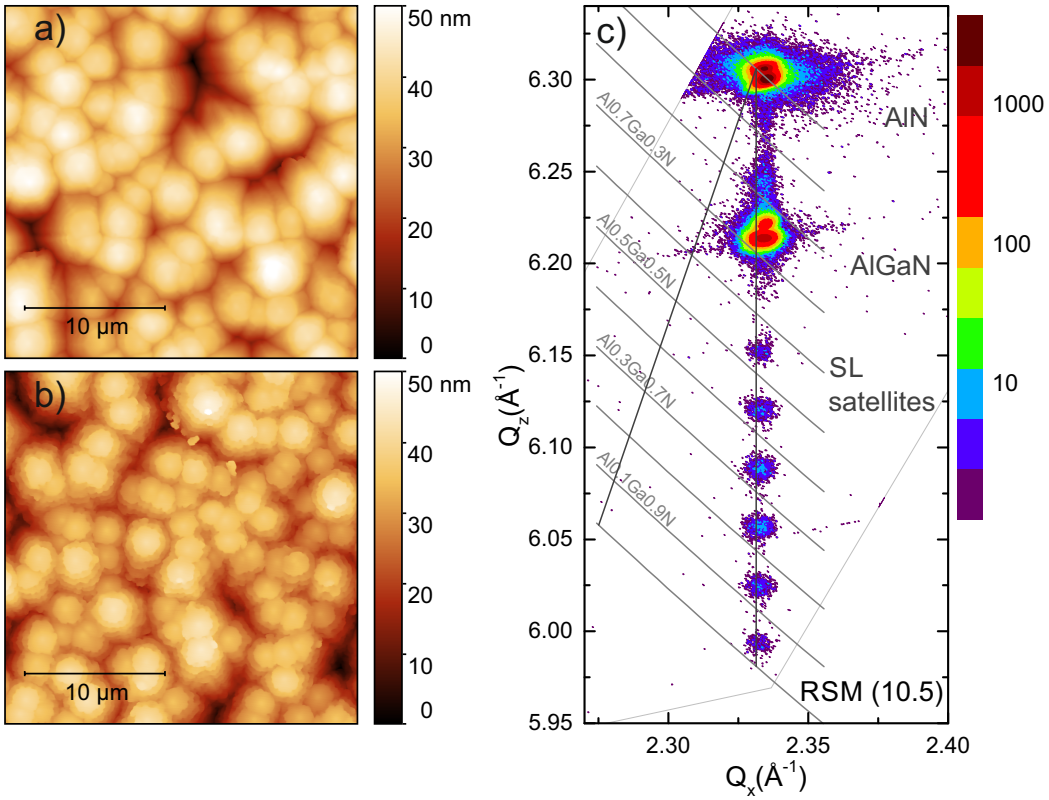

Figure 5.7: AFM images and XRD RSM of 5-period $Al_xGa_{1-x}N/Al_{0.75}Ga_{0.25}N$ superlattice stacks exhibiting stable surfaces for various compositions within the range between (a) $x = 0.3$ and (b) $x = 0$ as well as (c) pseudomorphic superlattice stack even for $x = 0$, i. e. GaN layers.

The growth of a 5-period superlattice stack composed of 3 nm $Al_xGa_{1-x}N$ and 15 nm $Al_{0.75}Ga_{0.25}N$ on 1200 nm $Al_{0.75}Ga_{0.25}N$:Si was chosen, as one single 3 nm thick layer could not provide sufficient interaction volume to obtain a reliable X-ray diffraction signal. AFM images of all samples with composition between $x = 0$ and $x = 0.3$

exhibit similar surfaces without any indication for a transition from two-dimensional to three-dimensional growth. The surfaces, shown in Figure 5.7a and Figure 5.7b, are mainly influenced by the spiral growth occurring in the thick AlGaN:Si layer. In Figure 5.7c, the XRD RSM near the (10.5) AlN reflection of the sample with $GaN/Al_{0.75}Ga_{0.25}N$ is shown and exhibits multiple satellite reflections originating from the 5-period GaN/AlGaN superlattice stack, next to the reflections from the AlN and the $Al_{0.75}Ga_{0.25}N$:Si layers. All reflections are located on a vertical line at the same Q_x position, indicating pseudomorphic growth of the entire GaN-containing superlattice stack. The large number and intensity of the satellite reflections attest the homogeneity and high layer quality as well as the accurate periodicity of 18 nm ± 1 nm. Next to GaN interlayers, also $Al_xGa_{1-x}N$ interlayers with low aluminum mole fraction are allowing for pseudomorphic superlattices, which was confirmed by reciprocal space maps of such layer stacks with $x = 0.1$, $x = 0.2$, and $x = 0.3$. As a result of this investigation, high structural quality of a 3 nm thin GaN or $Al_xGa_{1-x}N$ interlayer can be obtained by pseudomorphic growth within the range of $x \leq 0.3$ for the growth of a tunnel heterojunction LED.

5.3.4 AlGaN:Mg with very high magnesium concentrations

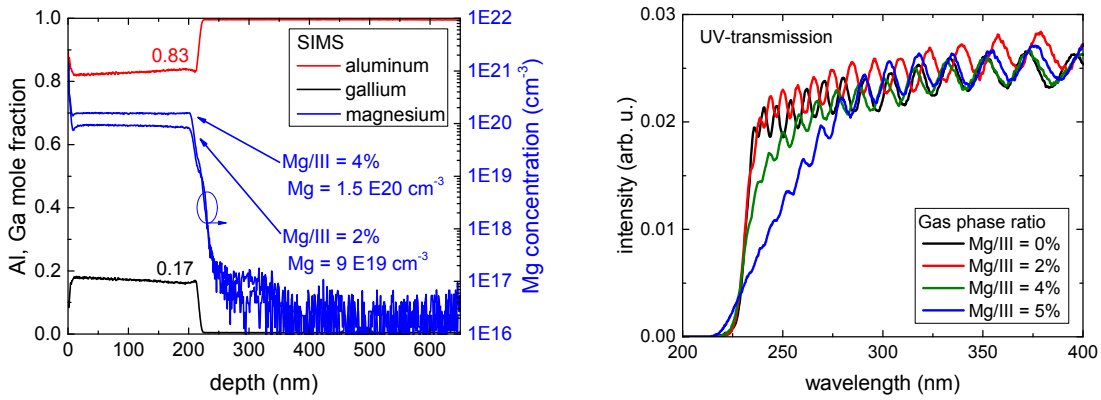

(a) (b)

Figure 5.8: (a) SIMS of the Mg concentration in 200 nm thick AlGaN:Mg^{++} SPSL layers. (b) Impact of varied Mg doping on the UV transparency of AlGaN:Mg^{++} SPSL.

In analogy to the previously described doping of the AlGaN:Si^{++} layer, a high acceptor concentration realized by substitutionally incorporated Mg at the tunnel heterojunction interface is required in order to enable a thin space charge region within the AlGaN:Mg^{++} layer. In this experiment, the magnesium doping concentration in the AlGaN:Mg SPSL was varied between zero (unintentionally doped) and $[Mg] = 2 \cdot 10^{20}$ cm^{-3} by changing the Mg/III partial pressure ratio of biscyclopentadienyl-magnesium and group-III precursors in the gas phase between 0% and 5%. The Mg concentrations are calibrated by SIMS data as shown in Figure 5.8a. An AlGaN:Mg layer thickness of 200 nm was chosen in order to obtain a stable Mg level. In contrast, for nanometer-thin AlGaN:Mg layers Mg incorporation could be influenced by a delayed turn-on or decay (memory effect) [186, 187]. Furthermore, due to a limited depth resolution of SIMS measurements, thicker

layers are more reliable in order to determine impurity concentrations in comparison to nanometer-thin AlGaN:Mg layers. In UV transmission spectroscopy measurements, a sharp absorption edge at 230 nm was obtained with AlGaN SPSLs with an average aluminum content of 80% without magnesium doping (Figure 5.8b). In this case and for Mg/III = 2%, the shape of the absorption edge is mainly determined by alloy broadening of the AlGaN compound semiconductor. In the case of heavy doping (i. e. Mg/III = 4% or higher), the samples exhibit strong Mg-induced sub band gap absorption between 230 nm and 270 nm. This might be due to excess doping introducing extended crystal defects. Symmetric XRD rocking curves of the unintentionally doped AlGaN SPSL sample show diffraction peaks for AlN and AlGaN as well as multiple and intense fringe oscillations indicating high structural quality and abrupt interfaces (Figure 5.9a). At lower angles near 15.6°, the first order satellite peak of the superlattice is visible, which is an indication of excellent superlattice periodicity. AFM images of this unintentionally doped sample exhibit smooth morphologies with AlGaN monolayer steps (Figure 5.9b). For the heavily doped AlGaN:Mg SPSL sample (i. e. Mg/III = 4%, $[Mg] = 1.5 \cdot 10^{20}\,cm^{-3}$), however, AFM images show high densities of V-pits on the surface. Taking into account the strong damping of fringe oscillations and the absence of a satellite peak, it becomes clear that the superlattice periodicity is damaged due to excess doping. Moreover, these results show a deterioration of the AlGaN:Mg^{++} crystal quality in case of excess doping (i. e. Mg/III = 4%, $[Mg] = 1.5 \cdot 10^{20}\,cm^{-3}$ or higher). As best compromise, a doping level of $[Mg] = 9 \cdot 10^{19}\,cm^{-3}$ (adjusted by Mg/III = 2%) was selected for the AlGaN:Mg^{++} layer growth within TJ-LED structures, thus ensuring best UV transparency combined with smooth morphology and accurate superlattice periodicity.

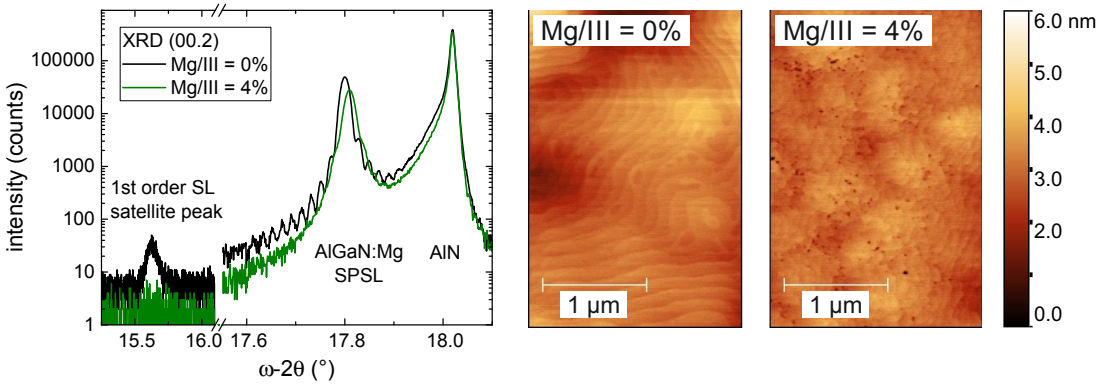

(a) (b)

Figure 5.9: (a) Impact of varied magnesium doping in 200 nm thick AlGaN:Mg^{++} SPSL layers on the structural quality determined by XRD and (b) on the surface morphology measured by AFM.

5.4 First demonstration of UVC emission from AlGaN-based tunnel homojunction LEDs

In this section, MOVPE growth and electroluminescence characterization of the first TJ-LED structures containing a transparent UVC LED and a tunnel junction in reverse

bias configuration are described. In order to fix a set of conditions for the first samples, the results of the pre-experiments described in section 5.3 have been implemented (e. g. AlGaN:Mg^{++} and AlGaN:Si^{++} doping concentration) in combination with information (e. g. the TJ thickness) derived from literature reports on TJ-LEDs emitting in the blue spectral range or from MBE-grown TJ-LEDs emitting in the UV spectral range, reviewed in subsection 5.1.2. After TJ-LED heterostructure growth, LED devices have been fabricated on-wafer with different mesa geometries. Metal electrodes were deposited on the top and bottom AlGaN:Si current spreading layers to form n-contacts with a V/Al/Ni/Au metallization scheme.

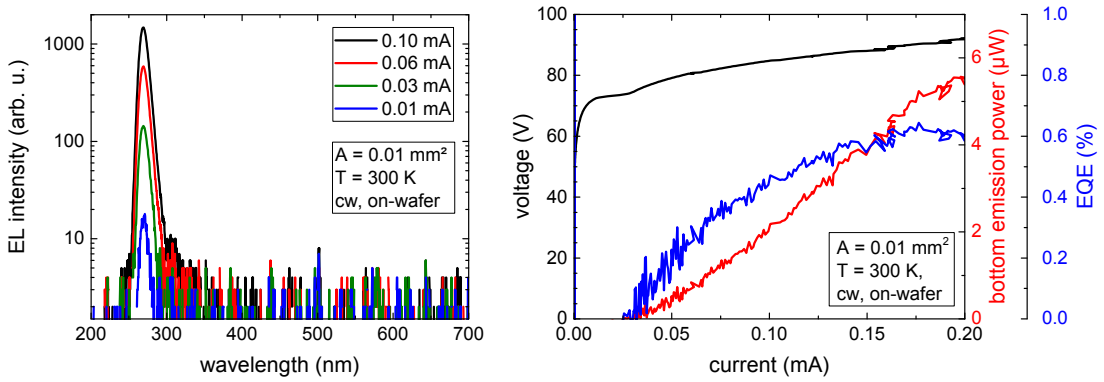

(a) (b)

Figure 5.10: Electroluminescence characteristics of the first UVC LED with AlGaN tunnel homojunction: (a) Emission spectra and (b) LIV-characteristics.

In Figure 5.10, the EL characteristics of a TJ-LED device without interlayer is shown (tunnel homojunction). The measured spectra exhibit single peak UVC emission near 270 nm without strong parasitic luminescence (Figure 5.10a). Although only very low currents (≤ 1 mA) could be injected at very high voltages (≥ 60 V), light emission was possible and an emission power of 5.5 µW was measured at 0.2 mA, as shown in Figure 5.10b. This emission power corresponds to an EQE of 0.6% reached at 0.2 mA, which is in the same order of magnitude as UVC LEDs with transparent AlGaN:Mg SPSL without tunnel junctions, described in chapter 4. This efficiency level indicates that the tunnel homojunction is not a detrimental factor strongly reducing the carrier injection efficiency of the device, despite the entirely different hole injection mechanism. Also, the radiative recombination within the MQW region does not seem to be influenced to a large extent, as the emission spectra are comparable to those of UVC LEDs without TJ. Nevertheless, the TJ strongly affects the operation voltage. The extremely high device resistance is mainly due to the non-optimized tunnel junction, injecting carriers by a combination of direct tunneling and field-assisted tunneling via defect states. These measurements represent the first experimental demonstration of an AlGaN/AlGaN tunnel homojunction in operation. However, the device performance leaves great room for improvement that will be explored in the following chapters.

Figure 5.11a shows an XRD RSM near the asymmetric (10.5) AlN reflection of a UVC LED with tunnel homojunction. Starting with the highest aluminum content at the topmost position, diffraction peaks of the AlN layer, the $Al_{0.8}Ga_{0.2}N$:Si top

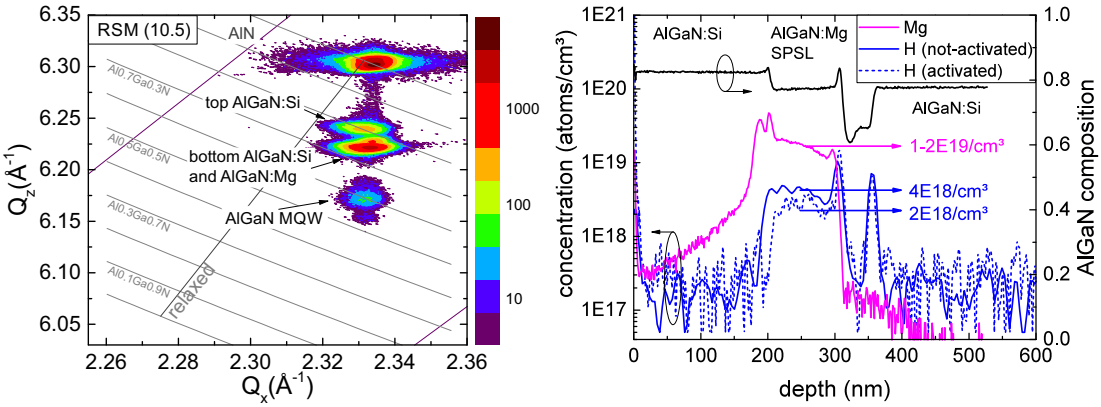

(a) (b)

Figure 5.11: (a) XRD reciprocal space map of a tunnel homojunction UVC LED with a pseudomorphically strained heterostructure without GaN and (b) SIMS of the magnesium and hydrogen concentration in the AlGaN:Mg layer of TJ-LEDs with different in-situ activation treatment.

current spreading layer, the $Al_{0.75}Ga_{0.25}N$:Si bottom current spreading layer (that is superimposed with the peak of the AlGaN:Mg SPSL with same composition) and the AlGaN MQW contribution are visible. The vertical alignment of all diffraction peaks at an almost constant Q_x of 2.334 Å^{-1} shows that the entire heterostructure is almost pseudomorphic to AlN without significant relaxation. Furthermore, the AlGaN MQW layers show the largest c-lattice parameter in the heterostructure, and no indication for low band gap AlGaN is visible from the RSM, which is in agreement with the heterostructure concept of tunnel junctions that enables entirely transparent UVC LEDs.

One crucial component of a TJ-LED is the AlGaN:Mg SPSL layer due to a high resistivity compared to the AlGaN:Si layers. As hydrogen can act as compensating defect reducing the Mg acceptor density in III-nitride compounds by Mg-H bond formation [103, 188, 189], the effect of an in-situ thermal annealing step on the hydrogen concentration within the AlGaN:Mg SPSL was investigated by means of SIMS profiles. In order to activate the Mg acceptors, pure nitrogen atmosphere without ammonia was supplied during the annealing step within the MOVPE reactor [190, 191]. Figure 5.11b shows SIMS profiles of the magnesium and hydrogen impurities in a TJ-LED. The magnesium incorporation will be discussed in more detail in section 5.5 and section 5.7. As shown in Figure 5.11b, even without any activation, the hydrogen concentration ($[H] = 4 \cdot 10^{18}$ cm^{-3}) in the AlGaN:Mg is much lower than the magnesium concentration ($[Mg] = 1\text{-}2 \cdot 10^{19}$ cm^{-3}), which means that only a small fraction of the Mg acceptors is passivated by hydrogen. In the sample with in-situ activation, the detected hydrogen concentration is further reduced by a factor of two to $[H] = 2 \cdot 10^{18}$ cm^{-3}. In this case, while only a minor fraction (10%-20%) of the magnesium acceptors is still passivated by hydrogen, there still is some room for improvement. In the investigated TJ-LEDs, the MOVPE overgrowth of the AlGaN:Si top current spreading layer might be crucial due to a potential re-passivation of the activated AlGaN:Mg layer, as the required supply of nitrogen occurs by pyrolysis of ammonia and additionally produces hydrogen. During overgrowth, the inert H_2 used as carrier gas is not dissociating at the growth

temperature of 960 °C and should not contribute to re-passivation. In the case of the presented AlGaN-based TJ-LEDs, the discussed SIMS data have been obtained from the full heterostructure (i. e. after AlGaN:Si overgrowth) and no detrimental re-passivation within these structures has been observed. For MOVPE-grown GaN-based TJ-LEDs presented in literature, however, severe Mg acceptor passivation has been reported as well as strategies for post-growth activation [164]: For instance, a post-growth thermal annealing step of the wafers, e. g., within a rapid thermal annealing (RTA) furnace is carried out after mesa definition, i. e. when the p-layer can be laterally accessed. It was theoretically described and experimentally verified that hydrogen diffusion is strongly suppressed within n-type III-nitride layers compared to p-type layers [192–194]. Therefore, hydrogen in-diffusion from the gas phase into AlGaN:Mg layers during AlGaN:Si overgrowth is reduced, but ex-situ hydrogen removal through the surface of TJ-LEDs featuring an n-type top current spreading layer is prevented. Lateral activation within an RTA system after mesa etching was demonstrated as a successful activation concept. Here, the higher mobility of hydrogen atom diffusion within p-type layers is exploited to remove hydrogen through the open side walls of the etched mesa [164]. At a fixed annealing temperature, a square-root dependency of the hydrogen diffusion length on the annealing time has to be considered when designing an appropriate lateral mesa size in order to achieve very low hydrogen concentrations close to complete activation [164].

5.5 Impact of a GaN interlayer on emission power and stability of TJ-LEDs

As described in subsection 5.1.2, an interlayer with low band gap inside the tunnel heterojunction can induce polarization charges that may reduce the total thickness of the space charge region. The tunnel barrier width is then reduced leading to increased tunnel probabilities and to a lower voltage drop at the tunnel junction. In this section, the influence of a GaN interlayer on the TJ-LED device performance such as the emission power and current level is investigated. Compared to the heterostructure in section 5.4, some minor changes are introduced: A slightly reduced aluminum content in the top current spreading layer (now $Al_{0.72}Ga_{0.28}N$:Si) and an increased thickness of the highly doped AlGaN:Mg^{++} SPSL (now 20 nm).

The UVC LEDs with tunnel heterojunction are more stable compared to UVC LEDs with tunnel homojunction. Maximum currents above 20 mA could be achieved compared to less than 1 mA in case of LEDs with tunnel homojunction shown in Figure 5.10b. This allows for more detailed and time-demanding investigations, e. g., the emission pattern of the 270 nm MQW luminescence. Figure 5.12a shows a microscope image of processed TJ-LEDs with "TU Berlin" logo geometry. Here, the top n-contact is located at the top left of the LED structure and extends as a frame on the mesa perimeter. The bottom n-contact is encompassing the entire mesa structure. The center area is not covered with metal, enabling light extraction of MQW emission through the top surface of the transparent AlGaN:Si current spreading layer. In Figure 5.12b, the same TJ-LED is imaged during cw operation. Here, light emitted from the quantum well plane was recorded and appears in blue color.

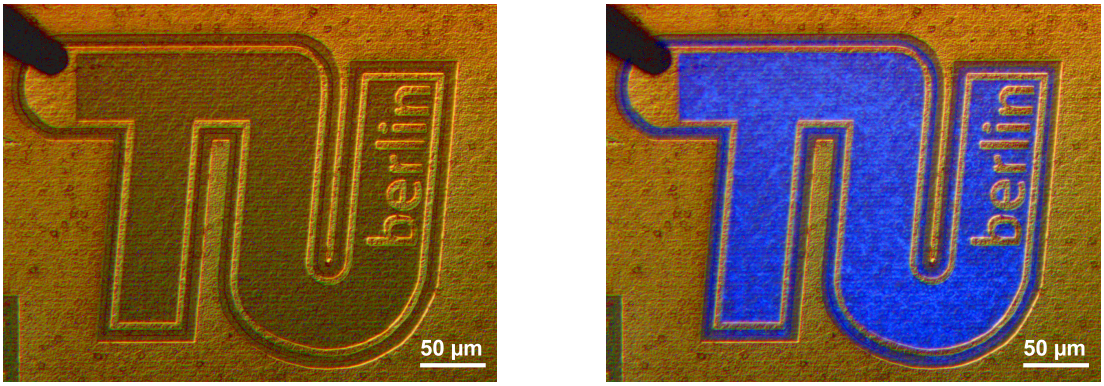

(a) (b)

Figure 5.12: (a) Microscope image of a UVC LED with tunnel heterojunction before operation (0 V bias voltage). (b) During operation, the light emitted from the quantum wells can be recorded from the transparent top side of the TJ-LED appearing blue in this microscope image [142]. (Measurement by Martin Guttmann - TU Berlin)

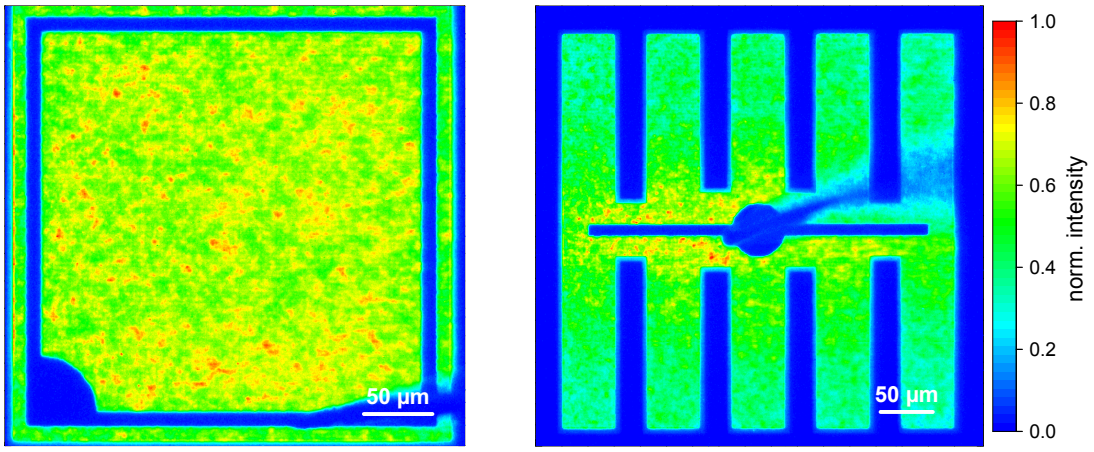

(a) (b)

Figure 5.13: UV-sensitive microscope images of TJ-LEDs including GaN interlayer with (a) square-shaped mesa and frame contact at the perimeter as well as with (b) finger-shaped mesa and stripe contact in the center both with 0.1 mm^2 emitting area, measured at a cw current of 5 mA from the top surface. Both TJ-LEDs show UV luminescence on the entire mesa area with a homogeneous distribution for (a) the frame contact and (b) only slight intensity enhancement under the central stripe contact [142]. (Measurement by Johannes Glaab - FBH).

In order to investigate lateral current spreading by the top AlGaN:Si layer and carrier injection in TJ-LEDs, the lateral distribution of the UV emission was measured through the top surface using a UV-sensitive microscope camera system. In Figure 5.13, the imaged emission from UVC LEDs with tunnel heterojunction is shown for a square-shaped mesa structure with frame top contact and for a finger-shaped mesa structure with central stripe top contact. A homogeneous distribution of the UV emission was measured for the TJ-LED with square mesa (Figure 5.13a), demonstrating effective vertical carrier injection via the tunnel junction on the entire mesa area. Holes injected via the tunnel junction into the 100 nm thick AlGaN:Mg SPSL can mainly drift vertically towards the MQW, as no significant lateral current spreading in the micrometer range can be expected from the AlGaN:Mg SPSL due to the high resistance in comparison to the top AlGaN:Si layer. The lateral current spreading by the more conductive top AlGaN:Si layer was investigated with the emission pattern from TJ-LEDs with finger-shaped mesa geometry, shown in Figure 5.13b. Here, the current on each position on a finger depends on the linear distance from the central metal contact. Also in this case, UV emission was detected from the entire mesa area with a slight intensity enhancement below the central stripe contact. This is an indication for imperfect current spreading of the top AlGaN:Si layer due to a compensation of donors that will be discussed in context of SIMS measurements in section 5.7.

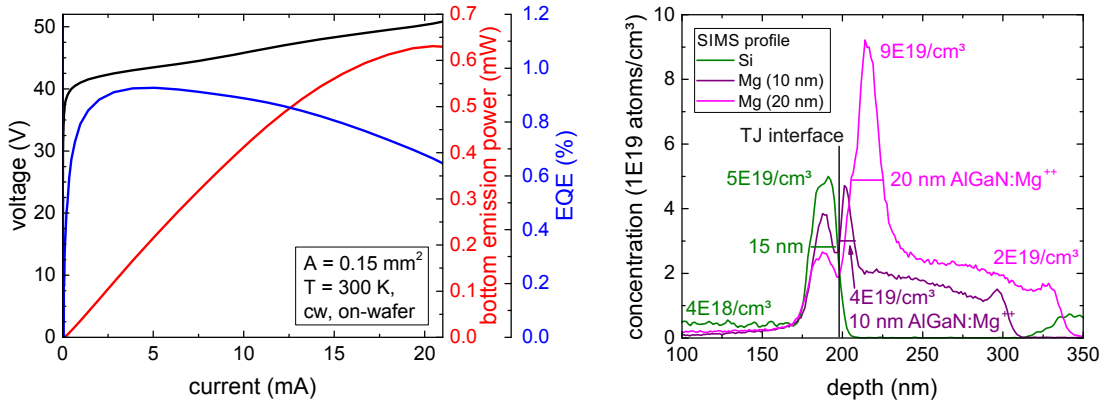

Figure 5.14: (a) Light output - current - voltage characteristics of UVC LEDs with tunnel heterojunction and (b) SIMS analysis of the influence of AlGaN:Mg^{++} layer thickness on the magnesium concentration at the TJ interface.

As briefly mentioned above, TJ-LEDs with tunnel heterojunction are more stable compared to TJ-LEDs with tunnel homojunction due to the incorporation of the GaN IL. One main outcome is the strongly increased emission power up to 0.6 mW due to a higher drive current of more than 20 mA. EQE values of 0.9% were reached (Figure 5.14a). Thermal roll-over and break-through of most diodes occurs slightly above 20 mA, which is caused by the high electrical power of 1 W given by an operation voltage of 50 V at 20 mA. Nevertheless, in comparison to the previous experiment on LEDs with tunnel homojunctions, the voltage is strongly reduced from more than 80 V down to 40 V at 1 mA demonstrating the effectivity of an interlayer. A tunnel heterojunction design is therefore superior to the tunnel homojunction for wide band gap TJ-LEDs.

In order to investigate the doping distribution near the tunnel junction, a SIMS analysis of the TJ-LED heterostructure containing 15 nm AlGaN:Si^{++} and 20 nm AlGaN:Mg^{++} SPSL was carried out. In Figure 5.14b, the measured SIMS profiles of silicon (green) and magnesium (pink) are shown, together with the magnesium profile of a previous TJ-LED with 10 nm AlGaN:Mg^{++} SPSL indicated by the darker violet line. The nanometer-thin interlayer is not fully resolved within the SIMS measurement.

The silicon concentration within the silicon-doped AlGaN layers is matching the intended values of 15 nm AlGaN:Si^{++} with $[Si] = 5 \cdot 10^{19}$ cm^{-3} followed by the AlGaN:Si top current spreading layer with moderate doping (i. e. $[Si] = 4 \cdot 10^{18}$ cm^{-3}). However, the measured Mg doping profile differs from the intended profile, in particular the intended concentration of $[Mg] = 9 \cdot 10^{19}$ cm^{-3} is not reached in the case of the 10 nm thick AlGaN:Mg^{++} layer (violet line). Instead, a lower concentration of $[Mg] = 4 \cdot 10^{19}$ cm^{-3} was incorporated, most likely due to the typically observed incorporation delay effect of magnesium in III-nitride growth [186, 187].

In order to realize a higher Mg concentration, the thickness of the AlGaN:Mg^{++} SPSL layer is adjusted to 20 nm in the second growth experiment (pink line), which leads to Mg incorporation with the intended concentration and a relatively sharp profile at the AlGaN:Mg^{++} interfaces. Additionally, the SIMS data show no monotonous decrease of the Mg content on top of the AlGaN:Mg^{++} layer but an unexpected second Mg peak with lower Mg concentration at a depth position near 190 nm, see Figure 5.14b. Unfortunately, this second Mg peak apparently covers the position of the AlGaN:Si^{++} layer, potentially compensating a large fraction of the Si donors. It should be noted that matrix effects related to the SIMS measurement cannot be fully excluded, which might lead to an overestimation of Mg concentrations in the second peak or to an underestimation at the dip position. Furthermore, the detected Mg profile can be influenced by composition-dependent Mg incorporation or Mg diffusion or sample surface roughness. Nevertheless, in order to understand a potential formation of such second Mg peak, the properties of Mg incorporation during AlGaN:Mg or GaN:Mg growth need to be considered. As reported for GaN:Mg growth, due to limited Mg solubility [195, 196] only a fraction of supplied Mg can be incorporated into the GaN crystal lattice, whereas Mg surface segregation is resulting in Mg accumulation in a thin film at the surface during growth [197]. Without further Mg supply during AlGaN:Si overgrowth a non-linear decay of such Mg film might cause the second Mg peak. In analogy, the formation of a second peak observed during InP growth with antimony [198] has been ascribed to strain-induced surface melting [199, 200] supported by experimental data demonstrating surface melting at temperatures below bulk melting temperature due to external strain [201]. The AlGaN:Mg peak formation must be subject to another investigation. As shown in Figure 5.14b, the incorporation of the second Mg peak is reproduced in both samples with different AlGaN:Mg^{++} SPSL thicknesses. 20 min in-situ annealing time at 830 °C was applied after AlGaN:Mg^{++} growth for Mg acceptor activation, that could in principle lead to Mg desorption. However, the reproduction of the Mg peak formation even after in-situ annealing is indicating a relatively stable Mg incorporation mechanism. Nevertheless, for the 20 nm thick AlGaN:Mg^{++} SPSL, the Mg concentration in the second Mg peak was reduced and the ratio between the first and second Mg peak is strongly increased, indicating an empirical solution to this problem.

5.6 Influence of n-metallization on operation voltage and light extraction

In this experiment, the influence of the n-contact fabrication on the operation voltage and light extraction efficiency of TJ-LEDs is investigated, including an ex-situ annealing procedure as well as the deposition of an aluminum reflector on the surface. A 2 nm thick interlayer within the tunnel heterojunction was intended. The interlayer thickness will be investigated in more detail in section 5.7. The contact fabrication is based on simultaneous deposition of n-contacts with V/Al/Ni/Au metal scheme on the top and bottom AlGaN:Si current spreading layers after mesa etching. In this experiment, a finger-shaped mesa with 0.15 mm^2 emitting area and central stripe top n-contact was measured. After metal deposition, an ex-situ annealing step was performed in a rapid thermal annealing (RTA) furnace for 1 minute at 800 °C under nitrogen atmosphere for contact formation. Finally, an Al reflector was deposited on the whole mesa area. In combination with the UV transparent TJ-LED heterostructure, the intention of this reflector is to increase the bottom light extraction efficiency. In fact, the fraction of light emitted from the MQW towards the top surface would be reflected enabling the extraction through the bottom surface. At the same time, the metal Al reflector could improve the heat dissipation during operation. Figure 5.15 is showing emission spectra and LIV characteristics of TJ-LEDs before n-contact annealing (as deposited), after n-contact annealing at 800 °C, and after Al reflector deposition. Before contact annealing, voltages of 28 V were measured at 1 mA. After contact annealing, measurements up to cw currents of 60 mA were possible and emission spectra could be recorded at different current levels, showing single peak UVC emission at 271 nm without any parasitic luminescence (Figure 5.15a). Furthermore, the operation voltage is reduced by 7 V after n-contact annealing at 800 °C (21 V at 1 mA), as shown in Figure 5.15b. Due to an enhanced stability, bottom emission power of almost 2 mW was measured at thermal roll-over near 40 mA and a maximum efficiency of EQE = 1.6% was obtained.

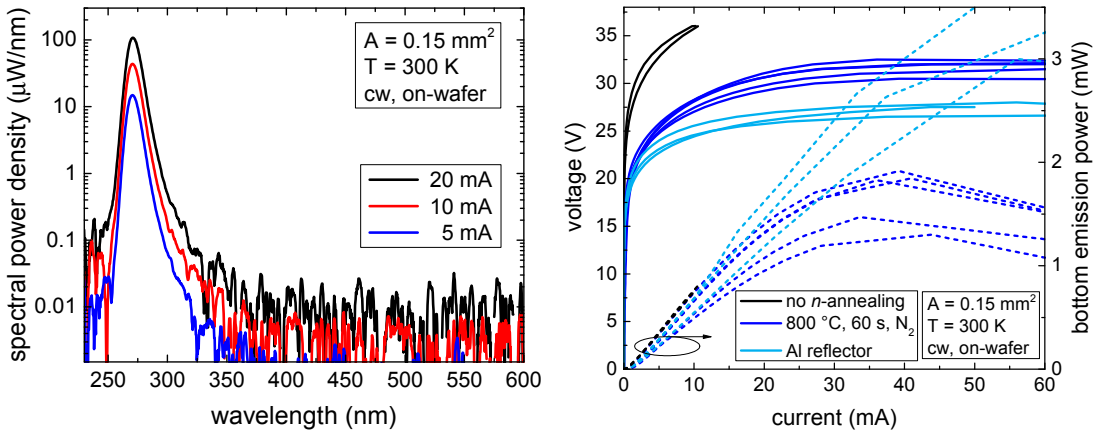

Figure 5.15: (a) Emission spectra of TJ-LEDs after ex-situ n-contact annealing at 800 °C and (b) LIV characteristics before annealing, after annealing, and after aluminum reflector deposition, exhibiting a strong impact of the n-contact fabrication on the operation voltage. (Measurements by Luca Sulmoni - TU Berlin)

Aluminum reflector deposition on the TJ-LED surface

The application of an Al reflector is strongly influencing the bottom emission power in the range of high cw currents (I > 30 mA). Without reflector, the top metal contact is only a central stripe, similar to Figure 5.13b. In this case, thermal roll-over limits the emission power to values below 2 mW. With Al reflector, more than 3 mW were measured on-wafer, which indicates more efficient heat dissipation. Furthermore, the measurements exhibit a voltage reduction with Al reflector by 3 V at 20 mA, certainly contributing to a reduction of device heating at even higher currents. On the one hand, this voltage reduction was unexpected, as the low resistive current path through the annealed V/Al/Ni/Au n-contact should not be shunted by a highly resistive metal/semiconductor interface between Al and AlGaN:Si. On the other hand, by applying an Al reflector, the metal covered area is enlarged by a factor of 30, which increases the chance of contacting low resistive areas on a surface with some inhomogeneities. Despite the higher contact resistance of AlGaN/Al, in presence of voltages way above 20 V a contribution to the vertical current appears not very unlikely due to such significant increase of the contact area. Unfortunately, it was not possible to reproduce such results in a subsequent experiment as instabilities such as shortcuts or leakage increased. The reason is probably related to a higher density of defects at the surface.

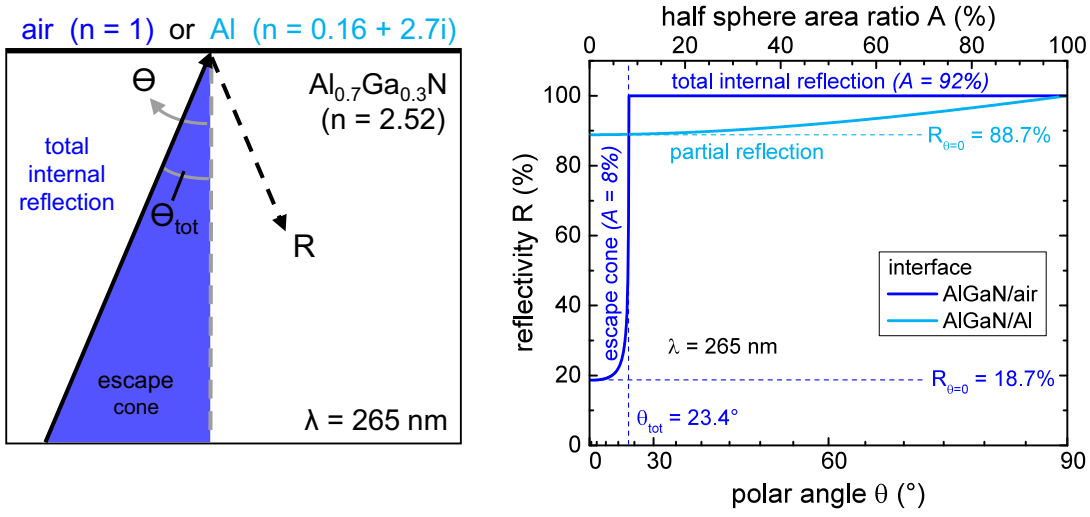

(a) (b)

Figure 5.16: (a) TJ-LED surface modeled by an $Al_{0.7}Ga_{0.3}N$/air interface (without reflector) and an $Al_{0.7}Ga_{0.3}N$/Al interface (with Al reflector). (b) Angle-dependent UVC reflectivity at the interfaces with and without aluminum reflector. (Calculations by Martin Guttmann - TU Berlin)

In the range of lower cw currents (I < 15 mA), the heating contribution can be considered modest and the impact of the Al reflector on the LEE can therefore be verified. As shown in Figure 5.15b, the measured emission power (0.5 - 0.7 mW at 10 mA) of samples with Al reflector is identical to samples without Al reflector. This means that the LEE and the external quantum efficiency are not increased by Al reflector deposition. In order to explain these results, the angle-dependent reflectivity R was analyzed, which is given by Fresnel's equation. R of the AlGaN/Al interface and R of the

AlGaN/air interface (including total reflection at high polar angles $\theta \geq \theta_{tot}$ and partial reflection within the escape cone $\theta < \theta_{tot}$), as well as the angular integration of these reflectivity data over the entire hemisphere ($0° \leq \theta \leq 90°$) were considered, illustrated in Figure 5.16a. For normal incidence ($\theta = 0°$), an $Al_{0.7}Ga_{0.3}N$/aluminum interface provides high UV reflectivity of R = 88.7% at 265 nm, calculated using the refractive index contrast [86, 202]. However, certain absorption by aluminum has to be considered in this optical system thus reducing the light extraction efficiency. For increasing polar angles $\theta > 0°$ the AlGaN/Al reflectivity increases ideally up to R = 100% at $\theta = 90°$. In Figure 5.16b, such partial reflection of AlGaN/Al is shown in light blue. In contrast, without Al reflector the reflectivity at the AlGaN/air interface is R = 18.7% for normal incidence, shown in dark blue. The average reflectivity is increasing for increasing angles within the escape cone. For $\theta \geq \theta_{tot}$ the AlGaN/air reflectivity is 100% due to total internal reflection for a critical angle of $\theta_{tot} = 23.4°$ from the interface normal. The angular integration of such escape cone with 23.4° half angle gives the fraction of the total solid angle of the hemisphere i. e. 8% of the half sphere area. The half sphere area ratio A is 92% for the case of total internal reflection. Obviously, the reflectivity of the AlGaN/Al interface is higher for $\theta < 23.4°$, whereas R of AlGaN/air is higher for $\theta > 23.4°$. The representation of reflectivity values in Figure 5.16b is chosen to enable a direct comparison of the total reflectance for both cases by the covered diagram area.

For isotropic MQW emission with degree of polarization DOP = 0, the calculations exhibit a total reflectance of 92.9% for the AlGaN/Al interface as well as 93.6% for the AlGaN/air interface, integrated over the complete half sphere. However, for AlGaN-based UVC LEDs emitting near 270 nm that are grown strained to AlN, TE emission is favored and the DOP is larger than zero ($DOP = 0.63 \pm 0.1$ was measured in section 3.5). In that case the angle-dependent emission is anisotropic with maximum intensity in c-direction $\theta = 0°$. For MQW emission with DOP = 0.7, the calculations exhibit a total reflectance of 92.4% for the AlGaN/Al interface as well as 91.5% for the AlGaN/air interface, including the anisotropic emission distribution integrated over the complete half sphere.

In consequence, even an AlGaN/Al interface with ideal Al reflector would have almost similar reflectance compared to the AlGaN/air optical system, and therefore no strong impact on the bottom light extraction, explaining the similar emission power of 0.5 - 0.7 mW measured at 10 mA (Figure 5.15b). In case of imperfect aluminum reflector deposition, e. g., incorporation of parasitic oxides or organic residuals during fabrication, additional absorption could reduce the AlGaN/Al interface reflectivity. Hence, the reflectivity of the AlGaN/Al interface is not significantly outperforming the AlGaN/air interface as the deposition of an Al top reflector cannot improve the bottom light extraction efficiency of such transparent TJ-LEDs. However, in order to facilitate high LEE within a flip-chip mounting process, the AlGaN/air interface would be no option. In this case, a high-reflective electrode (e. g. Al-based) could be a reliable option.

Light extraction from TJ-LEDs through surface and substrate side

One main advantage of tunnel heterojunctions is the use of highly conductive AlGaN:Si as top current spreading layers in UVC LEDs. In contrast to more resistive AlGaN:Mg layers, AlGaN:Si layers with a very high aluminum mole fraction up to 0.8 have a high

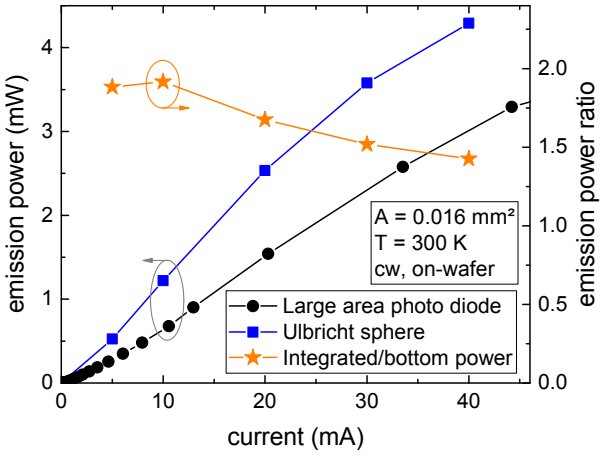

Figure 5.17: Emission power versus injected current from a transparent TJ-LED with 8 nm GaN:Si interlayer and small area top contact, measured on-wafer. Black circles represent data measured in bottom emission configuration using a large area silicon photo diode. Blue squares represent the integrated emission power measured in an Ulbricht sphere. Dependent on the current the integrated emission exceeds the bottom emission by a ratio of 1.4 to 1.9. (Measurement in Ulbricht sphere by Johannes Glaab - FBH)

conductivity near 0.025 Ω cm [49, 203]. The entire heterostructure of the TJ-LED is transparent to the UVC emission, with a possible exception of the nanometer-thin GaN interlayer in the case of a tunnel heterojunction, which will be discussed in section 5.7. Due to the absence of thick absorbing layers, light can be emitted both through the top and bottom surfaces of the TJ-LED and not only through the transparent substrate, as expected for conventional UV LEDs with thick UV absorbing GaN:Mg layers and large area metal contacts. This enables a higher total light extraction efficiency, however, the emission powers to the top and bottom direction are not necessarily equal to each other: The light escape cone covers the same solid angle at the AlGaN:Si/air interface for top emission on the one hand, and at the AlN/sapphire/air interfaces for bottom emission on the other hand. However, according to Snells law [204] the coefficients for transmission and reflection are slightly different for both directions of emission, favoring the emission in bottom direction through the substrate.

The total emission power was measured on-wafer within a calibrated integrating sphere (Ulbricht sphere) [205]. The transparent TJ-LED with small area top contacts is placed in the center of the hollow sphere with $BaSO_4$ coated inner surface. Due to almost Lambertian reflectance on the $BaSO_4$ coating with high reflectivity $> 90\%$ combined with low absorption within a large wavelength range (250 nm - 2000 nm), a homogeneous light intensity is generated by a large number of diffuse internal reflections of the emitted light [206–208]. In such integrating sphere configuration the total emission power of a TJ-LED with 8 nm thick GaN:Si interlayer was measured at different current levels and compared to measurements of the emission power of the same devices in bottom emission configuration. At 10 mA, a bottom emission power of 0.63 mW and an EQE of 1.4% was measured by large area Si photo diode, whereas the total emission power is 1.22 mW with an EQE of 2.6%, measured in the integrating sphere, as shown in Figure 5.17. The total EQE exceeds the EQE measured in bottom emission configuration by a ratio (integrated emission / bottom emission) of 1.9, proving that a significant fraction of the UVC light is emitted through the transparent top side or side walls of the TJ-LED. For larger currents (e. g. 40 mA with voltages > 25 V) the ratio is decreasing to 1.4. Due to the comparably long duration of the measurement within the integrating sphere, resistive heating is causing a thermally induced reduction of the emission power together with device degradation. As these devices were fabricated and measured on-wafer, extensive evaluation of the degradation behavior and determination of lifetimes were

beyond the scope of this investigation. In order to perform stress tests, dicing and flip-chip mounting of single LED chips on a submount are required, providing more controlled electrical and thermal coupling as well as a fixed set of operating conditions such as current, current density, temperature and gas atmosphere [209, 210].

5.7 Variation of the GaN:Si interlayer thickness in TJ-LEDs

In this section, TJ-LEDs with variation of the GaN:Si interlayer thickness between 0 nm and nominal 8 nm are compared. The growth rate was calibrated on a thick GaN layer using in-situ reflectometry. However, due to the large lattice mismatch of GaN to the AlN lattice constant, the thickness of GaN interlayers in the nanometer range may be additionally affected by strain relaxation and island formation. A 300 nm thick top AlGaN:Si current spreading layer with aluminum content of 65% was implemented. Note that the silicon concentration in the AlGaN:Si layers was reduced to $2 \cdot 10^{18}$ cm^{-3}, confirmed by SIMS analyses. The structures were grown in a subsequent series and processed simultaneously to ensure a high level of comparability from sample to sample.

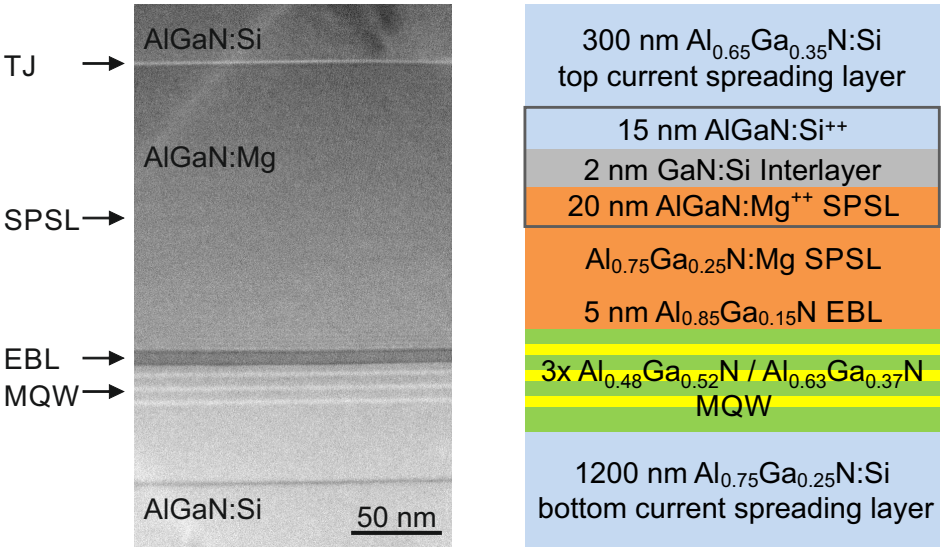

(a) (b)

Figure 5.18: (a) STEM-HAADF cross section image of a UVC LED with tunnel heterojunction showing the bottom AlGaN:Si current spreading layer, MQW, AlGaN:Mg SPSL, TJ and top AlGaN:Si, according to (b) the TJ-LED heterostructure scheme. (Measurement by Leonardo Cancellara - IKZ)

In Figure 5.18a, an STEM cross section image of a TJ-LED with 2 nm thick GaN:Si interlayer is shown, measured with HAADF contrast imaging. The TJ-LED heterostructure is containing a bottom AlGaN:Si current spreading layer, an AlGaN/AlGaN MQW, an EBL, a 100 nm thick AlGaN:Mg SPSL and an AlGaN:Si top current spreading layer. The tunnel heterojunction is composed of 20 nm thick AlGaN:Mg^{++} SPSL, GaN TJ interlayer with bright STEM contrast as well as 15 nm thick AlGaN:Si^{++}, schematically shown in Figure 5.18b. Following the TJ concept, lower voltages may be obtained in a further step using a thin AlGaN:Mg SPSL, which is beyond the scope of this work.

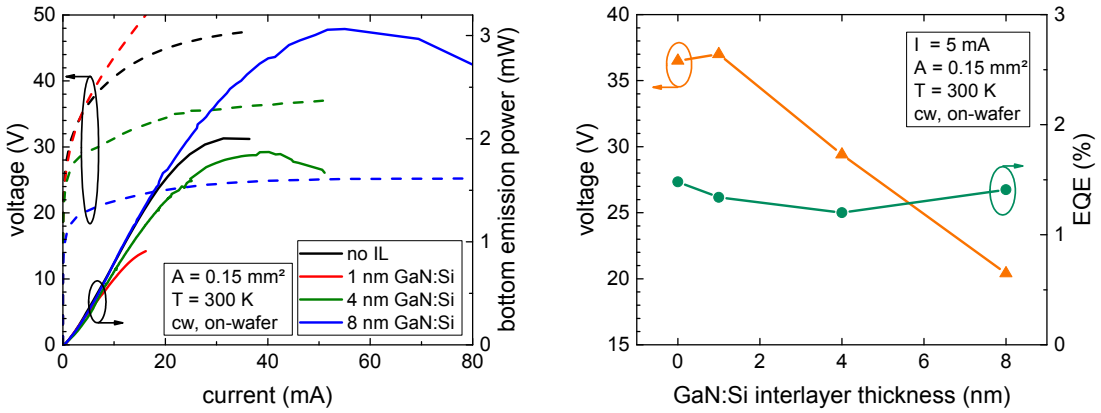

Figure 5.19: (a) LIV characteristics of TJ-LEDs with varying GaN:Si interlayer thickness and (b) depiction of the operation voltages and external quantum efficiencies measured at 5 mA dc [142].

As a first finding from the GaN thickness variation, in electroluminescence measurements current injection and UV light emission were measured and functional TJ-LEDs were obtained with all different interlayers in tunnel heterojunction LEDs as well as with the tunnel homojunction LED. Emission power levels between 1.4 mW and 1.7 mW were measured from the bottom surface at dc currents of 20 mA at room temperature without active cooling. Thermal roll-over for the sample with 8 nm GaN:Si IL is reached at 55 mA at an emission power of more than 3 mW (Figure 5.19a). For cw currents larger than 15 mA, resistive heating cannot be neglected. Therefore, the maximum achieved bottom emission power at thermal roll-over depends on the specific operation voltage of each sample. TJ-LEDs without an interlayer or with very thin interlayers exhibit very high operation voltages, occasionally causing device breakthroughs. In Figure 5.19b, the operation voltages at 5 mA are displayed for TJ-LEDs with varying GaN:Si IL thicknesses. TJ-LEDs without interlayer or with 1 nm thin interlayer exhibit voltages as high as 37 V at 5 mA. With increasing interlayer thickness the voltages are strongly decreasing down to 20 V at 5 mA for the TJ-LED with 8 nm GaN:Si IL, demonstrating the strong impact of the interlayer on the tunneling probabilities. The EQE at low currents is not strongly influenced by resistive heating effects and is nearly constant around 1.3% at 5 mA (dc), independent of the interlayer thickness. This means that the injection efficiency of carriers, which is combining tunneling from top AlGaN:Si to AlGaN:Mg and drifting into the MQW, is independent of the GaN:Si IL thickness, as shown by the constant EQE. This particularly excludes a strong influence of additional parasitic current paths or non-radiative recombination of carriers caused by different thickness of the interlayers.

Additionally, UV light absorption at the GaN:Si interlayer can occur as the band gap is lower than the energy of the emitted photons. However, no reduction of the TJ-LED EQE with increasing IL thickness was observed in the experiments, even for 8 nm nominal thickness. In order to investigate the interlayer absorption contribution, transmission spectra of as-grown TJ-LED heterostructures were recorded. In this series, GaN interlayers with varying nominal thickness between 2 nm and 20 nm were

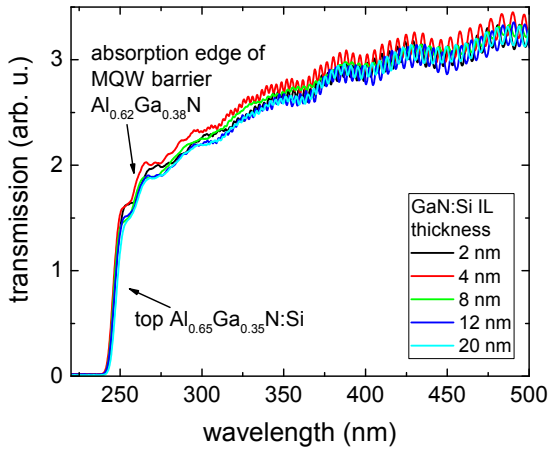

Figure 5.20: UV-VIS transmission spectra of TJ-LEDs with varied nominal GaN:Si IL thickness between 2 nm and 20 nm exhibiting the absorption edges of the $Al_{0.62}Ga_{0.38}N$ MQW barriers and $Al_{0.65}Ga_{0.35}N$:Si top current spreading layers as well as interference modulation from layer thickness oscillations. No GaN-related interlayer absorption edge near 360 nm is observed.

fabricated. For 265 nm wavelength, the absorption coefficient of bulk GaN layers is around 170000 cm^{-1} [211]. Although a 20 nm thick GaN layer should absorb almost 29% of the light intensity in UV-VIS transmission measurements, no additional absorption at 265 nm or GaN-related absorption edge near 360 nm is observed in the TJ-LED heterostructures (Figure 5.20). In the transmission spectra, only absorption edges of the $Al_{0.62}Ga_{0.38}N$ MQW barriers and $Al_{0.65}Ga_{0.35}N$:Si top current spreading layers as well as intensity modulations from layer thickness interference oscillations are observed. Hence, the absorption of GaN ILs within a tunnel heterojunction is lower compared to bulk GaN layers, which can be due to inhomogeneous thickness or relaxation, confinement-induced shift of the ground state energy, or electric fields that might influence the absorption properties of the nanometer-thin interlayer.

In order to obtain a thin space charge region at the tunnel pn-junction, very high silicon and magnesium doping concentrations (i. e. $[Si] = 5 \cdot 10^{19}$ cm^{-3}, $[Mg] = 9 \cdot 10^{19}$ cm^{-3}) at the interfaces are implemented as described in section 5.3. From SIMS measurements the doping concentrations as well as the concentration of unintended impurities like hydrogen are analyzed as a function of sputtering depth. Figure 5.21 shows the SIMS data of a TJ-LED with aluminum profile in black along the different layers, i. e., the surface near 0 nm, the top $Al_{0.65}Ga_{0.35}N$:Si current spreading layer, the tunnel heterojunction with increased doping concentrations near 300 nm depth, 100 nm thick AlGaN:Mg, EBL, active region as well as the bottom AlGaN:Si current spreading layer starting at 500 nm depth. The Mg profiles of the AlGaN:Mg ($[Mg] = 2 \cdot 10^{19}$ cm^{-3}) and AlGaN:Mg^{++} ($[Mg] = 9 \cdot 10^{19}$ cm^{-3}) layers were realized as intended. The additional second Mg peak in the AlGaN:Si^{++} layer near 290 nm depth was also discussed in section 5.5. Within the top AlGaN:Si current spreading layer, the SIMS profile exhibits a fast decay of the Si concentration to a level of $[Si] = 2 \cdot 10^{18}$ cm^{-3} and a comparably slow decay of the Mg concentration. As a result, within more than 50 nm of the top current spreading layer (at depths near 250 nm in Figure 5.21), the Mg concentration is similar or even slightly higher compared to the Si concentration, leading to a 50 nm thick AlGaN:Si layer with high donor compensation and lower conductivity. This might be one cause for the high operation voltages required (i. e. > 20 V), a factor of 4 higher than expected for ideal UVC LEDs with 265 nm emission (built-in potential of approximately 4.7 V). For future TJ-LED growth, a Mg reduction by desorption during GRI or a Si increase within the AlGaN:Si top current spreading layers can in principle counteract this problem.

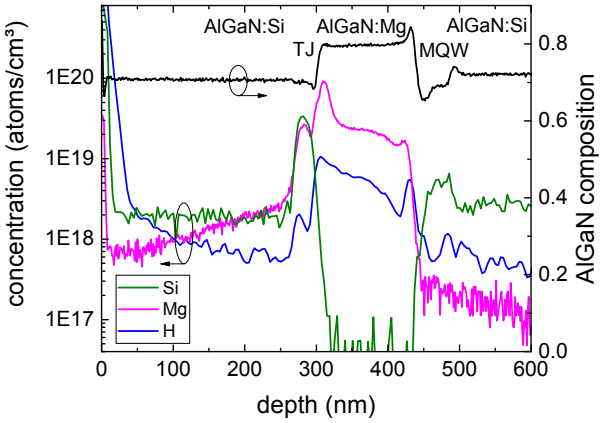

Figure 5.21: SIMS profile of TJ-LED with in-situ activation before interlayer growth, exhibiting high Si and Mg concentrations at the tunnel heterojunction as well as a comparably low H concentration.

Considering the SIMS measurements of further species, hydrogen is the dominating unintentional impurity type. Hydrogen incorporation during growth is strongly correlated to the magnesium concentration within AlGaN:Mg layers due to a low formation energy of H defects in p-type layers, which was also calculated for the MOVPE growth of GaN:Mg [192]. In case of Figure 5.21, the hydrogen concentration is below $1 \cdot 10^{18}\,\mathrm{cm}^{-3}$ within the AlGaN:Si layers and near $[\mathrm{H}] = 5 \cdot 10^{18}\ \mathrm{cm}^{-3}$ within the AlGaN:Mg layer. Therefore, the majority of 75% of the Mg atoms ($[\mathrm{Mg}] = 2 \cdot 10^{19}\ \mathrm{cm}^{-3}$) within the AlGaN:Mg layer are not passivated by hydrogen and can act as acceptors.

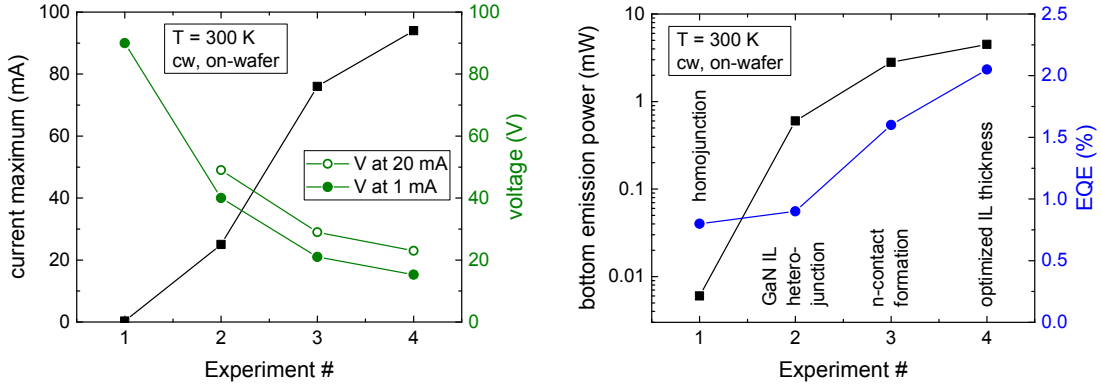

Figure 5.22: Progress in UVC TJ-LED development in each experimental stage, illustrated by (a) the operation voltage and maximum drive current with $0.15\,\mathrm{mm}^2$ contact area (except Experiment #1 with $0.01\,\mathrm{mm}^2$) as well as (b) the maximum achieved cw emission power and EQE.

In Figure 5.22, the development of UVC TJ-LED devices is summarized by reporting the progress of the most important device properties, i. e. maximum drive current, operation voltage, maximum EQE and bottom emission power measured on wafer. In each experimental stage, the operation voltages at 1 mA (or at 20 mA) are strongly reduced initially from 90 V down to 15 V (or 23 V) while the achieved maximum current levels are increased from about 1 mA up to more than 90 mA (Figure 5.22a) at the same time. Thanks to the higher current levels, the improvement of the electrical performance is followed by a strong increase in the maximum achieved emission power of almost three orders of magnitude, i. e. from 6 µW up to 3 mW. The maximum EQE is increased

from 0.8% up to more than 2%. All of these measurements have been conducted on wafer under cw operation at room temperature and the bottom emission power was measured through the substrate without active cooling of the wafers.

Reduced heating effects in pulsed operation of TJ-LEDs

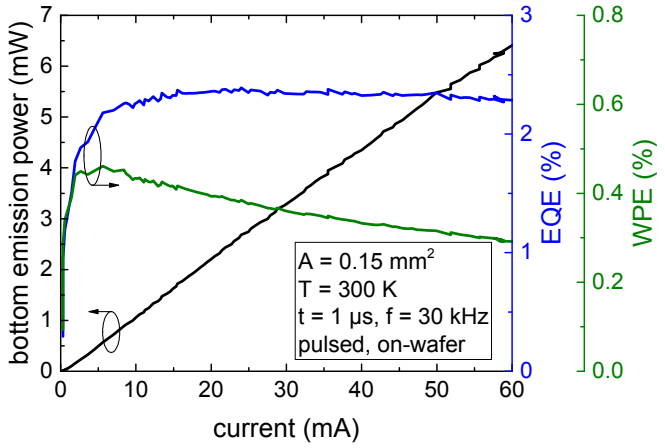

Figure 5.23: LI characteristic of TJ-LED with 8 nm GaN:Si interlayer thickness in pulsed operation with corresponding EQE and WPE.

In cw operation, resistive heating of the TJ-LEDs (on-wafer) becomes significant due to operation voltages larger than 20 V, causing thermal roll-over starting already near 20 mA (Figure 5.19). In pulsed operation, the impact of resistive heating effects can be strongly reduced. Pulsed EL measurements with pulse lengths of t = 1 µs and repetition rates of f = 30 kHz with 3% duty cycle were carried out on the TJ-LED sample with 8 nm GaN:Si IL (Figure 5.23). A linear increase of the emission power to values of more than 6 mW at 60 mA was measured through the substrate, without any indication of carrier leakage or parasitic current paths. At 20 mA, an emission power of 2.2 mW was recorded. The EQE is 2.3%, constant over a large current range. These values are comparable to LI characteristics of transparent UVC LEDs without TJ, as discussed in chapter 4, demonstrating the high potential of efficient TJ-LEDs for applications. Peak WPE values of 0.41% were obtained. The WPE is strongly affected by the operation voltage and electrical resistance of the TJ-LEDs that is subject to investigation in the following section.

Electrical resistance of tunnel junctions

Ideally, tunnel heterojunctions with degenerate doping levels would show very low resistance with zero voltage offset in reverse bias direction, as described in subsection 5.1.1 and allow for finite tunnel currents already at small bias voltages. However, the efficiency of the tunneling mechanism and the required voltages strongly depend on the precise design, material limitations, and the fabrication of tunnel heterojunctions in TJ-LEDs. In order to quantify the electrical properties of group-III nitride based tunnel heterojunctions, the TJ-LED device resistance is frequently used in literature, calculated as the differential resistance dV/dj from j-V-measurements of TJ-LED devices. In this case, the total calculated differential resistance of the devices is influenced by the resistance of the tunnel heterojunction, as well as by other components of the TJ-LEDs

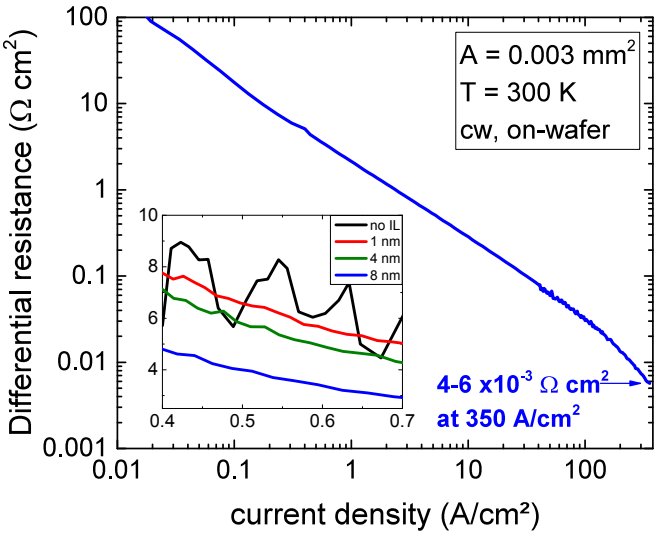

Figure 5.24: Differential resistance of TJ-LEDs with $Al_{0.75}Ga_{0.25}N$:Mg and 8 nm GaN:Si interlayer as a function of current density. The inset shows the differential resistance of TJ-LEDs with different IL thickness.

such as n-contact resistances or the AlGaN:Mg layer or the MQW pn-junction. Therefore, if the dominating resistance contribution is related to the tunnel heterojunction, the calculated differential resistance of the complete device provides a reasonable estimation of an upper limit of the resistance of the tunnel heterojunction. This assumption is supported by the fact, that the TJ-LED operation voltage is strongly influenced by the TJ design (Figure 5.22).

In Figure 5.24, the evaluated differential resistance is plotted over the current density for a TJ-LED with 8 nm GaN:Si interlayer and mesa area of $A = 0.003\,mm^2$. Such small contacts enable measurements up to high current densities with moderate drive currents and less device failure rates compared to larger contacts. In general, the device resistance is decreasing with increasing current density, as expected from a diode with $j = j_S \cdot \exp\{[(e \cdot V)/(n \cdot k_B T)] - 1\}$ characteristic (Shockley diode equation), where j_S is the saturation current density. In the inset of Figure 5.24, the evaluated differential resistances from TJ-LEDs with different GaN:Si interlayer thickness are shown in linear scale at a current density near $0.5\,A/cm^2$. Despite a large scattering of the data, especially from the tunnel homojunction LED without interlayer, a correlation of the GaN:Si interlayer thickness and the differential resistance is observed. The highest device resistances have been obtained from TJ-LEDs without or with very thin GaN:Si interlayers, and the device resistance is monotonously decreasing with increasing interlayer thickness. The TJ-LED with 8 nm thick interlayer exhibits by far the lowest differential resistance, which is in agreement with the lowest operation voltages measured on those devices (see Figure 5.19a). This proves that a dominating resistance contribution is given by the TJ and that the highest tunneling probabilities are obtained from tunnel heterojunctions with 8 nm thick GaN:Si interlayer. Furthermore, the lowest differential resistance of those structures was measured in the high current density range, shown in Figure 5.24. Values as low as 4 to $6 \cdot 10^{-3}\,\Omega cm^2$ have been obtained at current densities of $350\,A/cm^2$, for hole injection into $Al_{0.75}Ga_{0.25}N$:Mg layers via MOVPE-grown tunnel heterojunctions.

In Figure 5.25, device resistances of group-III nitride based tunnel junction devices in npn-configuration reported from different groups are shown with respect to the band

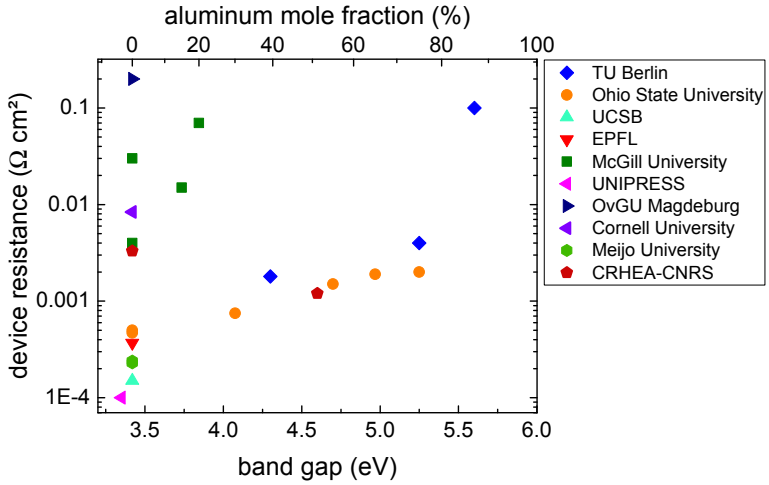

Figure 5.25: Comparison of reported differential device resistances for carrier injection by tunnel junctions into InGaN:Mg, GaN:Mg, or AlGaN:Mg with different band gap. Different current densities have been used for evaluation in TJ-LED reports from numerous groups. [142, 151–154, 158, 165–168, 212–221].

gap of the (In,Al,Ga)N:Mg layers. Since the tunnel barrier height is correlated to the band gap, the tunneling probabilities could be strongly influenced by the composition of the (In,Al,Ga)N:Mg layers. The reported values of differential resistances provide an interesting comparison of tunnel junction properties realized with different materials by various groups. Nevertheless, several other parameters can affect the evaluated device resistances, such as used current density, MBE or MOVPE approach, tunnel homo- or heterojunction concept, or further details of the heterostructure design. Figure 5.25 shows numerous publications on GaN-based TJ-devices (band gap near 3.4 eV) as well as InGaN- and AlGaN-based devices in dependence of the (In,Al,Ga)N:Mg band gap. The lowest device resistances near $1 \cdot 10^{-4}\,\Omega\mathrm{cm}^2$ have been obtained by MBE-grown GaN- or InGaN-based tunnel heterojunctions with InGaN interlayers. However, also for MOVPE-grown GaN tunnel homojunctions efficient carrier injection with slightly higher device resistance has been obtained, e. g., $2.4 \cdot 10^{-4}\,\Omega\mathrm{cm}^2$ from Meijo University. In Ref. [214], a collection of differential resistances from TJ-LEDs with (Al)GaN:Mg layers over a wide composition range fabricated by MBE is presented. The values are included in Figure 5.25 as orange circles (Ohio State University). An increase of the tunnel junction device resistance is observed with increasing band gap of the (Al)GaN:Mg layer from $1.2 \cdot 10^{-4}\,\Omega\mathrm{cm}^2$ for an optimized TJ-LED with GaN:Mg layer up to $2.1 \cdot 10^{-3}\,\Omega\mathrm{cm}^2$ for a TJ-LED with an $Al_{0.75}Ga_{0.25}N$:Mg layer. In this case, increasing TJ device resistances due to decreasing tunneling probabilities are correlated to an increasing band gap (Equation 5.2, [149]). However, these results demonstrate efficient carrier injection via tunneling processes also for wide band gap AlGaN alloys with very high aluminum content up to 75%. Furthermore, this is not limited to MBE-grown AlGaN-based tunnel heterojunctions but independent of the applied growth method. Also MOVPE-grown $Al_{0.75}Ga_{0.25}N$:Mg-based tunnel heterojunctions (band gap near 5.3 eV) can enable efficient tunneling with comparable or only slightly higher device resistances (Figure 5.25) as demonstrated by the results of this work that were already published in Kuhn et. al. [142]. In the outlook section, current injection into transparent TJ-LEDs with band gap of 5.6 eV is shown.

5.8 Outlook

Due to the replacement of UV absorbing or highly resistive GaN:Mg or AlGaN:Mg layers, hole injection using tunnel heterojunctions is enabling the fabrication of transparent UVC LEDs emitting at 268 nm with high efficiency. Short wavelength UVC emission from MBE-grown TJ-LEDs has been demonstrated at 257 nm [167] and 242 nm [22], however, no reports on MBE- or MOVPE-grown TJ-LEDs emitting in the wavelength range below 240 nm exist. By combining efficient UVC LEDs emitting at 232 nm [94] with an optimized tunnel heterojunction [142], MOVPE-grown TJ-LEDs with emission wavelengths as short as 232 nm are demonstrated which use a UV transparent AlGaN:Mg SPSL with average aluminum mole fraction as high as 87% [221].

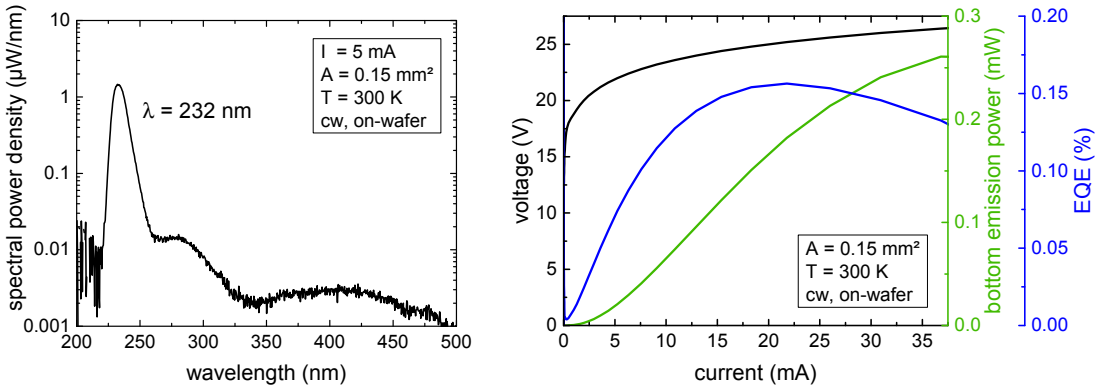

(a) (b)

Figure 5.26: Ultra short wavelength emission from transparent TJ-LED emitting at 232 nm: spectral power density (a) and LIV characteristics with EQE calculation (b). (Measurements by Verena Montag - TU Berlin)

In Figure 5.26a the emission spectrum of such TJ-LED with 8 nm GaN:Si interlayer is shown, exhibiting ultra short wavelength emission at 232 nm with weak parasitic luminescence at longer wavelengths. LIV characteristics of the TJ-LED with Al reflector are shown in Figure 5.26b. At a cw current of 5 mA, an emission power of 20 µW with 22 V operation voltage was achieved, as well as 260 µW at thermal rollover, demonstrating effective vertical current injection through the top $Al_{0.87}Ga_{0.13}N$:Si current spreading layer and the tunnel heterojunction. A TJ-LED device resistance of 0.1 Ωcm^2 was obtained at a current density of 40 A/cm^2 for tunnel injection into the UV transparent AlGaN:Mg SPSL with average aluminum mole fraction of 87% (band gap near 5.6 eV). Peak EQE of 0.16% is reached at 20 mA, which is exceeding EQE values of comparable LEDs with absorbing p-layers [94] and similar to state-of-the-art UVC LEDs at the same wavelength [222, 223]. These results are indicating promising device design options for carrier injection using tunnel heterojunctions that might become the design of choice for fully transparent UVC LEDs emitting in the ultra short wavelength range or for edge-emitting UVC laser diodes or surface-emitting VCSELs.

5.9 Summary

When realizing MOVPE-grown AlGaN-based UVC LEDs with tunnel junctions, relevant components of the tunnel heterojunction have been separately grown and investigated. As a result, maximum doping concentrations without structural degradation were obtained around $[\mathrm{Si}] = 5 \cdot 10^{19}$ cm^{-3} for $Al_{0.75}Ga_{0.25}N$:Si^{++} as well as $[\mathrm{Mg}] = 9 \cdot 10^{19}$ cm^{-3} for $Al_{0.75}Ga_{0.25}N$:Mg^{++}. A 3 nm thick interlayer was pseudomorphically grown for $Al_xGa_{1-x}N$ IL compositions between $x = 0$ and $x = 0.3$. The resistivity of $Al_{0.75}Ga_{0.25}N$:Si top current spreading layers grown at reduced temperatures of T = 960 °C was comparable to the optimized $Al_{0.75}Ga_{0.25}N$:Si layers grown at T = 1080 °C.

Utilization of these results enabled the experimental demonstration of:

1. the first AlGaN-based TJ-LEDs grown by metalorganic vapor phase epitaxy
2. the first AlGaN/AlGaN tunnel homojunction

From the investigations of TJ-LEDs it was found that

(I) TJ-LEDs with AlGaN/GaN tunnel heterojunctions enable higher current levels and emission powers compared to AlGaN/AlGaN tunnel homojunctions due to increased tunneling probabilities induced by polarization fields of a GaN interlayer.

(II) the magnesium acceptor activation is crucial due to potential re-passivation by hydrogen during AlGaN:Si overgrowth. Nevertheless, the hydrogen concentration within the AlGaN:Mg layer has been effectively reduced by a factor of two by applying in-situ annealing. No subsequent passivation after the growth of the top AlGaN:Si layer was observed by SIMS analyses.

(III) an AlGaN/Al interface with ideal Al top reflector (reflectivity close to 90%) has almost similar integrated reflectance of anisotropic MQW emission (DOP = 0.7) compared to the AlGaN/air optical system, and therefore no strong impact on the bottom light extraction efficiency of a TJ-LED. However, an AlGaN/Al reflector is a promising option for mounting in a flip-chip process enhancing the heat dissipation.

(IV) a GaN interlayer in TJ-LEDs exhibits lower UV absorption compared to bulk GaN. Even with a nominally 20 nm thick GaN IL, TJ-LEDs exhibit no GaN-related absorption edge near 360 nm, thus enabling the fabrication of fully transparent UVC LEDs with tunnel heterojunctions.

(V) the electrical resistance of tunnel heterojunctions is influenced by the GaN interlayer thickness. For tunnel injection of holes into AlGaN:Mg with band gap larger than 5 eV, MOVPE-grown tunnel junctions enable electrical resistances comparable to tunnel junctions grown by MBE.

The presented investigations of physical mechanisms triggered the development of improved TJ-LED devices. In comparison to the first demonstration, the achieved performance improvements in the last experiments include a voltage reduction by a factor 5, an increase of maximal drive current by a factor 500, an EQE increase by a factor 2.5, and an increase of the emission power by almost three orders of magnitude for TJ-LEDs with 268 nm emission wavelength.

6 Conclusion

In this thesis, AlGaN-based LEDs and lasers with emission wavelength in the UVC spectral range have been grown by metalorganic vapor phase epitaxy. The mechanisms determining structural properties and optoelectronic characteristics have been analyzed and optimized in order to improve material quality and device efficiency. The focus is on the UVC transparency of the heterostructures that is advantageous for efficient light extraction from UVC LEDs and required for UVC lasers with low modal absorption in the cavities.

AlN and AlGaN layers as well as AlGaN-based heterostructures were grown on ELO AlN/sapphire templates as well as on bulk AlN substrates. First, the influence of the AlN substrate offcut angle on the surface morphology of MOVPE grown AlN layers was analyzed. Offcut angles larger than 0.19° lead to AlN step bunching with macro step heights up to 6 nm for a fixed set of growth parameters. For offcut angles lower than 0.17°, atomically smooth AlN layers were reproducibly obtained on both types of substrates, providing ideal starting surfaces for the growth of AlGaN-based UV lasers.

The realization of UVC laser diodes emitting near 270 nm requires n-type AlGaN:Si cladding layers that are characterized by high conductivity, low UV absorption, uniform composition, and smooth morphology without relaxation or defect generation. It was shown that for 1200 nm thick $Al_xGa_{1-x}N$:Si layers strong plastic relaxation and UV absorption can be excluded for a composition of $x \geq 0.6$. With increasing aluminum content above $x = 0.8$, however, AlGaN:Si resistivities are strongly increasing. Furthermore, for $Al_{0.8}Ga_{0.2}N$ layers partial strain relaxation, compositional non-uniformities and rough morphologies caused by the growth of spiral hillocks were observed, which are detrimental for the laser performance. In a systematic investigation of growth parameters the influence of growth temperature, gas phase composition, and growth rate during $Al_{0.8}Ga_{0.2}N$ growth was separately analyzed. For the investigated layers, spiral formation and surface RMS roughness are barely affected by variations of these MOVPE growth conditions. In contrast, pseudomorphic, uniform, and smooth AlGaN:Si layers were obtained by the implementation of an AlGaN:Si superlattice concept with growth interruptions of 10 s after each individual layer which increase the diffusion length of metal adatoms.

Plastic relaxation of compressively strained AlGaN-based MQW laser structures with emission wavelength near 270 nm strongly depends on the waveguide composition. Whereas a low aluminum content $x \leq 0.55$ leads to partial relaxation due to a large lattice mismatch with respect to the AlN buffer layer, pseudomorphic laser structures have been obtained with $Al_{0.7}Ga_{0.3}N$ waveguides. In addition, surface and interface properties of such pseudomorphic MQW structures were investigated by AFM and TEM. The formation of V-pits in the MQW and waveguide system, which are potentially increasing modal losses by scattering of the optical mode, was successfully reduced by increasing the growth temperature from 900 °C to 1080 °C, leading to smooth and pit-free MQW surfaces. In combination with growth interruptions after each of the

quantum well and barrier layers, higher growth temperatures lead to more abrupt MQW interfaces. Finally, the influence of such individual growth optimization steps on laser emission properties has been analyzed. Optically pumped UVC lasers with threshold behavior, spectral linewidth reduction, and TE polarized emission above threshold were shown with lasing wavelengths near 270 nm. By reducing the laser surface roughness and correlated scattering losses, the laser threshold could be reduced by a factor of seven to 900 kW/cm^2.
In a next step, crucial layer properties for current injection and optical confinement in UVC laser diode heterostructures have been identified and optimized. For this purpose, charge carrier injection was experimentally analyzed by electroluminescence measurements on transparent UVC LEDs with implemented waveguide system. The results were combined with simulations of the vertical optical mode distribution in such waveguide structures and the corresponding modal losses in heavily absorbing layers such as GaN:Mg or palladium contact metals, or in less absorbing layers like AlGaN:Mg. By the variation of composition and layer thickness of AlGaN waveguide and cladding layers an optimized heterostructure design for UVC laser diodes with 200 nm thick $Al_{0.76}Ga_{0.24}N$:Mg cladding layers was found that simultaneously enables efficient carrier injection with high EQE and sufficient mode confinement with low modal losses of $40\,cm^{-1}$.
As an alternative hole injection concept to resistive AlGaN:Mg p-side layers, AlGaN-based tunnel junctions in reverse bias configuration were implemented into the UVC LED heterostructure. Using tunnel junctions, the highly resistive or UV absorbing AlGaN:Mg layers and p-contacts can be replaced by highly conductive and UV transparent AlGaN:Si layers and n-contacts. After the initial optimization of individual TJ components, such as Mg and Si doping concentrations at the TJ interface or the composition of an (Al)GaN interlayer, the first demonstration of functional TJ-LEDs with AlGaN/AlGaN tunnel homojunction was achieved, as well as the first demonstration of AlGaN-based TJ-LEDs grown by metalorganic vapor phase epitaxy. By UV-sensitive EL microscopy imaging of TJ-LEDs from the transparent top side, a homogeneous carrier injection through the tunnel junction interface was verified by a uniform MQW luminescence distribution over the entire mesa area. Based on these devices, the GaN interlayer thickness was varied in order to exploit polarization charges at the TJ interface to reduce the space charge region width and enhance the tunneling probability. With 8 nm thick GaN interlayers, a reduction of the TJ-LED operation voltage by almost 20 V was achieved in combination with an external quantum efficiency as high as 2.3% and emission power of more than 6 mW at 268 nm as well as 0.16% and 0.26 mW at 232 nm. All of these TJ-LED heterostructures were entirely grown by MOVPE in a single growth run. The evaluated differential device resistances of $4\,m\Omega cm^2$ for hole injection into $Al_{0.75}Ga_{0.25}N$:Mg layers are comparable to reported values from UVC LEDs with MBE-grown tunnel junctions. In conclusion, AlGaN-based tunnel heterojunctions are an excellent hole injection concept for transparent UVC LEDs, which can further be implemented for current injection into UVC laser diodes.
In LD heterostructures the required transparency and conductivity of top cladding layers with sufficient refractive index contrast to waveguide layers can be realized by tunnel junctions in combination with AlGaN:Si top cladding layers. Obviously, by replacing the AlGaN:Mg top cladding layers, Mg-related absorption is omitted. Restrictions for the composition and thickness of top cladding layers, which were discussed

for AlGaN:Mg in chapter 4 and summarized in Figure 4.18b, can be eased as long as fundamental absorption is avoided. Due to the excellent current spreading of AlGaN:Si, the top cladding layer thickness is not limited by the conductivity. Cladding layers with high thickness beyond 400 nm can be employed in order to strongly reduce the mode overlap with highly absorbing contact metals. Alternatively, very thin layers can be employed facilitating lateral current injection via buried TJs in combination with a vertical refractive index contrast to air. At this point, the best heterostructure concept for UVC LDs with TJs is open to be explored.

Bibliography

[1] M. Kneissl, J. Rass, Eds., *III-Nitride Ultraviolet Emitters: Technology and Applications*, Springer International Publishing, 2016.

[2] United Nations, *About the Sustainable Development Goals. www.un.org/sustainabledevelopment/sustainable-development-goals*, Sept 12th 2019.

[3] MRS-J, *Materials Research Meeting 2019, mrm2019.jmru.org*, Sept 12th 2019.

[4] M. Kneissl, T.-Y. Seong, J. Han, H. Amano, *The emergence and prospects of deep-ultraviolet light-emitting diode technologies*, Nature Photonics **13**, 223 (2019).

[5] T. Wernicke, L. Sulmoni, C. Kuhn, G. Tränkle, M. Weyers, M. Kneissl, *Group III-nitride-based UV laser diodes*, in *Semiconductor Nanophotonics: Materials, Models, and Devices*, Eds. M. Kneissl, A. Knorr, S. Reitzenstein, A. Hoffmann, Springer International Publishing, 2020.

[6] N. Johnson, B. Cheng, S. Choi, C. Chua, C. Knollenberg, J. Northrup, M. Teepe, T. Wunderer, Z. Yang, *Mid-UV AlGaN lasers on bulk AlN substrates*, in *Proc. Int. Workshop Nitrides*, pages 2–4, 2012.

[7] J. Jeschke, M. Martens, A. Knauer, V. Kueller, U. Zeimer, C. Netzel, C. Kuhn, F. Krueger, C. Reich, T. Wernicke, M. Kneissl, M. Weyers, *UV-C Lasing From AlGaN Multiple Quantum Wells on Different Types of AlN/Sapphire Templates*, IEEE Photonics Technol. Lett. **27**, 1969 (2015).

[8] Z. Bryan, I. Bryan, S. Mita, J. Tweedie, Z. Sitar, R. Collazo, *Strain dependence on polarization properties of AlGaN and AlGaN-based ultraviolet lasers grown on AlN substrates*, Applied Physics Letters **106**, 232101 (2015).

[9] Editorial, *Scrutinizing lasers*, Nature Photonics **11**, 139 (2017).

[10] H. Yoshida, Y. Yamashita, M. Kuwabara, H. Kan, *Demonstration of an ultraviolet 336 nm AlGaN multiple-quantum-well laser diode*, Applied Physics Letters **93**, 241106 (2008).

[11] S. Okawara, Y. Aoki, Y. Yamashita, Y. Yoshida, *presented at 6th Int. Symp. Growth III-Nitrides (ISGN-6)*, 2015.

[12] Z. Zhang, M. Kushimoto, T. Sakai, N. Sugiyama, L. J. Schowalter, C. Sasaoka, H. Amano, *A 271.8 nm deep-ultraviolet laser diode for room temperature operation*, Applied Physics Express **12**, 124003 (2019).

[13] K. Sato, S. Yasue, K. Yamada, S. Tanaka, T. Omori, S. Ishizuka, S. Teramura, Y. Ogino, S. Iwayama, H. Miyake, M. Iwaya, T. Takeuchi, S. Kamiyama, I. Akasaki, *Room-temperature operation of AlGaN ultraviolet-B laser diode at 298 nm on lattice-relaxed $Al_{0.6}Ga_{0.4}N$/AlN/sapphire*, Applied Physics Express **13**, 031004 (2020).

[14] J. Eichler, H. J. Eichler, *Laser - Bauformen, Strahlführung, Anwendungen*, Springer, 1998.

[15] L. A. Coldren, S. W. Corzine, *Diode Lasers and Photonic Integrated Circuits*, John Wiley & Sons, 1995.

[16] J. Xie, S. Mita, Z. Bryan, W. Guo, L. Hussey, B. Moody, R. Schlesser, R. Kirste, M. Gerhold, R. Collazo, Z. Sitar, *Lasing and longitudinal cavity modes in photo-pumped deep ultraviolet AlGaN heterostructures*, Applied Physics Letters **102**, 171102 (2013).

[17] V. G. Deibuk, A. V. Voznyi, *Thermodynamic stability and redistribution of charges in ternary AlGaN, InGaN, and InAlN alloys*, Semiconductors **39**, 623 (2005).

[18] A. Khan, K. Balakrishnan, T. Katona, *Ultraviolet light-emitting diodes based on group three nitrides*, Nature Photonics **2**, 77 (2008).

[19] T. Wunderer, C. L. Chua, J. E. Northrup, Z. Yang, N. M. Johnson, M. Kneissl, G. A. Garrett, H. Shen, M. Wraback, B. Moody, H. S. Craft, R. Schlesser, R. F. Dalmau, Z. Sitar, *Optically pumped UV lasers grown on bulk AlN substrates*, Physica Status Solidi (C) **9**, 822 (2012).

[20] C. Hartmann, J. Wollweber, S. Sintonen, A. Dittmar, L. Kirste, S. Kollowa, K. Irmscher, M. Bickermann, *Preparation of deep UV transparent AlN substrates with high structural perfection for optoelectronic devices*, CrystEngComm **18**, 3488 (2016).

[21] B. SaifAddin, C. J. Zollner, A. Almogbel, H. Foronda, F. Wu, A. Albadri, A. Al Yamani, M. Iza, S. Nakamura, S. P. DenBaars, J. S. Speck, *Developments in AlGaN and UV-C LEDs grown on SiC*, Proc. SPIE **10554**, 105541E (2018).

[22] S. Zhao, S. M. Sadaf, S. Vanka, Y. Wang, R. Rashid, Z. Mi, *Sub-milliwatt AlGaN nanowire tunnel junction deep ultraviolet light emitting diodes on silicon operating at 242 nm*, Applied Physics Letters **109**, 201106 (2016).

[23] O. Reentilä, F. Brunner, A. Knauer, A. Mogilatenko, W. Neumann, H. Protzmann, M. Heuken, M. Kneissl, M. Weyers, G. Tränkle, *Effect of AlN nucleation layer growth on AlN material quality*, Journal of Crystal Growth **310**, 4932 (2008).

[24] V. Kueller, A. Knauer, U. Zeimer, H. Rodriguez, A. Mogilatenko, M. Kneissl, M. Weyers, *(Al,Ga)N overgrowth over AlN ridges oriented in [1120] and [1100] direction*, Physica Status Solidi (C) **8**, 2022 (2011).

[25] N. Susilo, S. Hagedorn, D. Jaeger, H. Miyake, U. Zeimer, C. Reich, B. Neuschulz, L. Sulmoni, M. Guttmann, F. Mehnke, C. Kuhn, T. Wernicke, M. Weyers,

M. Kneissl, *AlGaN-based deep UV LEDs grown on sputtered and high temperature annealed AlN/sapphire*, Applied Physics Letters **112**, 041110 (2018).

[26] R. France, T. Xu, P. Chen, R. Chandrasekaran, T. D. Moustakas, *Vanadium-based Ohmic contacts to n-AlGaN in the entire alloy composition*, Applied Physics Letters **90**, 062115 (2007).

[27] E. F. Schubert, *Light-Emitting Diodes*, chapter 4, Cambridge University Press, 2nd edition, (2006).

[28] F. Bernardini, V. Fiorentini, D. Vanderbilt, *Spontaneous polarization and piezoelectric constants of III-V nitrides*, Physical Review B **56**, R10024 (1997).

[29] D. A. B. Miller, D. S. Chemla, T. C. Damen, A. C. Gossard, W. Wiegmann, T. H. Wood, C. A. Burrus, *Band-Edge Electroabsorption in Quantum Well Structures: The Quantum-Confined Stark Effect*, Physical Review Letters **53**, 2173 (1984).

[30] J. Piprek, *Semiconductor optoelectronic devices: Introduction to physics and simulation*, Elsevier, 2013.

[31] C. Reich, M. Guttmann, M. Feneberg, T. Wernicke, F. Mehnke, C. Kuhn, J. Rass, M. Lapeyrade, S. Einfeldt, A. Knauer, V. Kueller, M. Weyers, R. Goldhahn, M. Kneissl, *Strongly transverse-electric-polarized emission from deep ultraviolet AlGaN quantum well light emitting diodes*, Applied Physics Letters **107**, 142101 (2015).

[32] L. Q. Zhang, D. S. Jiang, J. J. Zhu, D. G. Zhao, Z. S. Liu, S. M. Zhang, H. Yang, *Confinement factor and absorption loss of AlInGaN based laser diodes emitting from ultraviolet to green*, Journal of Applied Physics **105**, 023104 (2009).

[33] K. Bellmann, *Epitaxial growth of GaN quantum dots on smooth AlN*, Dissertation, Technische Universität Berlin, 2018.

[34] G. B. Stringfellow, *Organometallic Vapor-Phase Epitaxy: Theory and Practice*, Academic Press, San Diego, 1999.

[35] C. Stampfl, C. Van de Walle, *Density-functional calculations for III-V nitrides using the local-density approximation and the generalized gradient approximation*, Physical Review B **59**, 5521 (1999).

[36] Y. Kida, T. Shibata, H. Naoi, H. Miyake, K. Hiramatsu, M. Tanaka, *Growth of Crack-Free and High-Quality AlGaN with High Al Content Using Epitaxial AlN (0001) Films on Sapphire*, Physica Status Solidi (A) **194**, 498 (2002).

[37] M. E. Levinshtein, S. L. Rumyantsev, M. S. Shur, *Properties of Advanced Semiconductor Materials: GaN, AIN, InN, BN, SiC, SiGe*, John Wiley and Sons, 2001.

[38] I. Bryan, Z. Bryan, S. Mita, A. Rice, J. Tweedie, R. Collazo, Z. Sitar, *Surface kinetics in AlN growth: A universal model for the control of surface morphology in III-nitrides*, Journal of Crystal Growth **438**, 81 (2016).

[39] W.-K. Burton, N. Cabrera, F. C. Frank, *The growth of crystals and the equilibrium structure of their surfaces*, Philosophical Transactions of the Royal Society of London. Series A, Mathematical and Physical Sciences **243**, 299 (1951).

[40] R. L. Schwoebel, E. J. Shipsey, *Step Motion on Crystal Surfaces*, Journal of Applied Physics **37**, 3682 (1966).

[41] K. Bellmann, U. W. Pohl, C. Kuhn, T. Wernicke, M. Kneissl, *Controlling the morphology transition between step-flow growth and step-bunching growth*, Journal of Crystal Growth **478**, 187 (2017).

[42] J. Enslin, A. Knauer, F. Mogilatenko, A. Mehnke, M. Martens, C. Kuhn, T. Wernicke, M. Weyers, M. Kneissl, *Determination of Sapphire Off-Cut and Its Influence on the Morphology and Local Defect Distribution in Epitaxially Laterally Overgrown AlN for Optically Pumped UVC Lasers*, Physica Status Solidi (A) **216**, 1900682 (2019).

[43] F. Mehnke, T. Wernicke, H. Pingel, C. Kuhn, C. Reich, V. Kueller, A. Knauer, M. Lapeyrade, M. Weyers, M. Kneissl, *Highly conductive n-$Al_xGa_{1-x}N$ layers with aluminum mole fractions above 80%*, Applied Physics Letters **103**, 212109 (2013).

[44] V. Küller, *Versetzungsreduzierte AlN- und AlGaN-Schichten als Basis für UV LEDs*, Dissertation, Technische Universität Berlin, (2014).

[45] M. Martens, F. Mehnke, C. Kuhn, C. Reich, V. Kueller, A. Knauer, C. Netzel, C. Hartmann, J. Wollweber, J. Rass, T. Wernicke, M. Bickermann, M. Weyers, M. Kneissl, *Performance Characteristics of UV-C AlGaN-Based Lasers Grown on Sapphire and Bulk AlN Substrates*, IEEE Photonics Technology Letters **26**, 342 (2014).

[46] U. W. Pohl, *Epitaxy of Semiconductors, Introduction to Physical Principles*, Graduate Texts in Physics, Springer-Verlag, 2013.

[47] T. Shitara, T. Nishinaga, *Surface Diffusion Length of Gallium during MBE Growth on the Various Misoriented GaAs(001) Substrates*, Japanese Journal of Applied Physics **28**, 1212 (1989).

[48] M. Pristovsek, K. Bellmann, F. Mehnke, J. Stellmach, T. Wernicke, M. Kneissl, *Surface reconstructions of (0001) AlN during metal-organic vapor phase epitaxy*, Physica Status Solidi (B) **254**, 1600711 (2017).

[49] C. Kuhn, T. Simoneit, M. Martens, T. Markurt, J. Enslin, F. Mehnke, K. Bellmann, T. Schulz, M. Albrecht, T. Wernicke, M. Kneissl, *MOVPE Growth of Smooth and Homogeneous $Al_{0.8}Ga_{0.2}N$:Si Superlattices as UVC Laser Cladding Layers*, WILEY-VCH, Weinheim. Physica Status Solidi (A) **215**, 1800005 (2018).

[50] T. Zywietz, J. Neugebauer, M. Scheffler, *Adatom diffusion at GaN* (0001) *and* (000$\bar{1}$) *surfaces*, Applied Physics Letters **73**, 487 (1998).

[51] A. Ishibashi, H. Takeishi, M. Mannoh, Y. Yabuuchi, Y. Ban, *Residual impurities in GaN/Al2O3 grown by metalorganic vapor phase epitaxy*, Journal of Electronic Materials **25**, 799 (1996).

[52] C. Kuhn, T. Simoneit, M. Martens, T. Markurt, J. Enslin, F. Mehnke, K. Bellmann, T. Schulz, M. Albrecht, T. Wernicke, M. Kneissl, *MOVPE Growth of Smooth and Homogeneous $Al_{0.8}Ga_{0.2}N$:Si Superlattices as UVC Laser Cladding Layers*, Physica Status Solidi (A) **215**, 1870032 (2018).

[53] S. A. Nikishin, *III-Nitride Short Period Superlattices for Deep UV Light Emitters*, Applied Sciences **8** (2018).

[54] H.-M. Wang, J.-P. Zhang, C.-Q. Chen, Q. Fareed, J.-W. Yang, M. A. Khan, *AlN/AlGaN superlattices as dislocation filter for low-threading-dislocation thick AlGaN layers on sapphire*, Applied Physics Letters **81**, 604 (2002).

[55] T. Wang, Y. H. Liu, Y. B. Lee, Y. Izumi, J. P. Ao, J. Bai, H. D. Li, S. Sakai, *Fabrication of high performance of AlGaN/GaN-based UV light-emitting diodes*, Journal of Crystal Growth **235**, 177 (2002).

[56] N. Nakada, H. Ishikawa, T. Egawa, T. Jimbo, *Suppression of Crack Generation in GaN/AlGaN Distributed Bragg Reflector on Sapphire by the Insertion of GaN/AlGaN Superlattice Grown by Metal-Organic Chemical Vapor Deposition*, Japanese Journal of Applied Physics **42**, L144 (2003).

[57] Z. Ren, Q. Sun, S.-Y. Kwon, J. Han, K. Davitt, Y. K. Song, A. V. Nurmikko, H.-K. Cho, W. Liu, J. A. Smart, L. J. Schowalter, *Heteroepitaxy of AlGaN on bulk AlN substrates for deep ultraviolet light emitting diodes*, Applied Physics Letters **91**, 051116 (2007).

[58] S. Keller, P. Waltereit, P. Cantu, U. K. Mishra, J. S. Speck, S. P. DenBaars, *Electrical and structural properties of AlGaN/AlGaN superlattice structures grown by metal-organic chemical vapor deposition*, Optical Materials **23**, 187 (2003).

[59] W. H. Sun, J. P. Zhang, J. W. Yang, H. P. Maruska, M. A. Khan, R. Liu, F. A. Ponce, *Fine structure of AlN/AlGaN superlattice grown by pulsed atomic-layer epitaxy for dislocation filtering*, Applied Physics Letters **87**, 211915 (2005).

[60] R. McClintock, A. Yasan, K. Mayes, D. Shiell, S. R. Darvish, P. K. M. Razeghi, *High quantum efficiency AlGaN solar-blind p-i-n photodiodes*, Applied Physics Letters **84**, 1248 (2004).

[61] F. Mehnke, X. T. Trinh, H. Pingel, T. Wernicke, E. Janzén, N. T. Son, M. Kneissl, *Electronic properties of Si-doped $Al_xGa_{1-x}N$ with aluminum mole fractions above 80%*, Journal of Applied Physics **120**, 145702 (2016).

[62] J. Enslin, F. Mehnke, A. Mogilatenko, K. Bellmann, M. Guttmann, C. Kuhn, J. Rass, N. Lobo-Ploch, T. Wernicke, M. Weyers, M. Kneissl, *Metamorphic Al0.5Ga0.5N:Si on AlN/sapphire for the growth of UVB LEDs*, Journal of Crystal Growth **464**, 185 (2017).

[63] M. Dauelsberg, D. Brien, H. Rauf, F. Reiher, J. Baumgartl, O. Häberlen, A. S. Segal, A. V. Lobanova, E. V. Yakovlev, R. A. Talalaev, *On mechanisms governing AlN and AlGaN growth rate and composition in large substrate size planetary MOVPE reactors*, Journal of Crystal Growth **373**, 103 (2014).

[64] B. Fultz, J. M. Howe, *Transmission Electron Microscopy and Diffractometry of Materials*, pages 583–609, Springer-Verlag Berlin Heidelberg, 3rd edition, 2008.

[65] T. Walther, H. Amari, I. M. Ross, T. Wang, A. G. Cullis, *Lattice resolved annular dark-field scanning transmission electron microscopy of (Al, In)GaN/GaN layers for measuring segregation with sub-monolayer precision*, Journal of Materials Science **48**, 2883 (2013).

[66] C. Kuhn, M. Martens, F. Mehnke, J. Enslin, P. Schneider, C. Reich, F. Krueger, J. Rass, J. B. Park, V. Kueller, A. Knauer, T. Wernicke, M. Weyers, M. Kneissl, *Influence of waveguide strain and surface morphology on AlGaN-based deep UV laser characteristics*, IOP Publishing. doi.org/10.1088/1361-6463/aadb84. Journal of Physics D: Applied Physics **51**, 415101 (2018).

[67] U. Zeimer, V. Kueller, A. Knauer, M. Weyers, M. Kneissl, *High quality AlGaN grown on ELO AlN/sapphire templates*, Journal of Crystal Growth **377**, 32 (2013).

[68] A. Mogilatenko, V. Kueller, A. Knauer, J. Jeschke, U. Zeimer, M. Weyers, G. Tränkle, *Defect analysis in AlGaN layers on AlN templates obtained by epitaxial lateral overgrowth*, Journal of Crystal Growth **402**, 222 (2014).

[69] A. Mogilatenko, J. Enslin, A. Knauer, F. Mehnke, K. Bellmann, T. Wernicke, M. Weyers, M. Kneissl, *V-pit to truncated pyramid transition in AlGaN-based heterostructures*, Semiconductor Science and Technology **30**, 114010 (2015).

[70] M. A. Moram, M. E. Vickers, *X-ray diffraction of III-nitrides*, Reports on Progress in Physics **72**, 036502 (2009).

[71] J. R. Grandusky, J. A. Smart, M. C. Mendrick, L. J. Schowalter, K. X. Chen, E. F. Schubert, *Pseudomorphic growth of thick n-type $Al_xGa_{1-x}N$ layers on low-defect density bulk AlN substrates for UV LED applications*, Journal of Crystal Growth **311**, 2864 (2009).

[72] B. Heying, E. J. Tarsa, C. R. Elsass, P. Fini, S. P. DenBaars, J. S. Speck, *Dislocation mediated surface morphology of GaN*, Journal of Applied Physics **85**, 6470 (1999).

[73] Q. Sun, C. D. Yerino, T. S. Ko, Y. S. Cho, I.-H. Lee, J. Han, M. E. Coltrin, *Understanding nonpolar GaN growth through kinetic Wulff plots*, Journal of Applied Physics **104**, 093523 (2008).

[74] M. S. Kumar, J. Y. Park, Y. S. Lee, S. J. Chung, C.-H. Hong, E.-K. Suh, *Effect of barrier growth temperature on morphological evolution of green InGaN/GaN multi-quantum well heterostructures*, Journal of Physics D: Applied Physics **40**, 5050 (2007).

[75] K. Koike, S. Lee, S. R. Cho, J. Park, H. Lee, J.-S. Ha, S.-K. Hong, H.-Y. Lee, M.-W. Cho, T. Yao, *Improvement of Light Extraction Efficiency and Reduction of Leakage Current in GaN-Based LED via V-Pit Formation*, IEEE Photonics Technol. Lett. **24**, 449 (2012).

[76] M. Kneissl, T. Kolbe, C. Chua, V. Kueller, N. Lobo, J. Stellmach, A. Knauer, H. Rodriguez, S. Einfeldt, Z. Yang, N. M. Johnson, M. Weyers, *Advances in group III-nitride-based deep UV light-emitting diode technology*, Semiconductor Science and Technology **26**, 014036 (2011).

[77] V. Kueller, A. Knauer, F. Brunner, U. Zeimer, H. Rodriguez, M. Kneissl, M. Weyers, *Growth of AlGaN and AlN on patterned AlN/sapphire templates*, Journal of Crystal Growth **315**, 200 (2011).

[78] C. Bazioti, E. Papadomanolaki, T. Kehagias, T. Walther, J. Smalc-Koziorowska, E. Pavlidou, P. Komninou, T. Karakostas, E. Iliopoulos, G. P. Dimitrakopulos, *Defects, strain relaxation, and compositional grading in high indium content InGaN epilayers grown by molecular beam epitaxy*, Journal of Applied Physics **118**, 155301 (2015).

[79] M. Kneissl, T. Wernicke, *Optical and structural properties of InGaN light-emitters on non-polar semipolar GaN*, in *III-Nitride Semiconductors and their Modern Devices*, Eds. B. Gil, Oxford University Press, 2013.

[80] C. Stampfl, C. G. Van de Walle, *Energetics and electronic structure of stacking faults in AlN, GaN, and InN*, Physical Review B **57**, R15052 (1998).

[81] J. Smalc-Koziorowska, C. Bazioti, M. Albrecht, G. P. Dimitrakopulos, *Stacking fault domains as sources of a-type threading dislocations in III-nitride heterostructures*, Applied Physics Letters **108**, 051901 (2016).

[82] E. V. Yakovlev, R. A. Talalaev, A. S. Segal, A. V. Lobanova, W. V. Lundin, E. E. Zavarin, M. A. Sinitsyn, A. F. Tsatsulnikov, A. E. Nikolaev, *Hydrogen effects in III-nitride MOVPE*, Journal of Crystal Growth **310**, 4862 (2008).

[83] P. Vennéguès, B. Beaumont, S. Haffouz, M. Vaille, P. Gibart, *Influence of in situ sapphire surface preparation and carrier gas on the growth mode of GaN in MOVPE*, Journal of Crystal Growth **187**, 167 (1998).

[84] Y.-T. Moon, D.-J. Kim, K.-M. Song, C.-J. Choi, S.-H. Han, T.-Y. Seong, S.-J. Park, *Effects of thermal and hydrogen treatment on indium segregation in InGaN/GaN multiple quantum wells*, Journal of Applied Physics **89**, 6514 (2001).

[85] S. Perkowitz, *Optical Characterization of Semiconductors. Infrared, Raman, and Photoluminescence Spectroscopy*, Academic Press, Harcourt Brace and Company, 1993.

[86] M. G. R. Martens, *Optical gain and modal loss in AlGaN based deep UV lasers*, Dissertation, Technische Universität Berlin, 2018.

[87] S. Okawara, Y. Aoki, M. Kuwabara, Y. Takagi, J. Maeda, H. Yoshida, *Nitride-based stacked laser diodes with a tunnel junction*, Applied Physics Express **11**, 012701 (2018).

[88] X.-H. Li, T. Detchprohm, T.-T. Kao, M. M. Satter, S.-C. Shen, P. D. Yoder, R. D. Dupuis, S. Wang, Y. O. Wei, H. Xie, A. M. Fischer, F. A. Ponce, T. Wernicke, C. Reich, M. Martens, M. Kneissl, *Low-threshold stimulated emission at 249 nm and 256 nm from AlGaN-based multiple-quantum-well lasers grown on sapphire substrates*, Applied Physics Letters **105**, 141106 (2014).

[89] W. W. Chow, M. Kneissl, *Laser gain properties of AlGaN quantum wells*, Journal of Applied Physics **98**, 114502 (2005).

[90] J. Jeschke, *Entwicklung von optisch pumpbaren UVC-Lasern auf AlGaN-Basis*, Dissertation, Technische Universität Berlin, 2018.

[91] T. Takano, T. Mino, J. Sakai, N. Noguchi, K. Tsubaki, H. Hirayama, *Deep-ultraviolet light-emitting diodes with external quantum efficiency higher than 20% at 275 nm achieved by improving light-extraction efficiency*, Applied Physics Express **10**, 031002 (2017).

[92] M. Kneissl, *UV LED Efficiency NOV 2018, www.ifkp.tu-berlin.de/fileadmin/i1/Kneissl/EQE_20181120.pdf*, Dec 18th 2019.

[93] Y. Taniyasu, M. Kasu, T. Makimoto, *An aluminum nitride light-emitting diode with a wavelength of 210 nm*, Nature **441**, 325 (2006).

[94] F. Mehnke, L. Sulmoni, M. Guttmann, T. Wernicke, M. Kneissl, *Influence of light absorption on the performance characteristicsof UV LEDs with emission between 239 and 217 nm*, Applied Physics Express **12**, 012008 (2019).

[95] Nobel Media AB, *The Nobel Prize in Physics 2014, https://www.nobelprize.org/prizes/physics/2014/summary*, Jan 23rd 2020.

[96] S. Nakamura, M. Senoh, S. ichi Nagahama, N. Iwasa, T. Yamada, T. Matsushita, H. Kiyoku, Y. Sugimoto, *InGaN-Based Multi-Quantum-Well-Structure Laser Diodes*, Japanese Journal of Applied Physics **35**, L74 (1996).

[97] I. Akasaki, S. Sota, H. Sakai, T. Tanaka, M. Koike, H. Amano, *Shortest wavelength semiconductor laser diode*, Electronics Letters **32**, 1105 (1996).

[98] S. ichi Nagahama, T. Yanamoto, M. Sano, T. Mukai, *Ultraviolet GaN Single Quantum Well Laser Diodes*, Japanese Journal of Applied Physics **40**, L785 (2001).

[99] R. Kirste, Q. Guo, J. H. Dycus, A. Franke, S. Mita, B. Sarkar, P. Reddy, J. M. LeBeau, R. Collazo, Z. Sitar, *6 kW/cm2 UVC laser threshold in optically pumped lasers achieved by controlling point defect formation*, Applied Physics Express **11**, 082101 (2018).

[100] F. Mehnke, C. Kuhn, M. Guttmann, C. Reich, T. Kolbe, V. Kueller, A. Knauer, M. Lapeyrade, S. Einfeldt, J. Rass, T. Wernicke, M. Weyers, M. Kneissl, *Efficient charge carrier injection into sub-250 nm AlGaN multiple quantum well light emitting diodes*, Applied Physics Letters **105**, 051113 (2014).

[101] J. R. Grandusky, S. R. Gibb, M. C. Mendrick, L. J. Schowalter, *Properties of Mid-Ultraviolet Light Emitting Diodes Fabricated from Pseudomorphic Layers on Bulk Aluminum Nitride Substrates*, Applied Physics Express **3**, 072103 (2010).

[102] H. Ibach, H. Lüth, *Solid-State Physics. An Introduction to Principles of Materials Science*, Springer Berlin, 4th edition, 2009.

[103] W. Götz, N. M. Johnson, C. Chen, H. Liu, C. Kuo, W. Imler, *Activation energies of Si donors in GaN*, Applied Physics Letters **68**, 3144 (1996).

[104] Y. Taniyasu, M. Kasu, N. Kobayashi, *Intentional control of n-type conduction for Si-doped AlN and $Al_xGa_{1-x}N$ ($0.42 \leq x < 1$)*, Applied Physics Letters **81**, 1255 (2002).

[105] M. L. Nakarmi, K. H. Kim, K. Zhu, J. Y. Lin, H. X. Jiang, *Transport properties of highly conductive n-type Al-rich $Al_xGa_{1-x}N$ ($x \geq 0.7$)*, Applied Physics Letters **85**, 3769 (2004).

[106] T. Tanaka, A. Watanabe, H. Amano, Y. Kobayashi, I. Akasaki, S. Yamazaki, M. Koike, *p-type conduction in Mg-doped GaN and $Al_{0.08}Ga_{0.92}N$ grown by metalorganic vapor phase epitaxy*, Applied Physics Letters **65**, 593 (1994).

[107] W. Götz, N. M. Johnson, J. Walker, D. P. Bour, R. A. Street, *Activation of acceptors in Mg-doped GaN grown by metalorganic chemical vapor deposition*, Applied Physics Letters **68**, 667 (1996).

[108] K. B. Nam, M. L. Nakarmi, J. Li, J. Y. Lin, H. X. Jiang, *Mg acceptor level in AlN probed by deep ultraviolet photoluminescence*, Applied Physics Letters **83**, 878 (2003).

[109] M. L. Nakarmi, N. Nepal, C. Ugolini, T. M. Altahtamouni, J. Y. Lin, H. X. Jiang, *Correlation between optical and electrical properties of Mg-doped AlN epilayers*, Applied Physics Letters **89**, 152120 (2006).

[110] M. L. Nakarmi, K. H. Kim, M. Khizar, Z. Y. Fan, J. Y. Lin, H. X. Jiang, *Electrical and optical properties of Mg-doped $Al_{0.7}Ga_{0.3}N$ alloys*, Applied Physics Letters **86**, 092108 (2005).

[111] R. Gross, A. Marx, *Festkörperphysik*, Oldenbourg Verlag München, 2012.

[112] T. Wunderer, J. E. Northrup, N. M. Johnson, *AlGaN-Based Ultraviolet Laser Diodes*, in *III-Nitride Ultraviolet Emitters: Technology and Applications*, Eds. M. Kneissl, J. Rass, Springer International Publishing, 2016.

[113] P. Kozodoy, M. Hansen, S. P. DenBaars, U. K. Mishra, *Enhanced Mg doping efficiency in $Al_{0.2}Ga_{0.8}N$/GaN superlattices*, Applied Physics Letters **74**, 3681 (1999).

[114] C. Hartmann, J. Wollweber, A. Dittmar, K. Irmscher, A. Kwasniewski, F. Langhans, T. Neugut, M. Bickermann, *Preparation of Bulk AlN Seeds by Spontaneous Nucleation of Freestanding Crystals*, Japanese Journal of Applied Physics **52**, 08JA06 (2013).

[115] K. Thonke, M. Lamprecht, R. Collazo, Z. Sitar, *Optical signatures of silicon and oxygen related DX centers in AlN*, Physica Status Solidi (A) **214**, 1600749 (2017).

[116] B. E. Gaddy, Z. Bryan, I. Bryan, R. Kirste, J. Xie, R. Dalmau, B. Moody, Y. Kumagai, T. Nagashima, Y. Kubota, T. Kinoshita, A. Koukitu, Z. Sitar, R. Collazo, D. L. Irving, *Vacancy compensation and related donor-acceptor pair recombination in bulk AlN*, Applied Physics Letters **103**, 161901 (2013).

[117] S. Dassonneville, A. Amokrane, B. Sieber, J.-L. Farvacque, B. Beaumont, P. Gibart, *Luminescence of epitaxial GaN laterally overgrown on (0001) sapphire substrate: Spectroscopic characterization and dislocation contrasts*, Journal of Applied Physics **89**, 3736 (2001).

[118] R. Rounds, B. Sarkar, A. Klump, C. Hartmann, T. Nagashima, R. Kirste, A. Franke, M. Bickermann, Y. Kumagai, Z. Sitar, R. Collazo, *Thermal conductivity of single-crystalline AlN*, Applied Physics Express **11**, 071001 (2018).

[119] M. Guttmann, J. Höpfner, C. Reich, L. Sulmoni, C. Kuhn, P. Röder, T. Wernicke, M. Kneissl, *Effect of quantum barrier composition on electro-optical properties of AlGaN-based UVC light emitting diodes*, Semiconductor Science and Technology **34**, 085007 (2019).

[120] F. Mehnke, *Design, Epitaxie und Charakterisierung AlGaN-basierter Leuchtdioden mit Emissionswellenlängen unterhalb von 250 nm*, Dissertation, Technische Universität Berlin, 2017.

[121] M. Guttmann, F. Mehnke, B. Belde, F. Wolf, C. Reich, L. Sulmoni, T. Wernicke, M. Kneissl, *Optical light polarization and light extraction efficiency of AlGaN-based LEDs emitting between 264 and 220 nm*, Japanese Journal of Applied Physics **58**, SCCB20 (2019).

[122] M. Martens, C. Kuhn, E. Ziffer, T. Simoneit, V. Kueller, A. Knauer, J. Rass, T. Wernicke, E. Einfeldt, M. Weyers, M. Kneissl, *Low absorption loss p-AlGaN superlattice cladding layer for current-injection deep ultraviolet laser diodes*, Applied Physics Letters **108**, 151108 (2016).

[123] M. Martens, C. Kuhn, T. Simoneit, S. Hagedorn, A. Knauer, T. Wernicke, M. Weyers, M. Kneissl, *The effects of magnesium doping on the modal loss in AlGaN-based deep UV lasers*, Applied Physics Letters **110**, 081103 (2017).

[124] J. F. Muth, J. D. Brown, M. A. L. Johnson, Z. Yu, R. M. Kolbas, J. W. Cook Jr., J. F. Schetzina, *Absorption coefficient and refractive index of GaN, AlN and AlGaN alloys*, in *MRS Internet J. Nitride Semicond. Res.*, Band 4S1, page G5.2, (1999).

[125] W. S. M. Werner, K. Glantschnig, C. Ambrosch-Draxl, *Optical Constants and Inelastic Electron-Scattering Data for 17 Elemental Metals*, Journal of Physical and Chemical Reference Data **38**, 1013 (2009).

[126] L. J. van der Pauw, *A method of measuring specific resistivity and Hall effect of discs of arbitrary shape*, Philips Research Reports **13**, 1 (1958).

[127] J. M. Shah, Y.-L. Li, T. Gessmann, E. F. Schubert, *Experimental analysis and theoretical model for anomalously high ideality factors (n≫2.0) in AlGaN/GaN p-n junction diodes*, Journal of Applied Physics **94**, 2627 (2003).

[128] S. X. Jin, J. Shakya, J. Y. Lin, H. X. Jiang, *Size dependence of III-nitride microdisk light-emitting diode characteristics*, Applied Physics Letters **78**, 3532 (2001).

[129] H. H. Poole, *VIII. On the dielectric constant and electrical conductivity of mica in intense fields*, The London, Edinburgh, and Dublin Philosophical Magazine and Journal of Science **32**, 112 (1916).

[130] J. Frenkel, *On pre-breakdown phenomena in insulators and electronic semiconductors*, Physical Review **54**, 647 (1938).

[131] J. Piprek, *AlGaN polarization doping effects on the efficiency of blue LEDs*, in *Gallium Nitride Materials and Devices VII*, Band 8262, page 82620E, International Society for Optics and Photonics, 2012.

[132] F. Römer, B. Witzigmann, *Acceptor activation model for III-nitride LEDs*, Journal of Computational Electronics **14**, 456 (2015).

[133] J.-Y. Duboz, *GaN/AlGaN superlattices for p contacts in LEDs*, Semiconductor Science and Technology **29**, 035017 (2014).

[134] I. D. Goepfert, E. F. Schubert, A. Osinsky, P. E. Norris, N. N. Faleev, *Experimental and theoretical study of acceptor activation and transport properties in p-type $Al_xGa_{1-x}N/GaN$ superlattices*, Journal of Applied Physics **88**, 2030 (2000).

[135] R. Dingle, H. L. Störmer, A. C. Gossard, W. Wiegmann, *Electron mobilities in modulation-doped semiconductor heterojunction superlattices*, Applied Physics Letters **33**, 665 (1978).

[136] A. Muhin, M. Guttmann, C. Kuhn, E. Mickein, L. Sulmoni, E. Ziffer, N. Susilo, J. R. Aparici, T. Wernicke, M. Kneissl, *Poole-Frenkel-ionization of acceptors in $Al_{0.86}Ga_{0.14}N/Al_{0.65}Ga_{0.35}N$:Mg short-period superlattices*, to be published, 2020.

[137] M. Le Gallo, M. Kaes, A. Sebastian, D. Krebs, *Subthreshold electrical transport in amorphous phase-change materials*, New Journal of Physics **17**, 093035 (2015).

[138] M. Kaes, M. Le Gallo, A. Sebastian, M. Salinga, D. Krebs, *High-field electrical transport in amorphous phase-change materials*, Journal of Applied Physics **118**, 135707 (2015).

[139] M. Kneissl, A. Knorr, S. Reitzenstein, A. Hoffmann, Eds., *Semiconductor Nanophotonics - Materials, Models, Devices*, Springer Nature, 2020.

[140] Z. Bryan, I. Bryan, J. Xie, S. Mita, Z. Sitar, R. Collazo, *High internal quantum efficiency in AlGaN multiple quantum wells grown on bulk AlN substrates*, Applied Physics Letters **106**, 142107 (2015).

[141] K. Sato, S. Yasue, Y. Ogino, S. Tanaka, M. Iwaya, T. Takeuchi, S. Kamiyama, I. Akasaki, *Light confinement and high current density in UVB laser diode structure using Al composition-graded p-AlGaN cladding layer*, Applied Physics Letters **114**, 191103 (2019).

[142] C. Kuhn, L. Sulmoni, M. Guttmann, J. Glaab, N. Susilo, T. Wernicke, M. Weyers, M. Kneissl, *MOVPE-grown AlGaN-based tunnel heterojunctions enabling fully transparent UVC LEDs*, Photonics Research **7**, B7 (2019).

[143] Ioffe Physico-Technical Institute, *Semiconductors on NSM: Ge - Germanium. Band structure and carrier concentration, www.ioffe.ru/SVA/NSM/Semicond/Ge/bandstr.html*, Jan 23rd 2020.

[144] L. Esaki, Y. Kurose, T. Suzuki, *19F-23 Ge P-N Junction - Internal Field Emission*, Meeting Abstracts of the Physical Society of Japan **12**, 85 (1957).

[145] L. Esaki, *New Phenomenon in Narrow Germanium p-n Junctions*, Physical Review **109**, 603. doi.org/10.1103/PhysRev.109.603 (1958).

[146] M. Grundmann, *The Physics of Semiconductors*, Springer Berlin, 2006.

[147] S. Rajan, T. Takeuchi, *III-Nitride Tunnel Junctions and Their Applications*, in *III-Nitride Based Light Emitting Diodes and Applications*, Eds. T.-Y. Seong, J. Han, H. Amano, H. Morkoç, Springer Singapore, 2017.

[148] Nobel Media AB, *The Nobel Prize in Physics 1973, https://www.nobelprize.org/prizes/physics/1973/summary*, Jan 23rd 2020.

[149] S. M. Sze, K. K. Ng, *Physics of Semiconductor Devices*, John Wiley & Sons, 3rd edition, 2007.

[150] M. J. Grundmann, U. K. Mishra, *Multi-color light emitting diode using polarization-induced tunnel junctions*, Physica Status Solidi (C) **4**, 2830 (2007).

[151] M. Malinverni, D. Martin, N. Grandjean, *InGaN based micro light emitting diodes featuring a buried GaN tunnel junction*, Applied Physics Letters **107**, 051107 (2015).

[152] S. M. Sadaf, Y.-H. Ra, H. P. T. Nguyen, M. Djavid, Z. Mi, *Alternating-Current InGaN/GaN Tunnel Junction Nanowire White-Light Emitting Diodes*, Nano Letters **15**, 6696 (2015).

[153] E. C. Young, B. P. Yonkee, F. Wu, S. H. Oh, S. P. DenBaars, S. Nakamura, J. S. Speck, *Hybrid tunnel junction contacts to III-nitride light-emitting diodes*, Applied Physics Express **9**, 022102 (2016).

[154] C. Skierbiszewski, G. Muziol, K. Nowakowski-Szkudlarek, H. Turski, M. Siekacz, A. Feduniewicz-Zmuda, A. Nowakowska-Szkudlarek, M. Sawicka, P. Perlin, *True-blue laser diodes with tunnel junctions grown monolithically by plasma-assisted molecular beam epitaxy*, Applied Physics Express **11**, 034103 (2018).

[155] I. P. Smorchkova, E. Haus, B. Heying, P. Kozodoy, P. Fini, J. P. Ibbetson, S. Keller, S. P. DenBaars, J. S. Speck, U. K. Mishra, *Mg doping of GaN layers grown by plasma-assisted molecular-beam epitaxy*, Applied Physics Letters **76**, 718 (2000).

[156] M. Stutzmann, O. Ambacher, A. Cros, M. Brandt, H. Angerer, R. Dimitrov, N. Reinacher, T. Metzger, R. Höpler, D. Brunner, F. Freudenberg, R. Handschuh, C. Deger, *Properties and applications of MBE grown AlGaN*, Materials Science and Engineering: B **50**, 212 (1997).

[157] S.-R. Jeon, Y.-H. Song, H.-J. Jang, G. M. Yang, *Lateral current spreading in GaN-based light-emitting diodes utilizing tunnel contact junctions*, Applied Physics Letters **78**, 3265 (2001).

[158] S. Neugebauer, M. P. Hoffmann, H. Witte, J. Bläsing, A. Dadgar, A. Strittmatter, T. Niermann, M. Narodovitch, M. Lehmann, *All metalorganic chemical vapor phase epitaxy of p/n-GaN tunnel junction for blue light emitting diode applications*, Applied Physics Letters **110**, 102104 (2017).

[159] D. Hwang, A. J. Mughal, M. S. Wong, A. I. Alhassan, S. Nakamura, S. P. DenBaars, *Micro-light-emitting diodes with III–nitride tunnel junction contacts grown by metalorganic chemical vapor deposition*, Applied Physics Express **11**, 012102 (2018).

[160] M. Feneberg, S. Osterburg, K. Lange, C. Lidig, B. Garke, R. Goldhahn, E. Richter, C. Netzel, M. D. Neumann, N. Esser, S. Fritze, H. Witte, J. Bläsing, A. Dadgar, A. Krost, *Band gap renormalization and Burstein-Moss effect in silicon- and germanium-doped wurtzite GaN up to* $10^{20}\mathrm{cm}^{-3}$, Phys. Rev. B **90**, 075203 (2014).

[161] J. Simon, Z. Zhang, K. Goodman, H. Xing, T. Kosel, P. Fay, D. Jena, *Polarization-Induced Zener Tunnel Junctions in Wide-Band-Gap Heterostructures*, Physical Review Letters **103**, 026801 (2009).

[162] T. Takeuchi, G. Hasnain, S. Corzine, M. Hueschen, J. R. P. Schneider, C. Kocot, M. Blomqvist, Y. l. Chang, D. Lefforge, M. R. Krames, L. W. Cook, S. A. Stockman, *GaN-Based Light Emitting Diodes with Tunnel Junctions*, Japanese Journal of Applied Physics **40**, L861 (2001).

[163] M. Diagne, Y. He, H. Zhou, E. Makarona, A. V. Nurmikko, J. Han, K. E. Waldrip, J. J. Figiel, T. Takeuchi, M. Krames, *Vertical cavity violet light emitting diode incorporating an aluminum gallium nitride distributed Bragg mirror and a tunnel junction*, Applied Physics Letters **79**, 3720 (2001).

[164] Y. Kuwano, M. Kaga, T. Morita, K. Yamashita, K. Yagi, M. Iwaya, T. Takeuchi, S. Kamiyama, I. Akasaki, *Lateral Hydrogen Diffusion at p-GaN Layers in Nitride-Based Light Emitting Diodes with Tunnel Junctions*, Japanese Journal of Applied Physics **52**, 08JK12 (2013).

[165] V. Fan Arcara, B. Damilano, G. Feuillet, A. Courville, S. Chenot, J.-Y. Duboz, *(Ga,In)N/GaN light emitting diodes with a tunnel junction and a rough n-contact layer grown by metalorganic chemical vapor deposition*, AIP Advances **9**, 055101 (2019).

[166] Y. Zhang, S. Krishnamoorthy, J. M. Johnson, F. Akyol, A. Allerman, M. W. Moseley, A. Armstrong, J. Hwang, S. Rajan, *Interband tunneling for hole injection in III-nitride ultraviolet emitters*, Applied Physics Letters **106**, 141103 (2015).

[167] Y. Zhang, S. Krishnamoorthy, F. Akyol, S. Bajaj, A. A. Allerman, M. W. Moseley, A. M. Armstrong, S. Rajan, *Tunnel-injected sub-260 nm ultraviolet light emitting diodes*, Applied Physics Letters **110**, 201102 (2017).

[168] V. Fan Arcara, B. Damilano, G. Feuillet, S. Vézian, K. Ayadi, S. Chenot, J.-Y. Duboz, *Ge doped GaN and Al0.5Ga0.5N-based tunnel junctions on top of visible and UV light emitting diodes*, Journal of Applied Physics **126**, 224503 (2019).

[169] Y. Zhang, S. Krishnamoorthy, F. Akyol, A. A. Allerman, M. W. Moseley, A. M. Armstrong, S. Rajan, *Design and demonstration of ultra-wide bandgap AlGaN tunnel junctions*, Applied Physics Letters **109**, 121102 (2016).

[170] J.-Y. Duboz, B. Vinter, *Theoretical estimation of tunnel currents in hetero-junctions: The special case of nitride tunnel junctions*, Journal of Applied Physics **126**, 174501 (2019).

[171] M. Malinverni, C. Tardy, M. Rossetti, A. Castiglia, M. Duelk, C. Velez, D. Martin, N. Grandjean, *InGaN laser diode with metal-free laser ridge using n^+-GaN contact layers*, Applied Physics Express **9**, 061004 (2016).

[172] M. Siekacz, G. Muziol, M. Hajdel, M. Żak, K. Nowakowski-Szkudlarek, H. Turski, M. Sawicka, P. Wolny, A. Feduniewicz-Żmuda, S. Stanczyk, J. Moneta, C. Skierbiszewski, *Stack of two III-nitride laser diodes interconnected by a tunnel junction*, Opt. Express **27**, 5784 (2019).

[173] Semiconductor Today, *BluGlass demonstrates functioning tunnel junctions, enabling cascaded LEDs. www.semiconductor-today.com/news_items/2019/jan/bluglass_040119*, Jan 4th 2019.

[174] Semiconductor Today, *BluGlass presents latest data on development of RPCVD-grown tunnel junctions for LEDs. www.semiconductor-today.com/news_items/2019/feb/bluglass_070219*, Feb. 7th 2019.

[175] S. Keller, P. Cantu, C. Moe, Y. Wu, S. Keller, U. K. Mishra, J. S. Speck, S. P. DenBaars, *Metalorganic chemical vapor deposition conditions for efficient silicon doping in high Al-composition AlGaN films*, Japanese Journal of Applied Physics **44**, 7227 (2005).

[176] C. G. V. de Walle, J. Neugebauer, *First-principles calculations for defects and impurities: Applications to III-nitrides*, Journal of Applied Physics **95**, 3851 (2004).

[177] Y. Arakawa, *Progress in GaN-based quantum dots for optoelectronics applications*, IEEE Journal of Selected Topics in Quantum Electronics **8**, 823 (2002).

[178] K. Bellmann, F. Tabataba-Vakili, T. Wernicke, A. Strittmatter, G. Callsen, A. Hoffmann, M. Kneissl, *Desorption induced GaN quantum dots on (0001) AlN by MOVPE*, Physica Status Solidi (RRL) **9**, 526 (2015).

[179] S. Nakamura, G. Fasol, *The Blue Laser Diode*, Springer Berlin, 1997.

[180] M. Hansen, J. Piprek, P. M. Pattison, J. S. Speck, S. Nakamura, S. P. DenBaars, *Higher efficiency InGaN laser diodes with an improved quantum well capping configuration*, Applied Physics Letters **81**, 4275 (2002).

[181] Y. Taniyasu, M. Kasu, T. Makimoto, *Electrical conduction properties of n-type Si-doped AlN with high electron mobility ($>100\,cm^2\,V^{-1}\,s^{-1}$)*, Applied Physics Letters **85**, 4672 (2004).

[182] A. E. Romanov, J. S. Speck, *Stress relaxation in mismatched layers due to threading dislocation inclination*, Applied Physics Letters **83**, 2569 (2003).

[183] I. C. Manning, X. Weng, J. D. Acord, M. A. Fanton, D. W. Snyder, J. M. Redwing, *Tensile stress generation and dislocation reduction in Si-doped AlxGa1-xN films*, Journal of Applied Physics **106**, 023506 (2009).

[184] F. Brunner, A. Mogilatenko, V. Kueller, A. Knauer, M. Weyers, *Stress evolution during AlxGa1-xN/AlN growth on sapphire*, Journal of Crystal Growth **376**, 54 (2013).

[185] P. Cantu, F. Wu, P. Waltereit, S. Keller, A. E. Romanov, U. K. Mishra, S. P. DenBaars, J. S. Speck, *Si doping effect on strain reduction in compressively strained Al0.49Ga0.51N thin films*, Applied Physics Letters **83**, 674 (2003).

[186] B. Kuhn, M. Welsch, M. Kessler, F. Scholz, *The Influence of Growth Conditions on the Electrical Properties of Magnesium-Doped GaN Grown by MOVPE*, Physica Status Solidi (A) **176**, 787 (1999).

[187] Y. Ohba, A. Hatano, *A study on strong memory effects for Mg doping in GaN metalorganic chemical vapor deposition*, Journal of Crystal Growth **145**, 214 (1994).

[188] W. Götz, N. M. Johnson, J. Walker, D. P. Bour, H. Amano, I. Akasaki, *Hydrogen passivation of Mg acceptors in GaN grown by metalorganic chemical vapor deposition*, Applied Physics Letters **67**, 2666 (1995).

[189] W. Götz, N. M. Johnson, D. P. Bour, M. D. McCluskey, E. E. Haller, *Local vibrational modes of the Mg-H acceptor complex in GaN*, Applied Physics Letters **69**, 3725 (1996).

[190] S. Nakamura, N. Iwasa, M. Senoh, T. Mukai, *Hole Compensation Mechanism of P-Type GaN Films*, Japanese Journal of Applied Physics **31**, 1258 (1992).

[191] S. Nakamura, T. Mukai, M. Senoh, N. Iwasa, *Thermal Annealing Effects on P-Type Mg-Doped GaN Films*, Japanese Journal of Applied Physics **31**, L139 (1992).

[192] J. Neugebauer, C. V. de Valle, *Role of hydrogen in doping of GaN*, Applied Physics Letters **68**, 1829 (1996).

[193] A. Y. Polyakov, N. B. Smirnov, S. J. Pearton, F. Ren, B. Theys, F. Jomard, Z. Teukam, V. A. Dmitriev, A. E. Nikolaev, A. S. Usikov, I. P. Nikitina, *Fermi level dependence of hydrogen diffusivity in GaN*, Applied Physics Letters **79**, 1834 (2001).

[194] R. Czernecki, E. Grzanka, R. Jakiela, S. Grzanka, C. Skierbiszewski, H. Turski, P. Perlin, T. Suski, K. Donimirski, M. Leszczynski, *Hydrogen diffusion in GaN:Mg and GaN:Si*, Journal of Alloys and Compounds **747**, 354 (2018).

[195] C. G. V. de Walle, C. Stampfl, J. Neugebauer, *Theory of doping and defects in III-V nitrides*, Journal of Crystal Growth **189-190**, 505 (1998).

[196] S. Nakamura, S. F. Chichibu, Eds., *Introduction to Nitride Semiconductor Blue Lasers and Light Emitting Diodes*, CRC Press, 2000.

[197] S. Figge, R. Kröger, T. Böttcher, P. L. Ryder, D. Hommel, *Magnesium segregation and the formation of pyramidal defects in p-GaN*, Applied Physics Letters **81**, 4748 (2002).

[198] S. Weeke, M. Leyer, M. Pristovsek, F. Brunner, M. Weyers, W. Richter, *Segregation and desorption of antimony in InP (0 0 1) in MOVPE*, Journal of Crystal Growth **298**, 159 (2007).

[199] D. J. Bottomley, *Melting Induced by Epitaxial Stress*, Japanese Journal of Applied Physics **37**, 2652 (1998).

[200] D. J. Bottomley, *Formation and shape of InAs nanoparticles on GaAs surfaces: fundamental thermodynamics*, Japanese Journal of Applied Physics **39**, 4604 (2000).

[201] A. Jayaraman, W. Klement Jr, G. Kennedy, *Melting and polymorphism at high pressures in some group IV elements and III-V compounds with the diamond/zincblende structure*, Physical Review **130**, 540 (1963).

[202] K. M. McPeak, S. V. Jayanti, S. J. P. Kress, S. Meyer, S. Iotti, A. Rossinelli, D. J. Norris, *Plasmonic Films Can Easily Be Better: Rules and Recipes*, ACS Photonics **2**, 326 (2015).

[203] N. Susilo, J. Weinrich, C. Kuhn, L. Sulmoni, T. Wernicke, A. Mogilatenko, M. Kneissl, *Influence of defect generation in the n-side current spreading layer on the performance characteristic of MOVPE grown AlGaN-based deep UV-LEDs*, to be published, 2020.

[204] E. Hecht, *Optik*, Addison-Wesley, 1989.

[205] H. Gobrecht, Eds., *Bergmann Schaefer, Lehrbuch der Experimentalphysik, Band III Optik*, Walter de Gruyter, 7 edition, 1978.

[206] F. Grum, G. W. Luckey, *Optical Sphere Paint and a Working Standard of Reflectance*, Applied Optics **7**, 2289 (1968).

[207] E. R. Young, K. C. Clark, R. B. Bennett, T. L. Houk, *Measurements and parameterization of the bidirectional reflectance factor of BaSO4 paint*, Applied Optics **19**, 3500 (1980).

[208] A. Ferrero, A. M. Rabal, J. Campos, A. Pons, M. L. Hernanz, *Spectral and geometrical variation of the bidirectional reflectance distribution function of diffuse reflectance standards*, Applied Optics **51**, 8535 (2012).

[209] J. Glaab, C. Ploch, R. Kelz, C. Stölmacker, M. Lapeyrade, N. Lobo-Ploch, J. Rass, T. Kolbe, S. Einfeldt, F. Mehnke, C. Kuhn, T. Wernicke, M. Weyers, M. Kneissl, *Degradation of (InAlGa)N-based UV-B light emitting diodes stressed by current and temperature*, Journal of Applied Physics **118**, 094504 (2015).

[210] J. Glaab, J. Haefke, J. Ruschel, M. Brendel, J. Rass, T. Kolbe, A. Knauer, M. Weyers, S. Einfeldt, M. Guttmann, C. Kuhn, J. Enslin, T. Wernicke, M. Kneissl, *Degradation effects of the active region in UV-C light-emitting diodes*, Journal of Applied Physics **123**, 104502 (2018).

[211] J. F. Muth, J. H. Lee, I. K. Shmagin, R. M. Kolbas, H. C. Casey, B. P. Keller, U. K. Mishra, S. P. DenBaars, *Absorption coefficient, energy gap, exciton binding energy, and recombination lifetime of GaN obtained from transmission measurements*, Applied Physics Letters **71**, 2572 (1997).

[212] S. Krishnamoorthy, F. Akyol, S. Rajan, *InGaN/GaN tunnel junctions for hole injection in GaN light emitting diodes*, Applied Physics Letters **105**, 141104 (2014).

[213] S. Krishnamoorthy, T. F. Kent, J. Yang, P. S. Park, R. C. Myers, S. Rajan, *GdN Nanoisland-Based GaN Tunnel Junctions*, Nano Letters **13**, 2570 (2013).

[214] Y. Zhang, Z. Jamal-Eddine, F. Akyol, S. Bajaj, J. M. Johnson, G. Calderon, A. A. Allerman, M. W. Moseley, A. M. Armstrong, J. Hwang, S. Rajan, *Tunnel-injected sub 290 nm ultra-violet light emitting diodes with 2.8% external quantum efficiency*, Applied Physics Letters **112**, 071107 (2018).

[215] S. M. Sadaf, Y. H. Ra, T. Szkopek, Z. Mi, *Monolithically Integrated Metal/Semiconductor Tunnel Junction Nanowire Light-Emitting Diodes*, Nano Letters **16**, 1076 (2016).

[216] S. M. Sadaf, S. Zhao, Y. Wu, Y.-H. Ra, X. Liu, S. Vanka, Z. Mi, *An AlGaN Core-Shell Tunnel Junction Nanowire Light-Emitting Diode Operating in the Ultraviolet-C Band*, Nano Letters **17**, 1212 (2017).

[217] F. Akyol, S. Krishnamoorthy, Y. Zhang, J. Johnson, J. Hwang, S. Rajan, *Low-resistance GaN tunnel homojunctions with 150 kA/cm2 current and repeatable negative differential resistance*, Applied Physics Letters **108**, 131103 (2016).

[218] D. Takasuka, Y. Akatsuka, M. Ino, N. Koide, T. Takeuchi, M. Iwaya, S. Kamiyama, I. Akasaki, *GaInN-based tunnel junctions with graded layers*, Applied Physics Express **9**, 081005 (2016).

[219] Y. Akatsuka, S. Iwayama, T. Takeuchi, S. Kamiyama, M. Iwaya, I. Akasaki, *Doping profiles in low resistive GaN tunnel junctions grown by metalorganic vapor phase epitaxy*, Applied Physics Express **12**, 025502 (2019).

[220] Y. Cho, S. Bharadwaj, Z. Hu, K. Nomoto, U. Jahn, H. G. Xing, D. Jena, *Blue (In,Ga)N light-emitting diodes with buried n^+–p^+ tunnel junctions by plasma-assisted molecular beam epitaxy*, Japanese Journal of Applied Physics **58**, 060914 (2019).

[221] F. Mehnke, C. Kuhn, M. Guttmann, L. Sulmoni, V. Montag, J. Glaab, T. Wernicke, M. Kneissl, *Fully transparent MOVPE grown AlGaN-based tunnel heterojunction LEDs emitting at 232 nm*, to be published, 2020.

[222] D. Liu, S. J. Cho, J. Park, J. Gong, J.-H. Seo, R. Dalmau, D. Zhao, K. Kim, M. Kim, A. R. K. Kalapala, J. D. Albrecht, W. Zhou, B. Moody, Z. Ma, *226 nm AlGaN/AlN UV LEDs using p-type Si for hole injection and UV reflection*, Applied Physics Letters **113**, 011111 (2018).

[223] C. G. Moe, S. Sugiyama, J. Kasai, J. R. Grandusky, L. J. Schowalter, *AlGaN Light-Emitting Diodes on AlN Substrates Emitting at 230 nm*, Physica Status Solidi (A) **215**, 1700660 (2018).

Appendix A: List of figures

Appendix B: List of abbreviations and symbols

ac	alternating current
ADF	annular dark field (TEM measurement mode)
AFM	atomic force microscopy
AlGaN	aluminum gallium nitride
Al	Aluminum (chem. element)
AlN	aluminum nitride
ArF	argon fluoride
ASE	amplified spontaneous emission
Au	Gold (chem. element)
$BaSO_4$	barium sulfate
BSF	basal plane stacking fault
CB	conduction band
CIE	carrier injection efficiency
Cp_2Mg	Biscyclopentadienyl-magnesium
cw	continuous wave
dc	direct current
DOP	degree of polarization
EBL	electron blocking layer
EL	electroluminescence
EQE	external quantum efficiency
FBH	Ferdinand-Braun-Institut, Leibniz-Institut für Höchstfrequenztechnik
FWHM	full width at half maximum
Γ	confinement factor of an optical mode
Ga	Gallium (chem. element)
GaAs	gallium arsenide
GaN	gallium nitride
GRI	growth interruption
H	Hydrogen (chem. element)
HAADF	high angle annular dark field (TEM measurement mode)
HRTEM	high resolution TEM (TEM measurement mode)
HT	high temperature
HTA	high temperature annealing
IKZ	Leibniz-Institut für Kristallzüchtung
IL	interlayer
In	Indium (chem. element)
InP	indium phosphide

IQE	internal quantum efficiency
k_B	Boltzmann constant
LD	laser diode
LED	light emitting diode
LEE	light extraction efficiency
LIV	light emission power - current - voltage
LT	low temperature
MBE	molecular beam epitaxy
Mg	Magnesium (chem. element)
MO	metalorganic (precursors)
MOCVD	metalorganic chemical vapor deposition
MOVPE	metalorganic vapor phase epitaxy
MQW	multiple quantum well
N	Nitrogen (chem. element)
Ni	Nickel (chem. element)
NDR	negative differential resistance
Pd	Palladium (chem. element)
PF	Poole-Frenkel
PL	photoluminescence
PVT	physical vapor transport
QCSE	quantum-confined Stark effect
QD	quantum dot
QW	quantum well
RSM	reciprocal space map
RTA	rapid thermal annealing
SCH	separate confinement heterostructure
SCR	space charge region
SEM	scanning electron microscopy
Si	Silicon (chem. element)
SIMS	secondary ion mass spectrometry
SPSL	short-period superlattice
STEM	scanning transmission electron microscopy
T	temperature
TDD	threading dislocation density
TEM	transmission electron microscopy
TLM	transfer length method
TJ	tunnel junction
uid	unintentionally doped
UV	ultraviolet
V	Vanadium (chem. element)
VB	valence band
VCSEL	vertical-cavity surface-emitting laser
WG	waveguide
WPE	wall-plug efficiency
x	$Al_xGa_{1-x}N$ aluminum content
XRD	X-ray diffraction

Appendix C: List of publications

Parts of this thesis have already been published in the following peer-reviewed publications

[5] T. Wernicke, L. Sulmoni, **C. Kuhn**, G. Tränkle, M. Weyers, M. Kneissl, *Group III-nitride-based UV laser diodes*, in M. Kneissl, A. Knorr, S. Reitzenstein, A. Hoffmann, Eds., *Semiconductor Nanophotonics - Materials, Models, Devices*, Springer (2020).

[142] **C. Kuhn**, L. Sulmoni, M. Guttmann, J. Glaab, N. Susilo, T. Wernicke, M. Weyers, M. Kneissl, *MOVPE-grown AlGaN-based tunnel heterojunctions enabling fully transparent UVC LEDs*, Photonics Research **7**, B7 (2019).

[119] M. Guttmann, J. Höpfner, C. Reich, L. Sulmoni, **C. Kuhn**, P. Röder, T. Wernicke, M. Kneissl, *Effect of quantum barrier composition on electro-optical properties of AlGaN-based UVC light emitting diodes*, Semiconductor Science and Technology **34**, 085007 (2019).

[42] J. Enslin, A. Knauer, A. Mogilatenko, F. Mehnke, M. Martens, **C. Kuhn**, T. Wernicke, M. Weyers, M. Kneissl, *Determination of Sapphire Off-Cut and Its Influence on the Morphology and Local Defect Distribution in Epitaxially Laterally Overgrown AlN for Optically Pumped UVC Lasers*, Physica Status Solidi A **216**, 1900682 (2019).

[49] **C. Kuhn**, T. Simoneit, M. Martens, T. Markurt, J. Enslin, F. Mehnke, K. Bellmann, T. Schulz, M. Albrecht, T. Wernicke, M. Kneissl, *MOVPE Growth of Smooth and Homogeneous $Al_{0.8}Ga_{0.2}N$:Si Superlattices as UVC Laser Cladding Layers*, Physica Status Solidi A **215**, 1800005 (2018).

[66] **C. Kuhn**, M. Martens, F. Mehnke, J. Enslin, P. Schneider, C. Reich, F. Krueger, J. Rass, J. B. Park, V. Kueller, A. Knauer, T. Wernicke, M. Weyers, M. Kneissl, *Influence of waveguide strain and surface morphology on AlGaN-based deep UV laser characteristics*, Journal of Physics D: Applied Physics **51**, 415101 (2018).

[123] M. Martens, **C. Kuhn**, T. Simoneit, S. Hagedorn, A. Knauer, T. Wernicke, M. Weyers, M. Kneissl, *The effects of magnesium doping on the modal loss in AlGaN-based deep UV lasers*, Applied Physics Letters **110**, 081103 (2017).

[122] M. Martens, **C. Kuhn**, E. Ziffer, T. Simoneit, V. Kueller, A. Knauer, J. Rass, T. Wernicke, S. Einfeldt, M. Weyers, M. Kneissl, *Low absorption loss p-AlGaN superlattice cladding layer for current-injection deep ultraviolet laser diodes*, Applied Physics Letters **108**, 151108 (2016).

[45] M. Martens, F. Mehnke, **C. Kuhn**, C. Reich, V. Kueller, A. Knauer, C. Netzel, C. Hartmann, J. Wollweber, J. Rass, T. Wernicke, M. Bickermann, M. Weyers, M. Kneissl, *Performance Characteristics of UV-C AlGaN-Based Lasers Grown on Sapphire and Bulk AlN Substrates*, IEEE Photonics Technology Letters **26**, 342 (2014).

[43] F. Mehnke, T. Wernicke, H. Pingel, **C. Kuhn**, C. Reich, V. Kueller, A. Knauer, M. Lapeyrade, M. Weyers, M. Kneissl, *Highly conductive n-$Al_xGa_{1-x}N$ layers with aluminum mole fractions above 80%*, Applied Physics Letters **103**, 212109 (2013).

Parts of this thesis have already been published in the following non peer-reviewed publications

- J. Enslin, A. Knauer, A. Mogilatenko, F. Mehnke, M. Martens, **C. Kuhn**, T. Wernicke, M. Weyers, M. Kneissl, *Determination of Sapphire Off-Cut and Its Influence on the Morphology and Local Defect Distribution in Epitaxially Laterally Overgrown AlN for Optically Pumped UVC Lasers (Cover Picture)*, Physica Status Solidi A **216**, 1970078 (2019).
- **C. Kuhn**, T. Simoneit, M. Martens, T. Markurt, J. Enslin, F. Mehnke, K. Bellmann, T. Schulz, M. Albrecht, T. Wernicke, M. Kneissl, *MOVPE Growth of Smooth and Homogeneous $Al_{0.8}Ga_{0.2}N$:Si Superlattices as UVC Laser Cladding Layers (Phys. Status Solidi A 11/2018) (Cover Picture)*, Physica Status Solidi A **215**, 1870032 (2018).
- M. Kneissl, F. Mehnke, **C. Kuhn**, C. Reich, M. Guttmann, J. Enslin, T. Wernicke, A. Knauer, V. Kueller, U. Zeimer, M. Lapeyrade, J. Rass, N. Lobo-Ploch, T. Kolbe, J. Glaab, S. Einfeldt, M. Weyers, *Deep Ultraviolet LEDs: From materials research to real-world applications*, IEEE Summer Topicals Meeting Series (SUM), Nassau, pp. 9-10 (2015).
- T. Wernicke, M. Martens, **C. Kuhn**, C. Reich, F. Mehnke, J. Jeschke, M. Feneberg, J. Rass, J. Enslin, M. Lapeyrade, U. Zeimer, A. Mogilatenko, S. Einfeldt, V. Kueller, S. Hagedorn, A. Knauer, C. Hartmann, J. Wollweber, R. Goldhahn M. Bickermann, M. Weyers, M. Kneissl, *Challenges for AlGaN Based UV Laser Diodes, Light, Energy and the Environment* Optical Society of America, paper DM2D.4 (2015).

In addition, the following scientific articles that are not part of this thesis have been published

- C. Trager-Cowan, A. Alasmari, W. Avis, J. Bruckbauer, P. R. Edwards, B. Hourahine, S. Kraeusel, G. Kusch, R. Johnston, G. Naresh-Kumar, R. W. Martin, M. Nouf-Allehiani, E. Pascal, L. Spasevski, D. Thomson, S. Vespucci, P. J. Parbrook, M. D. Smith, J. Enslin, F. Mehnke, M. Kneissl, **C. Kuhn**, T. Wernicke, S. Hagedorn, A. Knauer, V. Kueller, S. Walde, M. Weyers, P.-M. Coulon, P. A. Shields, Y. Zhang, L. Jiu, Y. Gong, R. M. Smith, T. Wang, A. Winkelmann,

Scanning electron microscope as a flexible tool for investigating the properties of UV-emitting nitride semiconductor thin films, Photonics Research **7**, B73 (2019).

- J. Glaab, J. Haefke, J. Ruschel, M. Brendel, J. Rass, T. Kolbe, A. Knauer, M. Weyers, S. Einfeldt, M. Guttmann, **C. Kuhn**, J. Enslin, T. Wernicke, M. Kneissl, *Degradation effects of the active region in UV-C light-emitting diodes*, Journal of Applied Physics **123**, 104502 (2018).
- N. Susilo, S. Hagedorn, D. Jaeger, H. Miyake, U. Zeimer, C. Reich, B. Neuschulz, L. Sulmoni, M. Guttmann, F. Mehnke, **C. Kuhn**, T. Wernicke, M. Weyers, M. Kneissl, *AlGaN-based deep UV LEDs grown on sputtered and high temperature annealed AlN/sapphire*, Applied Physics Letters **112**, 041110 (2018).
- K. Bellmann, U. W. Pohl, **C. Kuhn**, T. Wernicke, M. Kneissl, *Controlling the morphology transition between step-flow growth and step-bunching growth*, Journal of Crystal Growth **478**, 187 (2017).
- F. Mehnke, M. Guttmann, J. Enslin, **C. Kuhn**, C. Reich, J. Jordan, S. Kapanke, A. Knauer, M. Lapeyrade, U. Zeimer, H. Krüger, M. Rabe, S. Einfeldt, T. Wernicke, H. Ewald, M. Weyers, M. Kneissl, *Gas Sensing of Nitrogen Oxide Utilizing Spectrally Pure Deep UV LEDs*, IEEE Journal of Selected Topics in Quantum Electronics **23**, 2000108 (2017).
- J. Enslin, F. Mehnke, A. Mogilatenko, K. Bellmann, M. Guttmann, **C. Kuhn**, J. Rass, N. Lobo-Ploch, T. Wernicke, M. Weyers, M. Kneissl *Metamorphic $Al_{0.5}Ga_{0.5}N$:Si on AlN/sapphire for the growth of UVB LEDs*, Journal of Crystal Growth **464**, 185 (2017).
- M. Lapeyrade, J. Glaab, A. Knauer, **C. Kuhn**, J. Enslin, C. Reich, M. Guttmann, F. Mehnke, T. Wernicke, S. Einfeldt, M. Weyers, M. Kneissl, *Design considerations for AlGaN-based UV LEDs emitting near 235 nm with uniform emission pattern*, Semiconductor Science and Technology **32**, 045019 (2017).
- M. Lapeyrade, S. Alame, J. Glaab, A. Mogilatenko, R.-S. Unger, **C. Kuhn**, T. Wernicke, P. Vogt, A. Knauer, U. Zeimer, S. Einfeldt, M. Weyers, M. Kneissl, *Effect of Cl_2 plasma treatment and annealing on vanadium based metal contacts to Si-doped $Al_{0.75}Ga_{0.25}N$* Journal of Applied Physics **122**, 125701 (2017).
- J. Glaab, N. Lobo Ploch, J. Rass, T. Kolbe, T. Wernicke, F. Mehnke, **C. Kuhn**, J. Enslin, C. Stoelmacker, V. Kueller, A. Knauer, S. Einfeldt, M. Weyers, M. Kneissl, *Influence of the LED heterostructure on the degradation behavior of (InAlGa)N-based UV-B LEDs*, Proc. of SPIE Vol. **9748**, 97481O-1 (2016).
- J. Glaab, C. Ploch, R. Kelz, C. Stölmacker, M. Lapeyrade, N. Lobo Ploch, J. Rass, T. Kolbe, S. Einfeldt, F. Mehnke, **C. Kuhn**, T. Wernicke, M. Weyers, M. Kneissl, *Temperature induced degradation of InAlGaN multiple-quantum well UV-B LEDs*, Mater. Res. Soc. Symp. Proc. Vol. **1792**, Mrss15-2102646 (2015).
- F. Mehnke, **C. Kuhn**, J. Stellmach, T. Kolbe, N. Lobo-Ploch, J. Rass, M.-A. Rothe, C. Reich, N. Ledentsov Jr., M. Pristovsek, T. Wernicke, M. Kneissl, *Effect of heterostructure design on carrier injection and emission characteristics of 295 nm light emitting diodes*, Journal of Applied Physics **117**, 195704 (2015).
- U. Zeimer, J. Jeschke, A. Mogilatenko, A. Knauer, V. Kueller, V. Hoffmann, **C. Kuhn**, T. Simoneit, M. Martens, T. Wernicke, M. Kneissl, M. Weyers, *Spatial*

inhomogeneities in $Al_xGa_{1-x}N$ quantum wells induced by the surface morphology of AlN/sapphire templates, Semiconductor Science and Technology **30**, 114008 (2015).

- C. Reich, M. Guttmann, M. Feneberg, T. Wernicke, F. Mehnke, **C. Kuhn**, J. Rass, M. Lapeyrade, S. Einfeldt, A. Knauer, V. Kueller, M. Weyers, R. Goldhahn, M. Kneissl, *Strongly transverse-electric-polarized emission from deep ultraviolet AlGaN quantum well light emitting diodes*, Applied Physics Letters **107**, 142101 (2015).
- J. Glaab, C. Ploch, R. Kelz, C. Stölmacker, M. Lapeyrade, N. Lobo-Ploch, J. Rass, T. Kolbe, S. Einfeldt, F. Mehnke, **C. Kuhn**, T. Wernicke, M. Weyers, M. Kneissl, *Degradation of (InAlGa)N-based UV-B light emitting diodes stressed by current and temperature*, Journal of Applied Physics **118**, 094504 (2015).
- G. Kusch, M. Nouf-Allehiani, F. Mehnke, **C. Kuhn**, P. R. Edwards, T. Wernicke, A. Knauer, V. Kueller, G. Naresh-Kumar, M. Weyers, M. Kneissl, C. Trager-Cowan, R. W. Martin, *Spatial clustering of defect luminescence centers in Si-doped low resistivity $Al_{0.82}Ga_{0.18}N$*, Applied Physics Letters **107**, 072103 (2015).
- J. Jeschke, M. Martens, A. Knauer, V. Kueller, U. Zeimer, C. Netzel, **C. Kuhn**, F. Krueger, C. Reich, T. Wernicke, M. Kneissl, M. Weyers *UV-C Lasing From AlGaN Multiple Quantum Wells on Different Types of AlN/Sapphire Templates*, IEEE Photonics Technology Letters **27**, 1969 (2015).
- M. Lapeyrade, F. Eberspach, J. Glaab, N. Lobo-Ploch, C Reich, **C. Kuhn**, M. Guttmann, T. Wernicke, F. Mehnke, S. Einfeldt, A. Knauer, M. Weyers, M. Kneissl, *Current spreading in UV-C LEDs emitting around 235 nm*, Proc. of SPIE Vol. **9363**, 93631P (2015).
- J. Rass, T. Kolbe, N. Lobo Ploch, T. Wernicke, F. Mehnke, **C. Kuhn**, J. Enslin, M. Guttmann, C. Reich, A. Mogilatenko, J. Glaab, C. Stoelmacker, M. Lapeyrade, S. Einfeldt, M. Weyers, M. Kneissl, *High power UV-B LEDs with long lifetime*, Proc. of SPIE Vol. **9363**, 93631K (2015).
- F. Mehnke, **C. Kuhn**, M. Guttmann, C. Reich, T. Kolbe, V. Kueller, A. Knauer, M. Lapeyrade, S. Einfeldt, J. Rass, T. Wernicke, M. Weyers, M. Kneissl, *Efficient charge carrier injection into sub-250 nm AlGaN multiple quantum well light emitting diodes*, Applied Physics Letters **105**, 051113 (2014).
- T. Kolbe, F. Mehnke, M. Guttmann, **C. Kuhn**, J. Rass, T. Wernicke, M. Kneissl, *Improved injection efficiency in 290 nm light emitting diodes with Al(Ga)N electron blocking heterostructure*, Applied Physics Letters **103**, 031109 (2013).

Conference contributions and presentations

- C. Kuhn, *Tunnel junctions for UV lasers*, **Invited talk**, 1st International Workshop on AlGaN based UV-Laserdiodes 2019, JDZB, Berlin, Germany.
- C. Kuhn, *Epitaxial growth of AlGaN-based UVC LEDs and UVC laser diodes*, **Invited talk**, Seminar 2019, CRHEA, Valbonne, France.
- C. Kuhn, L. Sulmoni, M. Guttmann, J. Glaab, T. Wernicke, M. Weyers, M. Kneissl, *MOVPE grown AlGaN-based tunnel junctions enabling fully transparent UVC LEDs*, IWUMD 2018, Kunming, China.
- C. Kuhn, L. Sulmoni, M. Guttmann, J. Glaab, T. Wernicke, M. Weyers, M. Kneissl, *MOVPE grown AlGaN-based tunnel junctions enabling fully transparent UVC LEDs with high efficiency*, DGKK 2018, Paderborn, Germany.
- C. Kuhn, A. Muhin, M. Guttmann, N. Susilo, L. Sulmoni, T. Wernicke, M. Kneissl, *Electrical conduction in high aluminum mole fraction Mg-doped $Al_xGa_{1-x}N$ superlattices in UVC laser diode heterostructures*, ICMOVPE 2018, Nara, Japan.
- C. Kuhn, M. Guttmann, A. Muhin, M. Martens, N. Susilo, F. Mehnke, L. Sulmoni, T. Wernicke, M. Kneissl, *$Al_xGa_{1-x}N$:Mg short-period superlattice cladding layers with $x \geq 0.6$ for UVC laser diodes*, DPG spring meeting 2018, Berlin, Germany.
- C. Kuhn *Comparison of UVC LEDs grown on bulk AlN and sapphire substrates*, Seminar Kneissl workgroup 2017, Technische Universität Berlin, Germany.
- C. Kuhn, T. Teke, M. Guttmann, L. Sulmoni, A. Knauer, K. Bellmann, C. Hartmann, A. Dittmar, J. Wollweber, T. Wernicke, M. Bickermann, M. Weyers, M. Kneissl, *Comparison of UVC LEDs grown on bulk AlN and sapphire substrates*, E-MRS Fall Meeting 2017, Warsaw, Poland.
- C. Kuhn, *MOVPE growth of AlGaN for UVC emitters*, **Invited talk**, Nitride semiconductor seminar 2017, Department of Materials Science and Engineering, Meijo University, Nagoya, Japan.
- C. Kuhn, *MOVPE growth of AlGaN-based UVC lasers*, UV meeting 2016, Department of Materials Science and Engineering, Meijo University, Nagoya, Japan.
- C. Kuhn, *MOVPE growth of AlGaN-based UVC lasers*, School of Nanophotonics PhD student seminar 2016, Technische Universität Berlin, Germany.
- C. Kuhn, T. Simoneit, T. Markurt, J. Enslin, M. Martens, F. Mehnke, K. Bellmann, T. Schulz, M. Albrecht, T. Wernicke, M. Kneissl, *Smooth and homogeneous $Al_{0.8}Ga_{0.2}N$:Si superlattice cladding layers for deep UV laser diodes*, IWN 2016, Orlando, Florida, USA.
- C. Kuhn, F. Mehnke, T. Wernicke, J. Stellmach, M. Guttmann, C. Reich, T. Kolbe, J. Rass, V. Kueller, A. Knauer, M. Weyers, M. Kneissl, *Smooth and uniform $Al_{0.8}Ga_{0.2}N$:Si superlattice cladding layers for UV-C laser diodes*, DPG spring meeting 2016, Regensburg, Germany.
- C. Kuhn, M. Martens, F. Mehnke, T. Simoneit, F. Krueger, A. Knauer, V. Kueller, M. Lapeyrade, S. Einfeldt, T. Wernicke, M. Weyers, M. Kneissl, *MOVPE growth of p-AlGaN superlattices for UV-C lasers*, SPIE Photonics West 2016, San Francisco, California, USA.

- C. Kuhn, *Surface morphology and strain analysis of high aluminum content AlGaN layers for deep UV light emitters*, 29th International Workshop Heimbach 2015, Heldrungen, Germany.
- C. Kuhn, M. Martens, T. Wernicke, F. Mehnke, P. Schneider, C. Reich, F. Krueger, J. B. Park, V. Kueller, A. Knauer, J. Rass, M. Lehmann, M. Weyers, M. Kneissl, *Growth of AlGaN quantum well UV-C lasers on sapphire by MOVPE*, ISGN 2014, Atlanta, Georgia, USA.
- C. Kuhn, F. Mehnke, T. Wernicke, J. Stellmach, M. Guttmann, C. Reich, T. Kolbe, J. Rass, V. Kueller, A. Knauer, M. Weyers, M. Kneissl, *Sub 250 nm LEDs with enhanced charge carrier injection*, DPG spring meeting 2014, Dresden, Germany.
- C. Kuhn *Heterostructure design and efficiency of UV-B LEDs*, Seminar Kneissl workgroup 2013, Technische Universität Berlin, Germany.
- C. Kuhn, F. Mehnke, T. Wernicke, J. Stellmach, M. Guttmann, C. Reich, T. Kolbe, J. Rass, V. Kueller, A. Knauer, M. Weyers, M. Kneissl, *Comparison of different carrier injection mechanisms in 290 nm LEDs*, DPG spring meeting 2013, Regensburg, Germany.
- C. Kuhn, F. Mehnke, T. Wernicke, J. Stellmach, K. Bellmann, V. Kueller, A. Knauer, M. Weyers, M. Pristovsek, M. Kneissl, *Einfluss der MOVPE Wachstumsbedingungen auf die Oberflächenmorphologie von (0001) AlN-Schichten*, DGKK 2012, Erlangen, Germany.
- C. Kuhn, F. Mehnke, J. Stellmach, T. Kolbe, M.-A. Rothe, M. Martens, T. Wernicke, M. Pristovsek, M. Kneissl, *AlGaN-based UV-LEDs and LDs*, 26th International Workshop Heimbach 2012, Taltitz, Germany.

Appendix D:
List of growth samples

Figure 1.1	E4422-2, E4422-11, TS1892-2, TS2152, TS2167, TS2672, TS2675
Figure 3.2	E4448-4_CH761-1-3
Figure 3.3	E4448-4_CH761-1-3
Figure 3.4	TS4378, TS4381, TS4389, TS4391
Figure 3.5	TS4359, TS4373, TS4378, TS4379, TS4381, TS4383, TS4389, TS4391
Figure 3.6	TS4359, TS4373, TS4378, TS4381, TS4383, TS4389, TS4391
Figure 3.7	TS3218, TS3235, TS3238
Figure 3.8	TS3218, TS3220, TS3223, TS3235, TS3238
Figure 3.9	TS3218, TS3220, TS3223, TS3235, TS3238
Figure 3.10	TS3218, TS3464, TS3620
Figure 3.11a	TS3218, TS3220, TS3223, TS3235, TS3238, TS3253, TS3265, TS3269, TS3269, TS3275, TS3289, TS3290, TS3293, TS3294, TS3305, TS3306, TS3308, TS3334, TS3337, TS3342, TS3345, TS3348, TS3351, TS3387, TS3435, TS3435, TS3437, TS3437, TS3463, TS3464, TS3468, TS3546, TS3777, TS3793, TS3794, TS3796, TS3799, TS3800, TS3811, TS3828, TS3917, TS3954, TS3974, TS3982, TS4050, TS4080, TS4249, TS4330, TS4335, TS4354, TS4358, TS4359, TS4373, TS4378, TS4379, TS4381, TS4383, TS4389, TS4391
Figure 3.11b	TS3218, TS3223, TS3275, TS3294, TS3334, TS3337, TS3437, TS3437, TS3464, TS3546, TS3777, TS3917, TS3954, TS4050, TS4197, TS4330, TS4335, TS4358, TS4359
Figure 3.12	TS3218, TS3223, TS3275, TS3294, TS3334, TS3337, TS3437, TS3437, TS3464, TS3546, TS3777, TS3917, TS3954, TS4050, TS4197, TS4359
Figure 3.13	TS3275, TS3334, TS3337
Figure 3.14	TS3218, TS3275, TS3334, TS3337, TS3437, TS3464, TS3546
Figure 3.15	TS3218, TS3620
Figure 3.16	TS3218, TS3595
Figure 3.17	TS3592, TS3617
Figure 3.18	TS3589, TS3592, TS3617, TS3680
Figure 3.19	TS3592, TS3617
Figure 3.20	TS3592, TS3617
Figure 3.21	TS3218, TS3620

Figure 3.22	same as Figure 3.11a plus TS3586, TS3589, TS3592, TS3595, TS3598, TS3601, TS3604, TS3605, TS3610, TS3611, TS3614, TS3617, TS3620, TS3623, TS3625, TS3628, TS3630, TS3632, TS3642, TS3664, TS3668, TS3671, TS3673, TS3676, TS3680, TS3833, TS3839, TS3845, TS3855, TS3937, TS3942, TS3956, TS3994, TS4034, TS4338, TS4343
Figure 3.23	TS2669
Figure 3.24	TS1637, TS1696, TS2669
Figure 3.25	TS1892, TS2167
Figure 3.26	TS4535-1, TS4564-1, TS4575-1
Figure 3.27	TS4045-1
Figure 3.28	TS4509-1, TS5199-1, TS4640-1
Figure 3.29	TS4645, TS4662, TS4674, TS4681
Figure 3.30	TS4645, TS4681
Figure 3.31	TS1892, TS2167, TS4045, TS4048
Figure 3.32	TS1892, TS2167, TS4045, TS4048
Figure 3.33	TS4048
Figure 3.34	TS2672
Figure 4.2	TS4514-2, TS4514-1
Figure 4.3	TS4056-2H, TS4056-3
Figure 4.4	TS4051-2H, TS4051-3
Figure 4.5	TS4051-2H, TS4051-3, TS4056-2H, TS4056-3
Figure 4.6	TS3526, TS3527, TS3530, TS3532, TS3533, TS3535
Figure 4.7	TS3526, TS3527, TS3530, TS3532, TS3533, TS3535
Figure 4.8	TS3530, TS3532
Figure 4.9b	TS3993, TS3995, TS3997, TS4001, TS4015, TS4025, TS4027
Figure 4.11	TS4099, TS4104, TS4106, TS4109, TS4111
Figure 4.13	TS4099, TS4122, TS4125, TS4126, TS4127
Figure 4.15b	TS4099, TS4122, TS4125, TS4126, TS4127
Figure 4.16	TS4099, TS4122, TS4125, TS4126, TS4127
Figure 4.18	TS1696, TS1850-3, TS2669, TS2672, TS2684, TS2739, TS2783, TS2789, TS2793, TS3417, TS3420, TS3434, TS3935, TS3939, TS3946, TS3950, TS3993, TS3997, TS4001, TS4015, TS4025, TS4027, TS4056-2H, TS4056-3, TS4099, TS4122, TS4126, TS4359, TS4373, TS4378, TS4379, TS4381, TS4383, TS4389, TS4391, TS4442, TS4517
Figure 5.6	TS4697, TS4705, TS4706, TS4708, TS4711
Figure 5.7a	TS4603
Figure 5.7b	TS4614
Figure 5.7c	TS4614
Figure 5.8a	TS3418, TS3420
Figure 5.8b	TS3418, TS3420, TS3489, TS3497
Figure 5.9	TS3418, TS3420
Figure 5.10	TS4735
Figure 5.11a	TS4735
Figure 5.11b	TS4737, TS4743

Acknowledgements

I want to thank all the people who supported me in the last years. First of all, I would like to thank my doctoral supervisor Michael Kneissl for giving me the opportunity to work in his group and to research UV LEDs and lasers. I would also like to thank Jean-Yves Duboz and Markus Weyers for reviewing this thesis.

Thank you Tim Wernicke for his mostly quick and always helpful feedback regarding any scientific enquiry. A very insightful and unique scientific and cultural experience during my research stay in Japan was made possible by Tetsuya Takeuchi and his group members at Meijo university in Nagoya, supported by the School of Nanophotonics, that I will never forget.

I'm glad to have gotten the chance to assist and work together with my students Felix Krüger, Tolga Teke, Tino Simoneit, Pascal Röder, and Jan Klos, as well as the guest students Ivan Gamov and Hisanori Kojima. In their own way they were enriching my research, challenging my patience, questioning and answering problems, and expanding my horizon.

I enjoyed gathering knowledge about the nitride MOVPE system(s) and teaching what I learned as part of the epitaxy team at TU Berlin together with my colleagues Frank Mehnke, Joachim Stellmach, Konrad Bellmann, Martin Frentrup, Christian Meißner, Johannes Enslin, Norman Susilo, Humberto Foronda, as well as Matthias Dreier, Kathrin Schatke, and René Linke. A special "thank you" goes to Praphat Sonka. After introducing him to the MOVPE system, he supported dozens of my runs, and meanwhile I started to learn from his experience gathered on good and bad days running the MOVPE reactor.

The heterostructure variations in this work would not have been possible without the continuous supply of excellent templates and substrates from Viola Küller, Arne Knauer, Sylvia Hagedorn, Sebastian Walde, as well as Carsten Hartmann and Matthias Bickermann. For several device fabrication processes I want to thank Mickael Lapeyrade, Ji-Hye Kang, and Sven Einfeldt, as well as Luca Sulmoni. Various different simulations and measurements supporting my work were performed by Martin Martens, Martin Guttmann, Christoph Reich, Anton Muhin, Bettina Belde, Verena Montag, Carsten Netzel, Ute Zeimer, Johannes Glaab, Jan Ruschel, Jae-Bum Park, Anna Mogilatenko, Toni Markurt, and Leonardo Cancellara. Furthermore, I want to thank Neysha Lobo-Ploch, Jessica Schlegel, Jens Raß, Daria Skuridina, Farsane Tabataba-Vakili, Jörg Jeschke, Priti Gupta, Shaojun Wu, Giulia Cardinali, and all the members of the group that have not only been supportive during scientific discussions but also during numerous social activities, just to mention a few, karaoke nights and bike trips.

Finally, I want to say "thank you" to my family, my friends, Bettina, Nadine, Sina and all the important people for more than just proofreading but accompanying and supporting me in this phase of my life.